Title

Galaxies in the Young Universe: Structures, Masses, and Composition of Star-Forming Galaxies at z~1.5-3

Author

Price, Sedona H.

Publication Date

2017

Galaxies in the Young Universe:
Structures, Masses, and Composition of Star-Forming Galaxies at $z \sim 1.5 - 3$

By

Sedona H. Price

A dissertation submitted in partial satisfaction of the

requirements for the degree of

Doctor of Philosophy

in

Astrophysics

in the

Graduate Division

of the

University of California, Berkeley

Committee in charge:

Professor Mariska Kriek, Chair
Professor Adrian Lee
Professor Chung-Pei Ma

Summer 2017

Galaxies in the Young Universe:
Structures, Masses, and Composition of Star-Forming Galaxies at $z \sim 1.5 - 3$

Abstract

Galaxies in the Young Universe:
Structures, Masses, and Composition of Star-Forming Galaxies at $z \sim 1.5 - 3$

by

Sedona H. Price

Doctor of Philosophy in Astrophysics

University of California, Berkeley

Professor Mariska Kriek, Chair

Understanding the physical processes governing galaxy growth and evolution remains an outstanding challenge in astronomy. Constraining these processes requires observations at multiple epochs, but despite exquisite observations of galaxies in the local universe, relatively little is known about galaxies at early times. In the last decade, large photometric surveys have revealed many details about galaxies across the past 10 billion years. However, fully understanding galaxies in the early universe and how they connect to today's galaxy population requires observations of their physical properties through spectroscopy as well as photometry. Recent instrumentation advances have now paved the way for spectroscopic surveys of large samples of distant galaxies, which provide key insights into the earlier phases of galaxy evolution.

In this dissertation, I use detailed photometric and spectroscopic observations and simulations to investigate the dust content, masses, and kinematic structures of star-forming galaxies at $z \sim 1.5 - 3$, near the peak of cosmic star formation. I present results using *Hubble Space Telescope* (*HST*) grism observations of an unbiased sample of galaxies at $z \sim 1.5$ from the 3D-HST survey to measure the relation between nebular and stellar dust attenuation. These constraints on the dust content of distant galaxies enable accurate measurements of star formation rates, and help to characterize the dust distribution in early galaxies.

I also investigate the internal kinematics of galaxies at $z \sim 1.5 - 3$ using moderate-resolution near-infrared spectra from the MOSDEF survey with Keck/MOSFIRE together with high spatial-resolution *HST* imaging. I develop a set of models to measure and interpret kinematics from spectra taken with galaxy-slit misalignments, including galaxies without spatially-resolved spectra. I then use these models to derive independent, dynamical estimates of the galaxy masses, and to constrain the amount of support from ordered versus random motions for hundreds of galaxies with $M_* \sim 10^9 - 10^{11.5} M_\odot$. Additionally, I explore the correlation of kinematic structure with other properties and constrain how the dark matter fraction in star-forming galaxies changes over time.

Finally, I use mock observations of galaxies from the high-resolution MassiveFIRE cosmological simulation suite to determine how well intrinsic galaxy sizes and stellar masses are recovered from observations. I also explore the impact of random viewing angles on observed galaxy properties, which has implications for the interpretation of the scatter in galaxy scaling relations.

To everyone who reminded me to look down to Earth and not just up,
and to always keep moving forward.

Contents

Acknowledgments

Many people shaped this dissertation — without them, I could not have completed this work. This includes more people than I can name here, but I am grateful to all of you for sharing your wisdom, encouragement, and love.

This dissertation would not have been possible without the guidance and support of my advisor, Mariska Kriek. Thank you for your advice, support, and patience throughout my time at Berkeley! I had also the privilege to work with and learn from a number of fantastic people in multiple collaborations during my dissertation. Some of this research was carried out as a member of the 3D-HST and MOSDEF collaborations, but I also had the pleasure to work with the FIRE collaboration. Many thanks to everyone in these collaborations for enriching scientific discussions, your contributions to my projects, and your part in obtaining (and creating) fantastic observational and simulation data sets.

I am indebted to many of my colleagues at Berkeley. I thank Guillermo Barro, Robert Feldmann, Ryan Trainor, Freeke van de Voort, Peter Behroozi, James McBride, and Chung-Pei Ma for their guidance, conversations, and encouragement. Furthermore, I am indefinitely grateful for the administrative staff of the Berkeley Astronomy Department, including Dexter Stewart and Nina Ruymaker. I also thank Peter Williams for creating the ucastrothesis LaTeX template, which was used to typeset this dissertation.

Additionally, this journey has been strongly shaped by my research mentors before coming to Berkeley. Thank you to Joel Bergé and Jason Rhodes for the great summers at JPL, Kristin Madsen and Fiona Harrison for my first summer project at Caltech, Carrie Bridge for your guidance during my senior year at Caltech, and Cathy Cahill for mentoring me during my foray into atmospheric chemistry.

To my many friends here in the Bay Area: Andrew, Daniel, Austin, Casey, Melanie, Tom, Lauren, Lea, Wren, Abi, Paul, Karto, Francesca, and the rest of my undergrad friends and the BAD grads — thank you for the fun times, I wish they could last longer. My home and couch will always be open to you, and I hope to see you many times in the years to come.

Finally, I would like to thank my family for their support during my educational endeavors. I cannot imagine being at the end of this process without your encouragement of my studies from the beginning. Thank you to Channon for your patience when I was studying instead of hanging out with you, and later for joining me on world travels and for your guidance as I learned more sophisticated coding practices. And last, to Papa — thank you for the years of physics and fun. Here's to many more.

Chapter 1

Introduction

1.1 Galaxy evolution: the multi-billion year problem

Understanding how galaxies grow and evolve is a key problem in astronomy. This question spans billions of years: how did very small baryon density perturbations existing at recombination, 380,000 years after the Big Bang, grow and evolve into the galaxies we see today, some 13.4 billion years later?

Cosmic microwave background (CMB) temperature anisotropies show that baryons had density perturbations of order $\sim 10^{-4}$ at recombination (e.g., Sachs & Wolfe 1967, White & Hu 1997, Planck Collaboration et al. 2014), which would be unable to grow to the matter over-densities of modern-day galaxies within the age of the universe. However, under the Λ cold dark matter (ΛCDM) cosmological model, baryons are able to cool and collapse within dark matter halos, aiding the formation of stars and galaxies. Within this framework, the first collapsed structures then grow into larger galaxies, galaxy groups, and galaxy clusters by merging with other structures. This hierarchical structure formation model successfully describes much of the large-scale structure of matter in the universe (e.g., Springel et al. 2005, Boylan-Kolchin et al. 2009, Angulo et al. 2012).

However, ΛCDM cosmology cannot fully predict properties on small scales as it does not account for baryonic physics. These physical processes — including star formation, stellar winds, supernovæ and active galactic nuclei (AGN) feedback, and chemical evolution — all impact galaxy structure and growth. Indeed, there are many galaxy properties that do not appear to be predicted by halo mass alone, and thus reflect the complex, intertwined effects of both gravitational and baryonic processes.

For instance, present-day galaxies exhibit a color bimodality between red, passive galaxies and blue, star-forming galaxies (e.g., Blanton et al. 2003, Hogg et al. 2003, Kauffmann et al. 2003a, Baldry et al. 2004). This split between blue and red galaxies correlates with mass and environment (e.g., Hogg et al. 2004, Kauffmann et al. 2004, Blanton et al. 2005, Baldry et al. 2006), but is not uniquely predicted by either. Morphology also correlates with this bimodality, with many blue galaxies exhibiting disk-like structures and red galaxies having elliptical shapes (e.g., Roberts & Haynes 1994, Blanton et al. 2003, Kauffmann et al. 2004, Schawinski et al. 2014), but again galaxy shape does not appear to be fully determined by either mass or environment, reflecting the impact of other (possibly correlated) physical processes.

In recent years, numerous studies have characterized the detailed properties of local galaxies (e.g., Bacon et al. 2001, Kennicutt, Jr. et al. 2003, Abazajian et al. 2009, Cappellari et al. 2011, Bryant et al. 2015, Bundy et al. 2015). These observations reveal there are a number of general global scaling relations between galaxy properties, but also a staggering diversity within the nearby galaxy population. Models of galaxy evolution must be able to match both these general trends and the range of observed features.

Galaxy formation models — including both semi-analytical models (e.g., Dalcanton et al. 1997, Mo et al. 1998, van den Bosch 2001, Dutton 2009) and hydrodynamical simulations (e.g., Governato et al. 2007, Hopkins et al. 2014, Schaye et al. 2014, Vogelsberger et al. 2014, Davé et al. 2017) — are now able to reproduce a number of these local galaxy properties. However, in order to fully test these formation models and to further constrain how baryonic processes impact galaxy evolution, direct observations of galaxy populations across the history of the universe are necessary.

1.2 Observations of distant galaxies

While nearby galaxies are fairly well-studied, distant galaxies are much more poorly understood. Recent large surveys, including the NMBS (Whitaker et al. 2011), CANDELS (Grogin et al. 2011, Koekemoer et al. 2011), 3D-HST (van Dokkum et al. 2011, Brammer et al. 2012), UltraVISTA (McCracken et al. 2012, Muzzin et al. 2013a), and ZFOURGE (Straatman et al. 2016) surveys have provided crucial insights into the nature of galaxies across most of the history of the universe.

These observations have revealed a number of trends in how galaxy properties evolve. Stellar mass functions (SMFs) trace how stellar mass builds up in galaxy populations over billions of years (e.g., Muzzin et al. 2013b, Tomczak et al. 2014). Measurements of galaxy star-formation rates (SFRs) show that the bimodality between star-forming and quiescent galaxies and the tight relation between mass and SFR of star-forming galaxies (Brinchmann et al. 2004) were already in place by $z \sim 2.5$ (e.g., Whitaker et al. 2012b; Whitaker et al. 2011). These observations also reveal that on average, nearby galaxies are forming stars much less rapidly than in the past. The average cosmic SFR density increases looking back over the past $\sim$10 billion years, but then decreases as we look to even earlier times (e.g., Madau & Dickinson 2014).

Additionally, detailed imaging has shown distant galaxies had very different sizes and structures than their local counterparts. At fixed mass, galaxies were smaller at earlier times (e.g., van der Wel et al. 2014a). In particular, many of the most massive quiescent galaxies at $z \gtrsim 2$ are very compact relative to today's massive quiescent galaxies (e.g., Barro et al. 2013), and are even smaller than the massive star-forming galaxies found at similar times (e.g., Förster Schreiber et al. 2009, Kriek et al. 2009a).

While these studies have greatly expanded our understanding of distant galaxies, many questions remain. These include: How are the inter-stellar medium (ISM) and dust properties of these galaxies different from nearby galaxies? What are the internal dynamical structures of early galaxies, and how do they evolve? Does the initial mass function (IMF) vary with time or other galaxy properties? How is star-formation regulated and eventually shut-off in some galaxies? Are the methods used to measure galaxy characteristics — including stellar masses, sizes, SFRs, star-formation histories, and internal kinematics — valid for characterizing distant galaxies? Addressing these questions requires detailed observations of the physical properties for large, complete samples of galaxies in the early universe.

1.3 Star-forming galaxies at cosmic noon

The epoch of peak cosmic star formation — "cosmic noon", from $z \sim 1-3$ (e.g., Figure 9c of Madau & Dickinson 2014) — is a particularly interesting time to investigate galaxy evolution. During this period, galaxies are assembling rapidly: on average their stellar masses quintuple, growing from 5% to 25% of their present-day stellar mass in a span of just $\sim$3.5 billion years (Muzzin et al. 2013b). Moreover, compared to the local universe, star-forming galaxies dominated the stellar mass density of the universe at $z \gtrsim 1$ (Muzzin et al. 2013b, Tomczak et al. 2014). Understanding star-forming galaxies at cosmic noon and beyond is thus a crucial component of understanding the early stages of galaxy evolution.

Early work has revealed that star-forming galaxies at this time have very different (and potentially rapidly changing) properties compared to those of today's galaxies. Massive star-forming galaxies at this epoch have been shown to lack the relatively smooth thin disk morphology of similar-mass galaxies found today (e.g., Blanton & Moustakas 2009). Instead, these distant massive star-forming galaxies tend to have very clumpy morphologies (e.g., Elmegreen et al. 2007, Law et al. 2012b, Förster Schreiber et al. 2014), exhibit thicker disks (e.g., Elmegreen & Elmegreen 2006), and have higher gas fractions (e.g, Daddi et al. 2008, Tacconi et al. 2013). These studies have also demonstrated that $z \sim 1-3$ star-forming galaxies have different ISM conditions, metallicities, and dust properties compared to nearby galaxies (e.g., Reddy & Steidel 2004, Shapley et al. 2004, 2005, Erb et al. 2006a, Reddy et al. 2010; Reddy et al. 2006), and can have powerful outflows (e.g., Newman et al. 2012). Yet these studies are far from providing a complete picture of distant galaxies.

To probe the range of internal galaxy properties at cosmic noon, both high-resolution, multi-wavelength photometry and spectra are need for large samples. However, obtaining spectra of complete samples galaxies at this epoch is challenging. These objects are not only very faint, but to avoid biases against dusty and reddened galaxies, rest-frame optical (or even longer wavelength) spectra are needed. At this epoch, The rest-frame optical is unfortunately redshifted into the near-infrared (NIR) at this epoch, which is difficult to observe from the ground due to significant sky background contamination. Despite these challenges, previous work has amassed rest-frame optical spectra of $\sim$ 1000s of galaxies at $z \sim 1-3$ (e.g., Erb et al. 2006b, Kriek et al. 2008, Förster Schreiber et al. 2009, Mancini et al. 2011, Law et al.

2012b; see also Shapley 2011).

The most recent generation of NIR spectrographs have transformed studies of galaxies at cosmic noon, enabling surveys of uniformly-selected, statistical samples of galaxies. In particular, the MOSFIRE (McLean et al. 2010, 2012; on the Keck I telescope) and the KMOS (Sharples et al. 2013, 2004; at the VLT) spectrographs feature the sensitivity and spectral resolution necessary to study the physical processes within distant galaxies. Furthermore, these spectrographs feature multiplexing capabilities, which is crucial for studying large galaxy samples. The *Hubble Space Telescope* (*HST*) WFC3 grism also plays an important role in spectroscopic studies of distant galaxies, as this instrument is capable of efficiently conducting blind surveys down to relatively faint magnitudes. While the *HST*/WFC3 grism spectra are low-resolution, they provide sufficient detail to accurately measure redshifts and a number of galaxy properties (e.g., Brammer et al. 2012).

Surveys taking advantage of these new spectrographs now have observations for thousands of galaxies spanning the range of galaxy properties at $z \sim 1-3$. In particular, the 3D-HST survey (van Dokkum et al. 2011, Brammer et al. 2012) has low-resolution rest-frame optical spectra for $\sim$7000 galaxies, while the KBSS (Steidel et al. 2014), MOSDEF (Kriek et al. 2015), KMOS$^{\mathrm{3D}}$ (Wisnioski et al. 2015), and KROSS (Stott et al. 2016) surveys together have moderate resolution spectra for $\sim$3000 galaxies. These spectroscopic surveys now make it possible to address the above-mentioned outstanding questions.

1.4 Dissertation outline

In this dissertation, I use both observations and simulations to extend our understanding of galaxies at cosmic noon. Specifically, I combine photometric and spectroscopic observations for large samples of star-forming galaxies at $z \sim 1.5-3$ to characterize their structures, masses, and composition. I then use simulations to determine how accurately the masses and sizes of these galaxies are recovered.

First, in Chapter 2, I study dust attenuation and geometry in star-forming galaxies at $z \sim 1.3-1.5$ using grism spectra from the 3D-HST survey (van Dokkum et al. 2011, Brammer et al. 2012). Constraints of dust attenuation in distant galaxies are key to deriving comparable, accurate star formation rates at multiple epochs, and to understanding how dust distribution and attenuation has changed in galaxies over time.

Next, in Chapters 3 and 4, I combine spectra from the MOSDEF survey (Kriek et al. 2015) with spatially-resolved imaging and multi-band photometry of the CANDELS (Grogin et al. 2011, Koekemoer et al. 2011) and 3D-HST surveys to constrain the internal kinematics of star-forming galaxies at $z \sim 1.5-3$. Using these kinematic measurements, I measure the dynamical structures and masses of galaxies with stellar masses ranging from $\sim 10^9-10^{11.5} M_\odot$, and investigate how the kinematic properties and structures of star-forming galaxies change over time.

In Chapter 5, I use mock photometric observations of high spatial resolution cosmological simulations from the MassiveFIRE suite (Feldmann et al. 2016, Feldmann et al. 2017) to ascertain how well we recover intrinsic galaxy masses and sizes from observations. Testing the validity of the measured properties of distant galaxies is crucial for consistently studying how galaxies evolve over time.

Finally, in Chapter 6, I summarize the findings of this dissertation and discuss future directions. Furthermore, this dissertation includes three supplemental chapters. In Appendix A, I present the average photometry of the galaxies studied in Chapter 2. Appendices B and C contain detailed descriptions of the models and methods used to measure the kinematics of galaxies with and without resolved rotation, respectively, which are used in Chapters 3 and 4.

Chapter 2

Direct measurements of dust attenuation in $z \sim 1.5$ star-forming galaxies from 3D-HST: Implications for dust geometry and star formation rates

The nature of dust in distant galaxies is not well understood, and until recently few direct dust measurements have been possible. We investigate dust in distant star-forming galaxies using near-infrared grism spectra of the 3D-HST survey combined with archival multi-wavelength photometry. These data allow us to make a direct comparison between dust around star-forming regions ($A_{\mathrm{V,\,H\textsc{ii}}}$) and the integrated dust content ($A_{\mathrm{V,\,star}}$). We select a sample of 163 galaxies between $1.36 \leq z \leq 1.5$ with Hα signal-to-noise ratio ≥ 5 and measure Balmer decrements from stacked spectra to calculate $A_{\mathrm{V,\,H\textsc{ii}}}$. First, we stack spectra in bins of $A_{\mathrm{V,\,star}}$, and find that $A_{\mathrm{V,\,H\textsc{ii}}} = 1.86\,A_{\mathrm{V,\,star}}$, with a significance of $\sigma = 1.7$. Our result is consistent with the two-component dust model, in which galaxies contain both diffuse and stellar birth cloud dust. Next, we stack spectra in bins of specific star formation rate (log SSFR), star formation rate (log SFR), and stellar mass ($\log M_*$). We find that on average $A_{\mathrm{V,\,H\textsc{ii}}}$ increases with SFR and mass, but decreases with increasing SSFR. Interestingly, the data hint that the amount of extra attenuation decreases with increasing SSFR. This trend is expected from the two-component model, as the extra attenuation will increase once older stars outside the star-forming regions become more dominant in the galaxy spectrum. Finally, using Balmer decrements we derive dust-corrected Hα SFRs, and find that stellar population modeling produces incorrect SFRs if rapidly declining star formation histories are included in the explored parameter space.[1]

---

[1] This chapter has been previously published as Price *et al.*, 2014, ApJ, 788, 86, and is reproduced with the permission of all coauthors and the copyright holder. Copyright 2014, The American Astronomical Society.

2.1 Introduction

While dust makes up only a very small fraction of the baryonic mass in galaxies (Draine et al. 2007), it leaves a large signature on their spectral energy distributions (SEDs). Dust extinguishes light in a wavelength-dependent way, and therefore distorts the intrinsic SED of galaxies. This distortion, or net dust attenuation, may depend on the properties of the dust, the dust-to-star geometry, or both quantities. Therefore, recovering the intrinsic stellar SEDs from observations requires a thorough understanding of both factors.

Dust properties and geometry are studied using observations of both dust emission and attenuation. Studies of dust emission at mid- and far-infrared wavelengths have placed constraints on the composition, distribution, and mass of dust in nearby galaxies (e.g., Dale et al. 2012; Draine et al. 2007; Galliano et al. 2008). Measurements of dust attenuation are also needed to completely characterize the nature of dust, including the dust-to-star geometry.

One method of constraining the dust-to-star geometry is by comparing the integrated dust attenuation with the attenuation towards star-forming (SF) regions. Dust attenuation affecting the stellar continuum, $A_{\rm star}$, has been measured using a number of methods. These include *(i)* line of sight measurements (e.g., the MW, SMC, LMC), *(ii)* matching attenuated galaxies with unattenuated galaxies with similar intrinsic stellar populations (i.e. Calzetti et al. 2000; Wild et al. 2011), *(iii)* fitting the SED with stellar population synthesis models, including a prescription for dust, and *(iv)* the $L_{\rm IR}/L_{\rm UV}$ ratio (also known as IRX), which probes dust attenuation using energy conservation. The latter ratio is directly related to the UV continuum slope β (Meurer et al. 1999), which may be used to infer the dust content for galaxies for which no IR data is available. (See Conroy 2013 for more discussion on this topic).

Dust attenuation towards SF regions, $A_{\rm H\,II}$, has also been extensively studied in low-redshift galaxies. $A_{\rm H\,II}$ is most directly probed with recombination line flux ratios, often using the Balmer decrement Hα/Hβ. The intrinsic line ratio can be calculated given reasonable environmental parameters. As dust attenuation is wavelength dependent, the measured line ratio compared with the intrinsic ratio combined with an assumed dust law yields a measure of the amount of dust attenuation towards SF regions. This method was used by a number of studies to measure attenuation towards SF regions in nearby galaxies (e.g., Brinchmann et al. 2004; Calzetti et al. 2000; Garn & Best 2010).

By comparing $A_{\rm V,H\,II}$ and $A_{\rm V,star}$, Calzetti et al. (2000) find that there is extra dust attenuation towards star-forming regions relative to the integrated dust content for local starburst galaxies. Wild et al. (2011) expand on this work by finding that the amount of extra attenuation increases with the axial ratio and decreases with SSFR. This implies that the dust content of galaxies might have two components (e.g., Calzetti et al. 1994; Charlot & Fall 2000; Granato et al. 2000): a component associated with the short-lived birth clouds in SF regions and a diffuse component distributed throughout the ISM. In this model, the diffuse dust attenuates light from all stars, while the birth cloud dust component only attenuates light originating from the SF region.

At higher redshifts, the nature of dust attenuation is much more poorly understood.

Much of the work on dust attenuation in high-z galaxies has focused on the UV slope (e.g., Bouwens et al. 2012; Finkelstein et al. 2012; Hathi et al. 2013; Reddy et al. 2010; Reddy et al. 2012, 2006; Wilkins et al. 2011, also see Shapley 2011 for a comprehensive review), as it is relatively easy to observe. However, deviations from the Meurer et al. (1999) IRX-β relation have been found for various galaxy samples (e.g., Conroy et al. 2010; Gonzalez-Perez et al. 2013; Johnson et al. 2007; Kong et al. 2004). Additional methods of measuring attenuation in high-z galaxies include SED modeling of photometric or spectroscopic observations (e.g., Buat et al. 2012; Kriek & Conroy 2013) and comparison of star formation rate (SFR) indicators (e.g., Wuyts et al. 2013).

Direct measurements of dust attenuation toward HII regions using Balmer decrements are very challenging for $z > 0.5$ as both Hα and Hβ are shifted to the less-accessible near-infrared window. Careful survey design and instrument improvements have made measurements of the Balmer decrement possible for larger samples of intermediate redshift galaxies, e.g., between $0.4 \lesssim z \lesssim 1$ (Savaglio et al. 2005), $z \sim 0.5$ (Ly et al. 2012), and $z \sim 0.8$ (Momcheva et al. 2013; Villar et al. 2008). However, until recently Balmer decrements have been measured for only a small number of more distant galaxies (e.g., Hainline et al. 2009; Teplitz et al. 2000; van Dokkum et al. 2005; Yoshikawa et al. 2010).

Interestingly, current studies of dust properties in distant star-forming galaxies yield contrasting results. Erb et al. (2006b) and Reddy et al. (2010) find that extra attenuation towards HII regions leads to an overestimate of the Hα SFR relative to the UV slope SFR. However, Förster Schreiber et al. (2009) compare measured and predicted $L_{\mathrm{H}\alpha}$ and Hα equivalent widths and find the best agreement when $A_{\mathrm{V,\,H II}}$ includes extra attenuation relative to $A_{\mathrm{V,\,star}}$. A comparison of overlapping objects with Erb et al. (2006b) shows that the previous aperture corrections might be overestimated, which could have masked some extra attenuation. Yoshikawa et al. (2010) compare $A_{\mathrm{V,\,star}}$ from SED fitting and $A_{\mathrm{V,\,H II}}$ from Balmer decrements for a small sample and find that the high-z objects are consistent with the local universe Calzetti et al. (2000) prescription for extra dust attenuation. Additionally, Wuyts et al. (2011b; 2013), Mancini et al. (2011) and Kashino et al. (2013) find the best agreement between Hα SFRs and UV+IR/SED SFRs when extra attenuation is adopted, either the same as the Calzetti et al. (2000) relation (Mancini et al. 2011; Wuyts et al. 2011b) or a slightly lower ratio (Kashino et al. 2013; Wuyts et al. 2013). Kashino et al. (2013) also measure the Balmer decrement and find the amount of extra attenuation is lower than the Calzetti et al. (2000) relation.

These contrasting results may not be surprising, given the different and indirect methods and/or small and biased samples of most studies. Direct measurements of a statistical sample of distant galaxies are required to clarify these dust properties. This is now possible, as new NIR instruments with multiple object spectroscopy capabilities are able to measure the Balmer decrement for larger and more complete samples of high-redshift objects. In particular, the *Hubble Space Telescope*'s WFC3/G141 grism filter provides slit-less spectra, allowing for a non-targeted survey of a large number of high-redshift galaxies. The *HST* grisms also avoid atmospheric near-IR absorption.

A number of surveys, including the 3D-HST survey (Brammer et al. 2012; van Dokkum et al. 2011), CANDELS (Koekemoer et al. 2011), and the WISP survey (Atek et al. 2010), have taken advantage of the *HST* grism capabilities to survey high redshift galaxies. Domínguez et al. (2013) were the first to use WFC3 grism data to make measurements of the Balmer decrement on a large, non-targeted sample. However, as their sample was not drawn from regions of the sky with existing deep photometric coverage, they were unable to examine trends of dust versus integrated galaxy properties.

We present a statistical study of dust attenuation measured using the Balmer decrement for a large, non-targeted sample of galaxies at $z \sim 1.5$. Both rest-frame optical spectra and deep photometry are available, allowing us to compare attenuation towards HII regions with the total integrated dust attenuation and other galaxy properties, including stellar mass and SFR.

Throughout this paper we adopt a ΛCDM universe with $\Omega_m = 0.3$, $\Omega_\Lambda = 0.7$, and $H_0 = 70\,\mathrm{km\,s^{-1}\,Mpc^{-1}}$.

2.2 Data

2.2.1 Observations and catalog

Our sample is drawn from the 3D-HST survey (Brammer et al. 2012), a *Hubble Space Telescope (HST)* Treasury program adding ACS and WFC3 slit-less grism observations to the well-covered CANDELS (Koekemoer et al. 2011) fields: AEGIS, COSMOS, GOODS-S, and UDS. The 3D-HST data also include observations of the GOODS-N field from program GO-11600 (PI: B. Weiner).

In this work we use the 3D-HST WFC3/G141 grism spectra, which cover $1.1\,\mu\mathrm{m} < \lambda < 1.65\,\mu\mathrm{m}$. The raw grism dispersion is $46.5\,\text{Å}\,\mathrm{pixel}^{-1}$, but interlacing during data reduction improves the dispersion to $\sim 23\,\text{Å}\,\mathrm{pixel}^{-1}$ (corresponding to about 10 restframe $\text{Å}\,\mathrm{pixel}^{-1}$ for $z \sim 1.5$). The G141 grism has a maximum resolution of $R \sim 130$, corresponding to $\sim 110\,\text{Å}$ in the middle of our wavelength range.

The 3D-HST survey makes use of existing deep photometric coverage in each of the survey fields, combining the grism spectra with multi-wavelength photometric data. The 3D-HST photometric catalogs are discussed in detail in Skelton et al. (2014). This work uses version 2.1 of the photometric and grism catalogs.

A modified version of the EAZY code (Brammer et al. 2008) is used on the combined grism spectra + photometry to measure the redshifts, emission line fluxes, and rest-frame U, V, J fluxes of the individual 3D-HST galaxies. Stellar masses, integrated dust attenuation, SFRs, and specific star formation rates (SSFRs) are determined by fitting stellar population synthesis models to the photometric data using the FAST code (Kriek et al. 2009b). We use a separate set of parameters than those used by Brammer et al. (2012), for reasons discussed in Section 2.4.4. We use the Bruzual & Charlot (2003) stellar population synthesis models, assuming a Chabrier (2003) stellar initial mass function, solar metallicity, an exponentially declining star formation history with a minimum e-folding time of $\log_{10}(\tau_{\mathrm{min}}/\,\mathrm{yr}) = 8.5$, a minimum age of 40 Myr, and an integrated dust attenuation $A_{\rm V}$ between 0 and 4 assuming the dust attenuation law by Calzetti et al. (2000).

Brammer et al. (2012) provide complete details on the 3D-HST survey data reduction and parameter measurement procedure.

2.2.2 Sample selection

We select galaxies in the redshift range $1.36 \leq z \leq 1.5$, for which Hα and Hβ are generously covered by the G141 grism. In addition we impose a signal-to-noise ratio (SNR) cut for Hα of SNR ≥ 5, to measure a decent line signal. We make no Hβ SNR cut, to avoid biasing our sample against the dustiest galaxies.

We have a number of additional selection criteria, to ensure high quality of the spectra. First, to avoid cases of line misidentification, the photometric-only and grism+photometry redshifts (hereafter referred to as the grism redshifts) must have good agreement, i.e. $|z_{\rm phot} - z_{\rm grism}| \leq 0.2$. Second, the contamination from other sources (which is an issue because of the slit-less nature of the grism spectra) may not exceed 15%. Third, there must be grism coverage of at least 95% and must include the Hα and Hβ lines. Fourth, no more than 50% of the spectrum may be flagged as problematic (due to bad pixels or cosmic rays) during reduction.

To study dust attenuation towards star forming regions, we do not want AGN to contaminate our emission lines. To reject AGN, we exclude any objects that have a detected X-ray luminosity $L_X > 10^{42}\,{\rm erg\,s^{-1}}$ (Bauer et al. 2002; Mendez et al. 2013; Rosario et al. 2013) by matching against the Chandra Deep Field North and South surveys (Alexander et al. 2003; Xue et al. 2011) and the XMM-Newton serendipitous survey (Watson et al. 2009). Furthermore we reject all objects that fall within the Donley et al. (2012) IRAC AGN region, or that fall within the quiescent box in the UVJ diagram defined in Whitaker et al. (2012a) (as the line emission likely originates from an AGN).

Finally, we visually inspect the grism spectra and photometry of the preliminary sample to reject problematic objects (i.e. objects with incorrect line identification or poor quality broadband photometry). Our final sample includes 163 galaxies. Figure 2.1 shows how our sample compares to the full galaxy distribution at a similar redshift. The selected galaxies all have relatively high SFRs, and lie along the “star-forming main sequence” (e.g., Daddi et al. 2007; Nelson et al. 2013; Noeske et al. 2007b; Whitaker et al. 2012b; Wuyts et al. 2011a).

2.2.3 Stacking

The spectra of individual galaxies in this sample are too noisy to yield a clear measurement of the Balmer decrement, the ratio of the flux of Hα to Hβ ($F_{\rm H\alpha}/F_{\rm H\beta}$). Thus, we bin galaxies by parameter (SED $A_{\rm V}$, SSFR, SFR, stellar mass) and stack the spectra before measuring line fluxes.

Prior to stacking, we scale the spectra to match the photometry, as the spectra and photometry have a slightly different slope for most galaxies. A linear correction for this effect

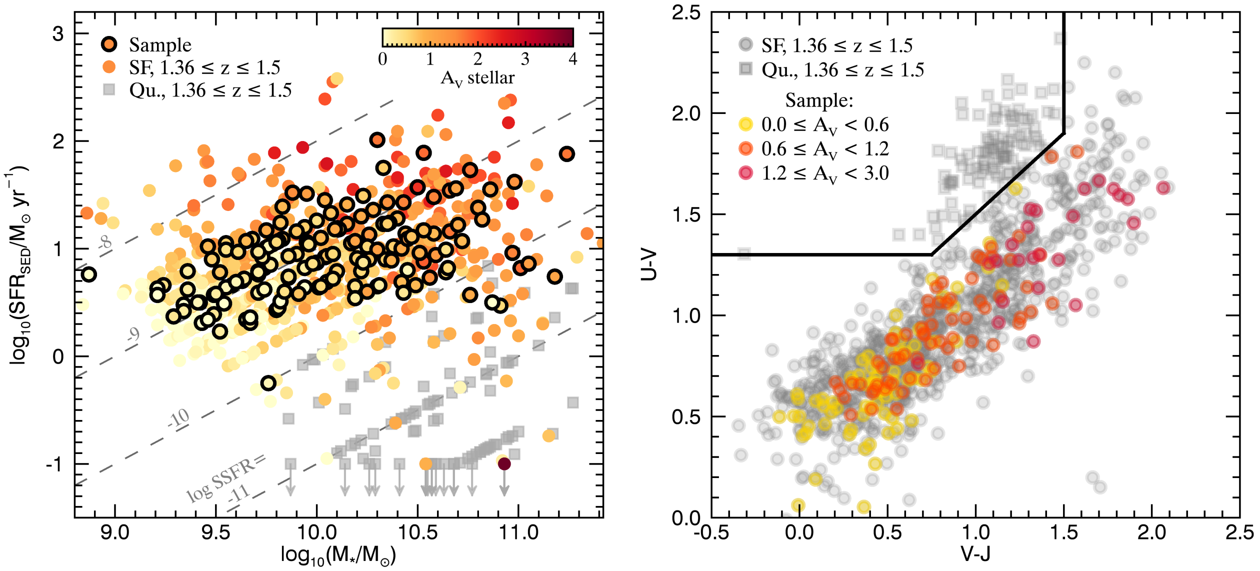

Figure 2.1: Sample characteristics relative to all 3D-HST galaxies in the same redshift range. The left panel shows $\log M_*$ vs. log SFR (from SED fitting) for all 3D-HST galaxies at $1.36 \leq z \leq 1.5$. The black circles indicate the sample selected for direct Balmer decrement measurements, consisting of galaxies with a strong Hα detection (i.e. S/N ≥ 5). Colors indicate the stellar $A_{\rm V}$ of the best-fit SED models found using the grism spectra and the photometry, as described in Section 2.2.1. The grey dashed lines show constant values of log SSFR. The right panel presents the rest-frame U-V and V-J colors for all 3D-HST galaxies between $1.36 \leq z \leq 1.5$ (in grey) and our sample (color-coded by stellar $A_{\rm V}$ bin). We discard any galaxies lying within the quiescent box (using the definition from Whitaker et al. 2012a) from our sample, as the emission lines for these galaxies likely originate from AGNs. In both panels, objects within the quiescent box of the UVJ diagram are shown as grey squares, while star-forming objects are shown as circles.

is calculated during the reduction stage, and we apply this linear correction to the individual grism spectra. Individual spectra are also corrected for contamination from other sources during the reduction process.

We adopt a uniform methodology for stacking spectra within a bin. First, we only use the portion of the grism spectra that falls between $1.13\,\mu$m and $1.65\,\mu$m (observed wavelength) to avoid noise at the edge of the grism coverage. Then the individual spectra are continuum normalized by scaling the biweighted mean value of the flux between $5500-6000$ Å (rest-frame) to unity. The individual spectra are then interpolated onto a common rest-frame wavelength grid.

The normalized, interpolated spectra are stacked at each wavelength. For each bin, simulated spectra ($N = 500$) are generated by perturbing the individual spectra, assuming that the flux errors are normally distributed, and then stacking the perturbed spectra using the same procedure as above. The simulated spectra are used in determining the errors of the emission lines (see Section 2.2.4).

The best-fit stellar population models are sampled over the same wavelength regime as the original spectra and used as the continua. The best fits are stacked in the same way: they are continuum normalized and interpolated onto a common rest-frame wavelength grid, then averaged together. We then convolve the stacked continua models with the stacked line profiles (discussed in Section 2.2.4) to match the resolution of the grism spectra.

To estimate the error in the continua, we perturb the photometry of an object and determine the FAST best-fit model for each perturbation. This procedure is repeated a number of times for each object. Within each bin, we randomly select a best-fit model to the perturbed photometry for each object and stack to construct a simulated continuum. This procedure is repeated 500 times, in order to create a continuum model for each simulated spectrum, as discussed above. The average photometry and stacked best-fit models with errors are shown in Appendix A.

Finally, we apply a second-order polynomial correction between the stacked grism spectra and the stacked best-fit stellar population continua, to further correct for possible mismatches. This small change corrects for otherwise uncharacterized differences across the grism spectra. The corrected, stacked spectra and continua for the different bins are shown in Figure 2.2.

The adopted continuum normalization scheme leads objects with higher scaled Hα+[NII] (see Section 2.2.4) fluxes to have more weight in our line stack. To correctly compare the parameters from SED fitting ($A_{\mathrm{V,star}}$, stellar mass, SFR, SSFR) with values calculated from the stacked lines, we compute the weighted average of each parameter. We use the scaled Hα+[NII] fluxes as the individual objects' weights. Errors on the average parameters are estimated with bootstrapping.

2.2.4 Line measurement

To measure line fluxes for the stacked spectra, we subtract the convolved, stacked continua from the tilt-corrected, stacked spectra. We then fit the emission lines in the resulting spectra using least-squares minimization. For our sample's redshift range, the grism spec-

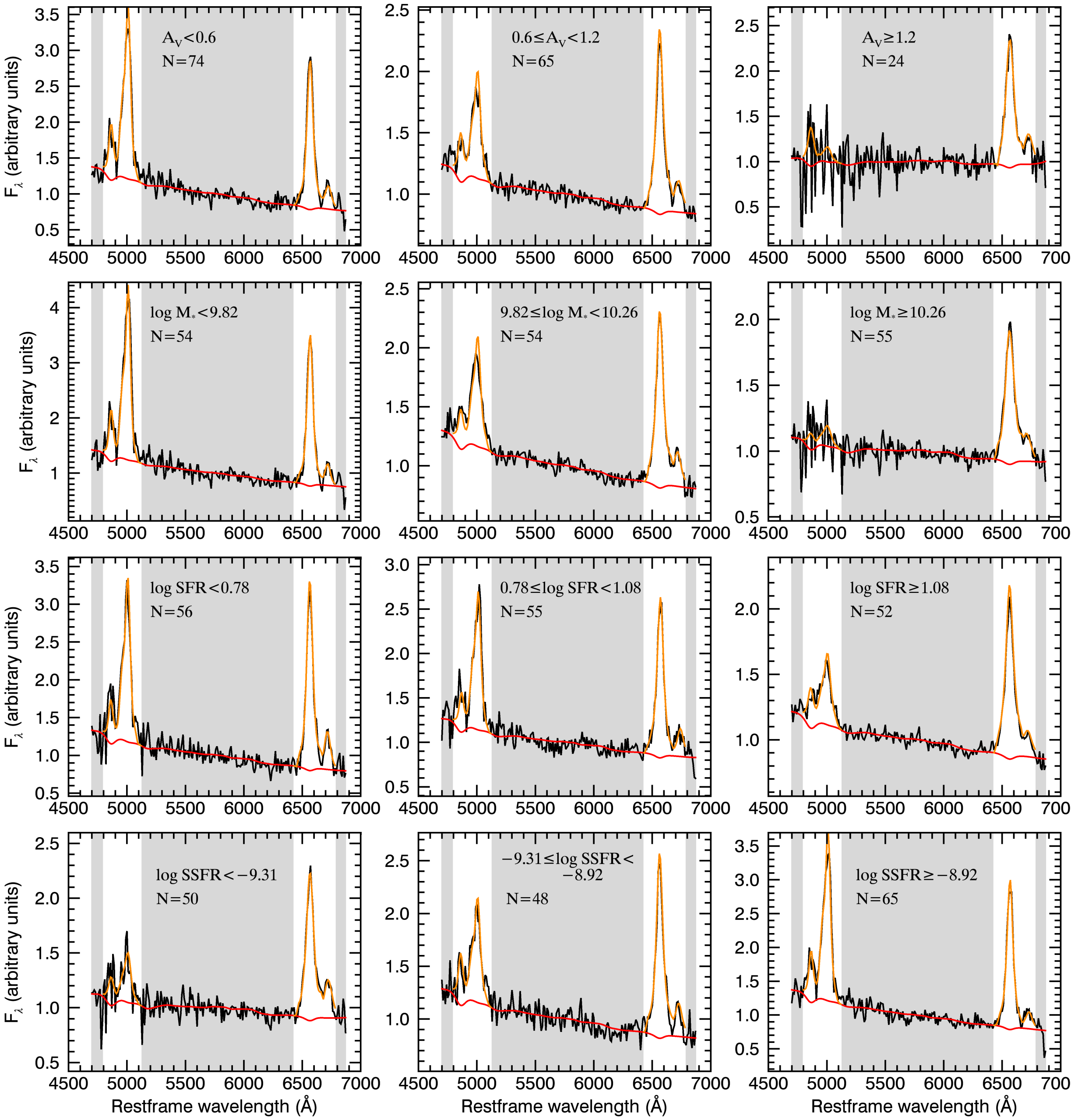

Figure 2.2: Stacked spectra for bins in stellar A_V (top), $\log M_*$ (second row), log SFR (third row) and log SSFR (bottom). In each panel, the stacked spectrum is plotted in black, with the continuum fit shown in red. The best-fit line measurements (from shortest to longest wavelength: Hβ, [OIII]$\lambda\lambda$4959, 5007 Å, blended Hα+[NII]$\lambda\lambda$6548, 6584 Å, and [SII]$\lambda\lambda$6717, 6731 Å) are shown in orange. The additional continuum correction is done by fitting the portions of the spectra within the shaded grey regions.

tra have rest-frame coverage of the following spectral lines: Hβ, [OIII]$\lambda\lambda 4959, 5007$ Å, Hα, [NII]$\lambda\lambda 6548, 6584$ Å, and [SII]$\lambda\lambda 6717, 6731$ Å. However, the resolution of the grism data is insufficient to separate the Hα and [NII] lines, so we measure the blended Hα+[NII]$\lambda\lambda 6548, 6584$ Å line.

The grism line shapes are not well described by gaussian profiles. Because the spatial resolution of the WFC3 detector ($\sim 0\farcs13$ pixel^{-1}) is much greater than the spectral resolution, the spectral line profiles are dominated by the object shapes. Thus, for each object the line profile is measured by summing the direct image from F140W or F160W over the spatial direction, which is perpendicular to the dispersion direction. The composite line profiles are created by flux-normalizing the individual profiles, multiplying each profile by the object's scaled Hα+[NII] flux (described in Section 2.2.3), and finally averaging. This method yields a composite profile with the same effective weighting of the objects as results from the spectrum stacking method. Finally, we scale the profile width to match the width of Hα+[NII], yielding the line profile template for each stack. The grism spectra have roughly constant spectral resolution. Thus for each line, we scale the line profile width by $\lambda_{\rm line}/\lambda_{\rm H\alpha}$.

Lines in a spectrum may not have the same profile, possibly due to dust, age gradients, or AGN contribution (e.g., Wuyts et al. 2012). However, the line fits obtained while using the same line profile (with appropriate width and amplitude scaling) match the data very well, suggesting that assuming a single profile for a stack is a reasonable approximation.

Because of the low spectral resolution of the grism spectra, we simultaneously fit the [OIII] doublet and Hβ, and similarly the blended Hα+[NII] line and the [SII] doublet. We fix the line ratio between [OIII]$\lambda 5007$ Å and [OIII]$\lambda 4959$ Å to 3:1 to reduce the number of degrees of freedom in our fit, and we fix the redshift of all lines to the value measured for Hα.

We compute the emission line fluxes and ratios from the best-fit line profile parameters. The errors on the line fluxes and ratios are estimated using the simulated stacked spectra and continua. For each simulation we measure the best-fit line fluxes and ratios in a similar fashion as for the real stacked spectrum. The errors on the line fluxes and ratios are calculated from the resulting distributions. The best-fit line measurements for our stacks are shown in Figure 2.2.

[NII] correction

To measure the Balmer decrement, we need to correct the blended Hα+[NII] line for the [NII] contribution. We use the stellar mass versus [NII]$\lambda 6584$/Hα relation measured in Erb et al. (2006a) for galaxies at $z \sim 2$, as our sample covers a similar range of masses and SFRs, and is close in redshift.

In Erb et al. (2006a) the stellar masses are calculated using the integrated SFH, while we use the current stellar mass. For the galaxies in our sample, which are all reasonably young, the mass from the integrated SFH is about 10% higher than the current stellar mass. We use this estimate to scale down the masses given by Erb et al. to match our stellar mass definition.

We interpolate the values Erb et al. report in Table 2 to estimate the ratio of [NII]$\lambda 6584$/Hα

given the weighted average stellar mass in each bin. We assume an intrinsic line ratio of 3:1 between [NII]λ6584 and [NII]λ6548 to scale this ratio to include the second [NII] line. We use the resulting ratio to calculate the Hα flux in each stack. We do not include the systematic errors in the [NII]/Hα ratio in our flux errors.

2.3 Dust attenuation compared with galaxy properties

2.3.1 Measuring dust attenuation towards star-forming regions

The Balmer decrement, Hα/Hβ, lets us determine the amount of dust attenuation towards star-forming regions by comparing the measured ratio with the expected line ratio given the physical conditions of the region. We assume that the HII region has a temperature $T = 10^4$ K, an electron density of $n_e = 10^2\,\mathrm{cm}^{-3}$, and that the ions undergo case B recombination. These assumptions result in an intrinsic ratio of $(\mathrm{H}\alpha/\mathrm{H}\beta)_{\mathrm{int}} = 2.86$ (Osterbrock & Ferland 2006). We assume the reddening curve $k(\lambda)$ of Calzetti et al. (2000), which gives us

$$E(\mathrm{B}-\mathrm{V}) = 1.97\log_{10}\left[\frac{(\mathrm{H}\alpha/\mathrm{H}\beta)_{\mathrm{obs}}}{2.86}\right]. \tag{2.1}$$

We combine this expression with $R_{\mathrm{V}} \equiv A_{\mathrm{V}}/E(\mathrm{B}-\mathrm{V})$, assuming the value $R_{\mathrm{V}} = (4.05 \pm 0.80)$ from Calzetti et al. (2000) to calculate the attenuation $A_{\mathrm{V,\,H\textsc{ii}}}$ from the Hα and Hβ flux measured for each stack.

2.3.2 Integrated stellar A_{V}

We first investigate $A_{\mathrm{V,\,H\textsc{ii}}}$ in bins of $A_{\mathrm{V,\,star}}$, to better constrain the currently contested relationship between the integrated dust content and the dust associated with SF regions for high-redshift galaxies. We choose bins of $A_{\mathrm{V,\,star}}$ to probe the full range of integrated stellar dust attenuation in our sample, from low to medium to high attenuation. We stack the spectra in these bins and measure $A_{\mathrm{V,\,H\textsc{ii}}}$ on the stack using the relations given in Section 2.3.1. The results are shown in Figure 2.3.

We perform a least-squares ratio fit to the data. The best-fit relation, assuming R_{V} is the same for the stellar continuum and the HII regions, is

$$A_{\mathrm{V,\,H\textsc{ii}}} = 1.86^{+0.40}_{-0.37}\,A_{\mathrm{V,\,star}}, \tag{2.2}$$

indicating that on average $A_{\mathrm{V,\,H\textsc{ii}}}$ is 1.86 times higher than $A_{\mathrm{V,\,star}}$ in star-forming galaxies at $z \sim 1.5$. This is a slightly lower amount of extra attenuation than the ratio of 2.27 which Calzetti et al. (2000) find for low redshift star-forming galaxies, but our data are not statistically different from the Calzetti et al. (2000) relation. The data are inconsistent with the assumption of no extra dust attenuation towards star-forming regions and are inconsistent with a constant value at the $\sigma = 1.2,\ 1.7$ levels, respectively.

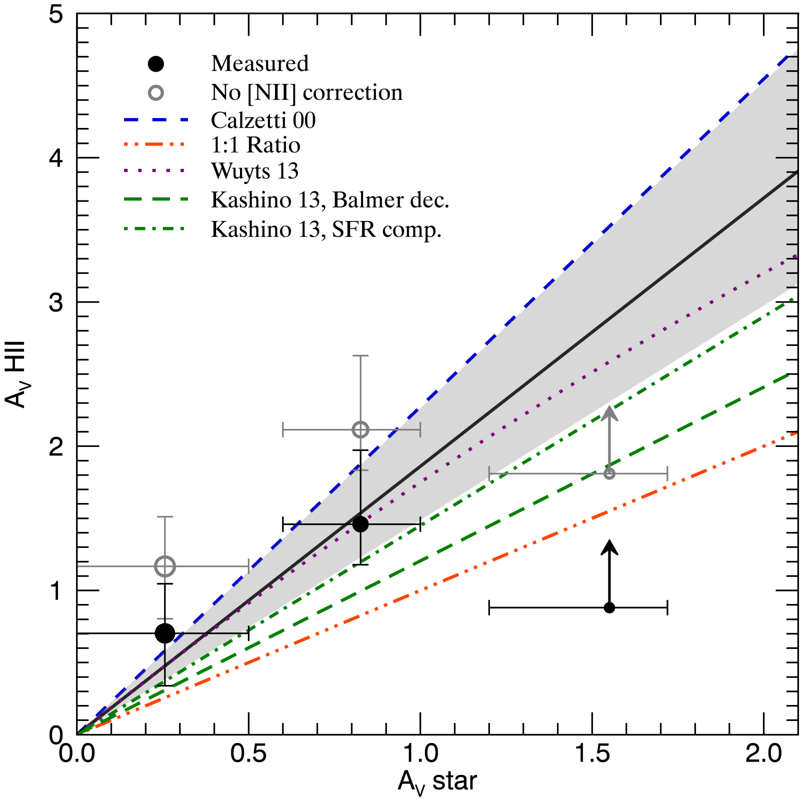

Figure 2.3: Weighted average of individual $A_{\mathrm{V,star}}$ vs. $A_{\mathrm{V,H\,II}}$ measured from the spectra stacked in bins of $A_{\mathrm{V,star}}$, shown in the top panel of Fig 2.2, both corrected (black circles) and uncorrected (open grey circles) for [NII] contamination. The size of the data points corresponds to the fraction of the scaled Hα+[NII] flux in each bin. Bins without a significant detection ($\geq 2\sigma$) of Hβ are shown as 2σ lower limits. The $A_{\mathrm{V,star}}$ errors shown are the 1σ scatter within the bins. The black line shows the best-fit line to our [NII] corrected values, which has a slope of 1.86. The fit error is shown with the shaded grey region. The best-fit indicates there is extra attenuation towards emission line regions. The data are consistent with the ratio of $A_{\mathrm{V,H\,II}}$ to $A_{\mathrm{V,star}}$ from Calzetti et al. (2000) (blue dashed line), Wuyts et al. (2013) (purple dotted line), and both relations found by Kashino et al. (2013) (green long dash, dash-dot lines). The data are inconsistent with the assumption of no extra dust attenuation towards emission line regions (orange dash-dot-dot line).

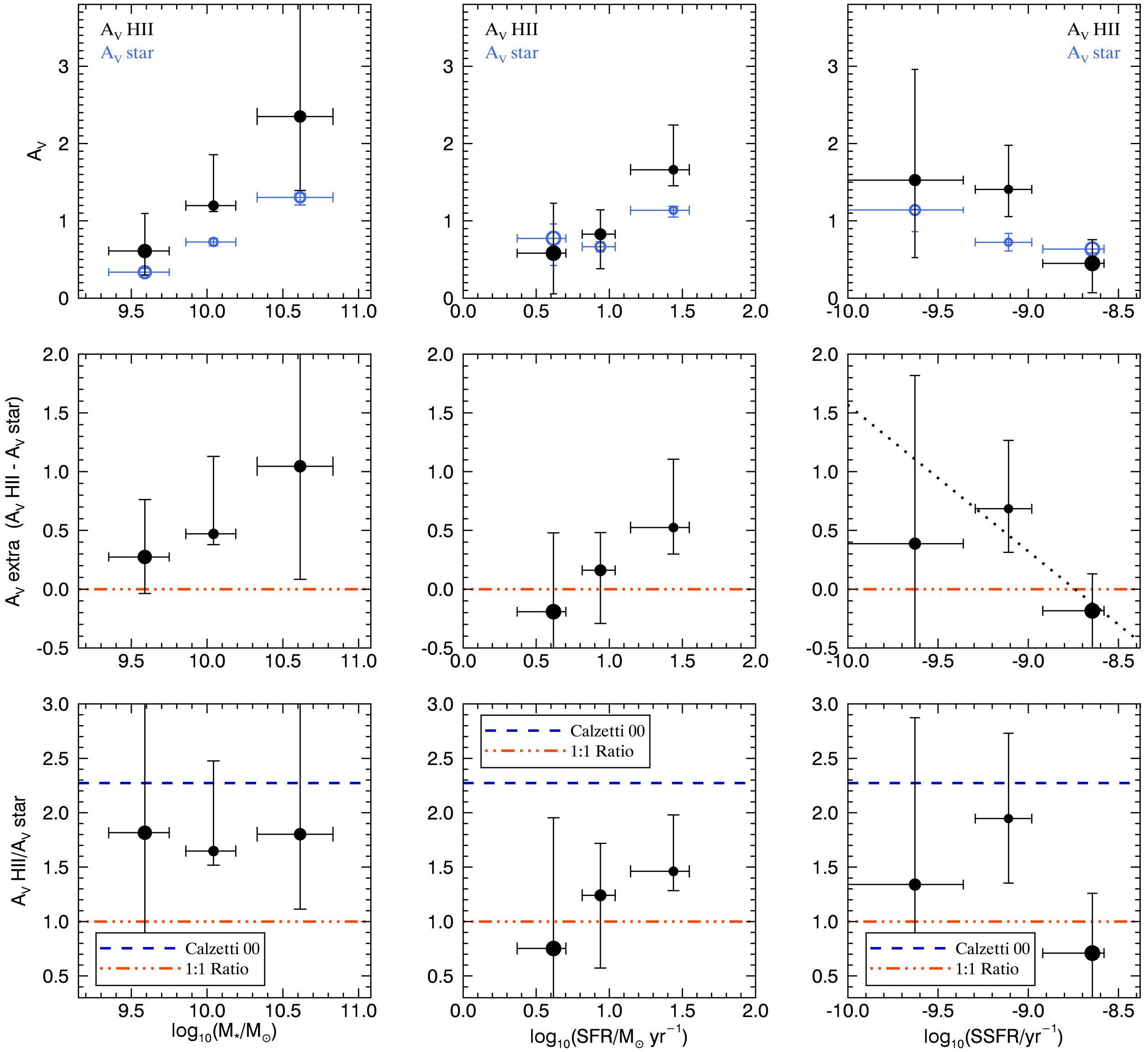

Figure 2.4: A_{V} measurements for bins in $\log M_*$, log SFR and log SSFR. The top row shows $A_{\mathrm{V,\,star}}$ and $A_{\mathrm{V,\,H\,II}}$ vs. the binned parameters. The middle row shows the difference between emission and stellar A_{V} ($A_{\mathrm{V,\,extra}}$) vs. the binned parameters. The orange dash-dot-dot line shows the case of no extra attenuation towards star-forming regions. The bottom row shows the ratio of $A_{\mathrm{V,\,H\,II}}$ to $A_{\mathrm{V,\,star}}$ vs. the binned parameters. The blue dashed and orange dash-dot-dot lines in the third row are the ratio between emission A_{V} and stellar A_{V} used in Calzetti et al. (2000) and the case of no extra attenuation towards star-forming regions, respectively. The size of the data points is described in Fig. 2.3. The errors in $\log M_*$, log SFR and log SSFR are the 1σ scatter within the bins. In the right panel the black dotted line shows the best-fit relation of $A_{\mathrm{V,\,extra}} = A_{\mathrm{V,\,H\,II}} - A_{\mathrm{V,\,star}}$ vs. log SSFR, with the fit errors shown with the shaded grey region.

The data are consistent with the results by Wuyts et al. (2013), who find an average relation between $A_{\mathrm{V,star}}$ and $A_{\mathrm{V,extra}} = A_{\mathrm{V,H\,II}} - A_{\mathrm{V,star}}$ for galaxies at $0.7 \leq z \leq 1.5$. Their relation (shown in Figure 2.3 by the dotted purple line) is the dust attenuation required for agreement between Hα SFRs and UV+IR SFRs, or if there was no IR detection, SED SFRs. Our data are also consistent with the relations Kashino et al. (2013) find by comparing UV and Hα SFR indicators (green dash-dot line) and measured from the Balmer decrement (green long dash line).

We also show the results without correcting the Hα flux for [NII] (open grey circles). These points overestimate the amount of $A_{\mathrm{V,H\,II}}$ relative to $A_{\mathrm{V,star}}$, demonstrating the necessity of correcting for [NII] when measuring the attenuation of the star-forming regions using grism data.

However, it is important to note that there may be considerable scatter in the $A_{\mathrm{V,star}}$ and $A_{\mathrm{V,H\,II}}$ values for individual galaxies, so this result only holds on average for a collection of galaxies.

2.3.3 Stellar mass, SSFR, and SFR

In this section we probe the change in dust properties over bins of stellar mass, SSFR, and SFR. We select bin boundaries for each of these properties to distribute the number of galaxies as equally as possible between the bins.[2]

The left panels of Figure 2.4 show the results for the stacks in stellar mass, including the measured $A_{\mathrm{V,H\,II}}$ and weighted average $A_{\mathrm{V,star}}$ (top) and the difference between $A_{\mathrm{V,H\,II}}$ and $A_{\mathrm{V,star}}$ ($A_{\mathrm{V,extra}}$, middle) as a function of stellar mass. We also plot the ratio $A_{\mathrm{V,H\,II}}/A_{\mathrm{V,star}}$ (bottom) to facilitate comparison with previous studies.

We see an increase in both $A_{\mathrm{V,star}}$ and $A_{\mathrm{V,H\,II}}$ with increasing stellar mass, inconsistent with a constant value at the $\sigma = 12$, 1.2 levels, respectively. The plot of $A_{\mathrm{V,extra}}$ shows a roughly constant amount of extra attenuation with mass. The data are consistent with a constant value of $A_{\mathrm{V,extra}}$. The ratio $A_{\mathrm{V,H\,II}}/A_{\mathrm{V,star}}$ is consistent with the value found by Calzetti et al. (2000) for all mass bins.

The results for stacks in SFR are shown in the center panel of Figure 2.4. Both $A_{\mathrm{V,star}}$ and $A_{\mathrm{V,H\,II}}$ show an increase with SFR, at the $\sigma = 4.3$, 1.0 levels, respectively. $A_{\mathrm{V,extra}}$ is consistent with no trend with SFR. As before, we show the ratio $A_{\mathrm{V,H\,II}}/A_{\mathrm{V,star}}$ for direct comparison with past work. On average, the ratio is below the value found in Calzetti et al. (2000).

The results for stacks in SSFR are shown in the right panel of Figure 2.4. Both $A_{\mathrm{V,star}}$ and $A_{\mathrm{V,H\,II}}$ decrease with increasing SSFR, and are inconsistent with a constant value at the $\sigma = 3.2$, 1.2 levels, respectively.

We also find a slight decreasing trend in $A_{\mathrm{V,extra}}$ with SSFR, however this trend is not significant as the difference between the data and a constant value is only $\sigma = 0.7$. Again, we

---

[2] The SED parameters are sampled from a discrete array, which sometimes results in a large number of objects with the same parameter value.

show the ratio $A_{\mathrm{V,\,H\,II}}/A_{\mathrm{V,\,star}}$ for comparison. Our ratio is consistent with the Calzetti et al. (2000) value for the lowest two SSFR bins, while our ratio for the highest SSFR bin is lower.

Interestingly, $A_{\mathrm{V,\,extra}}$ is most strongly correlated with SSFR, rather than stellar mass or SFR. We perform a least-squares linear fit to $A_{\mathrm{V,\,extra}}$ vs. log SSFR, using an offset in log SSFR to avoid correlated intercept and slope errors. We find a best-fit relation of

$$A_{\mathrm{V,\,extra}} = 0.48^{+0.41}_{-0.32} - 1.25^{+0.87}_{-0.91}\left[\log_{10}(\mathrm{SSFR/yr^{-1}}) + 9.13\right]. \tag{2.3}$$

This possible trend could be explained by the two-component dust model, as we discuss in Section 2.4.1.

2.4 Discussion

2.4.1 Physical interpretation

The observed extra attenuation towards emission-line regions, and the decrease in the amount of extra attenuation with increasing SSFR, are consistent with a two-component dust model (e.g., Calzetti et al. 1994; Charlot & Fall 2000; Granato et al. 2000; Wild et al. 2011). This model assumes there is a diffuse (but possibly clumpy) dust component in the ISM that affects both the older stellar populations and star-forming regions, as well as a component associated with the short-lived stellar birth clouds that only affects the stars within those regions.

For galaxies with the highest SSFRs, the continuum light is dominated by young, massive stars. These massive stars would predominately still reside in the birth clouds. So for the two-component model, both the emission lines and the continuum features would be attenuated by both the birth cloud and the diffuse dust components, resulting in $A_{\mathrm{V,\,H\,II}} \approx A_{\mathrm{V,\,star}}$. Galaxies with lower SSFRs would have a smaller continuum contribution from massive stars, so more of the continuum light would come from stars only attenuated by the diffuse dust, resulting in $A_{\mathrm{V,\,H\,II}}$ greater than $A_{\mathrm{V,\,star}}$. These different cases are illustrated in Figure 2.5.

We compare our results with those of Wild et al. (2011) for local galaxies. They also find increasing amounts of extra attenuation with decreasing SSFRs, in agreement with the trend we observe. Wild et al. find higher amounts of extra attenuation than we do, but the average SSFRs of their sample are lower than for our sample. The two-component dust model naturally explains this difference, based on the dependence of extra attenuation on SSFR as discussed above. This model may also explain the higher amount of extra attenuation found by Calzetti et al. (2000) if their sample has higher average SSFRs than our sample.

The two-component dust model could also explain the discrepancies found between different high-redshift studies, if the samples consist of galaxies with different ranges in specific SFR. For example, the Kashino et al. (2013) SFR-M_* relation implies a higher average SSFR than our sample, and they find a lower amount of extra attenuation. Erb et al. (2006a) find evidence for no extra attenuation, but the average SSFR is higher than for the Kashino et al. sample.

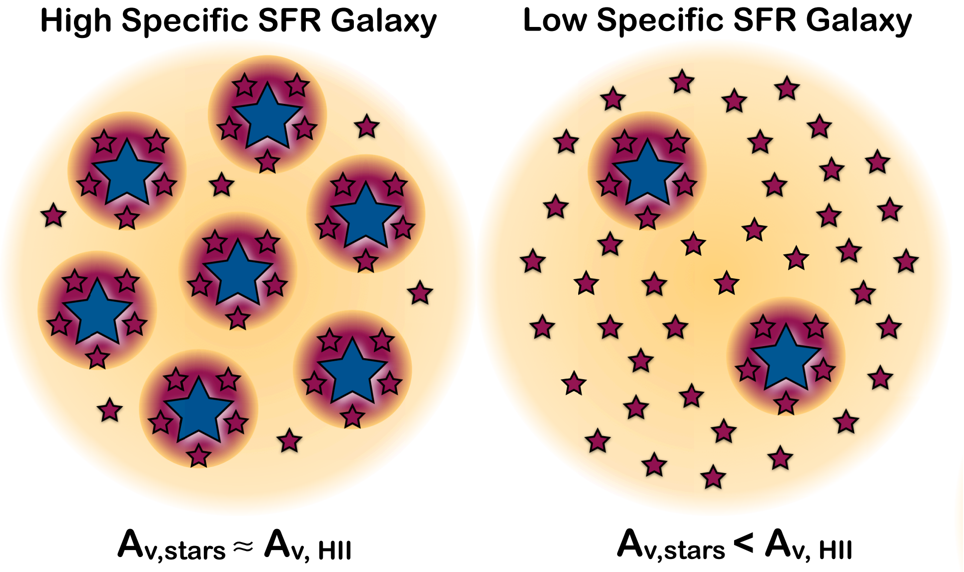

Figure 2.5: Illustration of the two-component dust model in galaxies with high (left panel) and low (right panel) specific SFRs. The yellow regions indicate the diffuse dust component in the ISM. The red regions indicate the dust component associated with the short-lived stellar birth clouds. The large blue stars show the young, massive stars which mostly are found in the birth clouds. The small red stars show the less massive stars (both young and old), which are found both within the birth clouds and elsewhere. For galaxies with higher specific SFRs, we expect the continuum light to be dominated by the young, massive stars in the birth clouds, so both the continuum and emission lines are attenuated by both dust components. Galaxies with lower specific SFRs would have a higher contribution to the continuum emission from less massive stars, which generally reside outside the birth clouds and are only attenuated by the diffuse dust component, while the emission lines are still attenuated by both dust components. Thus this leads to larger differences between $A_{\mathrm{V,star}}$ and $A_{\mathrm{V,H\,II}}$.

Our explanation for the trend between extra $A_{\rm V}$ and SSFR was previously mentioned by Wild et al. (2011). They suggest that the trend may alternatively be caused by a decline in diffuse dust with decreasing SSFR. However, we observe that $A_{\rm V,\,star}$ increases slightly with decreasing SSFR, so we do not expect a decline in diffuse dust with decreasing SSFR.

In absolute terms, we find that $A_{\rm V,\,H\,II}$ increases with mass and SFR, and decreases with SSFR. As stellar mass and SFR are correlated, the trend of increasing dustiness with SFR and mass could share the same cause. The trend of increasing $A_{\rm V,\,star}$ and $A_{\rm V,\,H\,II}$ with decreasing SSFR could also share the same cause, as the SSFR decreases slightly with increasing mass both in the local universe (Brinchmann et al. 2004) and at higher redshifts (Damen et al. 2009; Elbaz et al. 2007; Noeske et al. 2007b; Whitaker et al. 2012a; Zheng et al. 2007). As the trends of $A_{\rm V,\,star}$ and $A_{\rm V,\,H\,II}$ with increasing mass are the strongest, it is likely that mass is the key property. This finding may be explained by the fact that more massive star-forming galaxies have higher gas-phase metallicities (Erb et al. 2006a; Tremonti et al. 2004).

We do note that we assume a fixed attenuation law in our work. Recent work (e.g., Buat et al. 2012; Kriek & Conroy 2013; Wild et al. 2011) shows that the dust attenuation curve varies with SSFR. As the origin of these observed trends are not well understood, and this variation may be the consequence of age-dependent extinction in a two-component dust model, we have decided to use the same dust law for the derivation of the two dust measurements. However, we cannot rule out the possibility that variations in the dust attenuation law may have impacted the trends found in this work.

2.4.2 Dust attenuation vs. axial ratio

The two-component dust model also predicts a dependence of dust attenuation properties on the axial ratio. Under this model, the amount of dust attenuation from the stellar birth clouds is similar in face-on or edge-on systems, while the longer path length in edge-on systems results in a larger overall $A_{\rm V,\,star}$ and a smaller amount of extra attenuation towards the star-forming regions. Wild et al. (2011) find evidence for the two-component model from the trends of attenuation with axial ratio for objects in the local universe.

The spatially resolved WFC3 images yield excellent axial ratio measurements. However, the axial ratio distribution for our sample is heavily biased towards face-on systems. The more edge-on systems may be dustier, so our selection criteria likely introduce this bias against edge-on systems. It might also be that our sample objects are not disk-like galaxies. Because of sample incompleteness and the small range in axial ratios, we are unable to test the two-component model using the inclinations of the galaxies.

2.4.3 Comparison of results for $A_{\rm V,HII}$ vs. stellar mass

A number of past studies have measured Balmer decrements (and often $A_{\rm V,\,H\,II}$) versus stellar mass (Domínguez et al. 2013; Kashino et al. 2013; Momcheva et al. 2013; van Dokkum et al. 2005). Other studies have employed different methods of measuring $A_{\rm V,\,H\,II}$ versus stellar mass. These methods include comparing $L_{\rm IR}$ to $L_{\rm H\alpha}$ as by Ibar et al. 2013, or calibrating

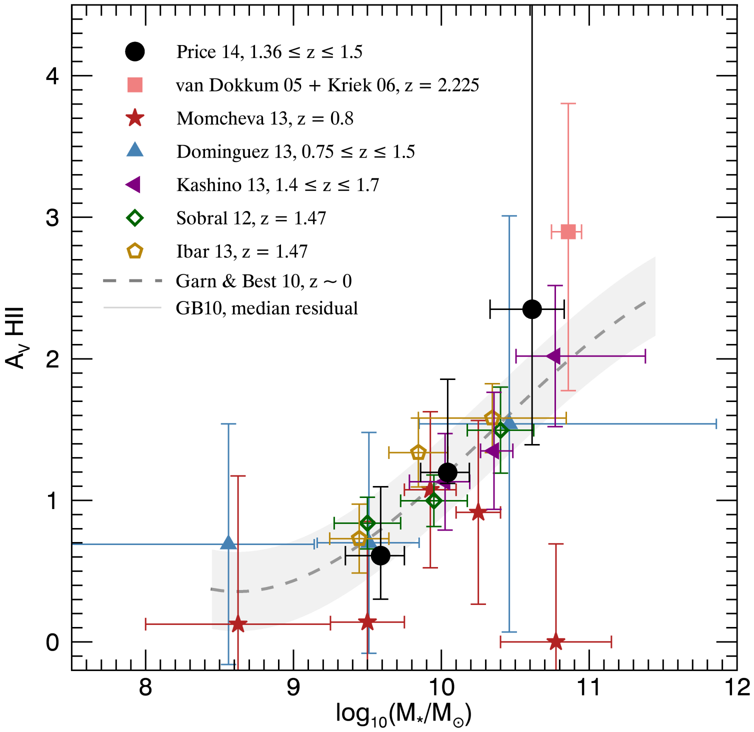

Figure 2.6: $A_{\rm V,\,H\,II}$ vs. stellar mass comparison between this work and past studies. The filled data (this work; Domínguez et al. 2013; Kashino et al. 2013; Momcheva et al. 2013; van Dokkum et al. 2005) indicate direct measurements of $A_{\rm V,\,H\,II}$ using Balmer decrements, while the open data indicate $A_{\rm V,\,H\,II}$ measured with a different method that is calibrated using Balmer decrements. The dashed line gives the median relation derived by Garn & Best (2010) using SDSS star-forming galaxies. With the exception of the single object from van Dokkum et al. (2005) (combined with information from Kriek et al. 2006), all other data are the result of stacks (using various stacking schemes, both mean and median) or are mean (Momcheva et al. 2013, combined with stacking) or median values (Garn & Best 2010; Sobral et al. 2012) from samples.

[OII]/Hα ratio as an alternate to Balmer decrements as by Sobral et al. 2012. We compare our results with their findings in Figure 2.6. As necessary, we convert stellar masses derived using a Salpeter or Kroupa IMF to match our assumption of a Chabrier IMF using the relations given in Equations 12 and 13 of Longhetti & Saracco (2009).

The collection of results over a range of redshifts makes it tempting to speculate that there is no redshift evolution in the mass-$A_{\rm V,\,H\,II}$ relation. However, the current data are not conclusive. First, there is incompleteness at all masses. Second, the measurements of $A_{\rm V,\,H\,II}$ are not necessarily equivalent.

The samples of Domínguez et al. (2013) and Kashino et al. (2013) are similar to ours in redshift and method (stacking) for measuring $A_{\rm V,\,H\,II}$. Concerning the work by Domínguez et al. (2013), we first note that their sample contains fewer objects than our sample. Second, we have a broad range of deep photometric coverage for our objects, which reduces the errors in our masses taken from SED modeling. We also do not combine measurements between different grisms, to avoid possible normalization mismatches affecting line fluxes. Compared with Kashino et al. (2013), our sample is larger and on average has slightly lower SSFRs. The trend we observe between $A_{\rm V,\,H\,II}$ and SSFR shows that the average $A_{\rm V,\,H\,II}$ decreases with increasing SSFR, which explains why their values of $A_{\rm V,\,H\,II}$ are lower (though consistent within the errors) than what we measure for similar masses.

2.4.4 Implications for Hα SFR compared with SED SFR

With our measurements of dust attenuation towards HII regions, we can for the first time directly measure Hα SFRs for a large sample of $z \sim 1.5$ galaxies. We calculate the Hα SFRs using the relation from Kennicutt (1998) converted to a Chabrier (2003) IMF. Hα fluxes are taken from the stacks in SED SFR, and are converted to physical units by comparing the flux of the stack with the weighted average (see Section 2.2.4) of the individual objects' Hα fluxes, each corrected for [NII]. The luminosity distance is taken as the weighted average of the individual objects' luminosity distances. We then use the Hα SFRs to test the much more debated SED SFRs.

The comparison of SFR indicators is shown in Figure 2.7. The Hα SFRs are compared to the weighted average of SED SFRs derived assuming an exponentially decaying SFH and a minimum e-folding time of $\log_{10}(\tau_{\rm min}/\,{\rm yr}) = 8.5$ (shown as filled black circles). For these parameters, the SED SFR values underestimate the Hα SFRs, and are inconsistent at the $\sim 1.5\sigma$ level. However, if a shorter decay time of $\log_{10}(\tau_{\rm min}/\,{\rm yr}) = 7$ (open red squares) is adopted, the SED SFRs are low and inconsistent with the Hα SFRs at the $\sim 4\sigma$ level. Thus for our sample, SED SFRs derived with $\log_{10}(\tau_{\rm min}/\,{\rm yr}) = 8.5$ are more in line with the Hα SFRs.

This is in general agreement with the work of Wuyts et al. (2011b). They compare UV+IR and SED SFRs and find good agreement between the SFR indicators for $\log_{10}(\tau_{\rm min}/\,{\rm yr}) = 8.5$, but when a shorter time of $\log_{10}(\tau_{\rm min}/\,{\rm yr}) = 7$ is adopted, they find that the SED SFRs underestimate the true SFRs. Reddy et al. (2012) also compare UV+IR SFRs with SED SFRs. However, instead of using a longer $\tau_{\rm min}$ for a decreasing SFH, they find the SED SFRs

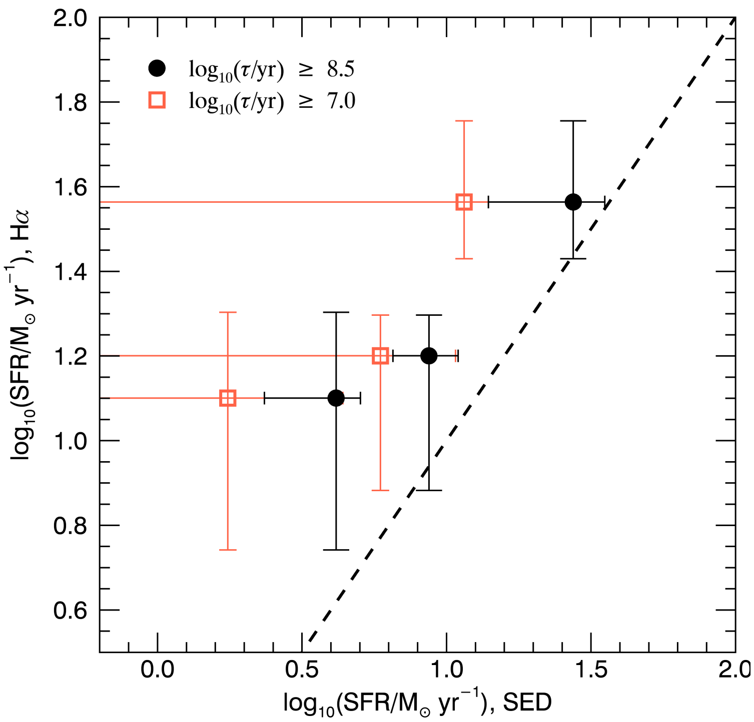

Figure 2.7: Comparison between measured Hα SFRs (Kennicutt 1998) and the SED SFRs. The two sets of SED SFRs differ only in the choice of the minimum star formation e-folding timescale, τ: $\log_{10}(\tau/\,\mathrm{yr}) \geq 7.0$ (open red squares) and $\log_{10}(\tau/\,\mathrm{yr}) \geq 8.5$ (closed black circles). (The dashed black line shows equal Hα SFRs and SED SFRs.) The Hα SFRs agree better with the SED SFRs calculated with the higher τ_{min}, which is similar to previous findings that setting $\tau_{min} \sim 300\,\mathrm{Myr}$ yields the most reasonable SED fits for star-forming galaxies. (See Section 2.4.4 for a full discussion.) The errors in log SED SFR are the 1σ scatter within the bins.

agree with UV+IR SFRs when increasing SFHs are adopted.

The SFR indicators may also differ because they probe different stellar mass ranges, and thus different star formation timescales. The Hα SFRs depend on OB stars, so are averaged over $\sim$ 10 Myr, while SED SFRs are limited by the discrete nature of SED fitting and depend on the UV flux from O, B and A stars, which live longer. These timescale differences could cause discrepancies for galaxies with episodic or rapidly increasing or decreasing SFHs. However, as we stack multiple objects and thus average over many SFHs, we expect that the timescale differences should not significantly influence the measured SFRs.

2.4.5 AGN contamination

As discussed in Section 3.2.2, we use a number of methods to reject AGNs from our sample. However, as almost all individual objects do not have sufficient line SNRs, and more importantly we do not have separate [NII] and Hα measurements, we cannot use a BPT (Baldwin et al. 1981) diagram to distinguish whether the line emission originates from star formation or AGN.

After stacking, there is sufficient line SNR to place the binned values in the BPT and alternative diagrams, which we show in Figure 2.8. These diagrams allow us to assess if there is AGN contamination in the stacks. We use the data from the stacks in stellar mass in these diagrams.

In the left panel, we show the traditional BPT diagram: [NII]/Hα vs. [OIII]/Hβ. Included are the theoretical limit for star-forming (SF) galaxies from Kewley et al. (2001) (dashed line) and the more conservative empirical division between SF galaxies and AGN by Kauffmann et al. (2003b) (dashed-dot line), both of which are derived for galaxies at $z \sim 0$. The SDSS DR7 galaxies (Abazajian et al. 2009) are divided into three categories based on these dividing lines: SF galaxies (blue contours), composite (green contours), and AGN (red contours). These same group definitions are used in the alternate BPT diagrams (middle and right of Figure 2.8). Because we do not measure [NII] directly (instead inferring a value as described in Section 2.2.4), we cannot use the traditional BPT diagram as a post-analysis check. Instead, we show that our inferred [NII]/Hα ratios and the observed [OIII]/Hβ ratios, shown as open grey circles, are consistent with values for SF galaxies. However, in agreement with other observational (e.g., Liu et al. 2008; Shapley et al. 2005) and theoretical studies (Kewley et al. 2013) of distant galaxies, the data points are moved slightly up (and possibly to the right) in the BPT diagram compared to the average values found in the local star-forming sequence.

An alternate BPT diagram is [SII]/Hα vs. [OIII]/Hβ. However, Hα is not a directly measured quantity, so using the deblended Hα values makes it impossible to detangle the assumptions of the [NII] correction with the possible presence of AGN. Instead, we make an alternate diagram with only directly measured quantities: [SII]/(Hα+[NII]) vs. [OIII]/Hβ, which we show in the middle panel of Figure 2.8. There is significant overlap between the different categories of SDSS galaxies, so we are unable to discriminate between SF galaxies and AGN using combinations of blended emission lines.

A final alternate to the BPT diagram, the Mass-Excitation (MEx) diagram (Juneau et al.

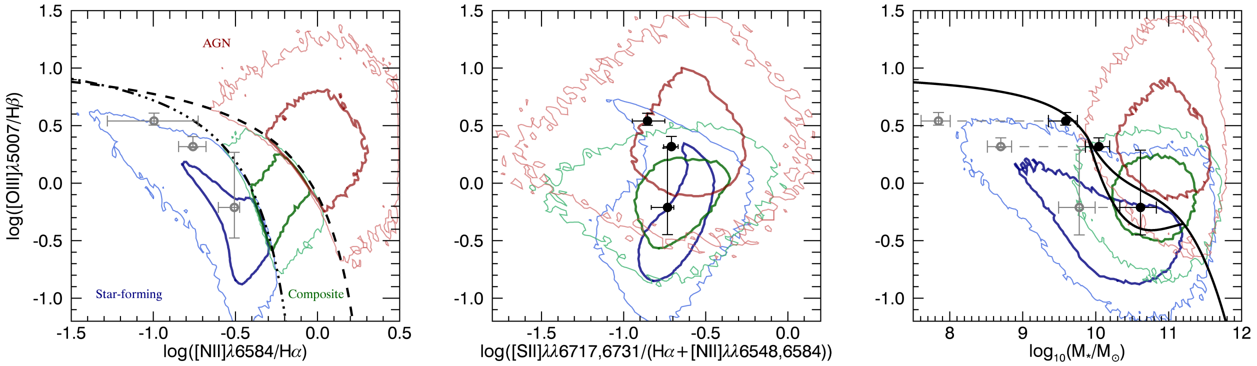

Figure 2.8: Left: Traditional BPT (Baldwin et al. 1981) diagram used to identify the ionizing mechanism for optical emission lines. The dashed line is the theoretical limit between star-forming (SF) galaxies and AGN, as derived in Kewley et al. (2001), and the dashed-dot line is the empirical division derived in Kauffmann et al. (2003b) for galaxies in the SDSS. The color contours represent SDSS galaxies, divided into three regions according to these dividing lines. The darker, thicker lines enclose 68% of the population, while the lighter, thinner lines enclose 95%. The grey open points represent our stacked spectra (in bins of M_*), with the [NII]/Hα measurement inferred from the average stellar masses (i.e. not directly measured from the data.) Middle: alternative BPT diagram, using the blended lines observed with the grism. Color contours correspond to the SDSS galaxies in the left panel. The black circles show the measurements from our stacked spectra. This panel illustrates that the combination of blended emission lines does not enable us to discriminate between SF galaxies and AGN. Right: the Mass-Excitation (MEx) diagnostic from Juneau et al. (2011), where the solid lines are the empirical divisions between SF galaxies and AGN, valid for $z < 1$ galaxies. Our stacked spectra (black circles) lie on the dividing line between the SF and AGN regions of the diagram. Recently Newman et al. (2014) have shown that high redshift SF galaxies tend to be offset to the right from lower redshift SF galaxies in this diagram. We also apply the empirical correction they derive for $z \sim 2$ galaxies (open grey circles) to better compare our sample to the $z \sim 0$ MEx divisions. (See Section 2.4.5 for more discussion.)

2011), is useful as we directly measure the necessary lines ([OIII] and Hβ) and derive stellar mass with SED fitting, which we show in the right panel of Figure 2.8. The solid black lines are their empirical divisions between SF, composite, and AGN, which are valid up to $z \sim 1$. We include the SDSS categories, using stellar masses from the MPA/JHU value-added catalogs (Kauffmann et al. 2003b), to demonstrate that while the separation is not as clean as the traditional BPT diagram, it does separate SF galaxies from AGN in the local universe. Our data are consistent with the SF region as defined by Juneau et al. (2011), though the data do lie on the division boundary. However, work by Newman et al. (2014) at $z \sim 2$ has shown that the low redshift empirical divisions in the MEx diagram incorrectly classify $z \sim 2$ SF galaxies as AGN. They use the shift in the mass-metallicity relation between $z \sim 0$ and 2 to derive a shift to lower mass to bring the high-z values into agreement with the $z \sim 0$ MEx diagram (see Fig. 14 of Newman et al. 2014). This empirical correction (shown as open grey circles in the right panel of Figure 2.8) shifts our data securely into the SF region of the diagram. These diagnostics demonstrate that there is likely not much AGN contamination to the line emission in our sample.

2.4.6 [NII] contamination

One of the largest sources of uncertainty in this analysis is our correction for [NII] in our measurement of Hα from the blended Hα+[NII] line. Figure 2.3 demonstrates how much our results change when we do not correct for [NII]. We use the relation between [NII]/Hα and stellar mass by Erb et al. (2006a) as a way of detangling the blended lines. We infer the [NII] contribution from the weighted average mass of each stack. Because the two samples have similar masses and SFRs, and are close in redshift, the average sample properties should be fairly similar. Still, the use of this relation may introduce bias into our results.

However, our gas phase metallicities may be different from those of Erb et al. (2006a), due to slight differences in redshift, mass or (S)SFR, which could affect both the slope and scaling of the [NII]/Hα relation. Such trends have been proposed by Mannucci et al. (2010), in the form of the fundamental metallicity relation (FMR). The FMR suggests that metallicity depends on both stellar mass and SFR.

We repeat our analysis using the FMR in conjunction with the Maiolino et al. (2008) [NII]/Hα metallicity calibration as an alternative way of calculating the [NII] correction. This allows us to test whether the trend of $A_{\mathrm{V,\,extra}}$ versus SSFR may be due to a variation in [NII]/Hα with SFR. If the FMR is adopted, the $A_{\mathrm{V,\,H{\small II}}}$ values are slightly lower than the $A_{\mathrm{V,\,H{\small II}}}$ values derived using the Erb et al. (2006a) values, which reduces the strength of the trend of $A_{\mathrm{V,\,extra}}$ with SSFR. In this case, the relation we observe between $A_{\mathrm{V,\,extra}}$ and SSFR is weaker than the trend presented in Section 2.3.3, and is consistent with no trend, as the difference is only $\sigma = 0.4$. However, the data are still suggestive of a possible decreasing trend of $A_{\mathrm{V,\,extra}}$ with SSFR, which would imply the signal is not entirely caused by trends with metallicity.

It is also possible that there is some AGN contamination at the highest masses (Kriek et al. 2007), which would also result in an underestimate of the [NII] fraction. In most cases, our corrected Hα flux would be higher than the true value, leading to an overestimate of $A_{\mathrm{V,\,H\textsc{ii}}}$.

We use the mass-[NII]/Hα relation presented in Erb et al. (2006a) for our analysis over the FMR due to uncertainty about metallicity relations at high redshifts. First, the FMR is still not well tested at these redshifts (Cullen et al. 2014). Second, recent work has also questioned whether [NII]/Hα correlates with metallicity at these redshifts (Kulas et al. 2013; Newman et al. 2014). Erb et al. (2006a) present direct measurements of [NII]/Hα, which allows us to avoid systematic problems with metallicity calibrations.

2.4.7 Incompleteness and other systematic uncertainties

One of the strengths of our analysis is that we draw a sample from a non-targeted grism survey, with sample cuts designed to avoid bias as much as possible. However, bias and incompleteness most likely still affect our sample.

The dustiest star-forming galaxies have very attenuated Hα fluxes. Our Hα SNR selection cut, designed to avoid adding noise to our analysis, introduces bias against galaxies with large $A_{\mathrm{V,\,H\textsc{ii}}}$. This bias affects the high mass, high SFR end of the sample, as these objects have the largest A_{V}. As lower mass, lower SFR galaxies tend to have lower Hα luminosities, the Hα SNR cut will also exclude objects with the largest A_{V} values in that mass range.

Our continuum normalization scheme also introduces bias into our analysis. We adopt a normalization scheme to improve the signal of our stack, but the cost is that some objects have much higher scaled Hα fluxes, and thus they dominate our stacks. This biases our results towards those objects with higher Hα equivalent widths in a given bin. Because the line measurements are biased based on the Hα flux, we take the weighted average of the continuum values within a bin to ensure a fair comparison. However, if we instead used a non-weighted average for $A_{\mathrm{V,\,star}}$, the $A_{\mathrm{V,\,star}}$ vs. $A_{\mathrm{V,\,H\textsc{ii}}}$ relationship does not change much.

2.5 Summary

In this paper, we investigate dust attenuation in $z \sim 1.5$ star-forming galaxies using data from the 3D-HST survey. We measure both the dust towards H$\textsc{ii}$ regions, using Balmer decrements, and the integrated dust properties, using SED modeling. We find that there is extra attenuation towards star-forming regions. On average the total attenuation of these regions, $A_{\mathrm{V,\,H\textsc{ii}}}$, is 1.86 times the integrated dust attenuation, $A_{\mathrm{V,\,star}}$.

However, the amount of extra attenuation is not the same for all galaxies. We find that the amount of extra attenuation decreases with increasing SSFR, in agreement with the results by Wild et al. (2011) for low-redshift galaxies. Our findings are consistent with the two-component dust model, which assumes there is a diffuse dust component in the ISM and a dust component associated with the short-lived stellar birth clouds. For galaxies with high SSFR, the stellar light will be dominated by continuum emission from the younger stellar population in the birth clouds, resulting in similar attenuation toward the line and continuum emission. For more evolved galaxies, much of the stellar light will only be attenuated by the diffuse ISM, leading to larger discrepancies between the two dust measures. The observed trend of $A_{\mathrm{V,\,extra}}$ with SSFR may be affected by uncertainties in the [NII] correction and possible dust attenuation law variations. Future work is necessary to determine what role these effects have on the relation between $A_{\mathrm{V,\,extra}}$ and SSFR.

Similar to previous studies (Förster Schreiber et al. 2009; Kashino et al. 2013; Wuyts et al. 2011b, 2013; Yoshikawa et al. 2010), we find less extra attenuation in distant galaxies than is found in the local universe (Calzetti et al. 2000). This effect can also be explained by the two-component model, as lower redshift objects tend to have lower SSFRs than higher redshift galaxies (e.g., Fumagalli et al. 2012; Noeske et al. 2007a; Whitaker et al. 2012b).

We find that both $A_{\mathrm{V,\,H\,II}}$ and $A_{\mathrm{V,\,star}}$ increase with increasing SFR and stellar mass, and decreasing specific SFRs. However, our data are biased against the dustiest objects, which may affect these trends. We also observe there to be little redshift evolution in the $A_{\mathrm{V,\,H\,II}}$-M_* relation, although uncertainties and incompleteness makes it impossible to make a definite claim.

Using the Balmer decrements, we calculate dust-corrected Hα SFRs to test the accuracy of SFRs derived from SED fitting. We find better agreement between the SFR indicators if short SFH decay times are not allowed and the constraint $\log_{10}(\tau/\mathrm{yr}) \geq 8.5$ is used. This generally agrees with the results of past studies comparing UV+IR and SED SFRs (Wuyts et al. 2011b) or Hα and SED SFRs (Wuyts et al. 2013). However, even with this constraint the SED SFRs slightly underestimate the Hα SFRs.

We note that our results are slightly impacted by incompleteness and systematic uncertainties. First, we employ SNR cuts on Hα to ensure quality data, which likely results in incompleteness of the dustiest galaxies. Second, to obtain significant Hβ detections, we stack spectra, and thus our normalization scheme or incorrectly measured integrated properties could impact our measurements.

Most of these issues can be overcome with future observations by a number of new multi-object near infrared spectrographs on 8-10 m class telescopes, among which is MOSFIRE on Keck (McLean et al. 2010). These instruments have higher spectral resolutions, which will avoid blended lines. They will also allow for deeper measurements, which will yield more accurate Balmer decrements of individual objects as well as allowing for investigation of dust to higher A_{V} limits. Additionally, including rest-frame mid- and far-IR data in future work will ensure more accurate values of $A_{\mathrm{V,\,star}}$. Better measurements of $A_{\mathrm{V,\,H\,II}}$ and $A_{\mathrm{V,\,star}}$ are necessary to better constrain the geometric distribution of dust in high redshift galaxies and the effects of the dust-to-star geometry on dust attenuation.

Acknowledgements

I thank Edward Taylor and Nick Hand for useful discussions, and David Sobral and Daichi Kashino for sharing data for comparison. I thank the anonymous referee of the published version of this chapter for constructive comments, which improved the publication. This chapter is based on observations taken by the 3D-HST Treasury Program (GO 12177 and 12328) with the NASA/ESA HST, which is operated by the Association of Universities for Research in Astronomy, Inc., under NASA contract NAS5-26555. I acknowledge support from STScI grant 12117.21-A and a National Science Foundation Graduate Research Fellowship under Grant No. DGE 1106400.

Chapter 3

The MOSDEF Survey: Dynamical and Baryonic Masses and Kinematic Structures of Star-Forming Galaxies at $1.4 \leq z \leq 2.6$

We present Hα gas kinematics for 178 star-forming galaxies at $z \sim 2$ from the MOSFIRE Deep Evolution Field survey. We have developed models to interpret the kinematic measurements from fixed-angle multi-object spectroscopy, using structural parameters derived from CANDELS *HST*/F160W imaging. For 35 galaxies we measure resolved rotation with a median $(V/\sigma_{V,0})_{R_E} = 2.1$. We derive dynamical masses from the kinematics and sizes and compare them to baryonic masses, with gas masses estimated from dust-corrected Hα star formation rates (SFRs) and the Kennicutt-Schmidt relation. When assuming that galaxies with and without observed rotation have the same median $(V/\sigma_{V,0})_{R_E}$, we find good agreement between the dynamical and baryonic masses, with a scatter of $\sigma_{\mathrm{RMS}} = 0.34\,\mathrm{dex}$ and a median offset of $\Delta \log_{10} M = 0.04\,\mathrm{dex}$. This comparison implies a low dark matter fraction (8% within an effective radius) for a Chabrier initial mass function (IMF), and disfavors a Salpeter IMF. Moreover, the requirement that $M_{\mathrm{dyn}}/M_{\mathrm{baryon}}$ should be independent of inclination yields a median value of $(V/\sigma_{V,0})_{R_E} = 2.1$ for galaxies without observed rotation. If instead we treat the galaxies without detected rotation as early-type galaxies, the masses are also in reasonable agreement ($\Delta \log_{10} M = -0.07\,\mathrm{dex}$, $\sigma_{\mathrm{RMS}} = 0.37\,\mathrm{dex}$). The inclusion of gas masses is critical in this comparison; if gas masses are excluded there is an increasing trend of M_{dyn}/M_* with higher specific SFR (SSFR). Furthermore, we find indications that V/σ decreases with increasing Hα SSFR for our full sample, which may reflect disk settling. We also study the Tully-Fisher relation and find that at fixed stellar mass $S_{0.5} = \left(0.5V_{2.2}^2 + \sigma_{V,0}^2\right)^{1/2}$ was higher at earlier times. At fixed baryonic mass, we observe the opposite trend. Finally, the baryonic and dynamical masses of the active galactic nuclei in our sample are also in excellent

agreement, suggesting that the kinematics trace the host galaxies.[1]

3.1 Introduction

In the local universe, most massive star-forming galaxies have traditional Hubble-type morphologies and relatively smooth and thin stellar disks (e.g., Blanton & Moustakas 2009). These disks are thought to form from the cooling of baryons within dark matter halos (White & Rees 1978, Fall & Efstathiou 1980, Blumenthal et al. 1984, White & Frenk 1991). Galaxy formation models (both semi-analytic models, e.g. Dalcanton et al. 1997; Mo et al. 1998, and hydrodynamic simulations, e.g. van den Bosch 2001; Governato et al. 2007; Dutton 2009) are able to reproduce realistic local disk galaxies. However, testing these specific models requires direct observations of galaxies throughout cosmic time.

Over the past two decades, technological advances have enabled observations that provide new insights into the nature of star-forming galaxies at intermediate and high redshifts, in particular due to the combination of high-resolution multi-wavelength imaging with the *Hubble Space Telescope* (*HST*) and near-infrared integral-field spectroscopy with ground-based telescopes. The kinematics and structures of star-forming galaxies have been measured out to $z \sim 2$ (e.g., Weiner et al. 2006, Kassin et al. 2007, 2012, Noeske et al. 2007b, Miller et al. 2011, 2012, 2013, Szomoru et al. 2011, Contini et al. 2012, Nelson et al. 2012, 2013, 2016, van Dokkum et al. 2013, Buitrago et al. 2014), the epoch during which the star formation rate (SFR) density in the universe is at its peak value. At this time, massive star-forming galaxies generally look very different from similar-mass star-forming galaxies today (e.g., Fan et al. 2001, Chapman et al. 2005, Hopkins & Beacom 2006, Reddy & Steidel 2009). They tend to be smaller (e.g., Williams et al. 2010, van der Wel et al. 2014a), morphologically clumpier (e.g., Elmegreen & Elmegreen 2006, Elmegreen et al. 2009, 2007, Law et al. 2009, 2007b, 2012b, Genzel et al. 2008, Förster Schreiber et al. 2009, 2014), have thicker disks (Elmegreen & Elmegreen 2006), and higher gas fractions (Daddi et al. 2008, 2010, Tacconi et al. 2008, 2010, 2013, Swinbank et al. 2011).

Many massive star-forming galaxies at $z \sim 2$ do have rotating disks – similar to their local counterparts – but tend to have higher velocity dispersions (and therefore lower V/σ, i.e. the ratio of rotation to velocity dispersion) than local star-forming galaxies (e.g., Epinat et al. 2010, 2008, Green et al. 2014). The higher velocity dispersions at higher redshifts are thought to reflect increased turbulence and thickened disks (e.g., Förster Schreiber et al. 2006, 2009, Wright et al. 2009, 2007, Genzel et al. 2008, 2011, Law et al. 2007a, 2009, 2012a, Wisnioski et al. 2012, 2015, Newman et al. 2013). Theoretical models suggest that the higher turbulence and clumpier morphology of massive star-forming galaxies at $z \sim 2$ relative to their local counterparts are the result of the higher gas fractions (e.g., Dekel et al. 2009, Bournaud et al. 2011, Genel et al. 2012), and that the gas-rich, thicker disks are built-up by smooth, cold-mode gas accretion or minor mergers (e.g., Kereš et al. 2009, 2005, Dekel &

---

[1] This chapter has been previously published as Price *et al.*, 2016, ApJ, 819, 80, and is reproduced with the permission of all coauthors and the copyright holder. Copyright 2016, The American Astronomical Society.

Birnboim 2006, Davé 2008, Dekel et al. 2009, Oser et al. 2010, Cacciato et al. 2012, Ceverino et al. 2012).

However, the theoretical interpretation of the structures of distant star-forming galaxies is complicated by observational limitations, including low spatial resolution and small sample sizes. For example, initial studies with SINFONI found that one third (14 of 47) of star-forming galaxies at $z \sim 2$ appeared to be small and dispersion dominated (i.e., $V/\sigma < 1$; Förster Schreiber et al. 2009). Nonetheless, Newman et al. (2013) revealed that objects that do not show evidence for rotation in the lower resolution observations, especially objects with sizes close to the previous resolution limit, do show evidence for rotation in follow-up adaptive-optics assisted IFU observations. Thus, small rotationally-supported galaxies may appear to be dispersion dominated because of smearing caused by resolution limitations.

New near-infrared (NIR) spectrographs, including KMOS (Sharples et al. 2013, 2004) and MOSFIRE (McLean et al. 2010, 2012) have multiplexing capabilities, and thus allow for extensive kinematic studies of large, complete samples of galaxies at $z \sim 2$. However, as both KMOS and MOSFIRE are seeing limited, kinematic measurements of the majority of the star-forming galaxies at $z \sim 2$ with $\log_{10}(M_*/M_\odot) \lesssim 10$ will suffer from the same resolution problem as the seeing-limited SINFONI studies. Additionally, multi-slit spectrographs like MOSFIRE have no IFU and a constant position angle for all slits in one mask. The mask orientation is generally set by the algorithm to maximize the number of targets in a mask, and thus the slit position angle is randomly oriented compared to the galaxy major axes. The random slit orientations introduce additional challenges to interpreting the observed kinematic information.

Despite these complications, we can take advantage of the large galaxy surveys afforded by multi-object NIR spectrographs by combining these observations with high-resolution rest-frame optical imaging from *HST*. Ancillary *HST*/WFC3 data accurately show what portion of a galaxy falls within the slit, and can be used to interpret the observed spectrum. Furthermore, by using large galaxy samples with detailed ancillary measurements, we can apply statistical approaches to constrain the kinematic structures of galaxies. For example, van der Wel et al. (2014b) use the distribution of observed axis ratios to constrain the structures of star-forming galaxies.

In this paper we study the dynamical and baryonic masses and kinematic structures of a sample of 178 star-forming galaxies using data from the MOSFIRE Deep Evolution Field (MOSDEF) survey (Kriek et al. 2015). The galaxies are observed with random orientations between the slit and kinematic major axes, and rotation is detected in only 35 galaxies. However, for the galaxies without detected rotation we take advantage of our large sample size, accurate Hα SFRs, stellar masses and detailed morphological information from imaging of the CANDELS survey (Koekemoer et al. 2011, Grogin et al. 2011) to constrain their kinematics. We derive dynamical masses for all galaxies, compare them with baryonic masses, and discuss the implications for the structures of the galaxies, the stellar initial mass function (IMF) and dark matter fraction, and the gas kinematics of active galactic nuclei (AGN) host galaxies.

The paper is organized as follows. In Section 4.2, we present our sample and the ancillary measurements. The methods of extracting kinematic information from both 2D spectra and integrated 1D spectra are detailed in Section 3.3. In Section 5.4, we present the baryonic and dynamical masses, as well as V/σ, for both the galaxies with and without detected rotation. The implications and caveats of our results are presented in Section 5.5. We summarize our results in Section 3.6.

Throughout this paper we adopt a ΛCDM cosmology with $\Omega_m = 0.3$, $\Omega_\Lambda = 0.7$, and $H_0 = 70\,\mathrm{km\,s^{-1}\,Mpc^{-1}}$.

3.2 Data

3.2.1 The MOSDEF Survey

We make use of data from the MOSDEF survey (Kriek et al. 2015), conducted using the MOSFIRE spectrograph (McLean et al. 2012) on the 10 m Keck I telescope. In this work, we use the spectra obtained during semesters 2012B, 2013A, and 2014A. When complete, the MOSDEF survey will contain moderate resolution ($R = 3000 - 3650$) rest-frame optical spectra for ~ 1500 H-band selected galaxies at $1.4 \leq z \leq 3.8$ in several Cosmic Assembly Near-Infrared Deep Extragalactic Legacy Survey (CANDELS; Koekemoer et al. 2011, Grogin et al. 2011) fields. A detailed overview of the survey, observations, data reduction, line measurements and sensitivities, success rate, redshift measurements, stellar population properties, and sample characteristics are given in Kriek et al. (2015).

For all galaxies observed with MOSFIRE, we measure structural parameters, including the Sérsic index, n (Sérsic 1968), the effective radius, R_E (assumed to be the semi-major axis, unless explicitly stated otherwise), the axis ratio, b/a, and the major axis position angle from the *HST*/F160W images (released by the CANDELS team) using GALFIT (Peng et al. 2010). See L. de Groot et al. (in preparation) for more details on the structural parameter measurements.

Stellar masses for all MOSDEF galaxies are derived by fitting the $0.3 - 8.0\,\mu$m photometry from the 3D-HST survey (Brammer et al. 2012, Skelton et al. 2014, Momcheva et al. 2016) with the flexible stellar population models (Conroy et al. 2009, Conroy & Gunn 2010) using FAST (Kriek et al. 2009b), while adopting the MOSFIRE redshifts (z_{MOS}). We assume a Chabrier (2003) stellar IMF, along with a Calzetti et al. (2000) dust attenuation curve, a delayed exponentially-declining star formation history, and solar metallicity. To account for template mismatch, we assume the default FAST template error function. Confidence intervals are calibrated using 500 Monte Carlo simulations. Hence, the stellar mass uncertainties do not include systematic uncertainties due to the choice of IMF, dust attenuation curve, or other assumptions. See Kriek et al. (2015) for more details on the stellar population modeling.

Following Taylor et al. (2010), we correct the stellar masses by the difference between the GALFIT ($m_{\textsc{Galfit}}$) and total photometric F160W magnitudes (m_{phot}), using

$$\log_{10} M_* = \log_{10} M_{*,\,\mathrm{FAST}} + 0.4(m_{\mathrm{phot}} - m_{\textsc{Galfit}}). \tag{3.1}$$

This correction makes the size and stellar mass measurements self-consistent.

Emission line fluxes are measured from the optimally extracted MOSFIRE 1D spectra by fitting adjacent lines simultaneously with Gaussians plus a linear fit to account for the underlying continuum. The Hα and Hβ lines are corrected for the underlying Balmer absorption, as estimated from the best-fit stellar population models. See Kriek et al. (2015) and Reddy et al. (2015) for more details on the emission line measurements.

We use the Hα emission lines to estimate SFRs and gas masses ($M_{\rm gas}$) using the following method. For galaxies with detected Hβ, the Balmer absorption-corrected Hα fluxes are corrected for dust using the Balmer decrement, assuming a Cardelli et al. (1989) extinction curve (Reddy et al. 2015). When Hβ is undetected, we assume the reddening of the nebular regions is related to that of the continuum by $A_{\rm V,neb,Calzetti} = 1.86\,A_{\rm V,cont,Calzetti}$ (Price et al. 2014). As this relation was derived by assuming the Calzetti et al. (2000) attenuation curve for both the continuum and line emission, we convert the inferred nebular attenuation to the Cardelli et al. (1989) curve, and correct the Hα fluxes accordingly. In order for Hβ to be used in the dust correction, it must be detected with a signal-to-noise ratio (S/N) ≥ 3, and the spectrum transmission at Hβ must be at least 50% of the maximum transmission.

The dust-corrected Hα fluxes are converted into Hα luminosities, that are then used to calculate the Hα SFRs following the relation of Kennicutt (1998) for a Chabrier (2003) IMF (Shivaei et al. 2015). Finally, the relation between $\Sigma_{\rm gas}$ and $\Sigma_{\rm SFR}$ by Kennicutt (1998) is used to estimate the gas masses, using $\Sigma_{\rm gas} = M_{\rm gas}/(\pi R_E^2)$ and $\Sigma_{\rm SFR} = {\rm SFR}/(\pi R_E^2)$, where R_E is the best-fit GALFIT major axis. In Section 4.5.2 we discuss the validity of this relation at high redshift. The gas mass uncertainties include uncertainties on the Hα and Hβ fluxes and on the slit-loss corrections. An uncertainty of 0.2 dex on $A_{\rm V,cont,Calzetti}$ is assumed when Hβ is undetected.

3.2.2 Sample selection

For this work, we select objects in the redshift ranges $1.34 \leq z \leq 1.75$ and $2.075 \leq z \leq 2.6$, to ensure coverage of the Hα emission line. We also require that Hα is detected (i.e., S/N ≥ 3), and that there is *HST*/F160W coverage, to make use of the GALFIT structural parameter measurements.

We use additional selection criteria to ensure we include only high-quality spectra. First, we consider only primary MOSDEF targets, excluding any serendipitously detected galaxies that happened to fall within the slit. Second, we exclude objects with non-negligible contamination to the Hα flux from neighboring skylines, to provide clean kinematic measurements. Third, we impose quality cuts for both the stellar population and structural parameters to ensure that the best fits adequately model the data. For the stellar population fits, we exclude objects for which the best-fit reduced chi-square $\chi^2_{\rm red} > 10$. For the structural parameters, we flag and exclude objects for which *(a)* the GALFIT runs did not converge, or *(b)* the GALFIT and *HST*/F160W total magnitudes differ by more than 0.5 mag. Fourth, we exclude any objects that fall within the quiescent region in the UVJ diagram (Wuyts et al. 2007, Williams et al. 2009). Fifth, we exclude AGN with outflow signatures or with very broad emission lines (Freeman et al. in preparation). Sixth, we exclude objects that appear to have an interacting counterpart at a similar redshift, as the velocity signatures of these systems may not reflect the internal kinematics. We consider AGN, as identified by their X-ray luminosity, IRAC color, or rest-frame optical emission lines ratios (Coil et al. 2015, M. Azadi et al. in preparation) separately from our sample of star-forming galaxies.

Our final sample includes 178 unique galaxies, with Hβ detected in 138. One object has been observed twice. We also consider 21 unique AGN (14 with Hβ detected) that meet all selection criteria, with 2 AGN having been observed twice.

We show the effective radii versus stellar masses for the galaxies and AGN in our sample in Figure 3.1. For comparison, we also show the best-fit size-stellar mass relations found by van der Wel et al. (2014a) for a complete sample of star-forming (late-type) galaxies at $z = 2.25$ and 1.75. The samples are complete down to $M_* \sim 10^{9.5} M_\odot$ at $z = 2.25$ and down to $M_* \sim 10^{9.1} M_\odot$ at $z = 1.75$, and are therefore a good representation of the star-forming galaxies at these redshifts. Our galaxies generally follow these best-fit size-stellar mass relations in both redshift ranges, though our galaxies at $z \sim 1.5$ may be somewhat smaller in size than the average as determined by van der Wel et al. (2014a).

3.3 Kinematic Measurements

We measure the kinematic properties of our galaxy sample from the Hα emission lines in combination with the *HST*/F160W structural parameters. For objects with spatially-resolved rotation curves, we constrain the rotation and dispersion velocity components by fitting models to the 2D Hα emission lines, as discussed in Section 3.3.1. The kinematics for objects without detected rotation are constrained from the 1D Hα profile, by simultaneously fitting Hα and [NII] lines following the method listed in Section 3.3.2. In Section 3.3.3, we determine for which objects we may reasonably expect to see rotation and for which we do not expect to see rotation at all. We compare these expectations with our observations and discuss what this may tell us about the kinematic structures of galaxies. The method for calculating the dynamical masses is discussed in Section 3.3.4. Finally, in Section 3.3.5, the 2D and 1D kinematic measurement methods are compared using the galaxies with rotation.

3.3.1 Rotation velocity measurements

In this section we constrain the rotational velocity and velocity dispersion simultaneously by modeling the 2D spectra in combination with the F160W structural parameters for each MOSDEF galaxy in our sample. Previous studies have presented methods for fitting 2D spectra, including Vogt et al. (1996), Simard & Pritchet (1999), and Weiner et al. (2006). However, the models of Simard & Pritchet (1999) and Weiner et al. (2006) do not account for misalignment between the slit and major axis, while Vogt et al. (1996) and Simard & Pritchet (1999) exclude velocity dispersion.

Instead, we define kinematic models that explicitly include the position angle misalignment and inclination, and simultaneously fit the rotation velocity and velocity dispersion. The

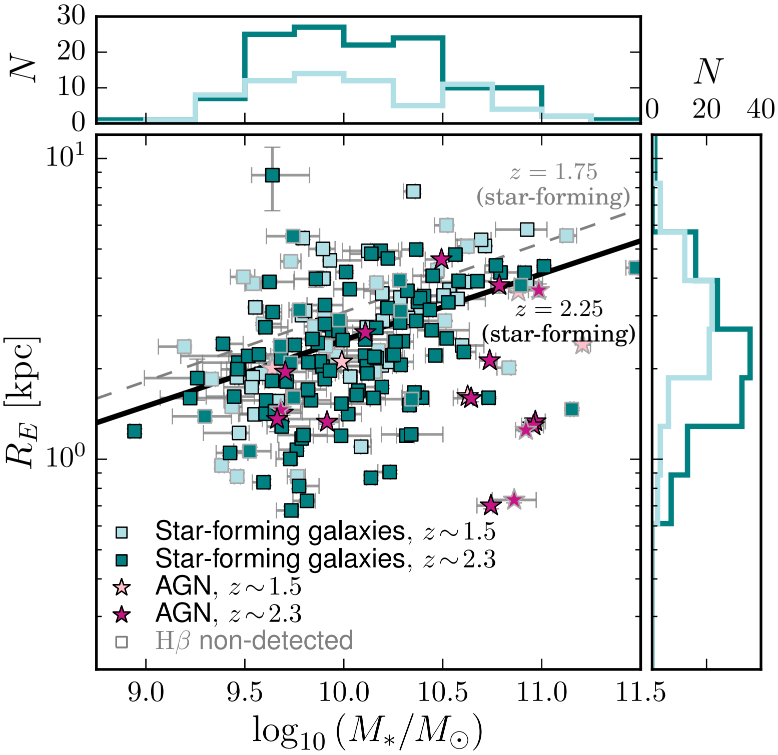

Figure 3.1: Effective radius, R_E, versus stellar mass, $\log_{10}(M_*/M_\odot)$, for the galaxies and AGN in our sample, split by redshift range. The galaxies at in the lower ($z \sim 1.5$) and higher ($z \sim 2.3$) redshift ranges are shown as light blue and teal squares, respectively. The AGN in the same redshift ranges are shown as pink and purple stars, respectively. Histograms of R_E and $\log_{10}(M_*/M_\odot)$ show the objects (galaxies and AGN) in the lower (light blue) and higher (teal) redshift ranges. Galaxies (and AGN) without Hβ detections are marked with grey outlines. The black solid and grey dashed lines represent the best-fit size-stellar mass relations for star-forming galaxies from van der Wel et al. (2014a) at $z = 2.25$ and $z = 1.75$, respectively. Our sample of star-forming galaxies generally follow the best-fit size-stellar mass relations.

kinematic models are discussed in detail in Appendix B.1. In summary, the kinematic models include both rotation and a constant velocity dispersion over the galaxy, and have a total of 3 free parameters: the asymptotic velocity (V_a) and turnover radius (r_t) of the arctan rotation curve model, and the constant intrinsic velocity dispersion ($\sigma_{V,0}$). We assume the best-fit GALFIT parameters and the position angles from the F160W observations. The model is collapsed along the line-of-sight, and convolved to match the seeing conditions of each spectrum. Using the position angle, inclination, brightness profile, and seeing information, we determine what portions of the model fall within the slit for each object. Finally, the model is collapsed in the spatial direction perpendicular to the slit and convolved by the instrumental resolution.

To fit the emission lines, we start by subtracting the continuum from each Hα 2D spectrum. We also trim the spectrum to exclude the [NII] emission lines and to include only the positive emission line image. We then construct a mask for the emission line spectrum to exclude missing data and low signal-to-noise rows from our fitting procedure. A detailed description of this procedure can be found in Appendix B.2.

We then find the best-fit models to the trimmed 2D Hα spectra and the corresponding confidence intervals by performing parameter space exploration using the `python` Markov-Chain Monte Carlo (MCMC) package `emcee` (Foreman-Mackey et al. 2013), following the method detailed in Appendix B.2. As the rotation curve turnover is not well constrained in our data, there is a degeneracy in the values of V_a and r_t. Nonetheless, the values of $V(R_E)$ and $V_{2.2} = V(2.2r_s)$ (assuming the arctan rotation curve model, see Equation B.6) are well constrained. We note that we explicitly include the structural parameters and projection effects in our model, so we directly constrain the intrinsic galaxy parameters, without projection or blending effects. Examples of the 2D Hα emission line fits are shown in Figure 3.2.

We use the values of $V(R_E)$ to determine which objects have spatially resolved rotation. We take objects with $V(R_E) \neq 0$ within the 95% one-sided distribution to be our sample with resolved rotation, and the objects that fail this cut to be our dispersion-only sample. The position-velocity diagrams of the 35 galaxies with detected rotation are shown in Appendix B.3.

3.3.2 Integrated velocity dispersion measurements

For all objects without resolved rotation (see Section 3.3.1), we measure the kinematics from the 1D spectra. As our sample consists of star-forming galaxies, we may expect that their intrinsic velocity support is at least partially rotational. This assumption is reinforced by the work of Newman et al. (2013), who find that galaxies that were initially classified as dispersion-dominated in fact do show evidence for rotation in observations with higher spatial resolution. Thus, we model the composite unresolved kinematics by assuming a value for $(V/\sigma_{V,0})_{R_E} = V(R_E)/\sigma_{V,0}$, while taking into account the GALFIT parameters and seeing conditions. We then use this model to convert the measured velocity dispersion to intrinsic quantities.

We measure the velocity dispersion from the optimally extracted 1D spectra by fitting

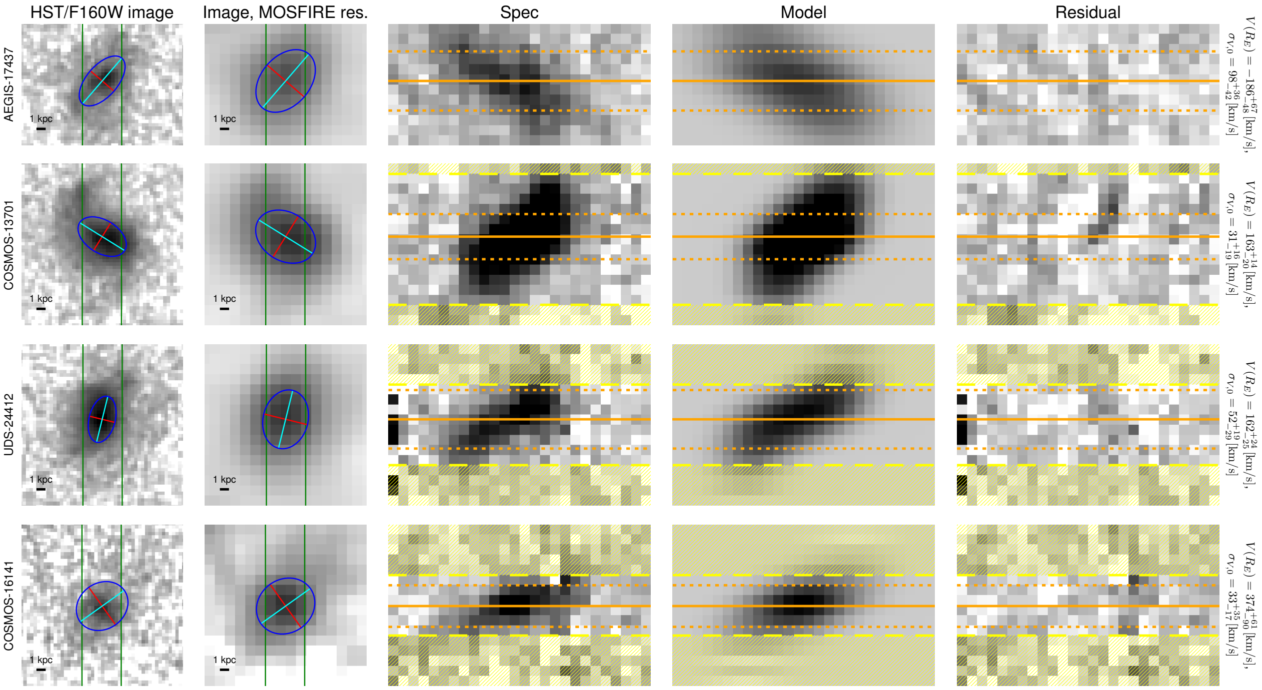

Figure 3.2: Example overviews of the spatially resolved kinematic modeling, as described in Section 3.3.1. The first column shows the *HST*/F160W image, the slit position (green lines) and the Galfit half-light ellipse (major axis in cyan, minor axis in red, ellipse in blue). The second column shows the *HST*/F160W image convolved to match the seeing resolution of the MOSFIRE spectra, with the Galfit parameters similarly convolved. The third column shows the continuum-subtracted 2D spectrum centered at Hα. The fourth column shows the best-fit kinematic model to the line emission. The fifth column shows the residual between the 2D spectrum and the best-fit model, on the same grey scale as the 2D spectrum. In the third-to-fifth columns, the vertical and horizontal axes are the spatial position and wavelength, respectively. The orange horizontal line shows the best-fit model center, y_0, with the dotted lines showing the convolved and projected R_E, and the yellow shading and yellow dashed lines indicate low signal-to-noise rows that are masked in the fitting procedure. For each object, the field and 3D-HST v4 ID number are shown at the left, and the best-fit $V(R_E)$ and $\sigma_{V,0}$ are given on the right.

Hα, the [N II] doublet, and the continuum simultaneously with a triple Gaussian and a linear component. We fit the spectrum between $6480\,\text{Å} \leq \lambda/(1+z_{\rm MOS}) \leq 6650\,\text{Å}$, and mask pixels with no coverage. We vary the coupled line centers, while constraining $\lambda_{\rm H\alpha,obs}$ to within ± 20Å of $\lambda_{\rm H\alpha}(1+z_{\rm MOS})$. The widths of the emission lines (in Å) are coupled in velocity space, with $\sigma_{\lambda,[\rm N\,II]\lambda\lambda 6584,48} = \sigma_{\lambda,\rm H\alpha}\left(\lambda_{[\rm N\,II]\lambda\lambda 6584,48}/\lambda_{\rm H\alpha}\right)$. We also assume $F([\text{N II}]\lambda 6548) = 1/3\,F([\text{N II}]\lambda 6584)$ (Osterbrock & Ferland 2006). Finally, we enforce $\sigma_{\lambda,\rm H\alpha} \geq \sigma_{\lambda,\rm sky}$, with the instrumental resolution measured from the median skyline width.

The Hα line widths are corrected for the line broadening due to the instrumental resolution by subtracting $\sigma_{\lambda,\rm sky}$ in quadrature from $\sigma_{\lambda,\rm H\alpha}$. Each corrected H$\alpha$ line width $\sigma_{\lambda,\rm H\alpha,\,corr}$ is converted to an observed velocity dispersion, $\sigma_{V,\,\rm obs}$, using the best-fit redshift.

The errors on the observed velocity dispersions are estimated by creating 500 realizations where the spectra are perturbed according to the corresponding error spectra. We then perform the same fitting and correction procedure on the perturbed spectra, and convert the corrected line widths to velocity dispersions using the best-fit redshift of each realization.

For each object, we convert the observed velocity dispersion into an intrinsic root mean square (RMS) velocity, $V_{\rm RMS} = \sqrt{V^2+\sigma_V^2}$, which explicitly includes both intrinsic rotation and dispersion velocities. This method is discussed in detail in Appendix C. In summary, we model each object as an inclined disk (using the GALFIT structural parameters R_E, n, b/a), with the major axis offset from the slit by ΔPA. The rotation and velocity dispersion kinematics are included by assuming a fixed ratio of $(V/\sigma_{V,0})_{R_E}$, and then the model is convolved to match the MOSFIRE seeing resolution. We determine which portions of the model fall within the slit width and the extracted width in the spatial direction, and then apply the optimal-extraction weighting. For this model, we calculate the ratio of the luminosity-weighted second velocity moment ($\sigma_{V,\,\rm model}$) to the RMS velocity at R_E ($V_{\rm RMS}(R_E)_{\rm model}$), and use this ratio to convert the observed, integrated velocity dispersion to the composite RMS velocity at R_E following

$$V_{\rm RMS}(R_E)_{\rm 1D,\,corr} = \sigma_{V,\,\rm obs}\left(\frac{\sigma_{V,\,\rm model}}{V_{\rm RMS}(R_E)_{\rm model}}\right)^{-1}. \tag{3.2}$$

van Dokkum et al. (2015) use an α parameterization to infer a rotational velocity from an observed velocity dispersion. This α value is empirically derived and combined with an inclination correction, with $\alpha = \sigma_{V,\,\rm obs}/\,(V\sin i)$. Hence, this correction does not take into account the exact portion of the galaxy observed through the slit or partial support from random motions. However, the galaxies by van Dokkum et al. are in general smaller than those in our sample, and will suffer less from slit losses.

In Figure 3.3 we show $\sigma_{V,\,\rm obs}$ and $V_{\rm RMS}(R_E)_{\rm corr}$ vs. R_E for galaxies and AGN without detected rotation. For now, we assume $(V/\sigma_{V,0})_{R_E} = 2.1$, the median of the values measured for galaxies with detected rotation. For reference, we also show the velocity dispersions measured from the integrated 1D spectra of the galaxies with detected rotation, with the corrections for these objects calculated using the exact $(V/\sigma_{V,0})_{R_E}$ measured for each object. The median observed 1D velocity dispersion for our sample with $M \geq 10^{9.5} M_\odot$ (the approximate

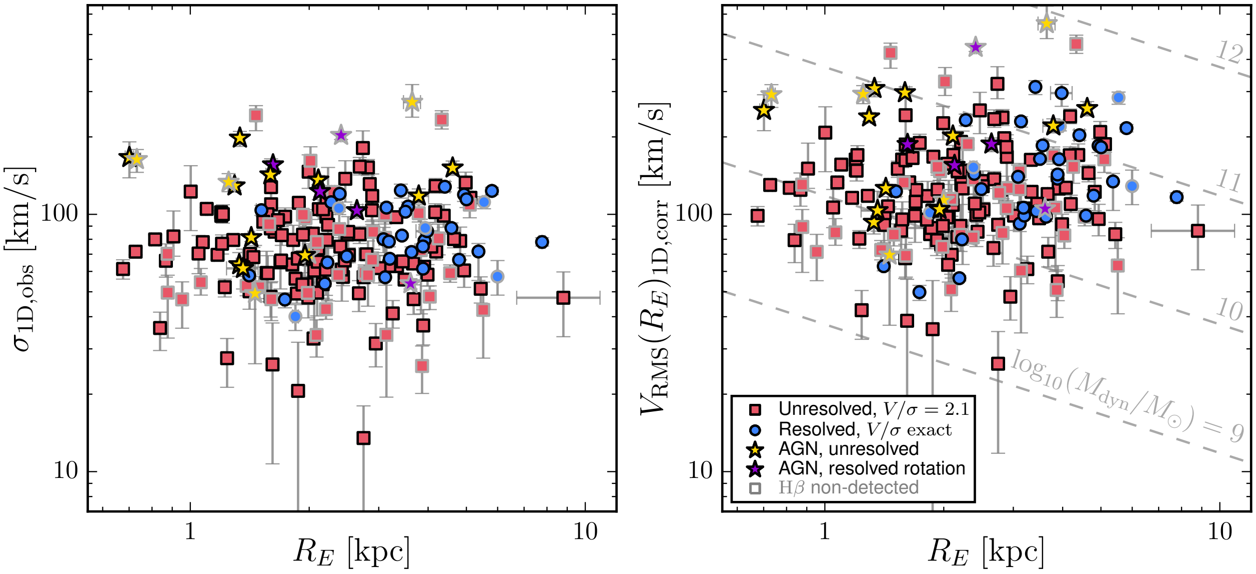

Figure 3.3: Observed velocity dispersion $\sigma_{\rm 1D,obs}$ (left) and the corrected velocities $V_{\rm RMS}(R_E)_{\rm 1D,corr}$ (right) vs. R_E. The corrections for the galaxies without resolved rotation (red squares) are derived assuming $[(V/\sigma_{V,0})_{R_E}]_{\rm 2D,median} = 2.1$. For comparison, the corrections for the galaxies with resolved rotation, derived using the measured $(V/\sigma_{V,0})_{R_E}$ of each object, are shown as well (blue circles). We also show the AGN in our sample, and denote those with and without resolved rotation by purple and yellow stars, respectively. Galaxies (and AGN) without Hβ detections are marked with grey outlines. Lines of constant dynamical mass, calculated using Equation 3.3 and assuming $(V/\sigma_{V,0})_{R_E} = 2.1$, are shown in the right panel (dashed grey lines). The RMS velocities are on average a factor of ~ 2 larger than the observed values.

completeness limit for star-forming galaxies in the MOSDEF survey, see Shivaei et al. 2015) is $(\sigma_{V,\,\mathrm{obs}})_{\mathrm{median}} = 78$ km/s. The median observed velocity dispersion $(\sigma_{V,\,\mathrm{obs}})_{\mathrm{median}} = 70$ km/s of the galaxies at $z \sim 1.5$ is slightly lower than the value of $(\sigma_{V,\,\mathrm{obs}})_{\mathrm{median}} = 80$ km/s for the galaxies at $z \sim 2.3$.

3.3.3 Resolved vs. unresolved kinematics

As our primary sample consists of star-forming galaxies, in Section 3.3.2 we have treated the objects for which we only observe velocity dispersion as being intrinsically disks, with some amount of thickening. Here we consider whether this is a reasonable assumption by considering the necessary conditions to observe rotation in a galaxy.

One reason why intrinsic rotation may not be observable is that the galaxy is small with respect to the seeing size. If there is only one resolution element across the galaxy disk, then any rotation signature will be washed out and we would only observe velocity dispersion. Additionally, the galaxy major axes may be misaligned with the slit axis. A position angle (PA) offset reduces the ability to detect rotation, as for more misaligned objects, the rotational information is projected into fewer resolution elements along the slit. At the most extreme, if a galaxy is completely misaligned with the slit (i.e. $\Delta\mathrm{PA} = 90°$), the rotational signature is collapsed into the same resolution element, and again we would only observe a velocity dispersion.

We consider the dual effects of object size and ΔPA, by calculating how much of the stellar light major axis falls within the slit, projected along the slit direction. The projected size of the object falling within the slit ($2\,R_{E,\mathrm{proj}}$) should be larger than the seeing for the object to be spatially resolved, or $R_{E,\mathrm{proj}} \geq \mathrm{FWHM}_{\mathrm{seeing}}/2$.

We divide our sample into four categories, based on combination of the projected spatial resolution criterion given above (resolved vs. unresolved) and whether we detect rotation or not (rotation vs. dispersion, see Section 3.3.1). This classification scheme gives 15 spatially resolved galaxies with observed rotation, 20 spatially unresolved galaxies with observed rotation, 20 spatially resolved galaxies with only dispersion observed, and 123 spatially unresolved galaxies with only dispersion observed. In Figures 3.4 & 3.5 we show example *HST* images and spectra, respectively, for objects in each category.

We show PA offset versus object size (R_E) as a function of seeing in Figure 3.6. At fixed R_E, we tend to have more "dispersion-only" objects and fewer objects with detected rotation as the position angle offset increases from aligned (0°) to completely misaligned (90°). We also note that on average, galaxies for which we observe rotation tend to be larger than those without observed rotation. This finding supports the possibility that we may not observe rotation for some objects simply because they are physically too small to resolve, even if there is no position angle offset between the semi-major axis and the slit. We can also see these trends in Figure 3.4, as the objects with observed rotation (left panels) tend to have better alignment between their major axes and the slit, and tend to have larger angular sizes relative to the objects for which we only observe dispersion (right panels).

However, not all objects follow the expected classifications. For instance, we observe

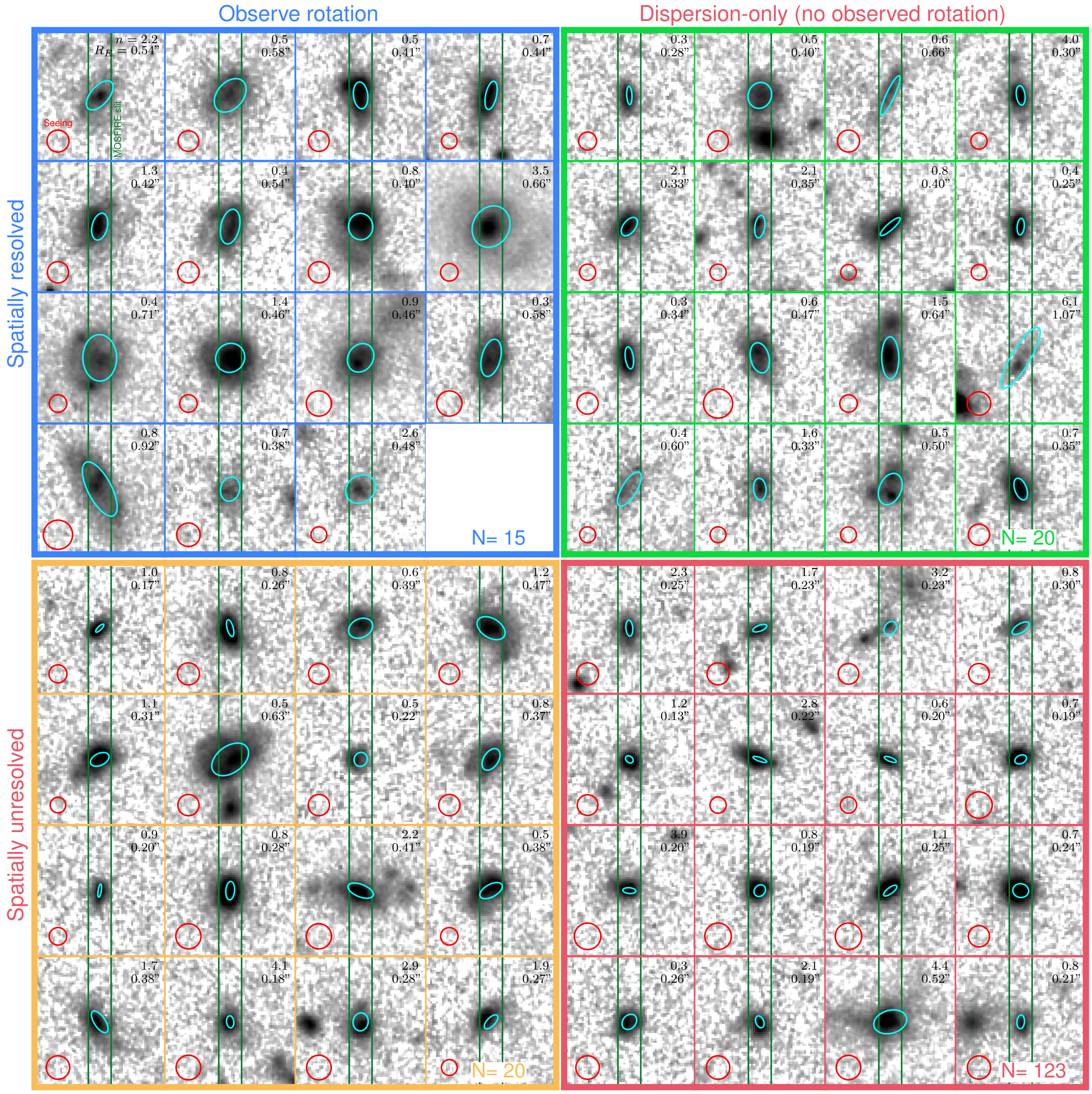

Figure 3.4: *HST*/F160W galaxy images ($4'' \times 4''$) for each of the 4 spatial/kinematic resolution categories: spatially resolved with observed rotation (upper left panel, blue), spatially unresolved with observed rotation (lower left, yellow), spatially resolved with only dispersion observed (upper right, green), and spatially unresolved with only dispersion observed (lower right, red). Each image is centered on the object center. The slit positions and orientations are shown with the green lines. We represent the GALFIT effective radius (R_E, measured from the major axis), axis ratio (b/a), and position angle relative to the slit (ΔPA) for each object with the cyan ellipses. The values of R_E and the Sérsic index n are annotated in the upper-right corners of the images. The atmospheric seeing FWHMs are shown with the red circles. The total number of objects in each of the 4 categories is displayed in the lower right corner of each quadrant. Spatially close companions of the target objects are located at different redshifts.

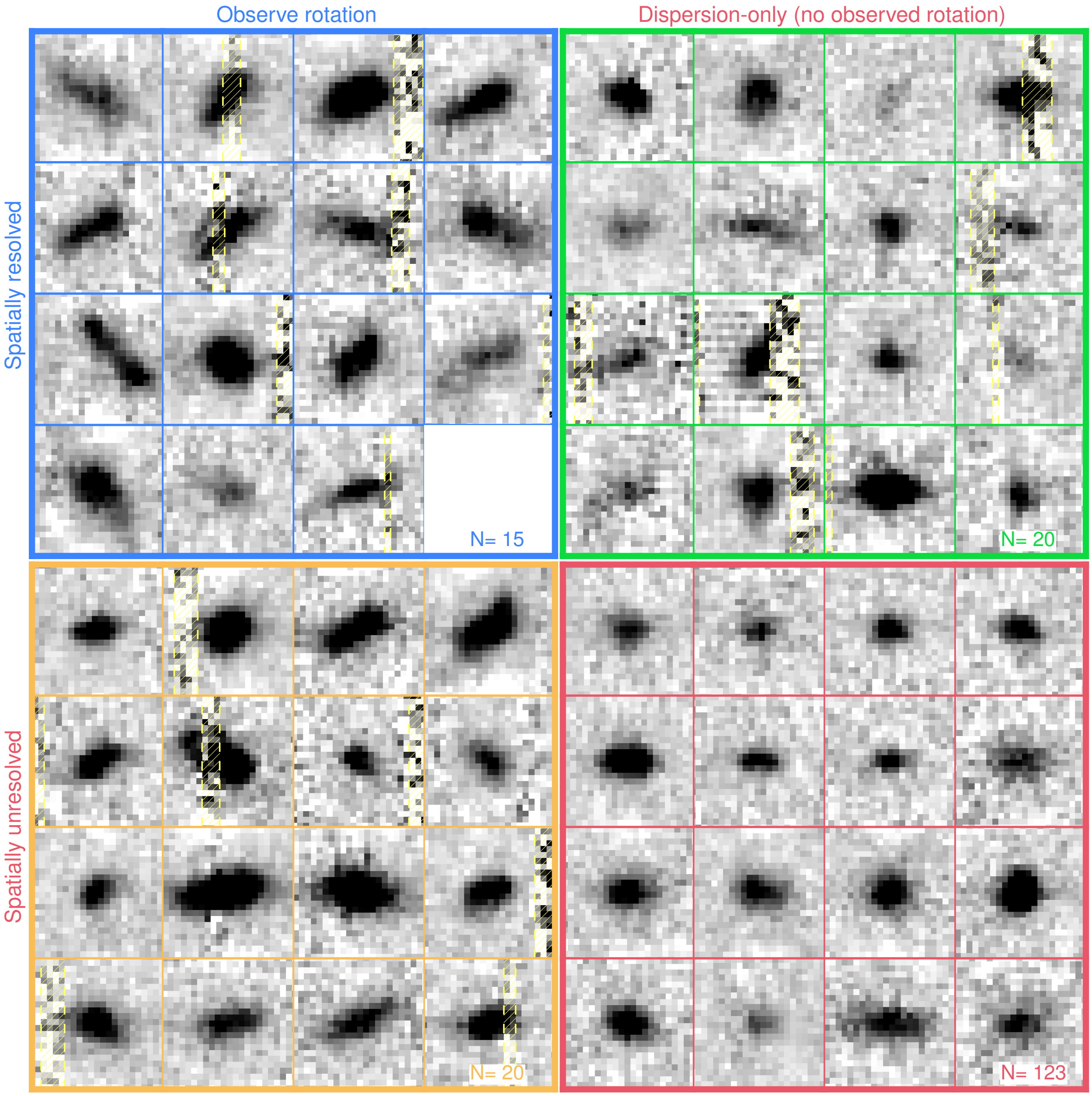

Figure 3.5: MOSFIRE spectra centered on Hα for galaxies in the 4 spatial/kinematic resolution categories. The displayed galaxies are the same as those shown in Figure 3.4, with each object vertically centered on the same position and same spatial scale as the *HST*/F160W images. The horizontal axis shows wavelength, where each stamp spans ~ 36 Å (H band) or ~ 48 Å (K band) in the observed frame.

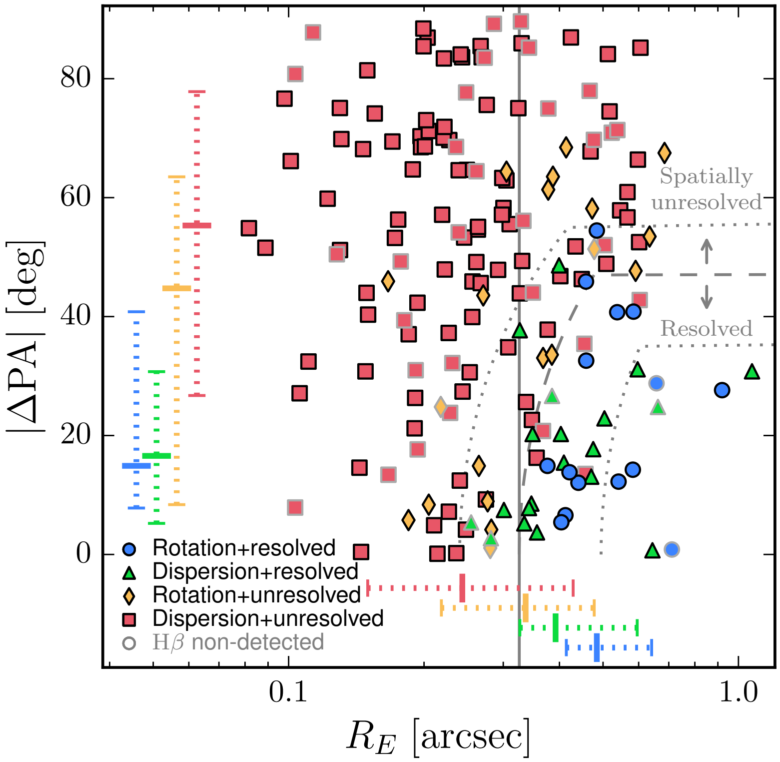

Figure 3.6: The position angle (PA) offset between the slit and photometric major axis versus the effective radius (R_E) for galaxies in our sample. The color coding is based on whether we observe rotation or not (rotation vs. dispersion), and whether the projected major-axis is larger than the seeing size or not (spatially resolved vs. unresolved). The colored lines denote the median R_E and $|\Delta\mathrm{PA}|$ for each subsample, with the dotted lines showing the 68% value ranges. Galaxies without Hβ detections are marked with grey outlines. The vertical grey line denotes 1/2 the median seeing FWHM ($0.\!\!''65$) for our sample. The dashed grey line shows the division between spatially resolved and unresolved objects described in Section 3.3.3, assuming the median seeing. Objects to the right and below this line would be classified as spatially "resolved" (assuming they were observed under the median seeing conditions), while objects to the left and above would be classified as spatially "unresolved". The upper and lower dotted grey lines show the dividing lines if the seeing were equal to the minimum ($0.\!\!''48$) and maximum ($0.\!\!''99$) effective seeing conditions, respectively (see Table 1, Kriek et al. 2015).

rotation for some spatially unresolved objects. These galaxies are shown as yellow diamonds in Figure 3.6, with example images and spectra shown in the lower left panels of Figures 3.4 and 3.5. Also, if all galaxies in our sample are intrinsically disk galaxies and have at least partial rotational support, we would expect to see rotation in all objects that are spatially resolved. Yet we do not observe rotation in some of the galaxies that meet the projected spatial resolution criterion, which are shown as green triangles in Figure 3.6, with examples in the upper right panels of Figures 3.4 and 3.5.

Other effects may influence the classification of our sample into these four sub-samples, which could explain why we see objects in the unexpected classification categories. First, the position angle offset between the kinematic major axis and the slit could be incorrect. This error may be due to uncertainties in the photometric major axis position angle estimation or to a misalignment between the kinematic and photometric major axes. The latter effect has been observed by Wisnioski et al. (2015) in galaxies at $z \sim 2$, and possibly indicates disturbed kinematics due to mergers (Epinat et al. 2012). If the position angle offset is incorrect, our projected size along the major axis may not match the true intrinsic projected size of the region that we probe with the kinematics. Thus objects may scatter from the “spatially resolved” category into the “spatially unresolved” category or vice versa.

Second, we use the rest-frame optical R_E in this classification, but we measure the kinematics from Hα emission. We show in Section 3.5.6 that the rest-frame optical and Hα sizes of the galaxies with detected rotation are very similar, so using R_E to determine spatial resolution is a reasonable approximation. Still, if an object is close to the detection limit, small differences between R_E and Hα size could change the spatial resolution classification.

Third, we do not incorporate inclination angle in our classification procedure. For face-on galaxies, we do not expect to detect rotation. If we consider galaxies with $b/a \geq 0.9$ (i.e., $i \lesssim 26^\circ$, assuming $(b/a)_0 = 0.19$) to be face-on, only 5 of our galaxies satisfy this criterion, three of which have detected rotation, and two of which had been classified as “spatially resolved”.

Fourth, we rely on single-component GALFIT fits to determine the photometric position angle, axis ratio b/a, and stellar effective radius R_E. Our galaxies often exhibit clumps, so they are not perfectly fit by a smooth Sérsic profile. Furthermore, GALFIT is unable to recover extreme inclination angles (i.e., close to edge-on or face-on; Epinat et al. 2012). These limitations could further influence the accuracy of the position angle, effective radius, and axis ratio, and could influence whether an individual galaxy is categorized as “spatially resolved” or not.

Fifth, the S/N of the observed spectra will influence the object kinematic categorization. Our 95% one-sided $V(R_E)$ detection requirement may result in classifying objects with intrinsic rotation but low S/N spectra as “dispersion-only.” The example spectra in Figure 3.5 in the spatially-resolved, dispersion-only quadrant (green upper-right panel) do appear to have either similar or lower signal-to-noise ratios relative to the spectra of the objects with detected rotation (shown in the left panels).

Sixth, neighboring skylines may overlap portions of a rotation curve, which may also cause an object to fail the $V(R_E)$ detection criterion. In Figure 3.5, we see some objects in the green quadrant with signifiant overlap with skyline contaminated columns (i.e., the fourth object, top row, and second object, third row, of the green, upper-right quadrant of Figure 3.5).

Between the four categories, 89% of the objects are consistent with having rotation. This includes the 69% of the galaxies that are unresolved and have no detected rotation, for which the kinematic structures of the individual galaxies are unknown. In Section 3.4.2, we find that galaxies without detected rotation are consistent with having kinematic support from both rotation and random motions. The only galaxies inconsistent with the assumption of intrinsic rotational support are those that are spatially resolved without observed rotation (green objects, Figure 3.6). However, as mentioned previously, there are sources of uncertainty in our categorizations that may imply these objects may still have intrinsic rotation.

3.3.4 Dynamical mass measurements

We combine the kinematic and structural information to calculate the dynamical masses of our galaxies. The rotation and dispersion velocities are combined by taking the RMS velocity, $V_{\rm RMS}(R_E) = \sqrt{\sigma_{V,0}^2 + V(R_E)^2}$, and we calculate the total dynamical mass as

$$M_{\rm dyn} = k_{\rm eff}\frac{V_{\rm RMS}(R_E)^2 R_E}{G}, \tag{3.3}$$

where G is the gravitational constant. Here we define an "effective" virial coefficient to account for the relative contribution to the RMS velocity from the rotation and dispersion velocities (i.e., including an "asymmetric drift" correction from the velocity dispersion, as in Meurer et al. 1996, Epinat et al. 2009, Daddi et al. 2010, Newman et al. 2013):

$$k_{\rm eff} = \frac{k_{\rm disp} + k_{\rm rot}((V/\sigma_{V,0})_{R_E})^2}{1 + ((V/\sigma_{V,0})_{R_E})^2}, \tag{3.4}$$

where $(V/\sigma_{V,0})_{R_E} = V(R_E)/\sigma_{V,0}$.[2] We assume $k_{\rm disp} = 5$ as the virial coefficient corresponding to the dispersion kinematic component, from the simple case of a sphere of uniform density (Pettini et al. 2001). We estimate the virial coefficient for the rotational kinematic component following Miller et al. (2011), who find $k = 1.33$ for the dynamical mass within $r = 2.2r_s = 1.3R_E$. To convert to the total dynamical mass, we approximate $k_{\rm rot} \approx 2k = 2.66$.

To calculate $k_{\rm eff}$ and the dynamical masses, we use the best-fit values of $V(R_E)$ and $\sigma_{V,0}$ measured in Section 3.3.1 for the galaxies with detected rotation. For the galaxies without observed rotation, we have to assume a value of $(V/\sigma_{V,0})_{R_E}$ to calculate $k_{\rm eff}$, $V_{\rm RMS}(R_E) = V_{\rm RMS}(R_E)_{\rm 1D,\,corr}$, and $M_{\rm dyn}$. We will discuss the assumption of $(V/\sigma_{V,0})_{R_E}$ in Section 5.4.

---

[2] Note that when $(V/\sigma_{V,0})_{R_E} \to \infty$ (i.e. only rotational support), we have $V_{\rm RMS}(R_E) = V(R_E)$ and $k_{\rm eff} \to k_{\rm rot}$, and Equation 3.3 is equivalent to the dynamical mass assuming only rotational support, $M_{\rm dyn} = k_{\rm rot}V(R_E)^2R_E/G$. In the opposite limit, when $(V/\sigma_{V,0})_{R_E} = 0$ (i.e. only pressure support), we have $V_{\rm RMS}(R_E) = \sigma_{V,0}$ and $k_{\rm eff} = k_{\rm disp}$, and we recover the case for pressure-only support: $M_{\rm dyn} = k_{\rm disp}\sigma_{V,0}^2R_E/G$.

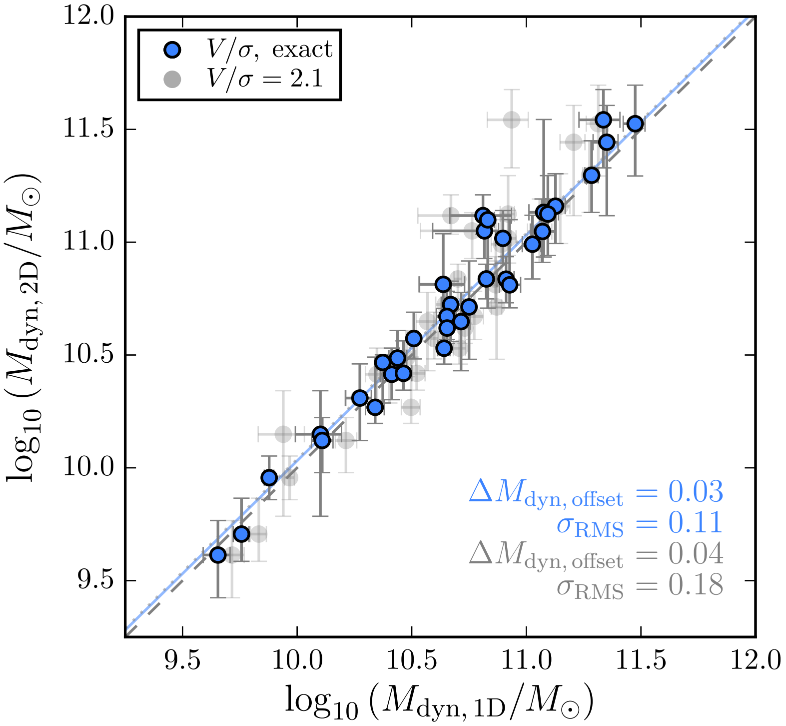

Figure 3.7: Comparison of the dynamical mass measurement methods. The masses of the galaxies with observed rotation are measured with both the resolved kinematic information ($M_{\rm dyn,\,2D}$) and from the aperture-corrected optimally-extracted 1D-spectra ($M_{\rm dyn,\,1D}$) assuming the exact value of $(V/\sigma_{V,0})_{R_E}$ for each objects (blue circles). There is little scatter ($\sigma_{\rm RMS} = 0.11\,$dex) between the two measurements, and a small median offset $\Delta M_{\rm dyn} = 0.03\,$dex (blue line), with $M_{\rm dyn,\,2D}$ being slightly higher than $M_{\rm dyn,\,1D}$. If instead a constant $(V/\sigma_{V,0})_{R_E} = 2.1$ were assumed in calculating the 1D velocity dispersion corrections (grey circles) the median offset (dotted grey line) and scatter are slightly larger ($\Delta M_{\rm dyn} = 0.04\,$dex, $\sigma_{\rm RMS} = 0.18\,$dex). Nonetheless, there is still excellent agreement between the measurements.

3.3.5 Dynamical mass method comparison: spatially resolved galaxies

We test the method for correcting the kinematics of disk galaxies without detected rotation using the spatially-resolved rotation sample of galaxies, for which we have more detailed kinematic information.

First, we measure the dynamical masses $M_{\mathrm{dyn,\,2D}}$ using the exact values of $V(R_E)$ and $\sigma_{V,0}$ from the 2D spectral fitting method in Section 3.3.1. We then measure the velocity dispersions from the optimally-extracted 1D spectra for the same sample of galaxies. We assume the exact $(V/\sigma_{V,0})_{R_E} = V(R_E)/\sigma_{V,0}$ measured from the 2D spectral fitting for each object to calculate the corrected 1D velocity dispersions (Equation 3.2), k_{eff} (Equation 3.4), and the resulting dynamical masses $M_{\mathrm{dyn,\,1D}}$.

We compare $M_{\mathrm{dyn,\,1D}}$ with $M_{\mathrm{dyn,\,2D}}$ in Figure 3.7. The corrected $M_{\mathrm{dyn,\,1D}}$ values are in excellent agreement with the $M_{\mathrm{dyn,\,2D}}$ values, with little scatter between them ($\sigma_{\mathrm{RMS}} = 0.11\,\mathrm{dex}$). We find a median offset of $\Delta \log_{10} M_{\mathrm{dyn,offset}} = 0.03\,\mathrm{dex}$ between the two measurements, such that the 2D-kinematic derived values of M_{dyn} are slightly larger than the values derived from the aperture-corrected 1D spectra.

However, if these galaxies would not have been resolved, we would not have known their intrinsic $(V/\sigma_{V,0})_{R_E}$, to be used in the dynamical mass estimate. Thus, we also calculate $M_{\mathrm{dyn,\,1D}}$ using the median $[(V/\sigma_{V,0})_{R_E}]_{\mathrm{2D,median}} = 2.1$ for each object (shown as the grey points in Figure 3.7). We find a slightly larger offset ($\Delta \log_{10} M_{\mathrm{dyn,offset}} = 0.04\,\mathrm{dex}$) and scatter ($\sigma_{\mathrm{RMS}} = 0.18\,\mathrm{dex}$). Hence, for the galaxies with detected rotation, assuming the average value of $(V/\sigma_{V,0})_{R_E}$ for each object yields dynamical masses that are nearly as accurate as the dynamical masses derived from the rotation curves. Based on this test, we conclude that the 1D velocity dispersion correction method works well, and should produce reasonable dynamical masses for the remainder of the galaxies without observed rotation if the average $(V/\sigma_{V,0})_{R_E}$ is known.

3.4 Results

We now consider the total sample, combining the samples with and without observed rotation, and compare the dynamical and the baryonic masses, and assess the kinematic structures of star-forming galaxies at $z \sim 2$.

3.4.1 Comparison of dynamical and baryonic masses

In order to measure the dynamical masses for all galaxies in our sample, we need a $(V/\sigma_{V,0})_{R_E}$ ratio for the galaxies without resolved kinematics. We assume that the kinematically resolved objects have a similar structure as the unresolved objects, and adopt the median $(V/\sigma_{V,0})_{R_E} = 2.1$ as measured from the rotation objects (see Section 3.3.1 and Appendix B).

In Figure 3.8 we compare the dynamical masses to the baryonic masses, $M_{\mathrm{baryon}} = M_* + M_{\mathrm{gas}}$ (as given in Section 3.2.1). They show a remarkable agreement, with a median

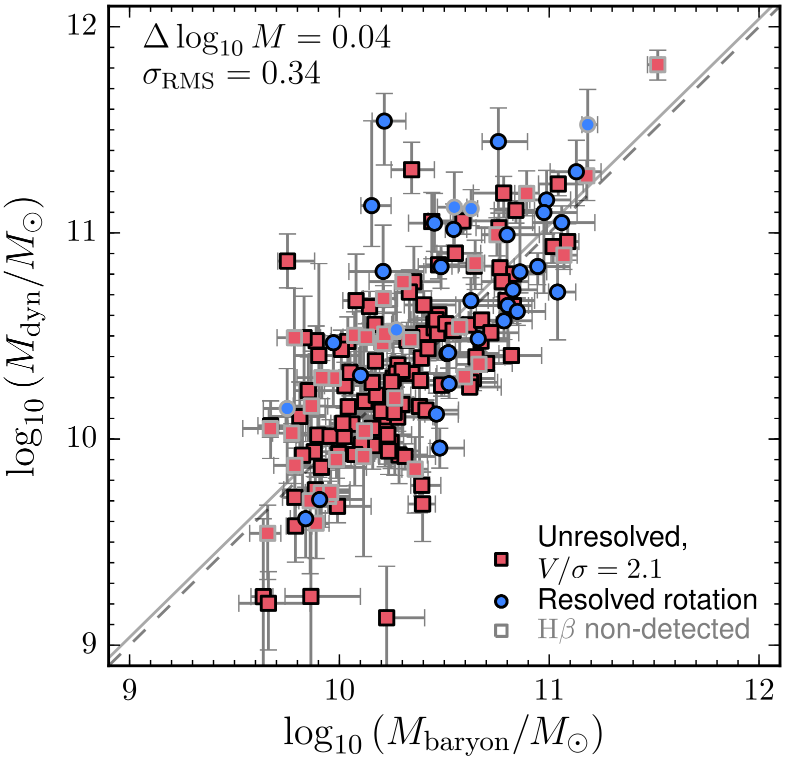

Figure 3.8: Comparison of dynamical and baryonic (stellar + gas) masses for all galaxies in our sample. Symbols are similar as in Figure 3.3. To calculate the velocity corrections for the sample without observed rotation, we assume the median $(V/\sigma_{V,0})_{R_E} = 2.1$ from the sample with observed rotation. The grey dashed line indicates equal $M_{\rm baryon}$ and $M_{\rm dyn}$, and the solid grey line indicates the median offset of $\Delta \log_{10} M = \log_{10} M_{\rm dyn} - \log_{10} M_{\rm baryon}$. The scatter of the data around the median offset is $\sigma_{\rm RMS} = 0.34\,$dex. The error bars do not include the systematic uncertainties discussed in Section 4.5.2.

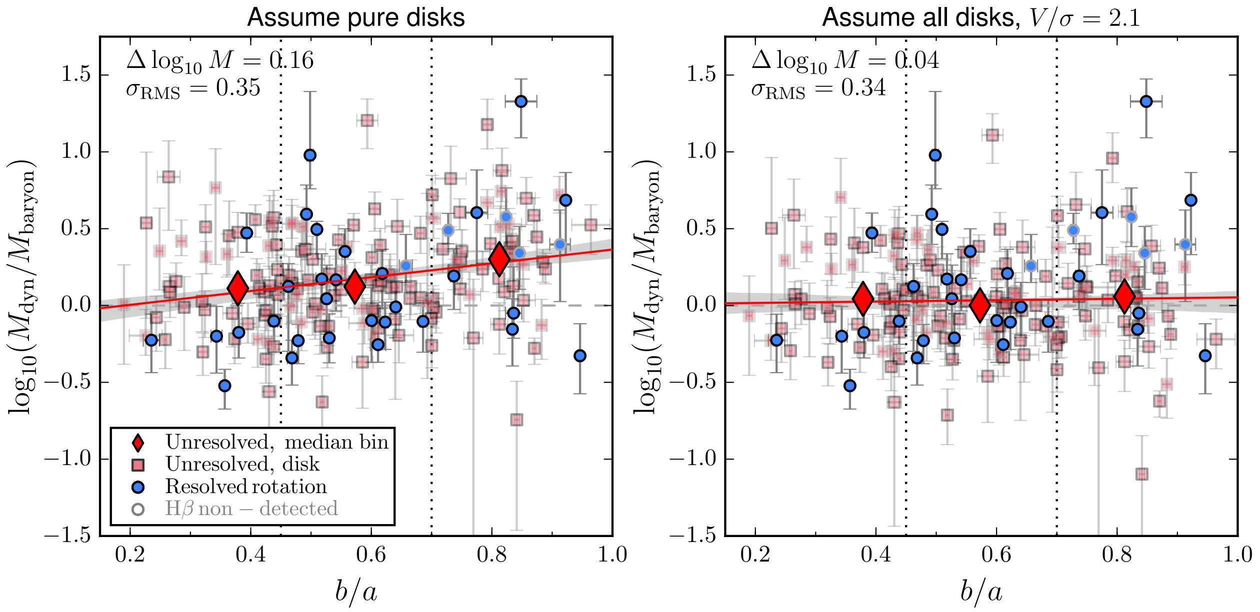

Figure 3.9: The difference between the dynamical and baryonic masses $\Delta\log_{10}M$ vs. axis ratio b/a under different assumptions of $(V/\sigma_{V,0})_{R_E}$. The galaxies with and without detected rotation are shown as blue circles and red squares, respectively. Galaxies without Hβ detections are marked with grey outlines. In the left and right panel, we assume no intrinsic velocity dispersion (i.e., $(V/\sigma_{V,0})_{R_E} \to \infty$) and $(V/\sigma_{V,0})_{R_E} = 2.1$, respectively, for the objects without observed rotation. We show the median values of $\Delta\log_{10}M$ and b/a for the objects without observed rotation within bins of b/a ($[0, 0.45), [0.45, 0.7), [0.7, 1]$) as red diamonds, and show the linear best-fit to the median points as the red line. The bin boundaries are shown as the black dotted lines.

offset of $\Delta\log_{10}M = 0.04\,\mathrm{dex}$, where $M_{\rm dyn}$ is slightly larger than $M_{\rm baryon}$ at a given $M_{\rm baryon}$. The scatter about the median $\Delta\log_{10}M$ is low, with $\sigma_{\rm RMS} = 0.34\,\mathrm{dex}$. Additionally, objects with and without detected rotation follow the same $M_{\rm baryon} - M_{\rm dyn}$ relation, which may support the assumption that the galaxies are all intrinsically rotating disks. We will investigate this in more detail in the next section.

The offset between the masses implies a dark matter fraction within R_E of 8%. This fraction is lower than the $\sim 30-50\%$ dark matter fractions within $2.2\ r_s$ for disk galaxies at $z \sim 0$ (which increase with decreasing stellar mass; Pizagno et al. 2005, Dutton et al. 2011a), and the $\sim 20-30\%$ within $r < 10\,\mathrm{kpc}$ at $z \sim 2$ (Förster Schreiber et al. 2009). This is expected, as these studies consider larger radii, and the dark matter fraction increases with increasing radius. Additionally, our measurement is dependent on several systematic uncertainties that we discuss in Section 4.5.2.

3.4.2 Rotational versus pressure support for unresolved galaxies

In the previous section we simply assumed that all kinematically resolved and unresolved objects have a similar median $(V/\sigma_{V,0})_{R_E}$. However, from Figure 3.6 we know that on average the unresolved objects are smaller, and thus they may be structurally different. In this section we use the average properties of the sample without resolved rotation to independently estimate the average $(V/\sigma_{V,0})_{R_E}$ for these objects.

The effects of varying the $(V/\sigma_{V,0})_{R_E}$ for all objects without observed rotation are demonstrated in Figure 3.9. In the left panel, we show the assumption of $(V/\sigma_{V,0})_{R_E} \rightarrow \infty$, or no intrinsic velocity dispersion, for the objects without detected rotation. For comparison, we show the galaxies with detected rotation, using the the dynamical masses calculated from the rotation velocities and velocity dispersions measured from the 2D fitting procedure (see Section 3.3.1). There is a positive correlation between the mass offset $\Delta\log_{10} M$ and b/a with Spearman correlation coefficient $\rho = 0.18$ at 2.2σ. We quantify this trend by fitting a line to median binned $\Delta\log_{10} M$ and b/a in bins of b/a. This trend of increasing $M_{\rm dyn}$ relative to $M_{\rm baryon}$ as b/a increases indicates that we have over corrected for inclination, and that our assumption of $(V/\sigma_{V,0})_{R_E} \rightarrow \infty$ is too extreme.

If we instead assume lower values of $(V/\sigma_{V,0})_{R_E}$, the inclination correction will be reduced at higher b/a, resulting in a reduced mass offset. Hence, we can constrain $(V/\sigma_{V,0})_{R_E}$ for the galaxies without detected rotation by examining the offset $\Delta\log_{10} M = \log_{10}(M_{\rm dyn}/M_\odot) - \log_{10}(M_{\rm baryon}/M_\odot)$ versus the axis ratio, b/a over a range of assumed $(V/\sigma_{V,0})_{R_E}$ values. For each assumed $(V/\sigma_{V,0})_{R_E}$, we calculate the dynamical masses for the galaxies without detected rotation. We then measure the χ^2 between the data and the value if there were no trend with b/a, or a constant $\Delta\log_{10} M$ equal to the median of the $\Delta\log_{10} M$ values. We determine the best-fit $(V/\sigma_{V,0})_{R_E}$ by minimizing the χ^2 statistic.

We find a best-fit $(V/\sigma_{V,0})_{R_E} = 2.1^{+0.2}_{-0.3}$ for the objects without detected rotation. We show the effects of assuming this $(V/\sigma_{V,0})_{R_E}$ value in the right panel of Figure 3.9. When we adopt $(V/\sigma_{V,0})_{R_E} = 2.1$, we notice very little offset in $\Delta\log_{10} M$ as a function of b/a, and the total scatter in $M_{\rm dyn}$-$M_{\rm baryon}$ is also slightly lower. We note that this measurement reflects an estimate of the typical $(V/\sigma_{V,0})_{R_E}$ of this sample; the scatter in the $M_{\rm dyn}$-$M_{\rm baryon}$ relation also includes variations introduced by a range of intrinsic $(V/\sigma_{V,0})_{R_E}$ values for the sample without observed rotation. The typical $(V/\sigma_{V,0})_{R_E}$ of the galaxies with and without observed rotation are identical, suggesting that on average all galaxies have similar support from random motions.

3.4.3 Trends between V/σ and other galaxy properties

The ratio V/σ is a measure of the amount rotational support versus support from random motions, and thus provides information about the structure of a galaxy. Higher V/σ are indicative of thin disks, while lower V/σ values may indicate thicker disks or high gas turbulence. To understand the physical processes setting the internal structure of star-forming galaxies at $z \sim 2$, we investigate the relation between V/σ and other galaxy properties.

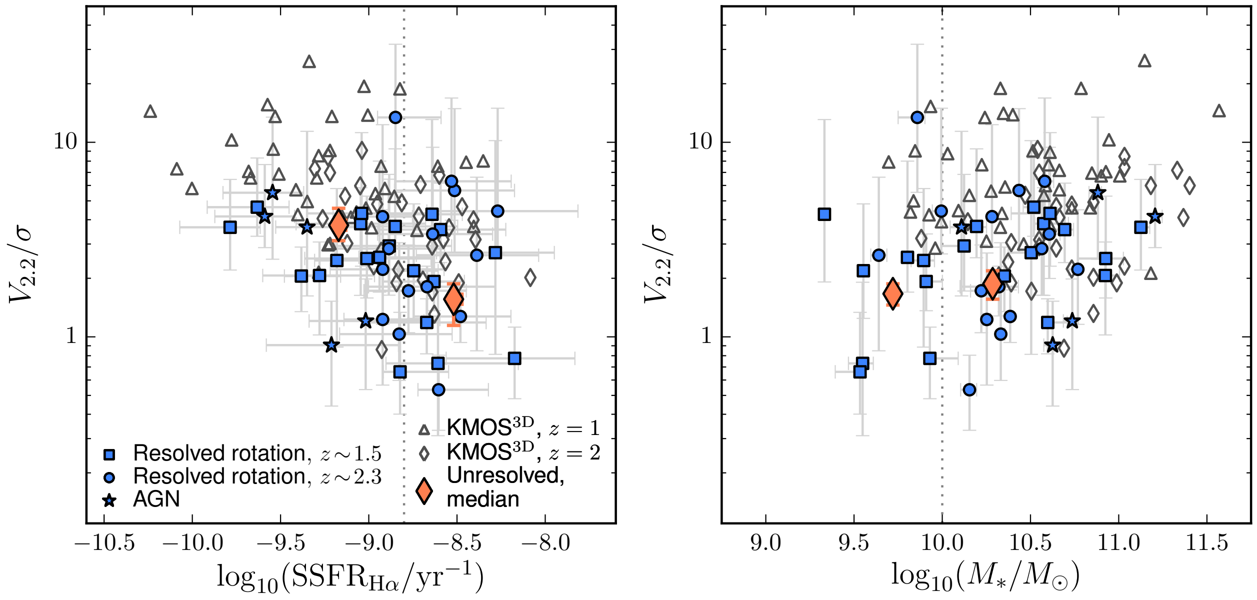

Figure 3.10: The ratio of support from rotation and random motions $(V/\sigma_{V,0})_{2.2}$ vs. Hα SSFR (left panel) and stellar mass (right panel) for our sample of galaxies with detected rotation. Galaxies at $z \sim 1.5$ and $z \sim 2.3$ are shown with blue squares and circles, respectively. We also show the AGN with detected rotation as blue stars. For the galaxies without observed rotation, we show the median $(V/\sigma_{V,0})_{2.2}$ in bins of Hα SSFR and stellar mass (orange diamonds). The bin boundaries are shown by the vertical grey dotted lines. For comparison, we also show the KMOS^{3D} values (Wisnioski et al. 2015) at $z = 1$ and $z = 2$ as the grey open triangles and diamonds, respectively. When considering both our data and the KMOS^{3D} data, there is a trend of decreasing V/σ with increasing SSFR, consistent with the trend found by Wisnioski et al. (2015). This trend may reflect disk settling, with the velocity dispersions decreasing as the gas fractions decrease.

We show the measured $(V/\sigma_{V,0})_{2.2} = V(2.2r_s)/\sigma_{V,0}$ values for our sample of galaxies as a function of Hα specific star formation rate (SSFR) and stellar mass in Figure 3.10. For the galaxies without observed rotation, we show the median $(V/\sigma_{V,0})_{2.2}$ values in bins of Hα SSFR and stellar mass, calculated using the method described in Section 3.4.2 and assuming $r_t = 0.4r_s$. For comparison, we also show the KMOS$^{\mathrm{3D}}$ results of Wisnioski et al. (2015) at $z = 1$ and $z = 2$ as the grey open triangles and diamonds, respectively. We note that Wisnioski et al. measure the rotation velocity from the difference between the observed minimum and maximum velocities along the major kinematic axis. However, we do not directly constrain the flat portions of the rotation curves, so instead we consider $V_{2.2} = V(r = 2.2r_s)$ – the radius at which an exponential rotation curve peaks – to attempt to provide a reasonable comparison with existing measurements. We also note that we assume a constant $\sigma_{V,0}$, while Wisnioski et al. measure σ_0 in the outer portions of the galaxies.

We see a trend of decreasing $(V/\sigma_{V,0})_{2.2}$ with increasing Hα SSFR, especially when considering the binned measurement for galaxies without observed rotation and when adding the results by Wisnioski et al. (2015). As suggested by Wisnioski et al. (2015), this trend may reflect disk settling, where galaxies with lower gas fractions (and lower SSFRs) have lower velocity dispersions. For the galaxies without observed rotation, this trend may also reflect a higher fraction of dispersion dominated galaxies at high SSFRs. Our measured $(V/\sigma_{V,0})_{2.2}$ values do not show a trend with stellar mass, but when considering our data together with the results of Wisnioski et al. (2015), we may see a weak trend of increasing V/σ with increasing stellar mass.

When measuring the kinematics, we assume that the velocity dispersion is constant. If the true velocity dispersion profile rises towards the center of a galaxy (as discussed in Section 4.5.2), our measured $\sigma_{V,0}$ may be systematically higher than what would be measured in the outer portions of our galaxies. This would systematically shift our measured $(V/\sigma_{V,0})_{2.2}$ to lower values than those found by Wisnioski et al. (2015). Thus the trends of V/σ with Hα SSFR and stellar mass found from the combined samples may be partially due to a systematic difference between the adopted V/σ values.

3.5 Discussion

In this section we analyze how different assumptions and caveats may influence our results. In Section 3.5.1, we consider the results if instead of baryonic masses we had compared just stellar and dynamical masses. Section 3.5.2 presents the implications of treating our galaxies as dispersion-dominated galaxies. In Section 3.5.3, we discuss constraints on the IMF based on our measured M_{baryon} and M_{dyn} values. In Section 3.5.4, we use our data to investigate the modified $S_{0.5}$ Tully Fisher relation (e.g., Kassin et al. 2007). We compare the $M_{\mathrm{baryon}} - M_{\mathrm{dyn}}$ relation of the selected AGN to the relation measured for our star-forming galaxy sample in Section 3.5.5. Section 3.5.6 examines differences between the stellar continuum and Hα intensity profiles. Finally, we discuss caveats to assumptions we have made in Section 4.5.2.

3.5.1 Importance of including gas in comparisons to dynamical masses

Previous studies have compared stellar masses to dynamical masses, especially using the stellar kinematics of quiescent galaxies (e.g., Newman et al. 2010, Taylor et al. 2010, Bezanson et al. 2013, van de Sande et al. 2013, Belli et al. 2014). For quiescent galaxies this may be a fair comparison, but for high redshift star-forming galaxies the gas mass is found to be a non-negligible fraction of the total baryonic mass (e.g., Tacconi et al. 2013).

To assess this finding, we consider the difference between the dynamical masses and the stellar masses alone versus Hα SSFR in the left panel of Figure 3.11. There is an offset between the masses, with the dynamical masses generally exceeding the stellar masses. When we split the sample into bins of Hα SSFR ($\log_{10}(\mathrm{SSFR}_{\mathrm{H}\alpha}) < -9.25$, $-9.25 \leq \log_{10}(\mathrm{SSFR}_{\mathrm{H}\alpha}) < -8.75$, $\log_{10}(\mathrm{SSFR}_{\mathrm{H}\alpha}) \geq -8.75$), we find that the higher SSFR bins have larger offsets between the dynamical and stellar masses than the lower SSFR bins. This result is not surprising, as the median inferred ratios of $f_{\mathrm{gas}} = M_{\mathrm{gas}}/(M_* + M_{\mathrm{gas}})$ are $f_{\mathrm{gas}} = 0.22$, $f_{\mathrm{gas}} = 0.44$, and $f_{\mathrm{gas}} = 0.58$ for the lowest to highest SSFR bins, respectively.

In contrast, the baryonic masses (right panel of Figure 3.11) show a much weaker SSFR-dependent offset with respect to the dynamical masses. The $M_{\mathrm{dyn}}/M_{\mathrm{baryon}}$ – SSFR relation also show a smaller observed scatter ($\sigma_{\mathrm{RMS}} = 0.34\,\mathrm{dex}$) than the M_{dyn}/M_* – SSFR relation ($\sigma_{\mathrm{RMS}} = 0.37\,\mathrm{dex}$). The agreement between the baryonic and dynamical masses, as well as the larger M_{dyn}/M_* offset for higher SSFR galaxies, suggests that our Hα SFR-based gas masses are reasonable estimates of the true values.

Thus, at least for star-forming galaxies, it is important to include the gas masses in the total baryonic mass when comparing it against the dynamical masses.

3.5.2 What if we assume that all galaxies without detected rotation are early-type galaxies?

As our sample consists of star-forming galaxies, we have assumed that there is some amount of rotational support for all galaxies, even for those that are not kinematically resolved. However, it might be the case that some, if not all, of these objects without observed rotation are early-type galaxies. To assess this possibility, we derive dynamical masses assuming instead that all the kinematically unresolved galaxies are dispersion-dominated ellipticals or lenticulars (S0s).

We calculate the dynamical masses as

$$M_{\mathrm{dyn}} = \beta(n)\frac{\sigma_{e,\mathrm{corr}}^2 R_{E,\mathrm{circ}}}{G}. \tag{3.5}$$

Here we use the Sérsic index dependent virial coefficient, $\beta(n)$, given in Cappellari et al. (2006), where $\beta(n)$ is a quadratic function of n (e.g., $\beta(n=1) \sim 8$ and $\beta(n=4) \sim 6$). The observed integrated velocity dispersions (σ_V) are corrected (to $\sigma_{e,\mathrm{corr}}$) using an aperture correction similar to that presented in van de Sande et al. (2013), modified to include the axis

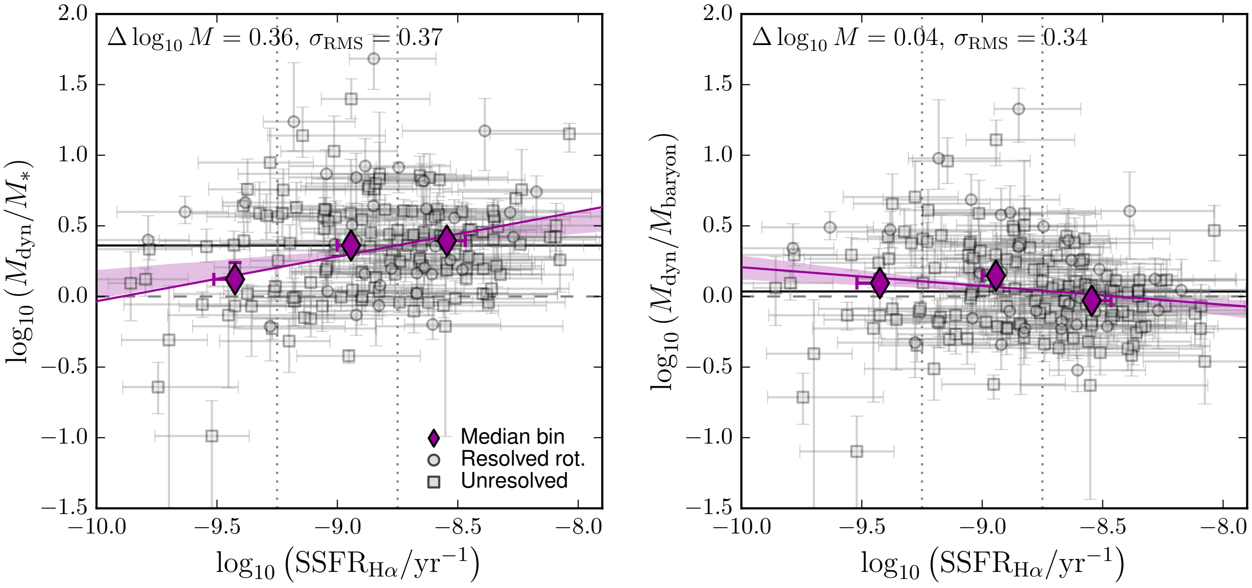

Figure 3.11: Difference between the dynamical and the stellar (left) and baryonic masses (right), versus the Hα SSFR. The objects with observed rotation are shown as circles, and the objects without observed rotation as squares. The median $\Delta(\log_{10} M)$ for the entire sample is shown with the black line. The data are binned in $\mathrm{SSFR}_{\mathrm{H}\alpha}$, with the median values shown as the purple diamonds, and a linear fit to the median points is shown with the purple line. In the left panel, we see a larger offset between the dynamical and stellar masses for galaxies with higher SSFR than those with lower SSFR. This offset is reduced when instead we compare the dynamical and baryonic masses. Additionally, the scatter between the mass values is larger when comparing the dynamical and the stellar ($\sigma_{\rm RMS} = 0.37\,\mathrm{dex}$) rather than the baryonic ($\sigma_{\rm RMS} = 0.34\,\mathrm{dex}$) masses. This figure illustrates the importance of including gas masses in the mass comparison.

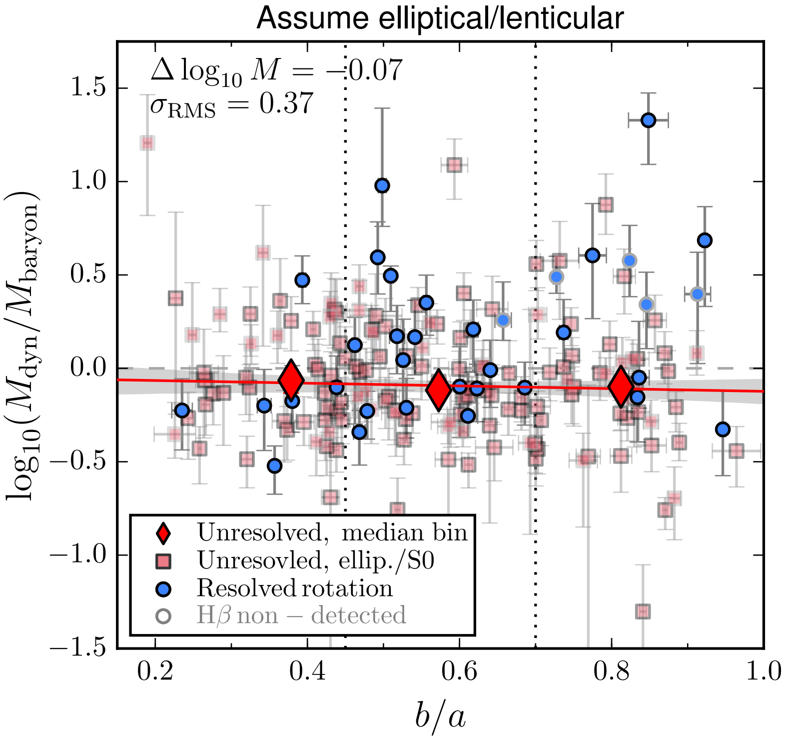

Figure 3.12: The difference between dynamical and baryonic masses vs. axis ratio b/a assuming that the galaxies without observed rotation are ellipticals or lenticulars (S0s). The observed velocity dispersions for the galaxies without apparent rotation are corrected using a modified aperture correction based on the method by van de Sande et al. (2013). The dynamical masses are then calculated using virial coefficient $\beta(n)$ and the circularized effective radii $R_{E,\mathrm{circ}}$. The plot point and line definitions are the same as in Figure 3.9. The Sérsic dependent virial coefficient combined with the circularized radius results in no trend with axis ratio, similar to the effect of applying inclination corrections when assuming the galaxies have partial rotational support.

ratio and position angle offset relative to the slit. When calculating the dynamical masses, we use the circularized effective radii, $R_{E,\mathrm{circ}} = R_E\sqrt{b/a}$, with R_E the GALFIT effective radius (which is equal to the semi-major axis) and b/a the axis ratio. It is necessary to use $R_{E,\mathrm{circ}}$ in this case, as $\beta(n)$ is derived using circularized radii. The resulting mass difference $\Delta\log_{10} M$ as a function of axis ratio, b/a, is shown in Figure 3.12.

Under these assumptions, the dynamical masses are also in reasonable agreement with the baryonic masses ($\Delta\log_{10} M = -0.07\,\mathrm{dex}$, $\sigma_{\mathrm{RMS}} = 0.37\,\mathrm{dex}$), though the mass offset is somewhat lower than measured for the galaxies with detected rotation. Remarkably, there is no trend of $\Delta\log_{10} M$ with b/a, which is due to the circularization of the effective radii. For objects with smaller axis ratios b/a, the circularized radii will be smaller, and thus the dynamical masses will be lower than if they were calculated using non-circularized radii. Thus, the Sérsic dependent virial coefficient, combined with the circularized radius has a similar effect as the inclination correction applied when assuming that the galaxies are primarily supported by rotation.

The agreement between the dynamical masses for the two separate methods may explain why both star-forming and quiescent galaxies, when treated as early-type galaxies, share "one mass fundamental plane," as found by Bezanson et al. (2015). In this work both star-forming and quiescent galaxies fall on the same surface in the 3D parameter space defined by effective radius R_E, velocity dispersion σ_V, and stellar mass surface density Σ_*. We note that when assuming all unresolved galaxies are early-type galaxies, the median offset $\Delta\log_{10} M$ is negative, with the typical galaxy lying in the unphysical regime where $M_{\mathrm{dyn}} < M_{\mathrm{baryon}}$. This result could suggest that more accurate dynamical masses are obtained when assuming the galaxies are rotationally supported. However, both the baryonic and dynamical masses are subject to systematic uncertainties, and thus we cannot definitively state whether the unresolved galaxies are rotationally supported or not.

3.5.3 Stellar initial mass function constraints

In this section we consider the implications of the measured M_{baryon} and M_{dyn} values of our galaxy sample for the stellar IMF. In estimating the baryonic masses, we have assumed a Chabrier (2003) IMF. An alternative choice is a Salpeter (1955) IMF, which would result in higher stellar masses, by a factor of 1.8 (e.g., Erb et al. 2006c). The relations between $L(\mathrm{H}\alpha)$ and SFR, and Σ_{SFR} and Σ_{gas} given by Kennicutt (1998) both contain an IMF dependence, but the relation between the intrinsic $L(\mathrm{H}\alpha)$ and Σ_{gas} does not depend on the IMF, so the gas masses do not change whether using a Salpeter or a Chabrier IMF.

We show the implications of assuming a Salpeter rather than a Chabrier IMF in Figure 3.13. The median $\log_{10}(M_{\mathrm{dyn}}/M_{\mathrm{baryon}})$ for the whole sample is shown as the solid black line. If we had instead adopted a Salpeter IMF (right panel), the zero-point of $\log_{10}(M_{\mathrm{dyn}}/M_{\mathrm{baryon}})$ is lower.

Physically, we expect that the dynamical mass, which traces all mass in a galaxy, must at least be as large as the observed baryonic mass, depending on the dark matter fraction within an effective radius. The median $\log_{10}(M_{\mathrm{dyn}}/M_{\mathrm{baryon}})$ we measure assuming a Chabrier

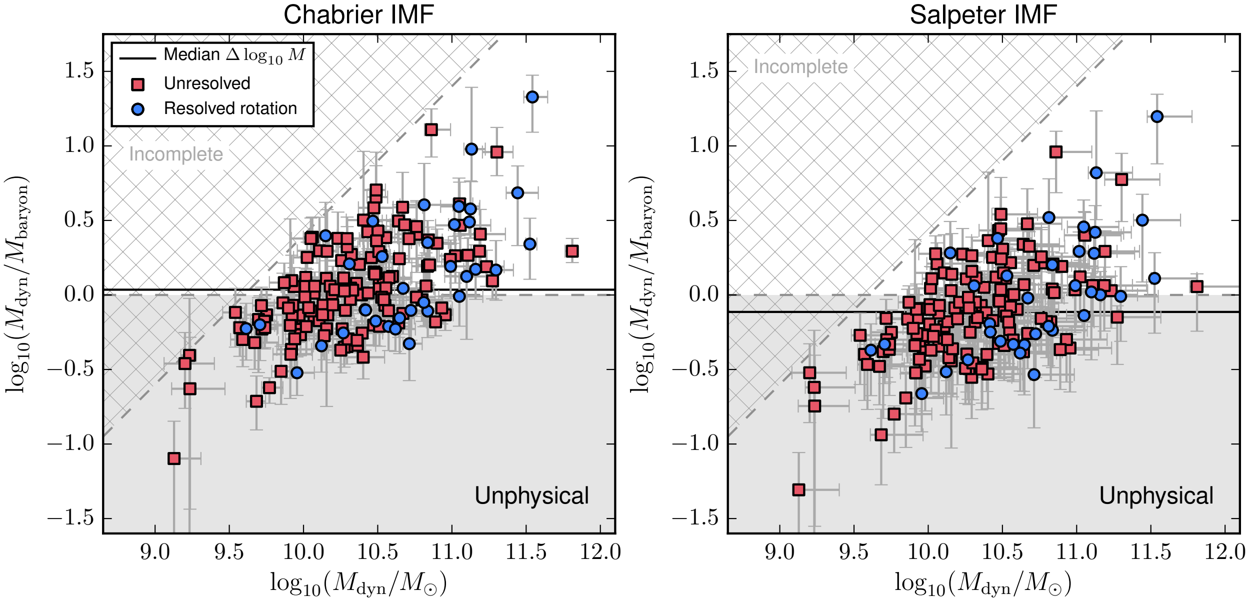

Figure 3.13: $\log_{10}(M_{\rm dyn}/M_{\rm baryon})$ vs. $\log_{10} M_{\rm dyn}$ for a Chabrier (left panel) and a Salpeter IMF (right panel). The galaxies with and without detected rotation are shown with the blue and red points, respectively. In each panel, the zero-point $\log_{10}(M_{\rm dyn}/M_{\rm baryon}) = 0$ is presented by the dotted grey line, and the median $\Delta \log_{10} M = \log_{10}(M_{\rm dyn}/M_{\rm baryon})$ of the whole galaxy sample by the solid black line. The unphysical region where $M_{\rm dyn} < M_{\rm baryon}$ is shaded grey. The mass incomplete region ($M_{\rm baryon} \lesssim 10^{9.6} M_\odot$) is shown with the grey hatched region. A Chabrier IMF is consistent with our measurements, while a Salpeter IMF is not; this IMF shifts the median to the region where $M_{\rm dyn} < M_{\rm baryon}$, which is unphysical.

IMF is consistent with this expectation, with 46% of the galaxies fall within the unphysical regime. However, for a Salpeter IMF 63% of the galaxies fall within the unphysical regime where $M_{\mathrm{dyn}} < M_{\mathrm{baryon}}$. Thus a Salpeter IMF is inconsistent with our measured values of M_{baryon} and M_{dyn}. This inconsistency with a Salpeter IMF is in agreement with the findings of other studies of star-forming, disk galaxies (Bell & de Jong 2001, Tacconi et al. 2008, Dutton et al. 2011a, Brewer et al. 2012). Nonetheless, our result is subject to potential systematic uncertainties that might decrease the measured dynamical masses, such that our measurements would be inconsistent with both a Salpeter (1955) and a Chabrier (2003) IMF. We discuss these systematic uncertainties in detail in Sections 3.5.6 and 4.5.2.

Finally, there is a suggestive trend between $M_{\mathrm{dyn}}/M_{\mathrm{baryon}}$ and M_{dyn}, such that more massive galaxies may have a steeper IMF (or a larger dark matter fraction). However, this trend primarily reflects the cutoff in observed baryonic masses (upper envelope). Thus, at fixed dynamical mass, we miss galaxies with the lower baryonic masses. These missed galaxies could increase the median baryonic-dynamical mass offset, leaving room for more dark matter, or bringing the Salpeter IMF into agreement with our data.

3.5.4 Modified stellar mass Tully-Fisher relation

The Tully-Fisher relation (TFR, Tully & Fisher 1977) - which relates the luminosity of disk galaxies to their rotation velocity - captures information about the interplay between the build-up of disk galaxies and their dark matter halos. As the luminosity-based TFR is subject to luminosity evolution (due to aging populations) and a possible evolution in the gas mass fraction, more recent works have focused on measuring the stellar mass or baryonic mass TFRs, as mass allows for more straight-forward comparisons between redshifts (e.g., Dutton et al. 2011b, Gnerucci et al. 2011, Miller et al. 2012, Vergani et al. 2012).

Furthermore, Kassin et al. (2007) argue that the stellar and baryonic TFRs may evolve due to the increase of non-rotational support in higher redshift galaxies. To account for the increased non-rotational support, they argue for the adoption of the $S_{0.5}$ kinematic indicator, with $S_{0.5} = \sqrt{0.5V_{\mathrm{rot}}^2 + \sigma_V^2}$. This study shows a reduction of scatter in the $S_{0.5}$-M_* TFR relative to the standard M_*-TFR at $z \sim 0.2 - 1$. Furthermore, they find that there is barely any evolution in the $S_{0.5}$-M_* TFR out to $z \sim 1$.

We use our kinematic measurements to examine the $S_{0.5}$-M_* and $S_{0.5}$-M_{baryon} TFRs for our sample of star-forming galaxies at $z \sim 1.5 - 2.6$, shown in Figure 3.14. We perform a weighted linear fit of $S_{0.5}$ vs M_* (left panel, Figure 3.14) to our sample of star-forming galaxies by fixing the slope to the average value Kassin et al. (2007) find at $z \sim 0.1 - 1.2$ (i.e., slope $= 0.34$). We find a moderate correlation between $S_{0.5}$ and M_*, with scatter in $S_{0.5}$ of $\sigma_{\mathrm{RMS}} = 0.17\,\mathrm{dex}$ for our star-forming galaxies. The scatter is similar to the average scatter Kassin et al. (2007) find (0.16 dex). Our best-fit relation is offset to higher $S_{0.5}$ compared to the average relation found by Kassin et al. (2007) (black dashed line, left panel of Figure 3.14), which may be explained by lower average gas fractions of star-forming galaxies at lower redshifts. We find a similar intercept if we fit the $S_{0.5} - M_*$ relation using only the galaxies with detected rotation.

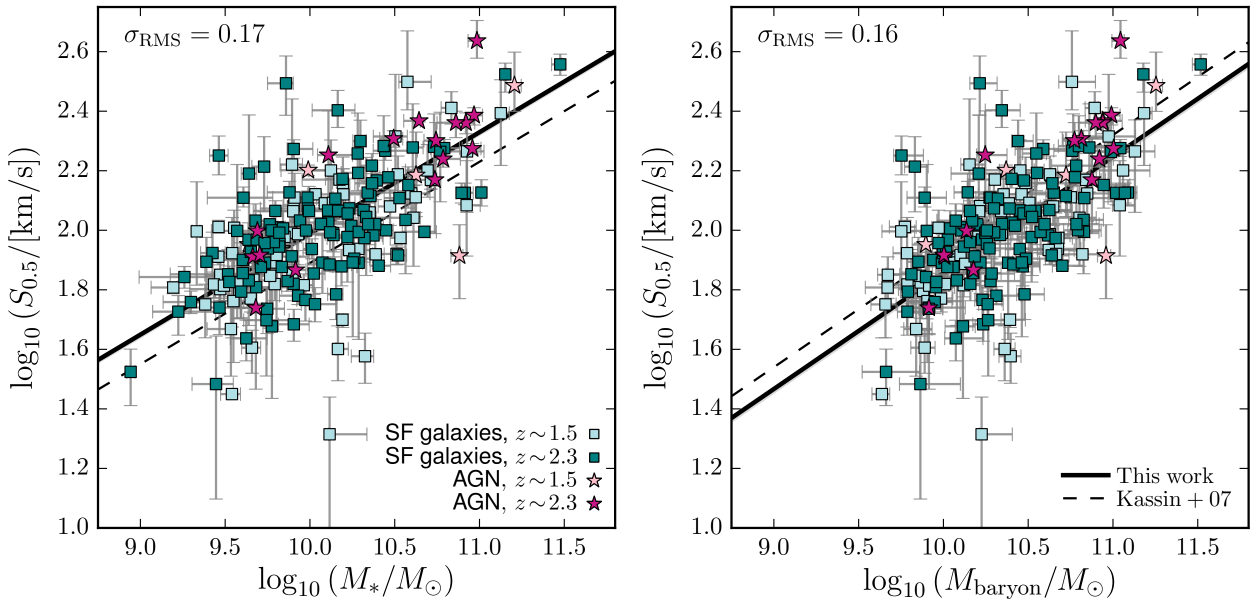

Figure 3.14: The modified $S_{0.5}$-M Tully-Fisher (TF) relation (Kassin et al. 2007) for our sample galaxies with and without detected rotation. The left and right panels show the stellar and baryonic $S_{0.5}$-M TF relations, respectively, with $S_{0.5} = \sqrt{0.5V_{2.2}^2 + \sigma_{V,0}^2}$ for our measurements. In each panel, the star-forming galaxies at $z \sim 1.5$ and ~ 2.3 are shown as light blue and teal squares, respectively, and the AGN at $z \sim 1.5$ and ~ 2.3 are shown as pink and purple stars, respectively. For the same slope of the $S_{0.5} - M_*$ relation, our sample has higher $S_{0.5}$ at fixed M_* than the sample of Kassin et al., which may reflect the trend of a decreasing average gas fraction. For the $S_{0.5} - M_{\rm baryon}$ relation we find that, for the same slope, our sample has lower $S_{0.5}$ at fixed $M_{\rm baryon}$ than the sample of Kassin et al. An increase in the average dark matter fraction over time could explain the higher $S_{0.5}$ values observed by Kassin et al.

We follow the same general method to fit $S_{0.5}$ vs $M_{\rm baryon}$ (right panel, Figure 3.14), adopting the slope of the $S_{0.5}$-$M_{\rm baryon}$ TFR at $z \sim 0.2$ measured by Kassin et al. (2007) (i.e., slope = 0.39), and find a correlation between $S_{0.5}$ and $M_{\rm baryon}$ with a scatter in $S_{0.5}$ of 0.16 dex. Our $S_{0.5}$ intercept is somewhat lower than found by Kassin et al. (2007) at $z \sim 0.2$ (dashed black line, right panel), suggesting an increase in $S_{0.5}$ at fixed $M_{\rm baryon}$ over time. We find the same result if we exclude the galaxies without detected rotation. The offset between $S_{0.5}$ intercepts may be explained by a higher dark matter fraction at later times. This trend may reflect the increasing radii of similar-mass star-forming galaxies with decreasing redshift (e.g., Williams et al. 2010, van der Wel et al. 2014a); as dark matter halo profiles are less concentrated than stellar mass profiles, a larger radius results in a higher dark matter fraction.

Nonetheless, systematic differences may affect the comparison of the $S_{0.5} - M$ TFRs. In particular, the rotation velocities are not measured uniformly, which could introduce systematic offsets. Kassin et al. (2007) use the maximum rotation velocity $V_{\rm max}$ (i.e., the velocity at the flat portion of an arctan rotation curve or at $2.2 r_s$ for an exponential disk). Our data do not sample the flat portion of the arctan rotation curve, so we instead adopt $V_{2.2}$ as our velocity measurement, as we have reasonable velocity constraints at this radius. Future work is necessary to quantify the differences between the literature measurements, in order to study the M-TFR evolution over time in a consistent manner.

3.5.5 Comparison of baryonic and dynamical masses for AGN

In this section we consider the kinematics of the AGN that fall within our galaxy sample. Interpreting the kinematics of AGN can be challenging, as the line profiles may have contributions from nuclear emission tracing non-virial motions. Therefore, we did not include the AGN in our analysis so far. Here we assess whether the kinematics may still provide a probe of the host-galaxy structure.

We calculate the stellar, gas, and baryonic masses following the procedure of Section 3.2.1. We measure the Hα kinematics from the resolved 2D or integrated 1D spectra, and derive dynamical masses following the procedures of Sections 3.3.1, 3.3.2, and 3.3.4. The resulting baryonic and dynamical masses for the AGN, along with those of the galaxy sample, are shown in Figure 3.15.

The AGN that meet our sample selection criteria generally follow the same relation of $M_{\rm dyn} - M_{\rm baryon}$ as the primary galaxy sample. For the AGN we find a median offset $\Delta \log_{10} M = 0.01\,\text{dex}$, which is slightly lower than the median offset for the star-forming galaxies ($\Delta \log_{10} M = 0.04\,\text{dex}$), and a scatter of $\sigma_{\rm RMS} = 0.35\,\text{dex}$. We note that the effective radii may be underestimated for some objects, due to the influence of a nuclear source.

The good agreement between the AGN and galaxies in the $M_{\rm dyn} - M_{\rm baryon}$ plane suggests that the rest-frame optical lines of most AGN in our sample are not dominated by line emission from the nuclear regions, and that we are probing the kinematics of the host galaxies. Our findings support the results of Gabor & Bournaud (2014), who show that in high-resolution hydrodynamic simulations of disk galaxies at $z \sim 2$, AGN have relatively little impact on the gas in galaxy disks.

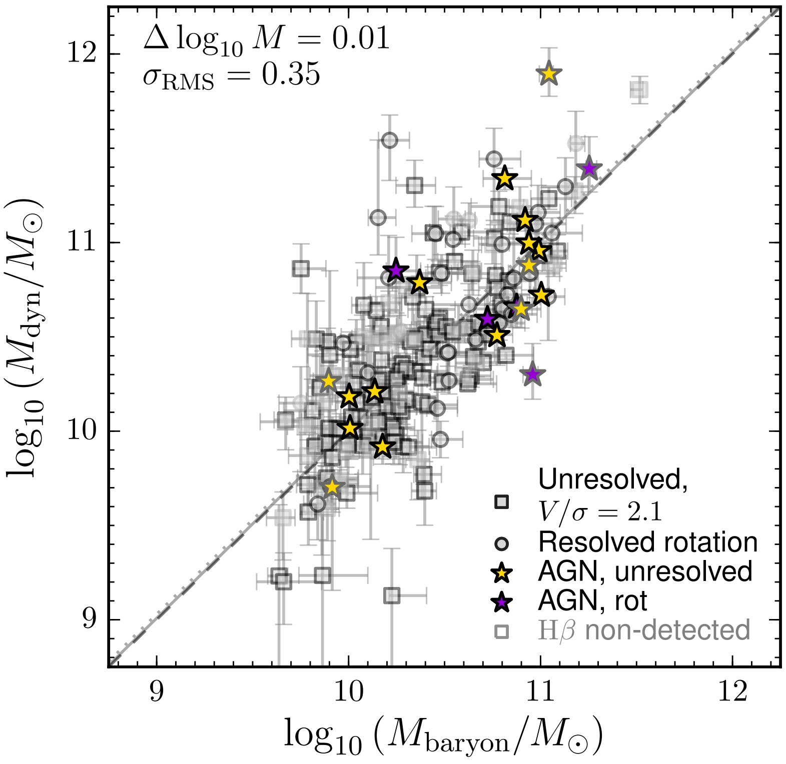

Figure 3.15: M_{dyn} vs. M_{baryon} for the AGN in comparison with the galaxy sample. Galaxies with and without detected rotation galaxies are represented by the grey circles and squares, respectively. The AGN with and without detected rotation are shown with the purple and yellow stars, respectively. The grey line shows the median offset of $\Delta(\log_{10} M) = 0.01$ dex for the AGN, and the dashed grey line shows $M_{\mathrm{dyn}} = M_{\mathrm{baryon}}$. For reference, the grey dotted line shows the median offset for the star-forming galaxies. The relation between baryonic and dynamical masses for the AGN is similar to the relation for primary galaxy sample, and thus the gas kinematics likely trace the dynamics of the host galaxies.

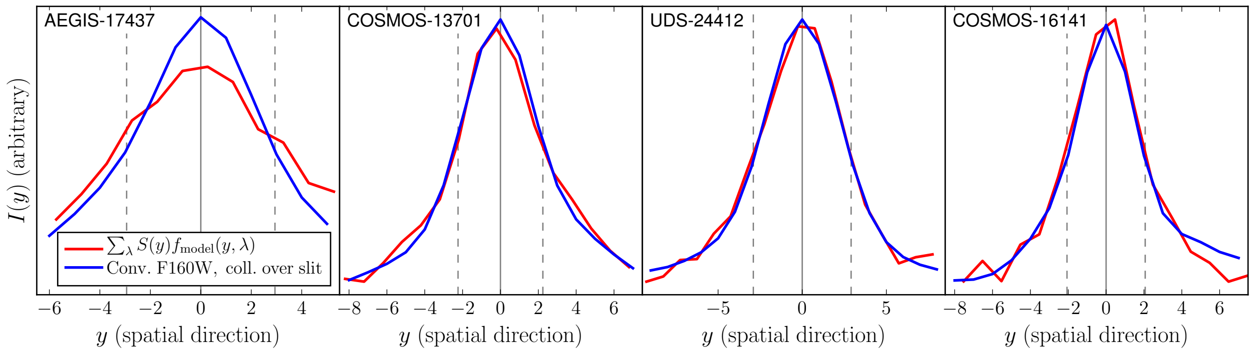

Figure 3.16: Intensity profiles for the stellar continuum and Hα for the four objects shown in Figure 3.2, with the field and 3D-HST v4 ID noted in the upper left corner of each panel. The normalized stellar light and Hα profiles are shown as the blue and red lines, respectively. The solid grey line shows the emission line center measured during the 1D spectra extraction. The dashed grey lines show the convolved, projected effective radius for each object. The profiles are generally in good agreement, with only the first object having a noticeably larger Hα profile width.

3.5.6 Mass-to-(Hα)-luminosity variations

When constructing kinematic models, we rely on structural parameters and radii measured from the stellar light distribution, but measure the kinematics from Hα emission. Ideally, we would measure the kinematics from stellar absorption features, but our galaxies are too faint for these measurements. Instead, we assume that the ionized gas and stellar mass have the same distribution and that the gas follows the gravitational potential of the galaxy.

When using kinematic models to measure rotation and interpret the velocity dispersion of unresolved objects, we weight the model velocity field by a luminosity distribution. For the galaxies with detected rotation, this weighting determines the composite velocity profile within a spatial slice, as there is a mix of line-of-sight velocity components, as well as components that fall within the slit, parallel to the spatial direction. The weighting also predicts a light profile along the spatial direction, but our method of fitting the 2D spectra with the models removes this variation in the spatial direction through the scaling factor $S(y)$. For the kinematically unresolved galaxies, the luminosity weighting affects all directions.

To be fully consistent, we should weight the model velocities by the Hα light profile, so there are no mis-matches between the model and observed luminosity profiles. However, the Hα profiles are not well constrained by the MOSDEF data, and most galaxies in our sample lie at redshifts where Hα falls outside of the wavelength coverage of the WFC3 grism (Brammer et al. 2012). We therefore assume that the stellar light profiles are a reasonable approximation for the luminosity weighting. We assess this assumption by comparing the stellar light profiles with the Hα profiles for the galaxies with detected rotation.

To measure the stellar light profile, we convolve the *HST*/F160W image to match the seeing resolution of the corresponding MOSFIRE spectrum. We then collapse all light falling within the slit along the slit direction. We approximate the Hα profile by collapsing the scaled emission line model, $S(y)f_{\rm model}(y, \lambda)$, over the wavelength direction. We show example F160W and Hα profiles in Figure 3.16 for the same galaxies shown in Figure 3.2. For three of the four examples, the stellar and Hα profiles are very similar. Only the first object, AEGIS-17437, has noticeable deviation between the Hα and stellar profiles, where the Hα profile is wider than the stellar light profile.

We quantify the profile differences for all galaxies with detected rotation by fitting the Hα and F160W profiles with Gaussians. We note that the profiles of a number of objects are not well-described by a Gaussian profile, but the FWHM measurements should provide a reasonable, albeit rough, comparison. We compare the widths of the seeing-matched stellar light and Hα profiles in Figure 3.17. Generally, the FWHMs are in reasonable agreement, and only a few objects have FWHMs that differ by more than 10% (objects lying outside the grey shaded region). Additionally, we show the relation $R_{E,\rm H\alpha} = 1.3 R_E$ found by Nelson et al. (2012) as the dotted grey line, converted to FWHMs and convolved with a median seeing FWHM of $\sim 0\farcs7$. All but a few of the galaxies lie below this line, suggesting that the Hα sizes for our sample are closer to the stellar light sizes than for the Nelson et al. sample. Thus, for most of our objects the stellar light profile is a reasonable substitute for the Hα profile, and hence the measured kinematics will not be biased.

However, for galaxies with more extended Hα, such as AEGIS-17437, we may overestimate the velocity dispersion and possibly the rotation velocity, when assuming the stellar light profile in the model construction. This velocity difference can be explained by the fact that the high velocities at large radii have been down-weighted when using the less extended stellar light instead of the Hα profile. The exact changes in the measured velocity and dispersion velocity from the 2D models depend on the misalignment between the major axis and the slit. If $\Delta\mathrm{PA} = 0$, there is symmetric mixing of velocities at different radii within a spatial slice, and the narrower stellar light profile therefore results in less broadening in the wavelength direction. Additionally, by weighting with the narrower stellar light profile, the composite of the velocity components along the line-of-sight direction also results in less broadening in the wavelength direction. Thus, when $\Delta\mathrm{PA} = 0$ and we weight the velocity fields with the stellar light profile, the measured $V(R_E)$ is the same, and $\sigma_{V,0}$ is larger than we would measure when using the Hα light profile. If a galaxy is misaligned with the slit, the measured $V(R_E)$ using the stellar light profile may also be larger than if we weighted with the Hα profile.

The 1D model for AEGIS-17437 would suffer a greater discrepancy if we would have weighted the velocities of the model with the Hα instead of the stellar light profile. The increased weight at large radii would increase the weighted integrated velocity dispersion of the model within the aperture. Thus the ratio $\sigma_{V,\,\rm model}/V_{\rm RMS}(R_E)_{\rm model}$ is higher for the Hα profile than for the stellar light profile, when using the same underlying rotation curve and assumed $(V/\sigma_{V,0})_{R_E}$. Therefore, the corrected RMS velocity values measured using the stellar light profile overestimate the true values.

An additional question is whether the stellar light sizes correctly probe the characteristic size of the underlying matter density profile. In particular, our current calculations have assumed that half of the total mass is enclosed within the half-light radius. However, the

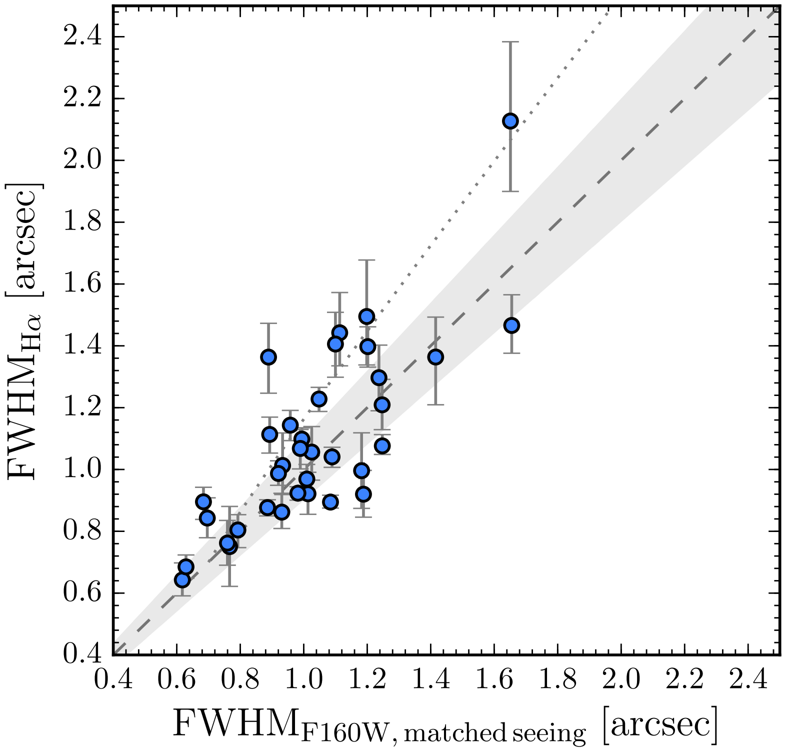

Figure 3.17: $\mathrm{FWHM}_{\mathrm{H}\alpha}$ vs. $\mathrm{FWHM}_{\mathrm{F160W}}$ for the galaxies with observed rotation. The Hα FWHM is measured from the scaled 2D emission line model, and the F160W FWHM is measured from the F160W image within the slit, convolved to match the MOSFIRE seeing conditions. The dashed grey line shows the line of equality. The grey shaded region shows the range of values when $\mathrm{FWHM}_{\mathrm{H}\alpha}$ is 10% smaller or larger than $\mathrm{FWHM}_{\mathrm{F160W}}$. The FWHMs are similar for most of the galaxies with detected rotation. Also, all but a few of the galaxies lie below the relation $R_{E,\mathrm{H}\alpha} = 1.3 R_E$ found by Nelson et al. (2012), with the converted FWHMs convolved with a median seeing FWHM of $\sim 0\farcs7$.

half-mass sizes are on average $\sim 25\%$ smaller than the half-light sizes (Szomoru et al. 2013). If we assume the same intrinsic rotation velocity curve, $V(R_E) > V(r_{1/2,\mathrm{mass}})$, and thus the measured $V(R_E)$ (for the resolved models) and $V_{\mathrm{RMS}}(R_E)$ (for the unresolved models) are larger than the velocities at $r_{1/2,\mathrm{mass}}$. If we assume a constant $\sigma_{V,0}$, this difference implies a lower V/σ. In combination with a smaller R_e, this results in a considerably lower dynamical mass. For example, if $r_{1/2,\mathrm{mass}}$ is 25% lower than R_E (as in Szomoru et al. 2013), then a galaxy with $(V/\sigma_{V,0})_{R_E} = 2.1$ at R_E and $r_t = 0.4r_s = 0.4R_E/1.676$ (following Miller et al. 2011, see Appendix C) has $M_{\mathrm{dyn}}(r_{1/2,\mathrm{mass}})$ which is 31% lower than $M_{\mathrm{dyn}}(R_E)$. When applying the correction found by Szomoru et al. (2013) the dynamical masses decline by 0.16 dex (to $\Delta \log_{10} M = -0.12\,\mathrm{dex}$) and are inconsistent with both a Chabrier (2003) and a Salpeter (1955) IMF.

We illustrate a lower limit of this systematic variation in the left panel of Figure 3.18, by approximating the changes of $\Delta \log_{10} M$ caused by varying $r_{1/2,\mathrm{mass}}/R_E$ and using $M_{\mathrm{dyn}} = M_{\mathrm{dyn}}(r_{1/2,\mathrm{mass}})$ (i.e., including variations to the RMS velocity and virial coefficient with the assumption of an arctan curve with $(V/\sigma_{V,0})_{R_E} = 2.1$ and $r_t = 0.4r_s = 0.4R_E/1.676$). Even $\sim 10\%$ changes in $r_{1/2,\mathrm{mass}}/R_E$ result in a $\sim 10\%$ change to the inferred dark matter fraction. However, if we instead assume a decreasing velocity dispersion with increasing radius, as we discuss in the next section, the $V_{\mathrm{RMS}}(r_{1/2,\mathrm{mass}})$ values would be larger. This moves in the opposite direction as the above trend, and may change the masses so they remain consistent with a Chabrier (2003) IMF.

3.5.7 Other caveats

In this section we consider caveats to assumptions made in the preceding analysis. Specifically, we focus on possible variations due to assumptions about the accuracy of the structural parameters, misalignment of the photometric and kinematic major axes, the intrinsic thickness of galaxy disks, the accuracy of our derived gas masses, the shape of the rotation curve, and the velocity dispersion profile being constant.

First, we have not fully accounted for the accuracy of the GALFIT-derived structural parameters. We depend on the structural parameters to model the kinematics of the detected rotation curves, to correct the kinematics from integrated 1D spectra, and to calculate the dynamical masses. We include estimated errors on the effective radii when calculating the dynamical masses, but do not include any errors when fitting the kinematic models. Thus, uncertainties in the structural parameters introduce scatter in our derived dynamical masses.

Second, for objects where the photometric and kinematic major axes are misaligned, the inferred velocities and dispersion velocities will be incorrect. If the true $\Delta\mathrm{PA}$ is closer to aligned, the corrected RMS velocities will be over-estimated, while if it is more misaligned, the velocities will be under-estimated (as seen in the first panel in Figure C.1). We expect similar over- and under-estimates in the measured velocities and dispersions for the galaxies with detected rotation. Additional misalignment uncertainties are introduced by slit alignment issues, which introduce the same trends as stated above.

Third, we assume an intrinsic disk thickness of $(b/a)_0 = 0.19$ to estimate inclination

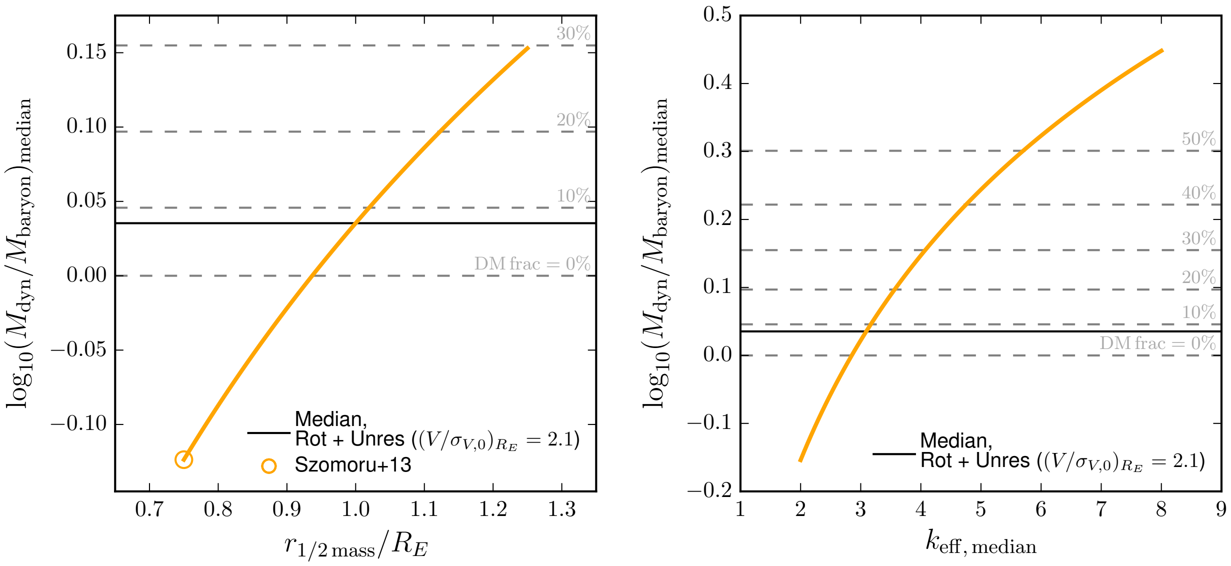

Figure 3.18: Systematic changes in the median $\log_{10}(M_{\rm dyn}/M_{\rm baryon}) = \Delta\log_{10} M$ with varying half-mass to half-light radius ratio ($r_{1/2\,{\rm mass}}/R_{E,*}$, left panel) and effective virial coefficient ($k_{\rm eff,\,median}$, right panel). In both panels the black horizontal line shows the median $\Delta\log_{10} M$ for the whole sample when adopting the default assumptions. Lines of constant dark matter fraction (assuming $f_{\rm DM} = M_{\rm DM}/M_{\rm dyn} = (M_{\rm dyn} - M_{\rm baryon})/M_{\rm dyn}$) are shown with grey dashed lines. In the left panel, the systematic changes with half-mass to half-light radius ratio include variations of the RMS velocity and virial coefficient assuming an arctan rotation curve with $(V/\sigma_{V,0})_{R_E} = 2.1$ and $r_t = 0.4R_E/1.676$. Szomoru et al. (2013) find that $r_{1/2\,{\rm mass}}$ is on average 25% lower than R_E (orange circle), which corresponds to the median offset $\Delta\log_{10} M$ shifted to the unphysical region, or $\Delta\log_{10} M \sim -0.12$ dex. In the right panel, the systematic changes with the effective virial coefficient are approximated by applying the same $k_{\rm eff,\,median}$ to all galaxies and calculating the resulting median offset $\Delta\log_{10} M$. Assuming $k_{\rm eff,\,median} \sim k_{\rm rot} = 2.66$ for all galaxies (without changing the assumed $(V/\sigma_{V,0})_{R_E}$) results in an unphysical $\Delta\log_{10} M < 0$, while assuming $k_{\rm eff,\,median} \sim k_{\rm disp} = 5$ results in a much higher inferred dark matter fraction of $f_{\rm DM} \sim 45\%$.

angles. If a galaxy is intrinsically thicker than the assumed value, the inferred inclination angle underestimates the true value. In this case, the inferred intrinsic rotation velocity and $(V/\sigma_{V,0})_{R_E}$ would be overestimated. If a galaxy is thinner, the inclination angle will be overestimated, producing an underestimate of both the rotation and $(V/\sigma_{V,0})_{R_E}$. Thus, variations in disk thickness within our sample will add scatter and a possible systematic offset in our dynamical masses.

Fourth, we assume that the galaxies in our sample follow the SFR-gas mass relation of Kennicutt (1998) for star-forming galaxies in the local universe. Based on a local sample of normal and starburst galaxies, Kennicutt (1998) measure $N = 1.4$ for $\Sigma_{\rm SFR} \propto \Sigma_{\rm gas}^N$, where $\Sigma_{\rm gas}$ includes both atomic and molecular gas. Analysis of galaxies at $z \sim 1-3$ find slopes that vary between $N = 1.28$ (Genzel et al. 2010) and $N = 1.7$ (Bouché et al. 2007). These values bracket the local slope, so our gas masses may be reasonable. However, if the true slope is lower than the local relation, our gas masses underestimate the true value, while a higher slope implies our gas masses overestimate the true value. An alternate method would be to adopt the gas mass scaling relations presented in Genzel et al. (2015), which relate the gas mass to the stellar mass, the offset from the star-forming main sequence, and the redshift. If we adopt this scaling relation, we see an offset $\Delta \log_{10} M = -0.12\,$dex and a scatter of $\sigma_{\rm RMS} = 0.368\,$dex between the dynamical and baryonic masses, with the median mass difference lying in the unphysical region where $M_{\rm baryon} > M_{\rm dyn}$. However, the gas mass scaling relations of Genzel et al. (2015) were calibrated for UV+IR SFRs, while we use Hα SFRs in this work. Mismatches between these SFR indicators could be causing the large ($\sim 0.2\,$dex) difference between the inferred baryonic masses when using the scaling relation method and the inverted Kennicutt-Schmidt relation. As Kennicutt (1998) calibrated the $\Sigma_{\rm SFR} - \Sigma_{\rm gas}$ relation using Hα SFRs, we opt to estimate the gas masses following this prescription.

Fifth, we have assumed that the rotation velocity profiles of our disk galaxies are well described by arctan models, as shown by Courteau (1997), Weiner et al. (2006), and Miller et al. (2011). Some distant star-forming galaxies exhibit rotation following a Freeman exponential disk model (Freeman 1970), as found by Wisnioski et al. (2015), while van Dokkum et al. (2015) find indications of Keplerian rotation in compact star-forming galaxies. However, preliminary analysis suggests that using an exponential disk rotation curve with our modeling produces poor fits to some of our galaxies. More detailed modeling is required to determine in detail whether an alternative rotation profile provides better agreement with our data and to assess the uncertainties introduced by this assumption.

Sixth, we have assumed that the intrinsic velocity dispersion is constant over all radii. However, the true velocity distribution may decrease with increasing radius, as seen in Genzel et al. (2014) and Wisnioski et al. (2015). For the unresolved objects, a decreasing velocity dispersion distribution would produce higher model RMS velocities for a given $(V/\sigma_{V,0})_{R_E}$ measured at R_E,[3] as matching the same $\sigma_V(R_E) \approx \sigma_{V,0}$ implies a higher central

---

[3] Other studies (e.g., Newman et al. 2013, Wisnioski et al. 2015) measure $\sigma_{V,0}$ in the outer portions of a galaxy, so taking $\sigma_V(R_E) \approx \sigma_{V,0}$ in the case of a non-constant velocity profile should be a reasonable comparison, though may be higher than the true value depending on the exact form of the additional velocity

velocity dispersion, $\sigma_V(r=0)$. A velocity dispersion profile which rises towards the center would increase the integrated model velocity dispersions but not the model RMS velocity at R_E, leading to lower corrected RMS velocities and lower dynamical masses. The trend of decreasing integrated RMS velocity with increasing inclination will also be less strong for a fixed $(V/\sigma_{V,0})_{R_E}$ than with a constant $\sigma_{V,0}$. The median $(V/\sigma_{V,0})_{R_E}$ required to remove the $\Delta\log_{10} M$ trend for the kinematically unresolved galaxies will therefore be higher, increasing the implied amount of rotational support relative to the random motions, which would indicate more settled or thinner disks. Preliminary calculations assuming an additional dispersion term that rises towards the center of a galaxy confirms these general trends, but more careful analysis is necessary to determine the correct form of a rising velocity dispersion profile.

Seventh, in our derivation of the dynamical masses we have not included the systematic uncertainties arising from the choice of virial coefficients, k_{disp} and k_{rot}. The matter distributions assumed when deriving the virial coefficients may not match the underlying profiles of the star-forming galaxies in our sample, but more detailed analysis is required to quantify the uncertainties introduced by the adopted virial coefficients. We note that the systematic shifts from a different choice of virial coefficient can be non-negligible, and have implications especially for the IMF constraints. For instance, the combination of $k_{\mathrm{disp}} = \beta(n)$ (from Cappellari et al. (2006)), $n=1$, and $(V/\sigma_{V,0})_{R_E} = 2.1$ would have resulted in dynamical masses that are larger by ~ 0.07 dex and an inferred dark matter fraction of $f_{\mathrm{DM}} \sim 22\%$. We approximate the systematic changes due to changing only the combined $k_{\mathrm{eff,\,median}}$ in the right panel of Figure 3.18. In this plot, we see that if we assume $k_{\mathrm{eff,\,median}} \sim k_{\mathrm{rot}} = 2.66$ for all galaxies (without changing the conversion from the integrated velocity dispersions to the RMS velocities for the unresolved galaxies), then the median $\Delta\log_{10} M < 0$, which lies in the unphysical region where $M_{\mathrm{dyn}} < M_{\mathrm{baryon}}$. If we instead assume $k_{\mathrm{eff,\,median}} \sim k_{\mathrm{disp}} = 5$ (again with no other changes), we would instead infer a much higher dark matter fraction of $f_{\mathrm{DM}} \sim 45\%$ rather than the 8% measured from the default assumptions.

3.6 Summary

In this paper, we use spectra from the MOSDEF survey to study the masses and kinematic structures of a sample of 178 star-forming galaxies at $1.4 \leq z \leq 2.6$. For all galaxies, structural parameters from CANDELS *HST*/F160W imaging, stellar masses from multi-wavelength photometry, and gas masses from dust-corrected Hα SFRs and the relation by Kennicutt (1998) are available. The gas kinematics have been measured from the Hα emission lines: for 35 of the galaxies we detect resolved rotation, while in the remaining 143 galaxies we only measure the velocity dispersion.

As our galaxies are observed with random orientations compared to the slit angle, we may not see rotation for some objects that are intrinsically rotating. Additionally, we may not

---

dispersion term. This notation is in contrast to velocity dispersions of elliptical galaxies, where the *central* velocity dispersions are often denoted as σ_0 or $\sigma_{V,0}$.

resolve rotation due to seeing limitations, as found by Newman et al. (2013). To estimate how many of our galaxies are consistent with rotation, we compare the projected Hα major axis size within the slit to the seeing and use this to estimate whether a galaxy is spatially resolved or not. The majority of our sample (80%) is too small relative to our seeing, and thus these galaxies may indeed be unresolved rotating disks.

We have developed models to convert the observed kinematic measurements into intrinsic rotation and dispersion velocities. These models use the sizes, Sérsic indices, axis ratios, and position angles measured from the F160W imaging to simultaneously account for the inclination of the galaxy, the misalignment of photometric major axis and the slit, and determine which portions of the galaxy fall within the slit. In the case of galaxies with detected rotation, we directly constrain $V(R_E)$ and $\sigma_{V,0}$, and find a median $[(V/\sigma_{V,0})_{R_E}]_{\text{2D,median}} = 2.1$. For the galaxies without observed rotation, the models allow us to convert the observed velocity dispersion into an RMS velocity for an assumed ratio of $(V/\sigma_{V,0})_{R_E}$.

When assuming that the galaxies with and without detected rotation have a similar V/σ, we find that the baryonic ($M_{\text{baryon}} = M_* + M_{\text{gas}}$) and dynamical masses of the total sample are in good agreement, with a median offset of $\Delta(\log_{10} M) = 0.04$ dex and a scatter of $\sigma_{\text{RMS}} = 0.34$ dex. Moreover, we directly constrain the mean $(V/\sigma_{V,0})_{R_E}$ for the galaxies without detected rotation by removing any trend of $\log_{10}(M_{\text{dyn}}/M_{\text{baryon}})$ with axis ratio b/a and find $[(V/\sigma_{V,0})_{R_E}]_{\text{1D,median}} = 2.1^{+0.2}_{-0.3}$. The offset between the dynamical and baryonic masses implies a dark matter fraction within R_E of 8% for a Chabrier (2003) IMF, which is lower than the value measured within $2.2r_s$ for local star-forming galaxies (Dutton et al. 2011a; Pizagno et al. 2005) or within $r < 10$ kpc for galaxies at $z \sim 2$ (Förster Schreiber et al. 2009).

The consistency between the dynamical and baryonic masses relies on the inclusion of gas masses. When comparing the dynamical masses with only stellar masses, we find a larger scatter ($\sigma_{\text{RMS}} = 0.37$ dex). Furthermore, the median offset between the stellar and dynamical mass increases with increasing Hα SSFR, which is suggestive of a larger gas fraction at higher SSFRs.

We examine trends in the ratio of support from rotation and random motions, V/σ, as a function of Hα SSFR and stellar mass. For galaxies without detected rotation, we bin by Hα SSFR and stellar mass and estimate V/σ by removing any variation of $\log_{10}(M_{\text{dyn}}/M_{\text{baryon}})$ with axis ratio. We see a trend of decreasing V/σ with increasing Hα SSFR and a possible weak trend of increasing V/σ with increasing stellar mass when combining our measurements with the sample by Wisnioski et al. (2015). The trend of decreasing V/σ with increasing Hα SSFR may reflect disk settling, such that galaxies with lower SSFRs have lower gas fractions and therefore lower velocity dispersions.

While our assumption that all galaxies without detected rotation are disks results in highly consistent dynamical and baryonic masses, we also find a strong correspondence between the two masses if we had instead assumed that all unresolved galaxies are dispersion dominated. Differences in the methods of calculating the dynamical masses (i.e., using circularized radii for early-type galaxies vs. inclination corrections for disks, different virial coefficients) may explain why the dynamical masses are so similar, and why there is no observed trend of

$\log_{10}(M_{\rm dyn}/M_{\rm baryon})$ with axis ratio.

The measured masses also provide insight into the stellar IMF in $z \sim 2$ star-forming galaxies. The baryonic and dynamical masses of our sample are consistent with a Chabrier (2003) IMF. A Salpeter (1955) IMF is disfavored by our data, as it would lead to baryonic masses that exceed the dynamical masses by ~ 0.1 dex on average. However, when assuming that the half-mass sizes are 25% smaller than the half-light sizes (Szomoru et al. 2013), the inferred masses are also inconsistent with a Chabrier (2003) IMF. Nonetheless, other systematic uncertainties, as discussed in detail in the discussion section, may reduce this mass difference.

We examine the modified $S_{0.5}$-M_* and $S_{0.5}$-$M_{\rm baryon}$ Tully Fisher relations (TFRs) for our sample of galaxies, with $S_{0.5} = \sqrt{0.5V_{2.2}^2 + \sigma_{V,0}^2}$. We find a higher intercept of $S_{0.5}$ than Kassin et al. (2007) measure for the average $S_{0.5} - M_*$ TFR at $z \sim 0.1 - 1.2$, which may be caused by a decrease in the average gas fraction of star-forming galaxies with time. For the $S_{0.5} - M_{\rm baryon}$ TFR, we measure a lower intercept than Kassin et al. (2007) find at $z \sim 0.2$. The change in the $M_{\rm baryon}$-TFR may reflect an increase in the average dark matter fraction with time, possibly caused by the increase in average galaxy size at fixed mass with decreasing redshift.

Our sample also contains 21 AGN, selected by either X-ray luminosity, IRAC colors, or optical line ratios. As the line emission may be associated with nuclear accretion activity, the broadening may not only probe the kinematics of the host galaxy. We measure the baryonic and dynamical masses for the AGN in our sample, and find that they follow the same trend as the star-forming galaxies. This finding suggests that on average the line profiles do indeed reflect the host galaxy kinematics.

This paper demonstrates the power of using large samples of galaxies observed with multi-object near-infrared spectrographs under seeing-limited conditions to study the average kinematic properties of high redshift galaxies. In particular, combining such observations with high-resolution imaging makes it possible to model the effects of axis misalignment, seeing, and velocity rotation and dispersion on the observed spectra. This technique will prove useful in future studies of galaxy kinematics with *JWST*/NIRSPEC, as this multi-object spectrograph will also suffer from random orientation of galaxies within the slits. Measurements from seeing-limited multi-object spectrographs are not sufficient to constrain kinematic properties of individual high-redshift galaxies, and need to be complimented by adaptive-optics assisted IFU observations. Together, these approaches will provide a powerful probe of the nature of galaxies at this key period of structure formation.

Acknowledgements

I acknowledge valuable discussions with J. van de Sande, R. Feldmann, P. van Dokkum, M. Franx, R. Genzel, N. Förster-Schreiber, E. Toloba, M. George, and I. Shivvers. I thank the anonymous referee of the published version of this chapter for constructive comments, which improved the publication. I thank the MOSFIRE instrument team for building this powerful instrument, and for taking data for the MOSDEF collaboration during their commissioning runs. I am grateful to M. Kassis at the Keck Observatory for his many valuable contributions to the execution of the MOSDEF survey, and to I. McLean, K. Kulas, and G. Mace for taking observations for MOSDEF in May and June 2013. This work would not have been possible without the 3D-HST collaboration, who provided the spectroscopic and photometric catalogs used to select the MOSDEF targets and derive stellar population parameters. I acknowledge support from NSF AAG collaborative grants AST-1313171 and archival grant AR-13907, provided by NASA through a grant from the Space Telescope Science Institute, and from a National Science Foundation Graduate Research Fellowship under grant DGE 1106400. The data presented in this chapter were obtained at the W. M. Keck Observatory, which is operated as a scientific partnership among the California Institute of Technology, the University of California, and the National Aeronautics and Space Administration. The Observatory was made possible by the generous financial support of the W. M. Keck Foundation. I wish to recognize and acknowledge the very significant cultural role and reverence that the summit of Mauna Kea has always had within the indigenous Hawaiian community. I and collaborators are most fortunate to have the opportunity to conduct observations from this mountain. This chapter is also based on observations made with the NASA/ESA Hubble Space Telescope, which is operated by the Association of Universities for Research in Astronomy, Inc., under NASA contract NAS 5-26555. Observations associated with the following GO and GTO programs were used: 12063, 12440, 12442, 12443, 12444, 12445, 12060, 12061, 12062, 12064 (PI: Faber); 12177 and 12328 (PI: van Dokkum); 12461 and 12099 (PI: Riess); 11600 (PI: Weiner); 9425 and 9583 (PI: Giavalisco); 12190 (PI: Koekemoer); 11359 and 11360 (PI: O'Connell); 11563 (PI: Illingworth).

Chapter 4

The MOSDEF Survey: Kinematic and Structural Evolution of Star-Forming Galaxies at $1.4 \leq z \leq 3.8$

Kinematics provide important independent constraints on galaxy structures and their evolution over time. We present ionized gas kinematics for 714 galaxies at $z \sim 1.4-3.8$ from the MOSFIRE Deep Evolution Field survey, measured using models which account for random galaxy-slit misalignments together with structural parameters derived from CANDELS *Hubble Space Telescope* imaging. We use the kinematics and sizes to measure dynamical masses, and determine baryonic masses by inferring gas masses from dust-corrected star formation rates (SFRs) and the Kennicutt-Schmidt relation. We measure resolved rotation for 116 galaxies, and use the dynamical and baryonic masses to statistically constrain the median V/σ for galaxies without observed rotation. By comparing the dynamical and baryonic masses, we find the the inferred dark matter fraction within the effective radius decreases with increasing redshift, even at fixed stellar mass. However, for the lowest masses at $z \sim 2$ and for all galaxies at $z \sim 3$, the median dynamical and baryonic mass offset is unphysical, with baryon fractions of $f_{\rm bar} > 100\%$. We find correlations of V/σ with increasing stellar mass and decreasing specific SFR (SSFR), which may be caused by disk settling in systems with lower gas fractions. Furthermore, we find that V/σ decreases on average with increasing redshift. Finally, we discuss possible explanations for the tension between baryonic and dynamical masses of the low mass galaxies at $z \sim 2$ and the the galaxies at $z \sim 3$.

4.1 Introduction

A key open question in galaxy formation and evolution is how galaxy structures arise and evolve over time. Today's massive star-forming galaxies are assumed to form by the collapse of baryons within dark matter halos (e.g., White & Rees 1978, Fall & Efstathiou 1980, Blumenthal et al. 1984), resulting in thin, smooth stellar disks. However, the exact details of how galaxy disks form and what impact baryons have on this process are not well understood. Constraining these physical processes and testing different formation models requires direct studies of galaxies at earlier times.

Recent work shows that massive star-forming galaxies in the early universe look very different from their local counterparts. In particular, at $z \sim 2$, the peak of cosmic star formation rate (SFR) density in the universe (e.g., Madau & Dickinson 2014), massive star-forming galaxies are generally smaller (e.g., van der Wel et al. 2014a), have large clumps (e.g., Elmegreen et al. 2007, Law et al. 2007b, Förster Schreiber et al. 2009), and have high gas fractions (e.g., Daddi et al. 2008, Tacconi et al. 2008, 2013). Despite these differences, high-redshift massive galaxies do appear to have rotating disks, though they are thicker (e.g., Elmegreen & Elmegreen 2006) and have higher velocity dispersions and increased turbulence compared to local massive star-forming galaxies (e.g., Epinat et al. 2008, Newman et al. 2013, Green et al. 2014, Wisnioski et al. 2015).

Current theoretical models suggest that the thick, gas-rich disks of $z \sim 2$ massive star-forming galaxies are assembled though smooth, cold-mode accretion or minor mergers (e.g., Kereš et al. 2009, 2005, Dekel & Birnboim 2006, Davé 2008, Dekel et al. 2009, Oser et al. 2010, Cacciato et al. 2012, Ceverino et al. 2012). In this framework, the high turbulence and clumpy morphologies of these galaxies at $z \sim 2$ could reflect higher average gas fractions compared to local galaxies (e.g., Dekel et al. 2009, Bournaud et al. 2011, Genel et al. 2012).

Recent instrumentation advances, including multiplexing near-infrared (NIR) spectrographs such as KMOS (Sharples et al. 2013, 2004) and MOSFIRE (McLean et al. 2010, 2012), have enabled large kinematic studies at high redshifts to test these theoretical models. Surveys with KMOS and MOSFIRE (e.g., KMOS^{3D}, Wisnioski et al. 2015; KROSS, Stott et al. 2016; MOSDEF, Kriek et al. 2015; and SIGMA, Simons et al. 2016) now provide the kinematics for thousands of galaxies at $z \sim 1-3$, augmenting previous studies of smaller samples. While these surveys have greatly expanded our understanding of high-redshift galaxies, many challenges to interpreting these results remain.

The majority of previous high-redshift kinematic studies are conducted using ground-based, seeing-limited instruments (e.g., MOSFIRE and KMOS). The low spatial resolution of these observations can mask rotation signatures in small and lower-mass galaxies (Newman et al. 2013). Additionally, multi-object slit spectrographs (e.g., MOSFIRE) often have a constant position angle for all slits in a mask, resulting in random galaxy orientations within the slits, which can further mask rotation signals.

Furthermore, fully constraining star-forming galaxy formation models requires observations of lower-mass galaxies at high redshifts. The progenitors of today's massive star-forming disk galaxies are lower-mass ($M_* \sim 10^9 - 10^{10} M_\odot$) galaxies at $z \sim 2$ (e.g., Leja et al. 2013, van Dokkum et al. 2013), but currently kinematic observations of these early, low-mass galaxies are limited to very small sample sizes. Additionally, the observational challenges are particularly pronounced for these low-mass galaxies, as the the majority of $z \sim 1-3$ star-forming galaxies with $M_* \lesssim 10^{10} M_\odot$ are unresolved under ground-based seeing-limited conditions (van der Wel et al. 2014a).

However, despite the limitations of ground-based slit spectrographs, it is possible to statistically constrain the structures of high-redshift galaxies by combining the information from seeing-limited spectra with high-resolution, space-based imaging (e.g., Price et al. 2016). This approach can be applied to galaxies both with and without spatially kinematics, and can thus be used to study the internal dynamics for galaxies over a wide range of masses and sizes at high redshifts.

In this chapter, we use observations from the MOSFIRE Deep Evolution Field (MOSDEF) survey (Kriek et al. 2015) to study the dynamical and baryonic masses and internal kinematic structures of a sample of 714 star-forming galaxies at $z \sim 1.4 - 3.8$. Rotation is detected in only 116 of the galaxies, but we use detailed structural information from *Hubble Space Telescope* (*HST*) imaging from the the CANDELS survey (Grogin et al. 2011, Koekemoer et al. 2011) and other ancillary information to statistically constrain the kinematics of the remaining 598 galaxies. We compare the derived dynamical masses with the galaxies' baryonic masses to infer the evolution of the baryon and dark matter fraction in galaxies with redshift and stellar mass. We also investigate how the derived rotation velocities (V), velocity dispersions (σ), and ratio of ordered to unordered motion (V/σ) correlate with other galaxy properties, and how these kinematic properties change over time.

We adopt a ΛCDM cosmology with $\Omega_m = 0.3$, $\Omega_\Lambda = 0.7$, and $H_0 = 70\,\mathrm{km\,s^{-1}\,Mpc^{-1}}$ throughout this work.

4.2 Data

4.2.1 The MOSDEF survey

This work is based on the complete data set from the MOSDEF survey (Kriek et al. 2015), which was carried out from semesters 2012B to 2016A using the MOSFIRE spectrograph (McLean et al. 2012) on the 10 m Keck I telescope. In total, the survey obtained rest-frame optical, moderate resolution ($R = 3000 - 3600$) spectra for ~ 1500 H-band selected galaxies in some of the CANDELS (Grogin et al. 2011, Koekemoer et al. 2011) fields. The full survey details, including targeting, observational strategy, data reduction, success rate, sensitivities, redshift measurements, and other sample properties, are given in (Kriek et al. 2015).

Structural parameters for the MOSDEF galaxies are measured from *HST*/F160W images from the CANDELS survey using GALFIT (Peng et al. 2010). These parameters include the effective radius, R_E (using the semi-major axis length as the effective radius), the Sérsic index, n (Sérsic 1968), axis ratio, b/a, and the major axis position angle. Most galaxies' parameters are fit as described in L. de Groot et al. (2017, in preparation), while the remainder are adopted from the catalogs presented in van der Wel et al. (2014a).

The stellar masses and other stellar population parameters are determined by fitting the $0.3 - 8.0\mu$m multi-wavelength photometry from the 3D-HST survey (Brammer et al. 2012, Skelton et al. 2014, Momcheva et al. 2016) with stellar population models, in the same way as described in Price et al. (2016) (see also Kriek et al. 2015). Briefly, FAST (Kriek et al. 2009b) is used to fit the flexible stellar population models (Conroy et al. 2009,

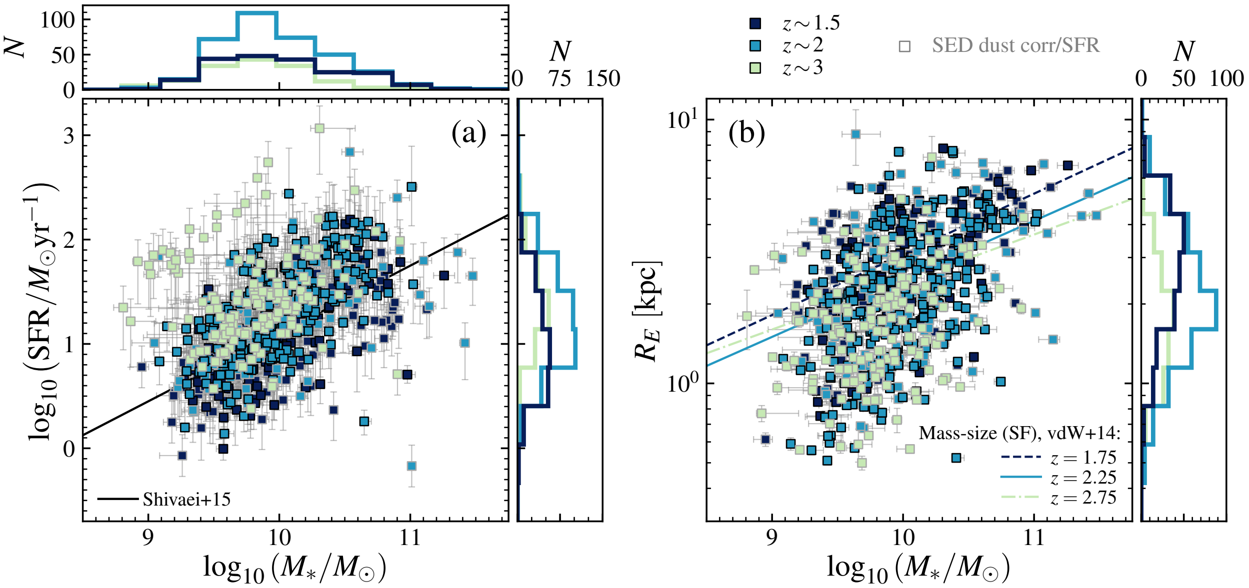

Figure 4.1: Stellar mass, $\log_{10}(M_*/M_\odot)$, versus *(a)* SFR and *(b)* effective radius, R_E, for the galaxies in our sample. Galaxies at $z \sim 1.5$, $z \sim 2$, and $z \sim 3$ are colored light green, teal, and navy, respectively. Histograms of $\log_{10}(M_*/M_\odot)$, SFR, and R_E show the distribution of galaxies in these redshift ranges. Galaxies without Balmer decrement dust-corrected SFRs are marked with gray outlines. The black solid line in the left panel shows the best-fit star-forming main sequence at $z \sim 1.4 - 2.6$ from Shivaei et al. (2015). The lines in the right panel show the best-fit mass-size relations for star-forming galaxies from van der Wel et al. (2014a) at $z = 1.75$ (navy dashed line), $z = 2.25$ (teal solid line), and $z = 2.75$ (light green dashed-dotted line). Our sample spans a wide range of properties, and generally follow the best-fit relations at these redshifts.

Conroy & Gunn 2010) to the multi-wavelength photometry, using the MOSFIRE redshifts and assuming a Chabrier (2003) stellar initial mass function (IMF), a Calzetti et al. (2000) dust attenuation curve, delayed exponentially declining star formation histories, and solar metallicity. We additionally correct the stellar masses for differences between the GALFIT and total photometric magnitudes following Taylor et al. (2010) (as in Equation 1 of Price et al. 2016), ensuring consistency between the radii and stellar masses.

Emission line fluxes (e.g., Hα, [OIII], Hβ) are calculated from the optimally extracted MOSFIRE 1D spectra by fitting the lines and underlying continuum simultaneously with Gaussian profiles and a linear component. The Hα and Hβ fluxes are additionally corrected for the underlying Balmer absorption, using the best-fit stellar population models. More details on emission line measurements are given in Kriek et al. (2015) and Reddy et al. (2015).

We use the following ranked approach to measure star formation rates (SFRs) and estimate gas masses ($M_{\rm gas}$) for our sample. This staggered method allows us to expand the sample selection from Price et al. (2016) to include galaxies over a wider range of redshifts. First, if both Hα and Hβ are detected (S/N ≥ 3 and the spectrum transmission at the line is at least 50% of the maximum transmission), then the Balmer absorption-corrected Hα fluxes are corrected for dust attenuation using the Balmer decrement, assuming a Cardelli et al. (1989) extinction curve (see Reddy et al. 2015). Hα luminosities are then calculated from the dust-corrected Hα fluxes, and then Hα SFRs are calculated from the luminosities using the relation of Kennicutt (1998) for a Chabrier (2003) IMF (Shivaei et al. 2015). Next, if only one Balmer line (Hα or Hβ) is detected, then we assume the dust attenuation of the nebular regions is related to the continuum attenuation by $A_{V,{\rm neb,Calzetti}} = 1.86 A_{V,{\rm cont,Calzetti}}$ (Price et al. 2014). We convert this inferred nebular attenuation to the Cardelli et al. (1989) curve, and use the resulting attenuation to correct the Balmer line flux. If only Hβ is detected, we convert the dust-corrected Hβ flux to an Hα flux assuming $f_{{\rm H}\alpha}/f_{{\rm H}\beta} = 2.86$ (Osterbrock & Ferland 2006). As with above, Hα (or Hβ) SFRs are then determined from the dust-corrected Balmer fluxes using the Kennicutt (1998) relation. Finally, if neither Balmer line is detected, SFRs from the spectral energy distribution (SED) fitting with FAST are adopted. We then estimate gas masses for every galaxy using the relation $\Sigma_{\rm SFR} \propto \Sigma_{\rm gas}^{N}$, with $N = 1.4$ following Kennicutt (1998). Here we use $\Sigma_{\rm SFR} = {\rm SFR}/(\pi R_E^2)$ and $\Sigma_{\rm gas} = M_{\rm gas}/(\pi R_E^2)$, where we adopt the best-available SFR and R_E is the best-fit GALFIT semi-major axis.

4.2.2 Sample selection

We select a kinematics sample from the full MOSDEF survey using the following criteria. Galaxies are selected in the redshift ranges $1.34 \leq z \leq 1.75$, $2.075 \leq z \leq 2.6$, and $2.9 \leq z \leq 3.8$, to include galaxies in all three redshift ranges covered by the survey. We next require that each galaxy has at least one emission line of Hα, [OIII]5007$\mathring{A}$, or Hβ detected with S/N ≥ 3. The sample is further restricted to only galaxies with *HST*/F160W coverage, as we require structural parameter measurements.

Additional selection criteria are applied to restrict the sample to galaxies with high-quality spectra, and structural and stellar population parameters. We use the same criteria as in

Price et al. (2016), with the following changes. The quality cuts on the emission lines are applied to the highest S/N line of Hα, [OIII]5007$\mathring{A}$, or Hβ. We also exclude AGN from our sample, using X-ray luminosity, IRAC color, and rest-frame optical emission line ratios to identify AGN (Coil et al. 2015, Azadi et al. 2017). Finally, we have not excluded objects which fall within the quiescent region in the UVJ diagram (Wuyts et al. 2007, Williams et al. 2009).

The final kinematic sample includes 714 galaxies. Of these galaxies, kinematics are measured using Hα, [OIII]5007$\mathring{A}$, and Hβ for 499, 208, and 7 galaxies, respectively. Within our sample, both Hα and Hβ are detected in 333 galaxies (e.g., Balmer-decrement corrected Hα SFRs are adopted), only one Balmer line is detected for 307 galaxies (e.g., Hα or Hβ SFRs are estimated using A_V from SED fitting), and neither line is detected for 74 galaxies (e.g., SED SFRs are adopted).

The stellar masses, SFRs, and effective radii of our final kinematics sample are shown in Figure 4.1, colored by redshift range. For comparison, we show the best-fit stellar mass-SFR relation at $z \sim 1.4 - 2.6$ by Shivaei et al. (2015) (left panel) and the best-fit size-stellar mass relations for star-forming galaxies at $z = 1.75$, $z = 2.25$, and $z = 2.75$ by van der Wel et al. (2014a) (right panel). The low and medium redshift galaxies in our sample are in excellent agreement with the best-fit relation of Shivaei et al. (2015), and overall the sample shows the expected trend of higher SFRs at higher redshifts. The galaxies also generally follow the size-mass relations measured in similar redshift ranges, though the galaxies at $z \sim 3$ are generally smaller than the relation measured at $z = 2.75$, as our sample redshift range ($2.9 \leq z \leq 3.8$) is higher than the highest redshift range of van der Wel et al. (2014a).

4.3 Kinematic Measurements

The kinematic properties of our sample are measured from an emission line (Hα, [OIII], or Hβ) together with the structural parameters derived from the *HST*/F160W imaging, using the 3D models and methods developed in Price et al. (2016). For galaxies with spatially resolved rotation, we fit both rotation and velocity dispersion from the 2D emission lines (Section 4.3.1). Kinematics for galaxies without detected rotation are derived from the 1D emission line profiles (Section 4.3.2). We finish by discussing the method for determining dynamical masses and fitting V/σ for galaxies without detected rotation (Section 4.3.3).

4.3.1 Resolved kinematics

For galaxies with spatially resolved rotation, the rotation velocity and velocity dispersion can be measured from 2D spectra. However, the MOSDEF galaxies were observed with random misalignments between the galaxy major axis and the slit. We thus use the 3D models and methods developed by Price et al. (2016) to fit the rotation and velocity dispersion from the 2D MOSFIRE spectra, using the spatial information from the *HST*/F160W imaging to account for the degree of slit-axis misalignment.

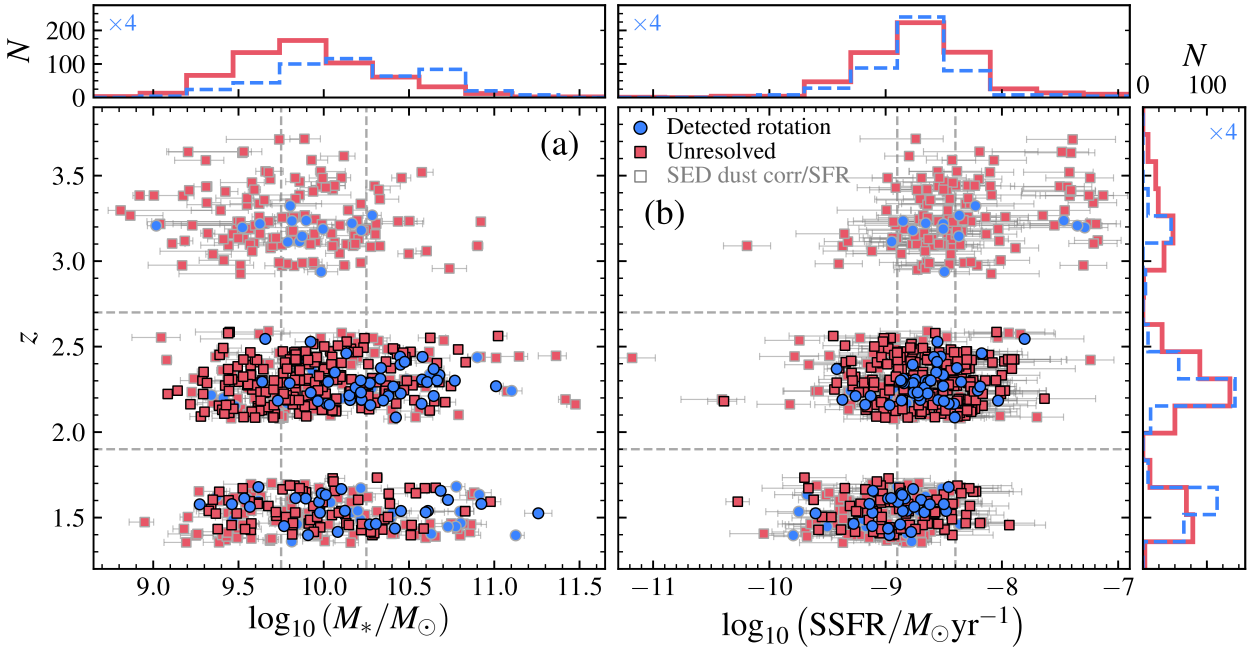

Figure 4.2: Comparison of redshift versus *(a)* stellar mass and *(b)* specific star formation rate (SSFR) for galaxies with (blue circles) and without resolved rotation (red squares). Histograms of z, $\log_{10}(M_*/M_\odot)$, and SSFR show the distribution of the galaxies with (dashed blue) and without (solid red) detected rotation (with the number of detected rotation galaxies multiplied by 4 for clarity). As in Figure 4.1, galaxies without Balmer decrement dust-corrected SFRs are marked with gray outlines. Bin boundaries in z, $\log_{10}(M_*/M_\odot)$, and SSFR used for later analysis (see Section 5.4) are marked with gray dashed lines. The galaxies with detected rotation tend to be slightly higher masses than the galaxies without resolved rotation at a given redshift, but have similar SSFRs.

Full details of the kinematic models and the fitting code (MISFIT) are given in Appendix A of Price et al. (2016). In brief, the models have three free kinematic parameters: the asymptotic velocity (V_a) and turnover radius (r_t) of an arctan rotation curve model, and a constant intrinsic velocity dispersion ($\sigma_{V,0}$). The models also account for inclination and the galaxy sizes, brightness profiles, slit misalignments, seeing conditions, and instrumental resolution. We subtract the continuum and mask the 2D emission lines similar to the procedure of Price et al. (2016), but adopt appropriate wavelength ranges that exclude neighboring features for the different emission lines (e.g., Hα, [O III], Hβ). The models are then fit to the masked, continuum-subtracted 2D emission lines using the `python` Markov-Chain Monte Carlo (MCMC) package `emcee` (Foreman-Mackey et al. 2013), yielding the best-fit values and confidence intervals for $V(R_E)$, $V_{2.2} = V(r = 2.2r_s)$ (where $r_s = R_E/1.676$ is the scale length of an exponential disk), and $\sigma_{V,0}$.

We apply this fitting procedure to the entire sample in order to determine which galaxies have spatially resolved rotation and which are unresolved. Galaxies with $V(R_E) \neq 0$ with 95% confidence (e.g., 95% of the posterior distribution is either greater than or less than zero) are classified as having resolved rotation, while objects which fail this criterion are classified as unresolved. Using this classification, we find that 116 galaxies in our sample have detected rotation, while the remaining 598 galaxies have unresolved kinematics. The distribution of galaxies with and without detected rotation are shown in Figure 4.2. Overall, the galaxies with detected rotation tend to have slightly higher masses than those without detected rotation, but have similar specific SFRs (SSFRs). Additionally, we detect rotation in relatively few galaxies at $z \sim 3$ compared to the galaxies at $z \sim 1.5$ and $z \sim 2$.

4.3.2 Unresolved kinematics

Kinematics for galaxies without rotation detected in the 2D spectra (Section 4.3.1) are instead measured from the integrated 1D spectra. However, while these galaxies have no detected rotation, we might expect that they have at least partial rotational support, as they are star-forming galaxies and the seeing-limited conditions together with misaligned slits may mask rotational signatures (Newman et al. 2013). Therefore, as in Price et al. (2016), we model the integrated, unresolved kinematics using the same set of 3D models while assuming a fixed value of $(V/\sigma_{V,0})_{R_E} = V(R_E)/\sigma_{V,0}$.

Briefly, we first measure the integrated velocity dispersions $\sigma_{V,\mathrm{1D,obs}}$ by fitting the emission line (Hα, [O III], or Hβ), any neighboring lines, and the continuum simultaneously using Gaussian profiles and a linear component, assuming the emission lines have the same width in velocity space. The measured velocity dispersion is then corrected for instrumental resolution by subtracting $\sigma_{V,\mathrm{sky}}$ in quadrature from $\sigma_{V,\mathrm{1D,obs}}$. Errors on the resulting $\sigma_{V,\mathrm{obs}}$ are estimated by repeating the fitting and correction procedure on 500 random, error-perturbed copies of each spectrum.

We then use the same 3D kinematic models to convert the observed velocity dispersions $\sigma_{V,\mathrm{obs}}$ to an intrinsic root mean square velocity $V_{\mathrm{rms}} = \sqrt{V^2 + \sigma_V^2}$, as described in Appendix B of Price et al. (2016). In summary, each galaxy is modeled as an inclined disk using the

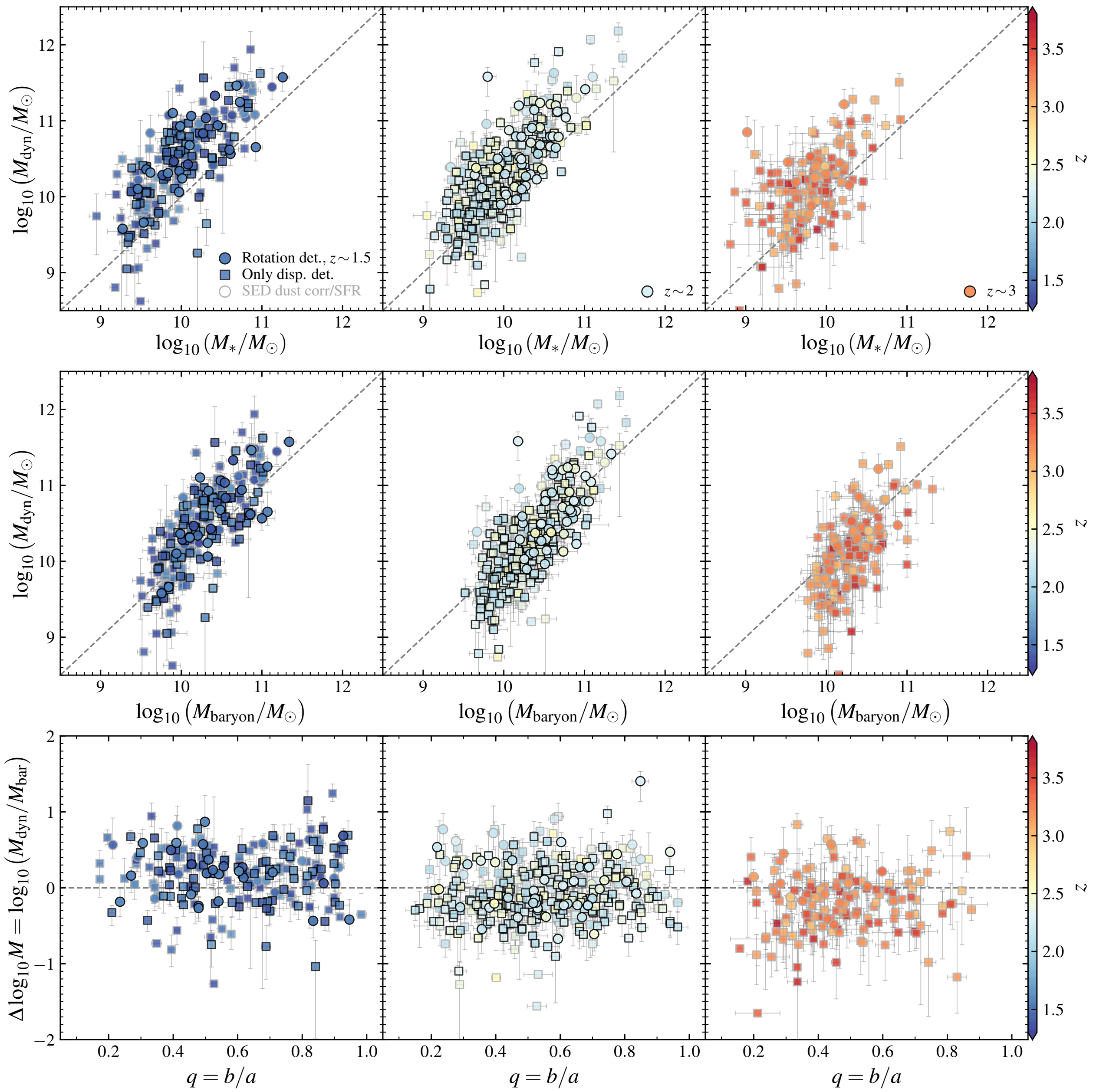

Figure 4.3: Comparison of dynamical and stellar *(top row)* and baryonic (stellar and gas; *middle row*) masses for galaxies at $z \sim 1.5$ *(left)*, $z \sim 2$ *(center)*, and $z \sim 3$ *(right)*, colored by redshift. Galaxies with and without detected rotation are shown as circles and squares, respectively. The average V/σ used to calculate $M_{\rm dyn}$ for the unresolved galaxies is fit in bins of z and M_* (see Figure 4.2a). Objects without Balmer decrement dust-corrected SFRs are denoted with gray outlines. The gray dashed lines show $M_{\rm dyn} = M_*$ (top row) and $M_{\rm dyn} = M_{\rm baryon}$ (middle row). *(Bottom row)* Comparison of ratio between dynamical and baryonic masses versus galaxy axis ratio, b/a for the three redshift ranges. The gray dashed horizontal line denotes no offset. Galaxies with and without detected rotation show good agreement between their dynamical and baryonic masses, and we see no differences between $M_{\rm dyn}/M_{\rm baryon}$ versus axis ratio (e.g., inclination) for these two sub-samples.

Galfit structural parameters, and is offset from the slit by the measured ΔPA. Rotation and velocity dispersion are included by assuming a fixed ratio of $(V/\sigma_{V,0})_{R_E}$ and assuming an arctan velocity curve where $r_t = 0.4 r_s = 0.4(R_E/1.676)$ (Miller et al. 2011). We then compute the luminosity-weighted, seeing-convolved integrated model velocity dispersion ($\sigma_{V,\mathrm{model}}$) and model rms velocity at R_E ($V_{\mathrm{rms}}(R_E)_{\mathrm{model}}$), and calculate the composite $V_{\mathrm{rms}}(R_E)_{\mathrm{1D,corr}}$ as in Equation 2 of Price et al. (2016).

4.3.3 Dynamical masses and measuring V/σ

We determine the dynamical masses for our sample by combining their measured kinematics and structural information. We first combine the rotation and velocity dispersions into an rms velocity, $V_{\mathrm{rms}}(R_E) = \sqrt{\sigma_{V,0}^2 + V(R_E)^2}$, and then calculate the effective virial coefficients k_{eff} and dynamical masses M_{dyn} using Equations 3 and 4 of Price et al. (2016). This composite allows us to account for dynamical support from both ordered and random motions (e.g., Meurer et al. 1996, Epinat et al. 2009, Newman et al. 2013, Übler et al. 2017).

For galaxies with detected rotation, we use the best-fit values of $V(R_E)$ and $\sigma_{V,0}$ to determine k_{eff} and M_{dyn}. Unfortunately, for the galaxies without detected rotation, we cannot simultaneously constrain $V(R_E)$ and $\sigma_{V,0}$. We must instead assume a fixed value of $(V/\sigma_{V,0})_{R_E}$ to determine $V_{\mathrm{rms}}(R_E)_{\mathrm{1D,corr}}$, k_{eff}, and M_{dyn}.

However, we can statistically constrain the average $(V/\sigma_{V,0})_{R_E}$ for the unresolved galaxies by examining the correlation between the difference between dynamical and baryonic ($M_{\mathrm{baryon}} = M_* + M_{\mathrm{gas}}$) masses as a function of galaxy axis ratio. If the average population value of $(V/\sigma_{V,0})_{R_E}$ is overestimated, the inclination-corrected rotation velocities will be too high. Thus M_{dyn} will be overestimated for more face-on galaxies (e.g., close to $b/a \sim 1$), and there will be a positive trend between $\Delta \log_{10} M = \log_{10}(M_{\mathrm{dyn}}/M_\odot) - \log_{10}(M_{\mathrm{baryon}}/M_\odot)$ and b/a.

We constrain the ensemble average $(V/\sigma_{V,0})_{R_E}$ using the trend of $\Delta \log_{10} M$ versus b/a, but use a slightly different procedure than in Price et al. (2016). First, we calculate the dynamical masses for the galaxies without detected rotation over a range of $(V/\sigma_{V,0})_{R_E}$ values. We then measure the slope between b/a and $\Delta \log_{10} M$ for these galaxies at every value of $(V/\sigma_{V,0})_{R_E}$, and determine the slope error through 500 realizations where $\Delta \log_{10} M$ of every galaxy is perturbed by the error. The best-fit $(V/\sigma_{V,0})_{R_E}$ is then estimated by finding the value which removes the trend of $\Delta \log_{10} M$ with b/a (e.g., a slope of zero). The confidence interval is taken to be the range of $(V/\sigma_{V,0})_{R_E}$ where the slopes are consistent with zero within the errors. Average $(V/\sigma_{V,0})_{R_E}$ for the unresolved galaxies are measured in bins of redshift, stellar mass, and SSFR. The bin boundaries are shown with gray dashed lines in Figure 4.2.

The dynamical, baryonic, and stellar masses of the galaxies in our sample are shown in Figure 4.3. For the galaxies with unresolved kinematics, the average $(V/\sigma_{V,0})_{R_E}$ is determined in bins of z and M_* (see Figure 4.2a). Overall, there is good agreement between the dynamical and stellar masses in all three redshift ranges. The dynamical and baryonic masses are also in fairly good agreement, though we will discuss the evolution of the $M_{\mathrm{dyn}} - M_{\mathrm{baryon}}$ offset

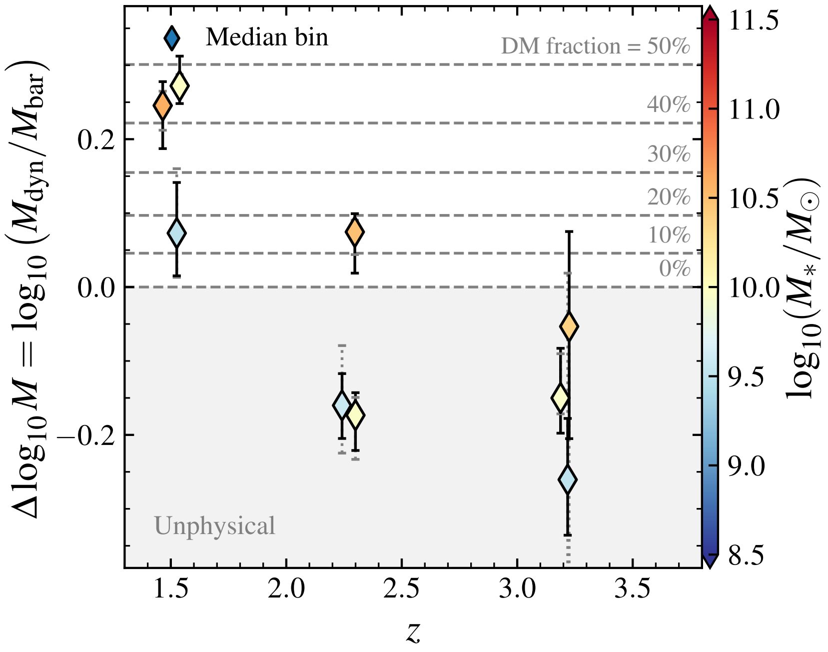

Figure 4.4: Evolution of $M_{\rm dyn}/M_{\rm baryon}$ and inferred dark matter fraction with redshift. Lines of constant dark matter fraction are shown as gray dashed lines, and the unphysical region where $M_{\rm dyn} < M_{\rm baryon}$ is shaded gray. The median mass offset $\Delta \log_{10} M = \log_{10}(M_{\rm dyn}/M_{\rm baryon})$ for all galaxies (both those with and without resolved rotation) in bins of z and M_* (Figure 4.2a) are shown as diamonds, colored by the median value of $\log_{10}(M_*/M_\odot)$ of the galaxies in each bin. The black bars denote the bootstrapped error on median for $\Delta \log_{10} M$. The dotted gray bars demonstrate how the median $\Delta \log_{10} M$ changes when using the $\pm 1\sigma$ range of median V/σ measured for the unresolved galaxies in each bin. We observe a decrease in $\Delta \log_{10} M$ and the inferred dark matter fraction towards higher redshifts. This is seen even at fixed mass, suggesting that the average growth of galaxy masses with time is not responsible for this trend. At fixed redshift, we also find that the median dark matter fraction within the effective radius is generally higher for galaxies with higher masses. For the higher redshift ranges, the median $\Delta \log_{10} M$ for the lower ($z \sim 2$) and all ($z \sim 3$) mass bins lie within the non-physical region where $M_{\rm dyn} < M_{\rm baryon}$. The negative values $\Delta \log_{10} M$ suggest that one, if not more, of the assumptions and methods used to measure the dynamical and baryonic masses may not be valid for these galaxies.

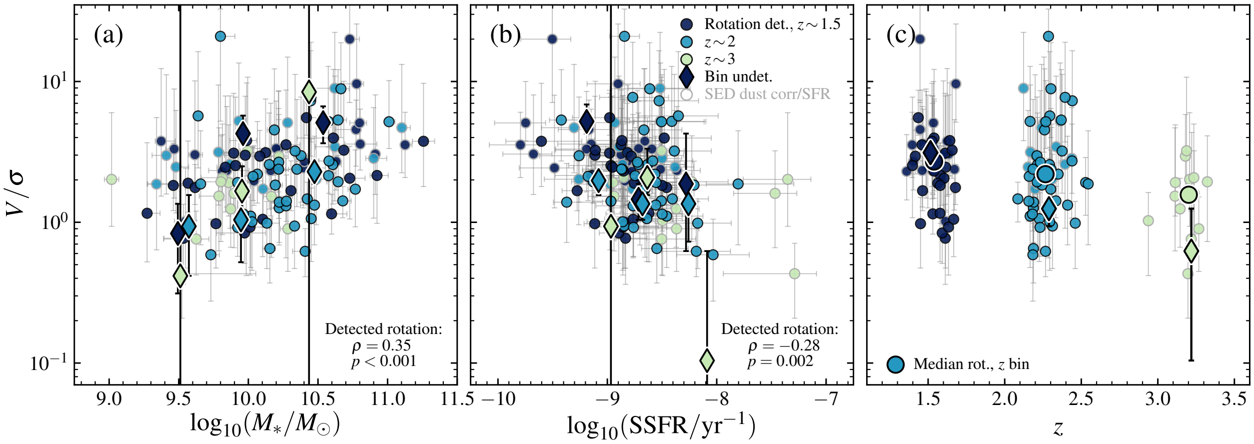

Figure 4.5: $(V/\sigma_{V,0})_{2.2}$ vs *(a)* stellar mass, *(b)* SSFR, and *(c)* redshift for the galaxies in our sample, colored by redshift range as in Figure 4.1. Galaxies with detected rotation are shown as circles. Gray outlines denote galaxies without Balmer decrement-corrected SFRs. Additionally, the median measured V/σ for bins of galaxies without detected rotation are shown with diamonds. The unresolved galaxy bin boundaries for panels *(a)* and *(b)* are as defined in Figure 4.2(a) and (b), respectively, and panel *(c)* is binned by redshift (also as in Figure 4.2). We find a positive correlation between M_* and V/σ (Spearman correlation coefficient $\rho = 0.35$ with $p < 0.001$) and a negative correlation between SSFR and V/σ ($\rho = -0.28$ with $p = 0.002$) for the galaxies with detected rotation. These trends reflect disk settling, where galaxies with lower SSFR (and gas fraction) and higher stellar mass have more support from ordered motions. We also observe an average increase in V/σ towards lower redshifts (panel c) for both the galaxies with detected rotation (median shown with large circles) and for the unresolved galaxies (diamonds) in bins of redshift, though the evolution is stronger for the median of the unresolved galaxies.

in Section 4.4.1. Furthermore, both the galaxies with and without detected rotation follow the same M_*-M_{dyn} and M_{baryon}-M_{dyn} relations. The two sub-samples also have similar distributions of $M_{\mathrm{dyn}}/M_{\mathrm{baryon}}$ versus axis ratio (e.g., inclination).

4.4 Results

We use these kinematic and structural observations for galaxies in the MOSDEF survey to constrain the evolution of the dark matter fraction and to explore connections between kinematics and other properties in galaxies between $z \sim 1.4 - 3.8$.

4.4.1 Evolution of inferred galaxy dark matter fractions

By comparing the dynamical and baryonic masses for the galaxies in our sample, we investigate how the inferred dark matter fraction evolves. We consider the sample into bins of redshift and stellar mass (as in Figure 4.2a). The ensemble average $(V/\sigma_{V,0})_{R_E}$ for the galaxies without resolved rotation are measured within these bins following the procedure described in Section 4.3.3. We then combine all galaxies within each bin (e.g., both galaxies with and without resolved rotation) and calculate the median offset between dynamical and baryonic masses, $\Delta\log_{10}(M) = \log_{10}(M_{\rm dyn}/M_{\rm baryon})$, and determine errors through bootstrap resampling. These mass offsets are shown versus redshift in Figure 4.4, where each bin is colored by the median stellar mass.

We find that the mass difference $\Delta\log_{10}(M)$ decreases towards higher redshifts, where galaxies have higher baryon fractions ($f_{\rm bar} = M_{\rm baryon}/M_{\rm dyn}$) at higher redshifts. At $z\sim 1.5$, the median mass offset in the medium and high mass bins ($9.75 < \log_{10}(M_*/M_\odot) \leq 10.25$, $10.25 < \log_{10}(M_*/M_\odot) \leq 12$) imply a median dark matter fraction within the effective radius of $\sim$45%, while the lowest mass bin ($8 < \log_{10}(M_*/M_\odot) \leq 9.75$) has an implied fraction of only $\sim$15%. The inferred dark matter fraction for the highest mass bin decreases to $\sim$15% at $z\sim 2.3$, while both the low and medium mass bins have negative offsets and lie within the unphysical region where $M_{\rm dyn} < M_{\rm baryon}$ (e.g., baryon fractions $f_{\rm bar} > 100\%$). For the highest redshift galaxies ($z\sim 3.25$), the median offsets of all three mass bins are negative, though the highest mass bin is consistent with a non-zero dark matter fraction. Our results at $z\sim 1.5$ and $z\sim 2.3$ for the highest mass bin are in excellent agreement with the offsets reported by Wuyts et al. (2016) for similar mass and redshift galaxies, who find offsets of $\Delta\log_{10} M \sim 0.25$ and ~ 0.05, respectively, also assuming a Chabrier (2003) IMF.

The general trend of decreasing $\Delta\log_{10}(M)$ (alternatively, increasing $f_{\rm bar}$) with redshift is seen even at fixed mass, suggesting that this result is not caused by differences in the masses of our sample for the different redshift ranges. We furthermore find that the offset is generally higher for higher masses at fixed redshift, suggesting that the dark matter fraction within the effective radius is higher for more massive galaxies. This trend with mass may be caused by average trends of galaxy sizes. More massive galaxies have higher effective radii (e.g., Williams et al. 2010, van der Wel et al. 2014a) and thus extend further into the dark matter halo, which results in a higher dark matter fraction within R_E. However, the negative offsets $\Delta\log_{10}(M)$ (e.g., $f_{\rm bar} > 100\%$) observed for the low and medium mass bins at $z\sim 2$ and all three mass bins at $z\sim 3$ imply that at least some of the assumptions used to measure the dynamical and baryonic masses may be invalid for these galaxies, as we would expect the dynamical mass to include, at minimum, all of the observed baryonic mass.

4.4.2 Comparison between internal kinematic structure (V/σ) and other galaxy properties

The amount of kinematic support from ordered versus random motions (V/σ) provides information about the internal structures of galaxies. In particular, low values of V/σ may indicate that a galaxy has a thick disk and high gas turbulence, while galaxies with high V/σ tend to have ordered, thin disks. We thus investigate the relationship between V/σ and other properties to constrain what processes drive the internal structures of star-forming galaxies at high redshifts.

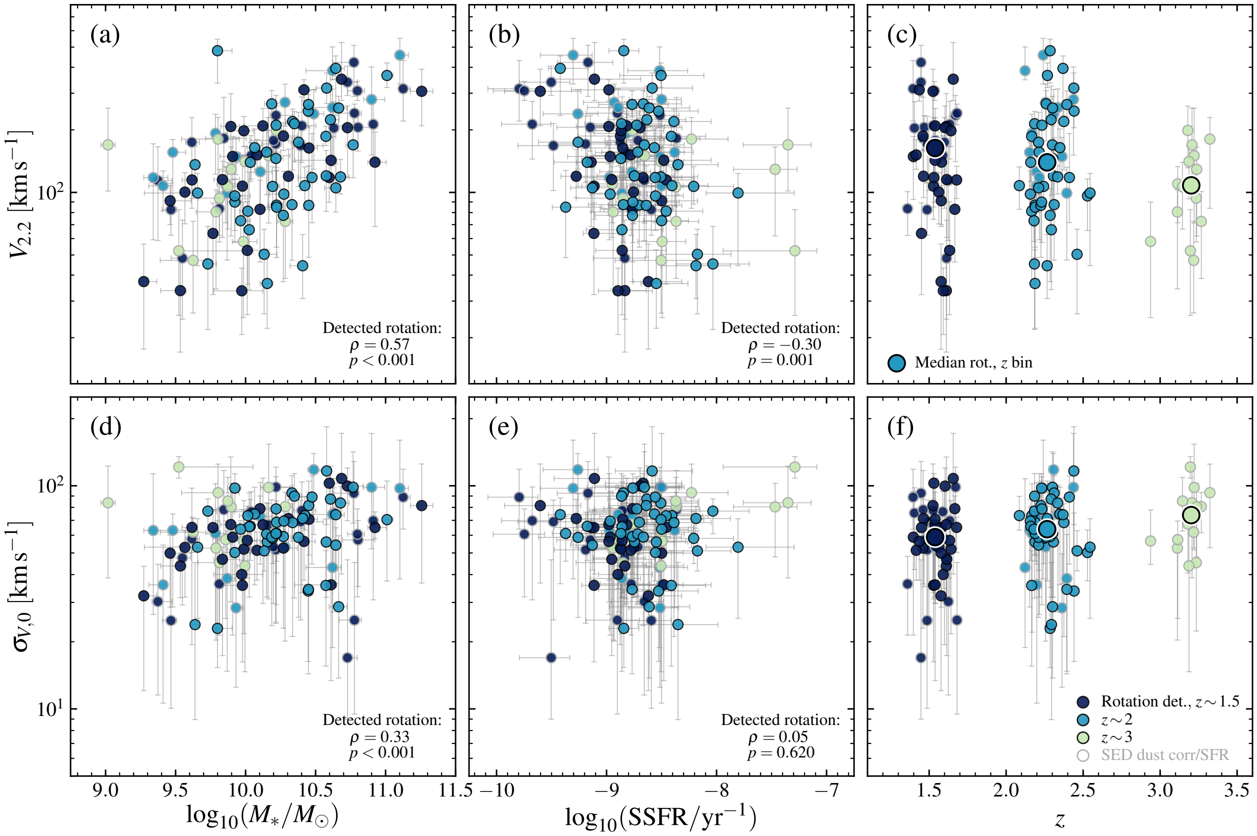

Figure 4.6: Comparison of $V_{2.2}$ *(top)* and $\sigma_{V,0}$ *(bottom)* versus stellar mass *(left)*, SSFR *(center)*, and redshift *(right)* for galaxies with detected rotation, colored by redshift range as in Figure 4.1. The point definitions are the same as in Figure 4.5. Spearman correlation coefficients and p-values between the parameters are marked in the panels. There are positive correlations between both $V_{2.2}$ and $\sigma_{V,0}$ and M_*, a negative correlation between $V_{2.2}$ and SSFR, and no discernible correlation of $\sigma_{V,0}$ and SSFR. We also find evolution in the median $V_{2.2}$ and $\sigma_{V,0}$ with redshift, where $V_{2.2}$ increases and $\sigma_{V,0}$ decreases at lower redshifts. The trends with $V_{2.2}$ appear to drive most of the observed trends of V/σ, but the decrease of $\sigma_{V,0}$ augments the increase in V/σ towards lower redshifts.

In Figure 4.5, we present $(V/\sigma_{V,0})_{2.2} = V(2.2r_s)/\sigma_{V,0}$[1] versus stellar mass (Figure 4.5a), SSFR (Figure 4.5b), and redshift (Figure 4.5c) for galaxies with detected rotation. For the galaxies without detected rotation, we also show the ensemble average $(V/\sigma_{V,0})_{2.2}$ measured in bins of redshift and stellar mass, redshift and SSFR, and redshift, respectively, using the procedure given in Section 4.3.3 for the bin boundaries displayed in Figure 4.2. We find a moderate positive correlation (Spearman rank correlation coefficient $\rho = 0.35$ with $>3\sigma$ significance) between stellar mass and V/σ for our entire sample of galaxies with detected rotation. We observe a similar trend in the V/σ values measured in bins of z and M_* for the unresolved galaxies. Additionally, there is a moderate negative correlation ($\rho = -0.28$ with $\sim 2.9\sigma$ significance) between V/σ and SSFR for the detected rotation galaxies, with a similar trend for the bins of unresolved galaxies.

These trends of V/σ with M_* and SSFR are in generally good agreement with the findings of Wisnioski et al. (2015) and Simons et al. (2016) using galaxies at $z \sim 1$ and $z \sim 2$. The findings of Wisnioski et al. (2015) suggests that the trend of V/σ with SSFR is indicative of disk settling, where galaxies tend to have lower velocity dispersions when they have lower gas fractions (which correlates with lower SSFRs). As SSFR and stellar mass are correlated, we would expect to observe both a decreasing trend of SSFR and an increasing trend of stellar mass towards higher V/σ. However, the stronger correlation of V/σ with M_*, as also observed by Simons et al. (2016), suggests that other properties beyond just gas fraction help to set a galaxy's dynamical structure.

The general trends of V/σ with M_* and SSFR are also seen for galaxies at $z \sim 1.5$ and $z \sim 2$ separately.[2] Thus, the processes regulating the internal structures of relatively massive star-forming galaxies appear to be in place by $z \sim 2$.

We also find that the median V/σ decreases with increasing redshift (Figure 4.5c), in excellent agreement with results of Wisnioski et al. (2015) (Figure 11). This likely reflects a combination of the decreasing average gas fraction (and decreasing SSFR) in galaxies from $z \sim 3$ to $z \sim 1.5$ and the difference in the mass distribution of the samples in the three redshift ranges (see Figure 4.1). We note that the evolution of the ensemble average V/σ of the unresolved galaxies is stronger than the trend of the median V/σ of the galaxies with detected rotation. This may be partly caused by differences in the mass distribution for the galaxies with and without rotation at $z \sim 2$ and $z \sim 3$ (see Figure 4.2), as the unresolved galaxies at these redshifts have lower stellar masses than the galaxies with detected rotation at the same epochs.

---

[1] We consider $V(r = 2.2r_s)$, the radius where an exponential rotation curve peaks, for the V/σ analysis to provide reasonable comparisons with existing measurements, as we do not directly constrain the turn-over or flattening for the rotation curves of our galaxies.

[2] The trends with V/σ at $z \sim 3$ are inconclusive due to the large errors caused by the limited number of galaxies some bins.

4.4.3 Trends between rotation, velocity dispersion and other properties for rotating galaxies

Additionally, we explicitly investigate correlations between rotation velocity, velocity dispersion, and other galaxy properties to directly examine how disk rotation velocity and turbulence evolves. Figure 4.6 shows measurements of $V_{2.2} = V(r = 2.2r_s)$ and $\sigma_{V,0}$ versus stellar mass, SSFR, and redshift for the galaxies in our sample with detected rotation. We find the strongest correlation for the full sample is between $V_{2.2}$ and M_* ($\rho = 0.57$ at $>3\sigma$), but also find moderate correlations between $\sigma_{V,0}$ and M_* ($\rho = 0.33$) and $V_{2.2}$ and SSFR ($\rho = -0.30$). We do not find any correlation between $\sigma_{V,0}$ and SSFR for the full detected rotation sample. These trends (or lack thereof) of $V_{2.2}$ and $\sigma_{V,0}$ are in rough agreement with results by Wisnioski et al. (2015) (e.g., $\sigma_{V,0}$ versus M_* and SSFR) and Simons et al. (2016) (e.g., rotation and dispersion versus M_*).

We also find that the median $V_{2.2}$ increases over time. Our observed trend of $V_{2.2}$ with z is generally consistent with the evolution from $z \sim 0.2$ to $z \sim 1.2$ found by Kassin et al. (2012). However, the evolution of $V_{2.2}$ with redshift may be impacted by different stellar masses of the sample in each range, as found in Simons et al. (2017). Mass selection effects would also influence the observed trends of V/σ (as discussed in Section 4.4.2).

In contrast, we find that the median $\sigma_{V,0}$ decreases with time. Our observed values of $\sigma_{V,0}$ at $z \sim 1.4 - 3.3$ are in excellent agreement with the findings of Wisnioski et al. (2015) and Simons et al. (2017). Furthermore, our results are in excellent agreement with the literature compilation and the expected evolution for marginally stable disks (e.g., Toomre 1964, Förster Schreiber et al. 2006, Genzel et al. 2011) presented in Figure 8 of Wisnioski et al. (2015). Overall, the strength of the correlations with $V_{2.2}$ suggest that the rotation velocity trends primarily drive the observed trends of V/σ, with relatively little impact from the galaxies' velocity dispersion, in agreement with the findings of Simons et al. (2016).

4.5 Discussion

We now discuss how various assumptions and caveats may impact our findings. In Section 4.5.1, we discuss implications and possible reasons for the tension between dynamical and baryonic masses for the lower mass galaxies at $z \sim 2$ and all galaxies at $z \sim 3$. Section 4.5.2 discusses caveats to the presented findings.

4.5.1 Reconciling baryonic and dynamical masses at high redshifts

While our results support a decreasing dark matter fraction within galaxies' effective radii towards higher redshifts, there is tension between the dynamical and baryonic masses in the higher redshift bins. The results at $z \sim 1.5$ and for the highest mass bin at $z \sim 2$ are consistent with non-zero dark matter fractions. Alternatively, these mass offsets would allow

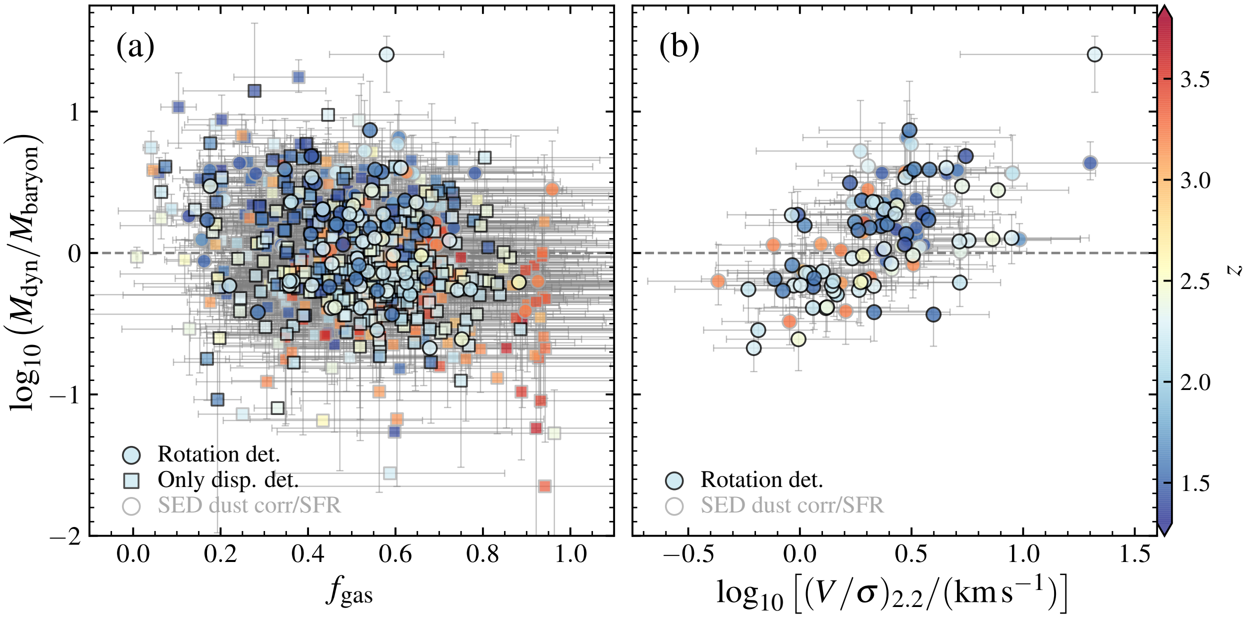

Figure 4.7: Distribution of *(a)* gas fraction, $f_{\rm gas}$, and *(b)* $(V/\sigma_{V,0})_{2.2}$ versus mass offset, $\log_{10}(M_{\rm dyn}/M_{\rm baryon})$ for the detected rotation galaxies (circles) across all redshifts. Galaxies without detected rotation are also shown in panel *(a)* as squares (ensemble V/σ measured in bins of redshift and stellar mass; Figure 4.2a). The points are colored by redshift, and galaxies without Balmer decrement dust-corrected SFRs are marked with gray outlines. The gray dashed line shows no offset (e.g., $M_{\rm dyn} = M_{\rm baryon}$). The galaxies with higher gas fractions tend to have $M_{\rm dyn} < M_{\rm baryon}$, while the lower gas fraction galaxies lie in the physical region ($M_{\rm dyn} > M_{\rm baryon}$). We also find that the highest V/σ values are seen in galaxies with high dynamical masses, that preferentially have $M_{\rm dyn} > M_{\rm baryon}$. In contrast, the lowest V/σ values (e.g., $V/\sigma \lesssim 1$) tend to have the lowest dynamical masses and lie in the unphysical region where $M_{\rm dyn} < M_{\rm baryon}$. The general trend of $f_{\rm gas}$ $M_{\rm dyn}/M_{\rm baryon}$ suggests that the galaxies with $M_{\rm dyn} < M_{\rm baryon}$ may have gas masses which are systematically overestimated. However, these trends could also be caused by systematic underestimates of the dynamical masses for galaxies with low V/σ.

for a more bottom-heavy IMF, (e.g., Salpeter 1955), but other studies suggest a Chabrier (2003) IMF is more appropriate for star-forming galaxies (e.g., Bell & de Jong 2001, Tacconi et al. 2008, Dutton et al. 2011a, Brewer et al. 2012). However, even for a Chabrier (2003) IMF, the dynamical masses are lower than the inferred baryonic masses for the galaxies in our sample with $\log_{10}(M_*/M_\odot) \leq 10.25$ at $z \sim 2$ and for the entire sample at $z \sim 3$.

The unphysical offsets where $M_{\rm dyn} < M_{\rm baryon}$ suggest that some of the assumptions used to derive masses are invalid for these galaxies. One possibility is that the gas masses, and therefore the baryonic masses, are overestimated. Here we have used the relation of Kennicutt (1998) to convert observed, dust-corrected SFRs into gas masses. However, this relation may not hold for our lower mass galaxies at $z \sim 2$ or our sample at $z \sim 3$. Work on galaxies at $z \sim 1-3$ find slopes which vary from $N = 1.28$ (Genzel et al. 2010) to $N = 1.7$ (Bouché et al. 2007), which bracket the local value of $N = 1.4$ by Kennicutt (1998). If the true slope for our galaxies is higher than the local relation (e.g., closer to $N = 1.7$), our inferred gas masses would overestimate the true values, which would ease the tension between our dynamical and baryonic masses.

We explore the possibility that the some of the gas masses may be overestimated in Figure 4.7(a) by examining the correlation between gas fraction, $f_{\rm gas}$, and mass offset, $\log_{10}(M_{\rm dyn}/M_{\rm baryon})$ for our entire sample. We find that galaxies with high $f_{\rm gas}$ tend to be found in the unphysical region ($M_{\rm dyn} < M_{\rm baryon}$). If the gas masses of our sample are overestimated, then at fixed dynamical mass, we would expect to find larger baryonic masses for galaxies with higher gas fractions. The observed trend of $f_{\rm gas}$ versus $M_{\rm dyn}/M_{\rm baryon}$ is in agreement with the expected offset resulting from overestimated gas masses.

Another possible explanation for the tension between dynamical and baryonic masses is that the dynamical masses are underestimated for some of our sample. For instance, the ionized gas kinematics may not trace the full potential of these galaxies. The inferred dynamical masses would thus not describe the true masses of the systems. Furthermore, if the lower mass and higher redshift galaxies are not oblate disks, the derived dynamical masses will be inaccurate. van der Wel et al. (2014b) examine the axis ratio distribution of galaxies out to $z \sim 2.5$ and argue that a large fraction of massive galaxies at $z \gtrsim 2$ have spheroidal geometries, while the majority of low-mass galaxies at $z \gtrsim 2$ are elongated. We do note that very few galaxies in our kinematics sample at $z \sim 3$ have axis ratios $b/a > 0.8$, as expected for elongated geometries, but this may only reflect the relatively small sample size at $z \sim 3$.

In Figure 4.7(b), we also show $(V/\sigma_{V,0})_{2.2}$ versus $\log_{10}(M_{\rm dyn}/M_{\rm baryon})$ for the sample of galaxies with detected rotation to examine how kinematic structure impacts the offset between baryonic and dynamical masses. We find that galaxies with low V/σ tend to have $M_{\rm dyn} < M_{\rm baryon}$, while the galaxies with more rotational support tend to have $M_{\rm dyn} > M_{\rm baryon}$. If the galaxies with low measured V/σ tend to have with non-oblate geometry, then these objects could have systematically underestimated dynamical masses. It is also possible that the galaxies with higher fractions of disordered motions may be objects where the ionized gas kinematics does not trace the full galaxy potential.

Further work is needed to fully understand the cause of the disagreement between the dynamical and baryonic masses for galaxies at higher redshifts and lower stellar masses. Direct observations of molecular gas are necessary to properly determine accurate gas and baryonic masses, instead of relying on indirect estimates (e.g., following Kennicutt 1998). Deeper observations of ionized gas kinematics with higher spatial resolution will also better constrain the kinematics of these lower mass and higher redshift galaxies, to directly determine whether these objects exhibit rotation These observations will also help to determine whether or not the ionized gas distributions and kinematics fully trace the galaxies' gravitational potentials.

4.5.2 Other analysis caveats

Here we consider additional caveats to the assumptions made in this work. In particular, we discuss the possible impacts of the accuracy of structural parameters, measurements of galaxy-slit misalignments, inferred galaxy thicknesses, rotation curve and velocity dispersion profiles, the accuracy of the inferred gas masses, and the impact of the assumed virial coefficients on the calculated dynamical masses.

First, many of the caveats discussed in Price et al. (2016) also apply to this analysis. Specifically, the accuracy of the GALFIT structural parameters is not fully accounted for in our kinematic measurements. These structural parameters are integral to both the 1D and 2D kinematic modeling, but no structural parameter errors are included in the kinematic fitting. Our analysis also will have over- and under-estimates in the measured kinematics if the photometric and kinematic major axes are misaligned, resulting in different position angle misalignments ΔPA for the slit and the photometric and kinematic major axes. Additionally, we assume a fixed intrinsic disk thickness of $(b/a)_0 = 0.19$ to derive galaxy inclinations. Variations in the true intrinsic thicknesses (e.g., thicker or thinner) will lead to over- and under-estimates (respectively) of the inclination correction for our galaxies, which could increase the scatter and may also introduce systematic offsets in the derived dynamical properties. Furthermore, we have assumed fixed forms for the kinematic profiles of our galaxies. We adopt an arctan rotation curve model (e.g., following Weiner et al. 2006, Miller et al. 2011). Some work suggests that Freeman exponential disk models (Freeman 1970) are more appropriate for high-redshift star-forming galaxies (e.g., Wisnioski et al. 2015, while other work suggests these galaxies may have falling rotation curves (e.g., van Dokkum et al. 2015, Genzel et al. 2017, Lang et al. 2017). However, for our objects, we only reliably probe the kinematics out to $\sim 2.2 r_s$. Arctan model profiles are similar to the other rotation curve models over this range, so our choice of rotation profile should not impact our results very strongly. We also assume a constant intrinsic velocity dispersion profile. If the true velocity dispersion may decrease with increasing redshift (e.g., as seen in Genzel et al. 2014, Wisnioski et al. 2015), this would result in higher median $(V/\sigma_{V,0})_{R_E}$ measured for the galaxies without resolved rotation (see discussion in Section 5.7 of Price et al. 2016). More careful analysis and higher spatial resolution observations are needed to properly constrain the form of the velocity dispersion profiles.

Second, as discussed in Section 4.5.1, our estimated gas masses may not be accurate. We assume that our sample follows the SFR-gas mass relation by Kennicutt (1998) for star-forming galaxies in the universe, but this assumption may not hold for galaxies at higher redshifts. Beyond the assumption of a SFR-gas mass relation, we also use a mix of SFR indicators as Balmer decrement-corrected Hα SFRs are not available for the entire sample. It is possible that the mix of SFR indicators could lead to systematic differences in the inferred gas masses for our galaxies. Further work directly comparing and calibrating the SFR indicators for star-forming galaxies at $z \sim 1.5 - 3$ is needed to determine how the mix of SFR indicators impacts our results. Moreover, measurements of molecular gas are needed to directly measure gas masses and to determine what biases (if any) the assumed SFR-gas mass relation introduces.

Third, our choice of virial coefficients, $k_{\rm disp}$ and $k_{\rm rot}$, could introduce systematic uncertainties into the calculated dynamical masses. These virial coefficients are derived assuming an idealized matter profile, but this profile may not match the intrinsic matter distribution of our galaxies. For instance, as noted in Price et al. (2016), if we assumed $k_{\rm disp} = \beta(n)$ (following Cappellari et al. 2006) instead of $k_{\rm disp} = 5$ (Pettini et al. 2001), the inferred dynamical masses would be higher, especially for galaxies with very low V/σ (e.g., $(V/\sigma_{V,0})_{R_E} \lesssim 1$). This increase of dynamical masses would reduce the tension between the baryonic and dynamical masses, especially for lower mass and higher redshift galaxies (which tend to have lower V/σ; see Section 4.5.1).

4.6 Conclusions

In this chapter, we use spectra from the MOSDEF survey together with CANDELS *HST*/F160W imaging to study the kinematics and dynamical masses of 714 galaxies at $1.34 \leq z \leq 3.8$, with stellar masses ranging from $M_* \sim 10^9 M_\odot$ to $M_* \sim 10^{11.5} M_\odot$. In addition to kinematics and structural parameters, we derive stellar masses from multi-wavelength photometry, and infer gas masses from either dust-corrected Hα or Hβ SFRs or SED SFRs if Balmer lines are unavailable.

We use the 3D kinematic models developed in Price et al. (2016) to measure the galaxy kinematics from the misaligned galaxy-slit MOSFIRE observations. We use these models to measure both rotation and velocity dispersions for the 116 galaxies where we detect rotation in the 2D spectra. For the remaining 598 galaxies, we measure only velocity dispersion and use the kinematic models to convert the observed velocity dispersions into combined kinematic rms velocities and dynamical masses, assuming a fixed ratio $(V/\sigma_{V,0})_{R_E}$. We then constrain the ensemble average $(V/\sigma_{V,0})_{R_E}$ for the galaxies without detected rotation within bins of redshift, stellar mass, and SSFR by removing any trend between $\log_{10}(M_{\rm dyn}/M_{\rm baryon})$ and axis ratio b/a (e.g., inclination).

Using these mass measurements, we find that the median offset between dynamical and baryonic masses decreases with increasing redshift, and that galaxies with higher stellar masses tend to have higher offsets. The observed offset evolution implies an evolving dark matter fraction, where galaxies at $z \sim 2$ are very strongly baryon dominated, in excellent agreement with the results of Wuyts et al. (2016). However, we find tension between the dynamical and baryonic masses at $z \sim 3$ and for the lower-mass galaxies at $z \sim 2$. For these galaxies, the measured baryonic masses exceed the estimated dynamical masses (e.g., $M_{\rm dyn} < M_{\rm baryon}$), which is unphysical as the dynamical masses should account for all of the enclosed baryonic mass. We discuss possible explanations for the tension between the measured dynamical and baryonic masses, and how future measurements can better constrain the masses of these galaxies.

We also explore the relation between the ratio of rotation to velocity dispersion, V/σ, as a function of stellar mass, SSFR, and redshift. We find that V/σ increases with increasing stellar mass, decreases with increasing SSFR, and decreases towards higher redshifts. These trends may indicate disk settling, where galaxies with lower gas fractions (e.g., lower SSFR or higher stellar mass) will have less turbulent motions. Furthermore, we examine the relation between $V_{2.2}$ and $\sigma_{V,0}$ and stellar mass, SSFR, and redshift for the galaxies with detected rotation in our sample. Our observed values of $\sigma_{V,0}$ versus redshift are in excellent agreement with the findings of Wisnioski et al. (2015) at similar redshifts. The trend of $V_{2.2}$ over time is in general agreement with the results of Kassin et al. (2012) from $z \sim 0.2$ to $z \sim 1.2$. Moreover, the strength of the observed correlation between $V_{2.2}$ and these properties suggests that rotation velocity primarily drives the observed trends of V/σ.

The approach of using multiplexing, seeing-limited NIR spectrographs to constrain the average properties of high-redshift galaxies allows us to study kinematics for one of the largest samples of star-forming galaxies at $z \sim 1.5 - 3$, extending down to much lower stellar masses than other surveys. However, further observations are necessary to reconcile the tension between the dynamical and baryonic masses at high redshifts and lower stellar masses. In particular, direct observations of molecular gas masses are necessary to accurately measure baryonic masses. Furthermore, detailed follow-up observations with adaptive optics-assisted integral-field unit (IFU) spectrographs are crucial to better constrain the dynamical structures of these galaxies.

Chapter 5

Testing the Recovery of Intrinsic Galaxy Sizes and Masses of $z \sim 2$ Massive Galaxies Using Cosmological Simulations

Accurate measurements of galaxy masses and sizes are key to tracing galaxy evolution over time. Cosmological zoom-in simulations provide an ideal test bed for assessing the recovery of galaxy properties from observations. Here, we utilize galaxies with $M_* \sim 10^{10} - 10^{11.5} M_\odot$ at $z \sim 1.7 - 2$ from the MassiveFIRE cosmological simulation suite, part of the Feedback in Realistic Environments (FIRE) project. Using mock multi-band images, we compare intrinsic galaxy masses and sizes to observational estimates. We find that observations accurately recover stellar masses, with a slight average underestimate of ~ 0.06 dex and a ~ 0.15 dex scatter. Recovered half-light radii agree well with intrinsic half-mass radii when averaged over all viewing angles, with a systematic offset of ~ 0.1 dex (with the half-light radii being larger) and a scatter of ~ 0.2 dex. When using color gradients to account for mass-to-light variations, recovered half-mass radii also exceed the intrinsic half-mass radii by ~ 0.1 dex. However, if not properly accounted for, aperture effects can bias size estimates by ~ 0.1 dex. No differences are found between the mass and size offsets for star-forming and quiescent galaxies. Variations in viewing angle are responsible for $\sim 25\%$ of the scatter in the recovered masses and sizes. Our results thus suggest that the intrinsic scatter in the mass-size relation may have previously been overestimated by $\sim 25\%$. Moreover, orientation-driven scatter causes the number density of very massive galaxies to be overestimated by ~ 0.5 dex at $M_* \sim 10^{11.5} M_\odot$.[1]

---

[1] This chapter has been previously published as Price *et al.*, 2017, ApJL, 844, L6, and is reproduced with the permission of all coauthors and the copyright holder. Copyright 2017, The American Astronomical Society.

5.1 Introduction

Tracing the evolution of galaxy stellar masses and sizes across multiple cosmological epochs provides direct constraints on the growth of galaxies. Recent photometric studies have probed stellar masses for large galaxy samples out to $z \sim 3$ (e.g., Tomczak et al. 2014), and for small samples out to $z \sim 9 - 11$ (e.g., Oesch et al. 2013). Deep, high-resolution *Hubble Space Telescope* (*HST*) imaging has also provided measurements of rest-frame optical sizes for large samples of galaxies out to $z \sim 2.5$ (e.g., van der Wel et al. 2014a, Peth et al. 2016). Together, these measurements make it possible to trace the evolution of the mass-size relation (Shen et al. 2003) out to $z \sim 2.5$ (van der Wel et al. 2014a).

Despite their central role in galaxy evolution studies, it is uncertain how well measured masses and sizes reflect the intrinsic properties of galaxies. Recovered galaxy properties may be impacted by complex dust-to-star geometry and projection effects. Furthermore, galaxy sizes are often measured from the stellar light distribution, even though light does not directly trace stellar mass in most galaxies. Half-light radii are larger than half-mass radii for many galaxies (Wuyts et al. 2012). Color gradients can be used to estimate half-mass radii (e.g., Szomoru et al. 2013), but it is unclear how accurately they reflect the intrinsic galaxy sizes.

Evaluating parameter recovery requires a galaxy sample with known intrinsic properties. Mock observations of simulated galaxies are ideally suited to this task, as cosmological simulations now probe the complex star, gas, and dust geometry in the interstellar medium with high (sub-kiloparsec scale) resolution (e.g., Hopkins et al. 2014, Schaye et al. 2014, Vogelsberger et al. 2014, Feldmann et al. 2016). Recent studies have investigated the recovery of stellar masses (e.g., Wuyts et al. 2009, Hayward & Smith 2015, Torrey et al. 2015) and sizes (e.g., Wuyts et al. 2010, Snyder et al. 2015a,b, Taghizadeh-Popp et al. 2015, Bottrell et al. 2017) using mock observations. However, these studies have not simultaneously included dust, multiple viewing angles, high spatial resolution, observational point-spread functions (PSFs), and noise to test parameter recovery in high-redshift galaxies.

In this Letter, we present a study of the recovery of galaxy masses and sizes using mock observations over multiple projections of $z \sim 2$ galaxies from MassiveFIRE (Feldmann et al. 2016), following the same procedures used for observations. Throughout this work, we adopt a ΛCDM cosmology with $\Omega_m = 0.3$, $\Omega_\Lambda = 0.7$, and $H_0 = 70\,\mathrm{km\,s^{-1}\,Mpc^{-1}}$.

5.2 Mock observations

We use simulations from the FIRE project (Hopkins et al. 2014) to constrain how well intrinsic galaxy properties can be recovered from observations. Specifically, we analyze the MassiveFIRE suite of cosmological zoom-in simulations (Feldmann et al. 2016, 2017), focusing on a sample of 50 massive galaxy snapshots. We consider all massive ($M_* \sim 10^{10} - 10^{11.5} M_\odot$) central and satellite galaxies from the high-resolution runs, using snapshots at both $z \sim 1.7$ and $z \sim 2$ of 21 galaxies (Series A and B in Feldmann et al. 2017) and at $z \sim 2$ of 8 galaxies (Series C in Feldmann et al. 2017, including 4 unpublished galaxies). The sample includes large star-forming disks, irregular star-forming galaxies, and quiescent galaxies.

We construct mock multi-filter images of the galaxies using the method described below. To understand how viewing angle affects measurements, we generate images of each galaxy along 25 different projections. First, we generate noise-free multi-filter rest-frame images for each projection of each simulated galaxy. Every stellar particle is assigned the spectral energy distribution (SED) of a simple stellar population based on its mass, age, and metallicity using the Bruzual & Charlot (2003) stellar population synthesis (SPS) models assuming a Chabrier (2003) initial mass function (IMF). Dust attenuation is incorporated by tracing the amount of dust along the line of sight, assuming a Calzetti et al. (2000) curve. Dust content is inferred from the gas particle masses and metallicities, assuming a fixed dust-to-metal ratio. Scattering is indirectly applied by using an empirical dust attenuation curve. Dust emission is omitted as we do not sample the SEDs at long wavelengths. We then sample the dust-attenuated SED in a set of rest-frame filters to obtain mock rest-frame images.

The images are artificially redshifted to the snapshot redshift ($z = 2.02$ and 1.67) by applying cosmological dimming, adjusting the angular size, and resampling to match the typical *HST*/WFC3 drizzled pixel scale ($0.''06$). The images are convolved with a typical WFC3 PSF (measured from a stack of stars from CANDELS *HST*/F160W imaging; Skelton et al. 2014).[2] For simplicity, we apply the same PSF to all bands. Mismatches between the PSFs of different photometric bands can introduce uncertainties in the relative flux calibration. Investigating this uncertainty is beyond the scope of this Letter. However, we note that other studies have investigated the accuracy of flux recovery from low-resolution photometry (e.g., Labbé et al. 2006, Laidler et al. 2007, Wuyts et al. 2008). Finally, we add noise in each band using random CANDELS *HST*/F160W postage stamps, which contain no detected objects in the 3D-HST catalogs (Skelton et al. 2014) and have typical noise levels. Mock images of each galaxy are constructed for 16 rest-frame filters: ST-UV14, ST-UV17, ST-UV22, ST-UV27 (from Bruzual & Charlot 2003), SDSS ugriz, U, B, V, R, J, H, and K. Figure 5.1 shows an example face-on and edge-on view of one galaxy, demonstrating the underlying mass distribution, the rest-frame UVJ colors, the PSF-convolved rest-frame V-band image, and the final mock image including noise.

We detect objects and extract photometry from the mock images following the procedure by Skelton et al. (2014). For every projection of each simulation, we use Source Extractor (Bertin & Arnouts 1996) in dual-image mode, adopting the parameters used by Skelton et al. and using the rest-frame V-band for detection (roughly covered by F160W at $z \sim 2$). The multi-band aperture and total photometry and errors of the objects are determined following Skelton et al. In some projections, dust lanes or bright star-forming clumps lead to multiple detected objects for a single galaxy. To account for this issue, we classify all objects with segmentation maps falling within 2.5 kpc of the galaxy center as part of the galaxy.

---

[2] Observationally, images are first convolved with the PSF and subsequently sampled within pixels. We find no difference in the mock images when inverting the calculation order.

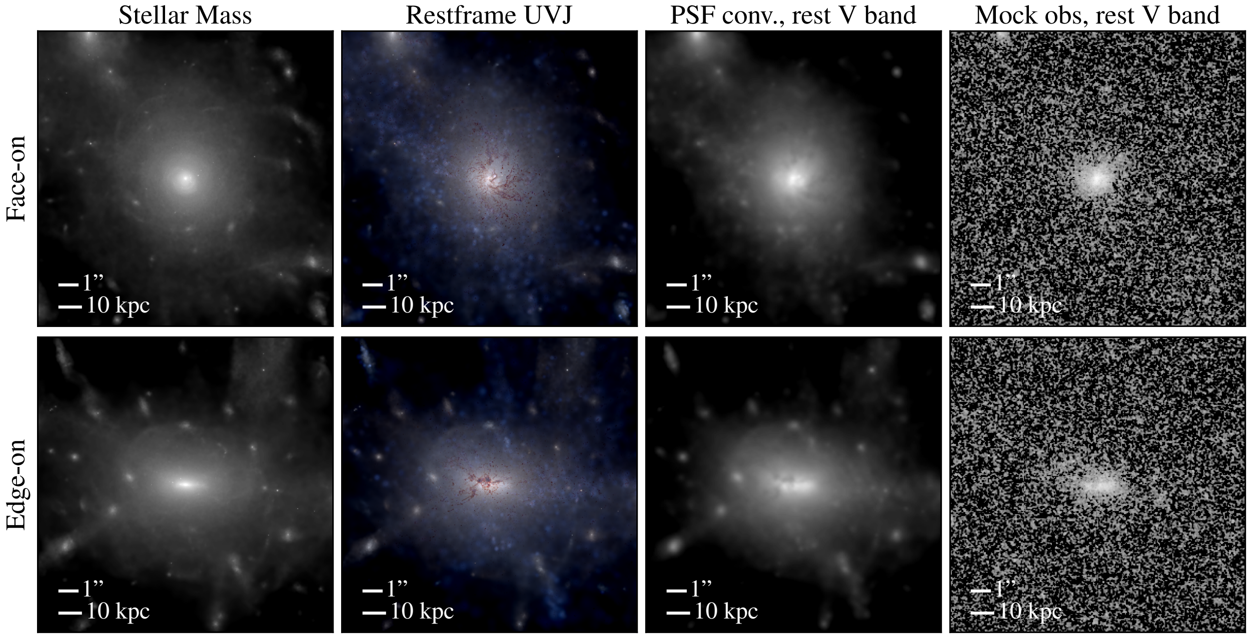

Figure 5.1: Example simulated star-forming disk galaxy ($M_* \sim 10^{10.9} M_\odot$, $r_{1/2,*} \sim 4\,\mathrm{kpc}$) viewed face-on (top) and edge-on (bottom). The first column shows the stellar mass maps. Rest-frame UVJ images (second column) highlight the distribution of dust and stars. We also show the PSF-convolved simulation image (third column) and the resulting mock observation (fourth column) for the rest-frame V band. Each image is 144 kpc on each side.

5.3 Recovering sizes and masses

We measure masses and sizes from the mock images following established observational techniques. Stellar masses M_* are determined by fitting the Bruzual & Charlot (2003) SPS models to all bands of the mock photometry of every object using FAST (Kriek et al. 2009b). We assume a Chabrier (2003) IMF, a Calzetti et al. (2000) dust attenuation curve, a delayed exponentially declining star formation history, and solar metallicity.

Structural parameters of the simulated galaxies, including the effective radius R_E, Sérsic index n (Sérsic 1968), and axis ratio b/a, are measured using GALFIT (Peng et al. 2010) on the rest-frame V-band images. We use the GALFIT parameter limits of van der Wel et al. (2012) and flag and exclude from analysis projections for which (a) the GALFIT and V-band total magnitudes differ by > 0.5 mag and (b) fit parameter(s) reached the enforced limit(s). We adopt the semi-major axis R_E as the half-light radius. We also estimate half-mass radii following Szomoru et al. (2013). This method uses rest-frame u- and g-band GALFIT profiles and residuals together with an empirical mass-to-light ratio versus color relation to derive a stellar mass profile out to 100 kpc.

To determine the fiducial intrinsic masses and sizes of the simulated galaxies, we measure the stellar masses and half-mass radii directly from the mass maps of each galaxy. We define the intrinsic stellar mass for each projection of each galaxy as the mass[3] enclosed within the Source Extractor Kron ellipse (Kron 1980), masking neighboring detections. Thus, the recovered and intrinsic masses are defined for the same aperture (Skelton et al. 2014). The 2D intrinsic major-axis half-mass radii are defined from growth curves on the projected mass maps, using self-similar ellipses out to the elliptical Kron aperture for each projection as well. We take the median over all projections to obtain the fiducial intrinsic stellar mass and half-mass radius for each galaxy. These intrinsic masses are similar to those derived by Feldmann et al. (2017), which are measured within a sphere of radius $0.1r_{\text{halo}}$, but the adopted definition allows comparable aperture corrections to be measured from the noise-free light images and recovered mass profiles (see Section 5.4).

The recovered sizes and masses for four simulated galaxies over 25 random projections are shown in Figure 5.2. The top panel demonstrates that the measured half-light and half-mass radii are generally larger than the intrinsic radii, while the bottom panel shows that the recovered stellar masses are similar to the intrinsic masses. We observe scatter in both the recovered sizes and masses between different viewing angles. There is a slight trend of increasing radii with decreasing axis ratio b/a for some galaxies, which could be caused by inclination-dependent color gradients. Investigating this trend is beyond the scope of this Letter.

---

[3] Bruzual & Charlot (2003) model masses are used to avoid discrepancies between the recovered and intrinsic masses due to variations in mass-loss prescriptions between the SPS models and the FIRE feedback model (Hopkins et al. 2014), as testing mass-loss variations is beyond the scope of this Letter. These masses are calculated as the current Bruzual & Charlot (2003) model stellar mass given every star particle's age, initial mass, and metallicity.

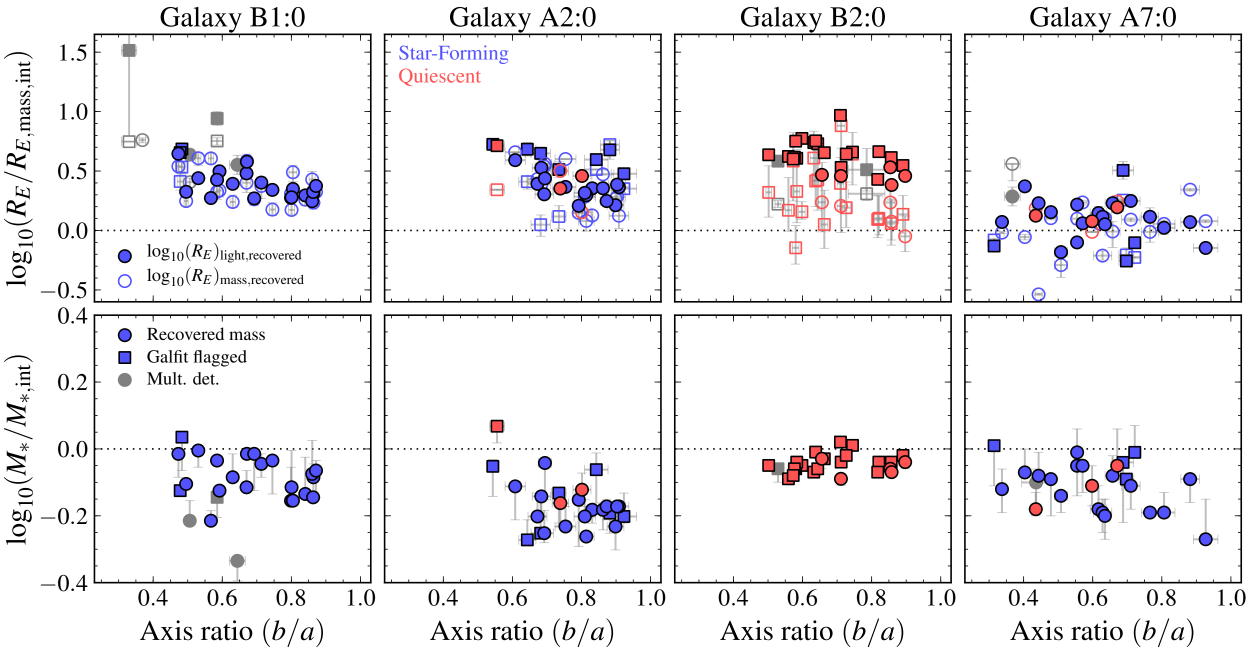

Figure 5.2: Comparison of recovered and intrinsic sizes and masses over 25 random viewing angles for four simulated MassiveFIRE galaxy snapshots with $M_* \sim 10^{10} - 10^{11} M_\odot$ at $z \sim 2$ as a function of GALFIT axis ratio. In the top row, we show the ratio of the GALFIT half-light radii from the rest-frame V band (filled symbols) and half-mass radii following Szomoru et al. (2013) (open symbols) to the intrinsic half-mass radii. In the bottom row, we show the ratio of the recovered and intrinsic masses. Star-forming and quiescent projections (see Section 5.4) are colored blue and red, respectively. GALFIT-flagged detections are marked with squares. Projections with multiple detections are colored gray, and only the largest radius or mass component is shown. Most orientations for Galaxy B2:0 are flagged due to the Sérsic index reaching the upper limit $(n = 8)$.

5.4 Size and mass comparisons

To understand how well observations recover the sizes and masses of galaxies, we examine the median offset between the recovered and intrinsic sizes and masses for the sample of 50 MassiveFIRE galaxy snapshots, each with 25 projections. Furthermore, we examine whether these offsets differ for star-forming and quiescent galaxies. We use the empirical UVJ criterion by Muzzin et al. (2013b) at $z > 1$ to classify each projection of all galaxies as star-forming or quiescent.

In Figure 5.3, we show the median recovered half-light and half-mass radii versus intrinsic radii, excluding all GALFIT-flagged detections. We also show all projections and their 1σ scatter. We use all unflagged orientations of all galaxies to determine the median offset between the recovered and intrinsic sizes. The offset uncertainties are estimated by bootstrapping the error on the median.

We find that GALFIT radii overestimate the intrinsic radii (Figure 5.3a), with median offsets of $\Delta \log_{10} R_E = 0.21$ and 0.27 dex for the star-forming and quiescent samples, respectively. The scatter in $\log_{10} R_{E,\mathrm{light,recovered}}$ over all projections for star-forming and quiescent galaxies is $\sigma_{\mathrm{RMS}} = 0.21$ dex and 0.19 dex, respectively. The scatter of the median sizes of star-forming and quiescent galaxies ($\langle \log_{10} R_{E,\mathrm{light,recovered}} \rangle$; weighted by the fraction of unflagged projections) is $\sigma_{\mathrm{med}} = 0.16$ and 0.15 dex, respectively. Thus, orientation increases the total scatter by $\sigma_{\mathrm{orient}} \sim 0.14$ and 0.11 dex for star-forming and quiescent galaxies, respectively (accounting for measurement errors).

The recovered half-mass radii are also offset from the intrinsic radii (Figure 5.3b), by $\Delta \log_{10} R_E = 0.20$ and 0.24 dex for the star-forming and quiescent galaxies, respectively. The scatter of $\log_{10} R_{E,\mathrm{mass,recovered}}$ over all projections is slightly larger ($\sigma_{\mathrm{RMS}} = 0.26$ and 0.23 dex), with a similar fraction caused by orientation (0.18 and 0.15 dex). In comparison to Szomoru et al. (2013), our sample has relatively flat u-g profiles, resulting in similar half-light and half-mass radii.

However, these size comparisons do not account for aperture effects. The intrinsic half-mass radii are defined within finite elliptical apertures (Section 5.3), whereas GALFIT Sérsic profiles are parametric and integrated out to infinity. To quantify the aperture effects on the measured light-mass size offsets, we compare GALFIT effective radii to median aperture half-light radii and the recovered half-mass radii to median recovered aperture half-mass radii. Aperture half-light radii are measured directly from the noise-free V-band images, analogous to the half-mass radii measurements. Similarly, recovered aperture half-mass radii are derived from the measured mass profiles. In all cases, aperture effects account for ~ 0.1 dex of the size offsets.

We find that aperture-corrected half-light radii are in fairly good agreement with the intrinsic half-mass radii (Figure 5.3c), with larger half-light radii by 0.11 dex and 0.13 dex for star-forming and quiescent galaxies, respectively, in agreement with previous studies (Wuyts et al. 2010, Wuyts et al. 2012, Szomoru et al. 2013). The aperture-corrected half-mass and intrinsic half-mass radii have similar systematic offsets (0.10 dex and 0.06 dex; Figure 5.3d).

The difference between the aperture-corrected half-light and half-mass radii (Figure 5.3c)

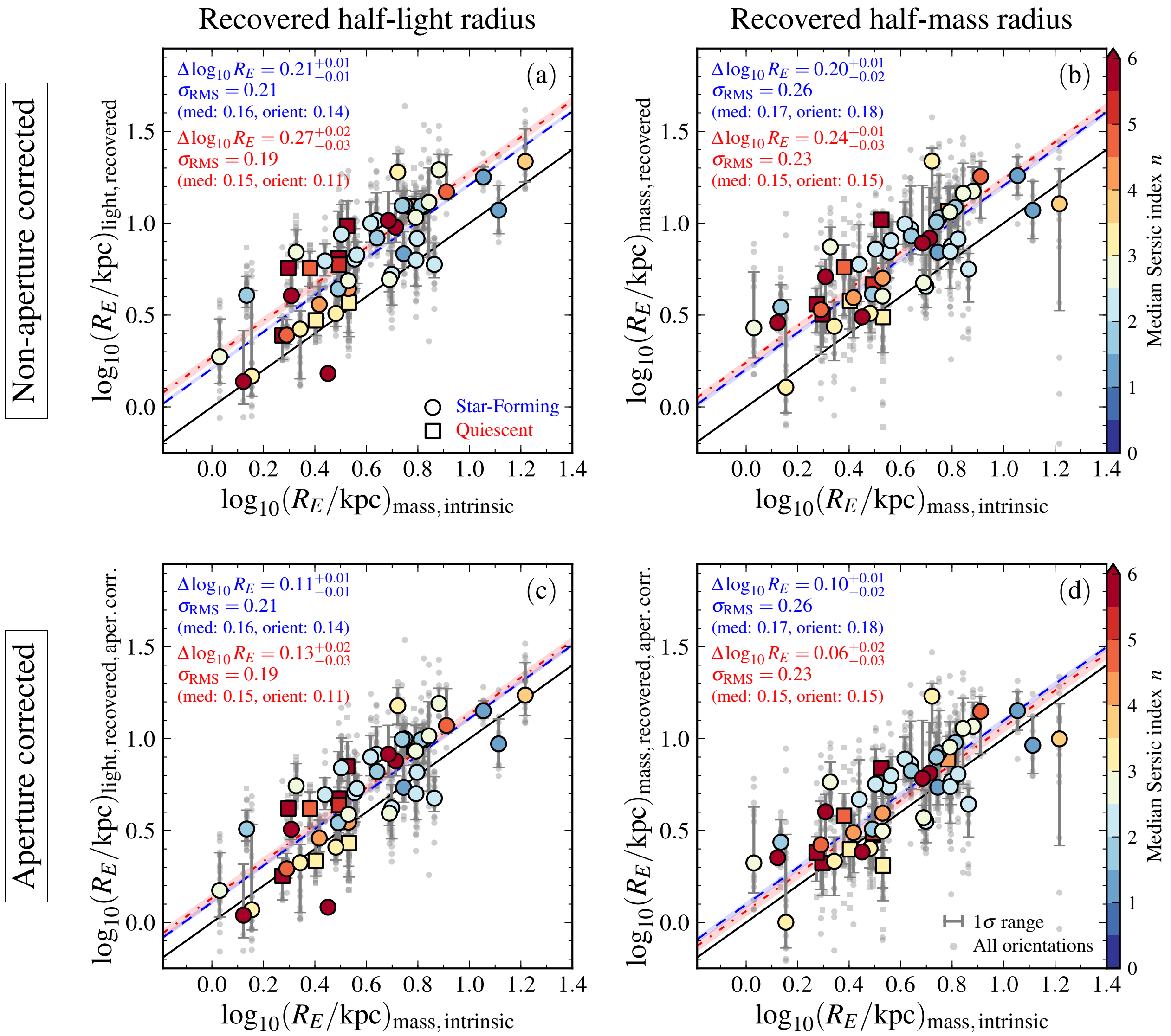

Figure 5.3: Comparison between intrinsic half-mass radii and the median recovered (a) half-light and (b) half-mass radii, colored by the median (across all orientations) Sérsic index, not accounting for aperture differences. We also compare the intrinsic half-mass radii with aperture-corrected recovered (c) half-light and (d) half-mass radii. Star-forming and quiescent galaxies are shown with circles and squares, respectively. Median U-V and V-J colors are used to categorize each galaxy. GALFIT-flagged detections are excluded from the median and scatter calculations. The black line shows the one-to-one relationship, and the star-forming and quiescent median size offsets (over all projections) are shown with dashed blue and dashed-dotted red lines, respectively. The shaded regions show the 1σ offset uncertainties. The small gray circles (squares) show the radii of all non-flagged star-forming (quiescent) orientations, and the bars denote the 1σ range of radii for each galaxy.

appears to be caused by the presence of dust-obscured high central mass concentrations (within $\lesssim 1\,\mathrm{kpc}$) in many of the galaxies. We would expect that observed color gradients would enable us to recover the central mass component. However, the high central dust content results in saturated color profiles, so this mass component is not recovered using the method of Szomoru et al. (2013) (Figure 5.3d). Another potential source of bias between the intrinsic and recovered radii is the use of smooth, single-Sérsic models, as these galaxies have complex structures. Nonetheless, we find that single-Sérsic models introduce little to no bias to the recovered sizes, in agreement with other studies (e.g., Davari et al. 2016, 2014).

Recovered and intrinsic stellar masses are compared in Figure 5.4, using the same the median calculation method and set of non-flagged detections as for the size comparison. We find that the recovered masses are generally in good agreement with the intrinsic masses, with an offset of only -0.06 dex for both star-forming and quiescent galaxies, and have a scatter of $\sigma_{\mathrm{RMS}} = 0.14$ and 0.11 dex over all projections, with 0.10 and 0.05 dex due to orientation effects. Uncertainties in stellar masses can arise from both measured photometry and from mass-to-light ratios derived from SED fitting. We find that photometric uncertainties do not strongly affect the accuracy of the recovered stellar masses. The Source Extractor-derived fluxes recover the intrinsic aperture fluxes very well, with a median fractional flux difference of -0.3% and an rms scatter of 7.5%. The small offset and scatter show that stellar masses are recovered well on average over a wide mass range ($\sim 10^{9.75} - 10^{11.25} M_{\odot}$) and dust attenuation range ($A_{\mathrm{V}} \sim 0 - 2$), but do vary with galaxy viewing direction. Our result of no large systematic mass offset is in good agreement with the findings of other tests of stellar mass recovery using mock observations of simulations (e.g., Wuyts et al. 2009, Torrey et al. 2015).

5.5 Discussion and implications

Using mock multi-band images of MassiveFIRE simulated galaxies, we show that recovered half-light radii are in good agreement with the intrinsic half-mass radii, with an offset of $\log_{10} R_{E,\mathrm{light,recovered}} - \log_{10} R_{E,\mathrm{mass,intrinsic}} \sim 0.1$ dex (correcting for aperture effects). When we recover half-mass radii by accounting for color gradients due to dust, metallicity, and age, the radii have a similar offset of $\sim$0.1 dex. Stellar masses are also recovered well on average, with an offset of $\log_{10} M_{*,\mathrm{recovered}} - \log_{10} M_{*,\mathrm{intrinsic}} \sim -0.06$ dex.

By considering the multiple viewing angles of every galaxy, we show that a sizable fraction of the mass and radii scatter is caused by orientation effects. These projection effects may result from the random distribution of bright clumps within a galaxy, a non-uniform or patchy dust distribution, or gradients in metallicity and stellar population age (Kelvin et al. 2012).

We find no systematic differences between the recovery of masses or radii for massive star-forming and quiescent galaxies. Thus, observed differences between star-forming and quiescent galaxy sizes at $z \sim 2$ likely indicate true differences in their stellar mass distributions.

These results have important implications for measuring galaxy structural growth through mass-size relations. First, the mass-size relation zero-point will be systematically overestimated by $\sim$0.1 dex if half-light radii are used rather than half-mass radii. Second, the

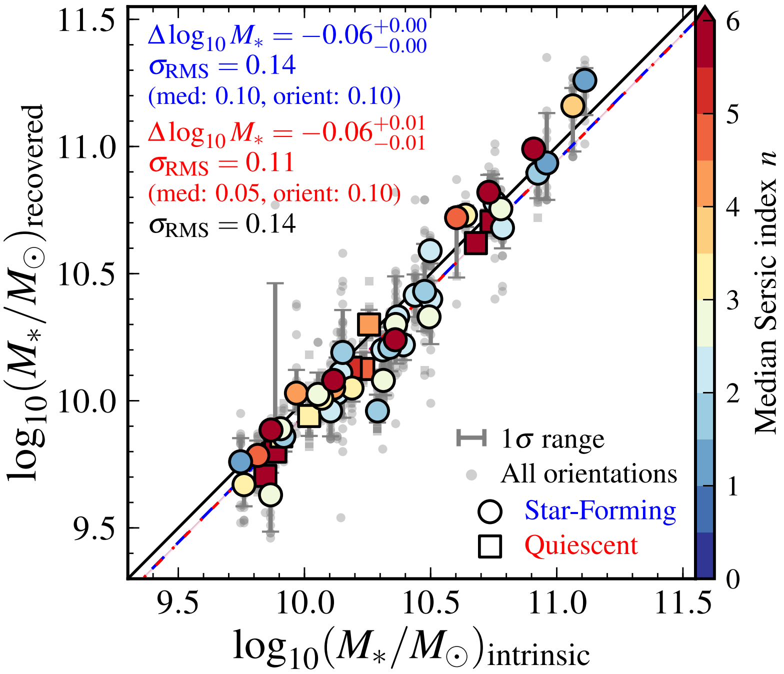

Figure 5.4: Comparison between intrinsic and median recovered stellar masses, colored by the median Sérsic index. The symbol definitions are the same as in Figure 5.3, and again GALFIT-flagged detections are excluded. The median offset between the recovered and intrinsic masses is small for both star-forming and quiescent galaxies.

intrinsic scatter of the light-based mass-size relation may be overestimated due to random variations in viewing angle, implying the intrinsic mass-size relation could be tighter than previously thought. To quantify the effect of orientation on the mass-size relation scatter, we compare the combined orientation-corrected mass and radius scatters with the combined total scatter. We use the scatter of the medians, $\sigma_{\rm med}$, as the "intrinsic" scatter (as the mass and radii offsets are uncorrelated), and take the error-corrected RMS scatter as the total scatter, $\sigma_{\rm tot} = \sqrt{\sigma^2_{\rm RMS} - \sigma^2_{\rm err}}$. The orientation-corrected mass-size relation scatter is $\sim$75% of the error-corrected total scatter ($\sigma_{\rm med}/\sigma_{\rm tot}$) for both star-forming and quiescent galaxies.

We illustrate the differences between the observed mass-size relations at $z \sim 1.75$ by van der Wel et al. (2014a) and the inferred half-mass radii mass-size relations corrected for orientation effects for both star-forming and quiescent galaxies in Figure 5.5a. This figure demonstrates both the zero-point offset due to using intrinsic half-mass versus recovered half-light radii (corrected for aperture effects; Figure 5.3) and stellar mass recovery (Figure 5.4), and the reduced intrinsic scatter once orientation effects are corrected.

Even though masses are recovered well on average, the scatter in stellar masses has important implications for studying galaxy populations. For example, scatter impacts the measurement of stellar-mass functions (SMFs). In Figure 5.5b, we demonstrate how orientation scatter causes an overestimate of the number density of high-mass galaxies. We draw a galaxy population directly from an input SMF, perturb the masses by the orientation scatter, and then measure the SMF. The input parameters are chosen so the recovered SMF roughly approximates the best-fit $1.5 < z < 2$ SMF by Tomczak et al. (2014). The true SMF falls off faster than the observed SMF at high masses due to the combination of projection-driven scatter and the steepness of the SMF at the high-mass end, by up to $\sim$0.5 dex at $M_* \sim 10^{11.5} M_\odot$. Hence, many massive galaxies may have such large observed masses as a result of orientation effects. Orientation-driven scatter will also impact other measurements, including the scatter of the star-forming main sequence (e.g., Whitaker et al. 2014, Shivaei et al. 2015) and inferred dynamical masses (e.g., Price et al. 2016, Wuyts et al. 2016).

Furthermore, our results demonstrate the difficulty of comparing the sizes of observed and simulated galaxies (see Figure 5.3a). When directly comparing 3D-aperture half-mass radii derived from the simulations and GALFIT effective radii, we find an offset of $\sim$0.2 dex for both star-forming and quiescent galaxies. To make a fair comparison between observations and simulations, simulated galaxy half-light radii should be measured from mock images using the same methodology applied to observations.

We note the following caveats to this analysis. First, the selected galaxies may not be fully representative of the properties of massive galaxies at $z \sim 1.7 - 2$. Thus, the measured offsets may not be applicable to all galaxies at these redshifts. Moreover, the relative corrections for star-forming and quiescent galaxies may depend on the realism of the specific simulation models. Finally, we do not account for systematic modeling errors. We have only considered one set of stellar population models and one dust law, applied with a simple line-of-sight attenuation. Modeling choices could affect the recovered offsets and the scatter through systematic color gradient trends and variation in dust attenuation over different viewing

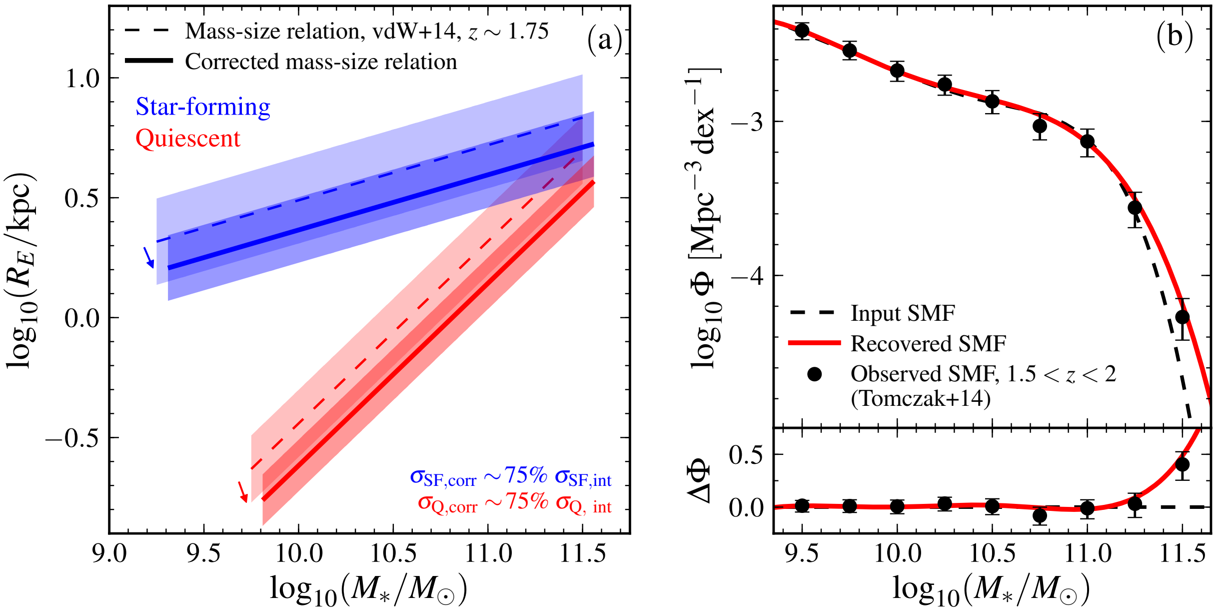

Figure 5.5: Possible systematic effects on observed galaxy properties at $z \sim 1.7-2$. (a) Shift and scatter reduction of observed mass-size relations. Dashed lines show the star-forming (blue) and quiescent (red) mass-size relations by van der Wel et al. (2014a) at $z \sim 1.75$, with light shaded regions showing the observed intrinsic scatter $\sigma\log_{10}(R_{\mathrm{eff}})$. Corrected mass-size relations (based on half-mass radii) are shown with solid lines, demonstrating the inferred zero-point offset (Figures 5.3 and 5.4). The darker shaded regions represent the intrinsic scatter corrected for orientation effects. (b) Effect of orientation-based scatter on stellar-mass functions (SMFs). The recovered SMF (red line), similar to the SMF at $1.5 < z < 2$ observed by Tomczak et al. (2014) (black circles), deviates from the true SMF (black dashed line) at high masses when mass scatter is applied to a sample drawn from the true SMF.

angles. Future work is needed to fully understand the impact of dust, non-smooth galaxy morphologies, and specifics of the dust radiative transfer modeling when measuring simulated galaxy properties.

Acknowledgements

I acknowledge valuable discussions with M. Franx, D. Szomoru, K. Whitaker, C. Hayward, C.-P. Ma, and K. Suess. This work made use of `astropy` (Robitaille et al. 2013) and `pysynphot` (Lim et al. 2015). I acknowledge support from a National Science Foundation Graduate Research Fellowship under grant DGE 1106400.

Chapter 6

Conclusion

In this dissertation, I have used observations and simulations to investigate the dust content, kinematics, masses, and structures of galaxies near the peak of cosmic star formation. Below I summarize the primary results of this dissertation, and discuss the outstanding questions and future prospects for studying distant galaxies.

First, I used grism spectra from the 3D-HST survey to investigate dust properties in star-forming galaxies at $z \sim 1.5$ (Chapter 2). Stacked spectra reveal that there is a lower average ratio of nebular to continuum attenuation in these galaxies compared to local starbursts that have comparable SFRs (Calzetti et al. 2000). This attenuation difference supports a two-component dust model (i.e., Wild et al. 2011). These nebular attenuation measurements also allowed us to determine Balmer-decrement corrected Hα SFRs, which provide constraints to derive more accurate SFRs from spectral energy distribution (SED) fitting.

I then used spectra from the first two semesters of the MOSDEF survey together with *HST* imaging from the CANDELS survey to investigate the kinematic structures and masses of $z \sim 2$ star-forming galaxies (Chapter 3). The dynamical and baryonic (stellar and gas) masses of these galaxies are in good agreement, but there is evidence for lower dark matter fractions within the effective radius than for local galaxies. I also found that average kinematic properties can be statistically recovered even for spatially unresolved galaxies. These measurements support a Chabrier (2003) over a Salpeter (1955) IMF for $z \sim 2$ star-forming galaxies. Additionally, the observed trend of increasing V/σ with decreasing specific SFR (SSFR) may reflect disk settling.

This kinematic study was then extended using the full MOSDEF sample (Chapter 4). I found evidence for evolution of the dark matter fraction within galaxies' effective radii between $z \sim 1.5 - 3$, with lower dark matter fractions at earlier times. These observations provide additional support for increased V/σ at lower redshifts, in agreement with the evolving average gas fractions inferred from SSFRs. However, there is tension between the dynamical and baryonic masses at $z \gtrsim 2$, as the median offset between these masses lies in the nonphysical regime where $M_{\mathrm{dyn}} < M_{\mathrm{baryon}}$. This suggests that the current methods of estimating dynamical or gas masses may not work at these redshifts, or that these galaxies may not be virialized.

Finally, I used mock observations of high-resolution simulated galaxies from the Massive-FIRE suite to investigate how well stellar masses and sizes are recovered in star-forming and quiescent galaxies at $z \sim 2$ (Chapter 5). On average, both measured stellar masses and half-light radii match the intrinsic galaxy masses and half-mass radii fairly well, with only a slight offset between the half-light and half-mass radii. However, both the recovered masses and radii exhibit large scatter due to variations along different projection angles. This scatter suggests that previous measurements of the intrinsic scatter in the galaxy mass-size relation may be overestimated. Furthermore, this orientation scatter may lead to overestimates of the number density of very massive galaxies.

This dissertation has helped to address a number of the open questions regarding dust, structure, and masses of star-forming galaxies at cosmic noon. Nonetheless, many uncertainties remain regarding the nature of distant galaxies, and the core question of how galaxies evolve is far from settled.

Future work will help further characterize star-forming (and quiescent) galaxies at $z \sim 1-3$, and will help us to better understand how these galaxies evolve into modern galaxies. For instance, observations of lower mass galaxies are relatively limited at this epoch, due to their faintness and small sizes. Deeper observations, or observations with more sensitive instruments or larger telescopes are needed to comprehensively study these lower-mass galaxies. Additionally, many of these ground-based spectroscopic observations are seeing-limited, which makes it impossible to spatially resolve a large fraction of these small, distant galaxies. This resolution issue can be circumvented with space-based or extensive adaptive optics (AO)-assisted observations. Many of these current spectroscopic studies also only probe the ionized gas, and not the properties of the galaxies' stellar populations. Again, more sensitive instruments will pave the way for joint studies of the stars and gas in early galaxies. These present surveys are also relatively limited in area, so surveys of much larger cosmological volumes will certainly reveal new rare and surprising objects.

The next generation of instruments and telescopes — including the *James Webb Space Telescope* (*JWST*), future 30m class telescopes, and improved spectrographs and AO systems — will enable us to move past these limitations. The coming years will certainly provide us with new insights into galaxies at cosmic noon and to even earlier stages of galaxy evolution.

Bibliography

Abazajian, K. N., Adelman-McCarthy, J. K., Agüeros, M. A., et al. 2009, ApJS, 182, 543

Alexander, D. M., Bauer, F. E., Brandt, W. N., et al. 2003, AJ, 126, 539

Angulo, R. E., Springel, V., White, S. D. M., et al. 2012, MNRAS, 426, 2046

Atek, H., Malkan, M., McCarthy, P., et al. 2010, ApJ, 723, 104

Azadi, M., Coil, A. L., Aird, J., et al. 2017, ApJ, 835, 27

Bacon, R., Copin, Y., Monnet, G., et al. 2001, MNRAS, 326, 23

Baldry, I. K., Balogh, M. L., Bower, R. G., et al. 2006, MNRAS, 373, 469

Baldry, I. K., Glazebrook, K., Brinkmann, J., et al. 2004, ApJ, 681

Baldwin, J. A., Phillips, M. M., & Terlevich, R. 1981, PASP, 93, 5

Barro, G., Faber, S. M., Pérez-González, P. G., et al. 2013, ApJ, 765, 104

Bauer, F. E., Alexander, D. M., Brandt, W. N., et al. 2002, AJ, 124, 2351

Bell, E. F., & de Jong, R. S. 2001, ApJ, 550, 212

Belli, S., Newman, A. B., & Ellis, R. S. 2014, ApJ, 783, 117

Bertin, E., & Arnouts, S. 1996, A&A, 117, 393

Bezanson, R., Franx, M., & van Dokkum, P. G. 2015, ApJ, 799, 148

Bezanson, R., van Dokkum, P., van de Sande, J., Franx, M., & Kriek, M. 2013, ApJ, 764, L8

Blanton, M., Eisenstein, D., Hogg, D., Schlegel, D., & Brinkmann, J. 2005, ApJ, 629, 143

Blanton, M. R., & Moustakas, J. 2009, ARA&A, 47, 159

Blanton, M. R., Hogg, D. W., Bahcall, N. a., et al. 2003, ApJ, 594, 186

Blumenthal, G. R., Faber, S. M., Primack, J. R., & Rees, M. J. 1984, Nature, 311, 517

Bottrell, C., Torrey, P., Simard, L., & Ellison, S. L. 2017, MNRAS, 467, 1033

Bouché, N., Cresci, G., Davies, R., et al. 2007, ApJ, 671, 303

Bournaud, F., Chapon, D., Teyssier, R., et al. 2011, ApJ, 730, 4

Bouwens, R. J., Illingworth, G. D., Oesch, P., et al. 2012, ApJ, 754, 83

Boylan-Kolchin, M., Springel, V., White, S. D. M., Jenkins, A., & Lemson, G. 2009, MNRAS, 398, 1150

Brammer, G. B., van Dokkum, P. G., & Coppi, P. 2008, ApJ, 686, 1503

Brammer, G. B., van Dokkum, P. G., Franx, M., et al. 2012, ApJS, 200, 13

Brewer, B. J., Dutton, A. A., Treu, T., et al. 2012, MNRAS, 422, 3574

Brinchmann, J., Charlot, S., White, S. D. M., et al. 2004, MNRAS, 351, 1151

Bruzual, G., & Charlot, S. 2003, MNRAS, 344, 1000

Bryant, J. J., Owers, M. S., Robotham, A. S. G., et al. 2015, MNRAS, 447, 2857

Buat, V., Noll, S., Burgarella, D., et al. 2012, A&A, 545, A141
Buitrago, F., Conselice, C. J., Epinat, B., et al. 2014, MNRAS, 439, 1494
Bundy, K., Bershady, M. A., Law, D. R., et al. 2015, ApJ, 798, 7
Cacciato, M., Dekel, A., & Genel, S. 2012, MNRAS, 421, 818
Calzetti, D., Armus, L., Bohlin, R. C., et al. 2000, ApJ, 533, 682
Calzetti, D., Kinney, A. L., & Storchi-Bergmann, T. 1994, ApJ, 429, 582
Cappellari, M. 2008, MNRAS, 390, 71
Cappellari, M., Bacon, R., Bureau, M., et al. 2006, MNRAS, 366, 1126
Cappellari, M., Emsellem, E., Krajnović, D., et al. 2011, MNRAS, 413, 813
Cardelli, J. A., Clayton, G. C., & Mathis, J. S. 1989, ApJ, 345, 245
Ceverino, D., Dekel, A., Mandelker, N., et al. 2012, MNRAS, 420, 3490
Chabrier, G. 2003, PASP, 115, 763
Chapman, S. C., Blain, A. W., Smail, I., & Ivison, R. J. 2005, ApJ, 622, 772
Charlot, S., & Fall, S. M. 2000, ApJ, 539, 718
Ciotti, L., & Bertin, G. 1999, A&A, 352, 447
Coil, A. L., Aird, J., Reddy, N., et al. 2015, ApJ, 801, 35
Conroy, C. 2013, ARA&A, 51, 393
Conroy, C., & Gunn, J. E. 2010, ApJ, 712, 833
Conroy, C., Gunn, J. E., & White, M. 2009, ApJ, 699, 486
Conroy, C., Schiminovich, D., & Blanton, M. R. 2010, ApJ, 718, 184
Contini, T., Garilli, B., Le Fèvre, O., et al. 2012, A&A, 539, A91
Courteau, S. 1997, AJ, 114, 2402
Cullen, F., Cirasuolo, M., McLure, R. J., Dunlop, J. S., & Bowler, R. a. a. 2014, MNRAS, 440, 2300
Daddi, E., Dannerbauer, H., Elbaz, D., et al. 2008, ApJ, 673, L21
Daddi, E., Dickinson, M., Morrison, G., et al. 2007, ApJ, 670, 156
Daddi, E., Bournaud, F., Walter, F., et al. 2010, ApJ, 713, 686
Dalcanton, J. J., Spergel, D. N., & Summers, F. J. 1997, ApJ, 482, 659
Dale, D. a., Aniano, G., Engelbracht, C. W., et al. 2012, ApJ, 745, 95
Damen, M., Labbé, I., Franx, M., et al. 2009, ApJ, 690, 937
Davari, R., Ho, L. C., & Peng, C. Y. 2016, ApJ, 824, 112
Davari, R., Ho, L. C., Peng, C. Y., & Huang, S. 2014, ApJ, 787, 69
Davé, R. 2008, MNRAS, 385, 147
Davé, R., Rafieferantsoa, M. H., Thompson, R. J., & Hopkins, P. F. 2017, MNRAS, 467, 115
Dekel, A., & Birnboim, Y. 2006, MNRAS, 368, 2
Dekel, A., Sari, R., & Ceverino, D. 2009, ApJ, 703, 785
Domínguez, A., Siana, B., Henry, A. L., et al. 2013, ApJ, 763, 145
Donley, J. L., Koekemoer, A. M., Brusa, M., et al. 2012, ApJ, 748, 142
Draine, B. T., Dale, D. a., Bendo, G., et al. 2007, ApJ, 663, 866
Dutton, A. A. 2009, MNRAS, 396, 121
Dutton, A. A., Conroy, C., van den Bosch, F. C., et al. 2011a, MNRAS, 345, 322
Dutton, A. A., van den Bosch, F. C., Faber, S. M., et al. 2011b, MNRAS, 410, 1660

Elbaz, D., Daddi, E., Le Borgne, D., et al. 2007, A&A, 468, 33
Elmegreen, B. G., & Elmegreen, D. M. 2006, ApJ, 650, 644
Elmegreen, D. M., Elmegreen, B. G., Marcus, M. T., et al. 2009, ApJ, 701, 306
Elmegreen, D. M., Elmegreen, B. G., Ravindranath, S., & Coe, D. A. 2007, ApJ, 658, 763
Epinat, B., Amram, P., Balkowski, C., & Marcelin, M. 2010, MNRAS, 401, 2113
Epinat, B., Amram, P., Marcelin, M., et al. 2008, MNRAS, 388, 500
Epinat, B., Contini, T., Le Fèvre, O., et al. 2009, A&A, 504, 789
Epinat, B., Tasca, L., Amram, P., et al. 2012, A&A, 539, A92
Erb, D. K., Shapley, A. E., Pettini, M., et al. 2006a, ApJ, 644, 813
Erb, D. K., Steidel, C. C., Shapley, A. E., et al. 2006b, ApJ, 647, 128
—. 2006c, ApJ, 646, 107
Fall, S. M., & Efstathiou, G. 1980, MNRAS, 193, 189
Fan, X., Strauss, M. A., Schneider, D. P., et al. 2001, AJ, 121, 54
Feldmann, R., Hopkins, P. F., Quataert, E., Faucher-Giguère, C.-A., & Kereš, D. 2016, MNRAS, 458, L14
Feldmann, R., Quataert, E., Hopkins, P. F., Faucher-Giguère, C.-A., & Kereš, D. 2017, MNRAS, 470, 1050
Finkelstein, S. L., Papovich, C., Salmon, B., et al. 2012, ApJ, 756, 164
Foreman-Mackey, D., Hogg, D. W., Lang, D., & Goodman, J. 2013, PASP, 125, 306
Foreman-Mackey, D., Price-Whelan, A., Ryan, G., et al. 2014, corner.py v0.1.1, Zenodo, doi:10.5281/zenodo.11020
Förster Schreiber, N. M., Genzel, R., Lehnert, M. D., et al. 2006, ApJ, 645, 17
Förster Schreiber, N. M., Genzel, R., Bouché, N., et al. 2009, ApJ, 706, 1364
Förster Schreiber, N. M., Genzel, R., Newman, S. F., et al. 2014, ApJ, 787, 38
Freeman, K. C. 1970, ApJ, 160, 811
Fumagalli, M., Patel, S. G., Franx, M., et al. 2012, ApJ, 757, L22
Gabor, J. M., & Bournaud, F. 2014, MNRAS, 441, 1615
Galliano, F., Dwek, E., & Chanial, P. 2008, ApJ, 672, 214
Garn, T., & Best, P. N. 2010, MNRAS, 409, 421
Genel, S., Dekel, A., & Cacciato, M. 2012, MNRAS, 425, 788
Genzel, R., Burkert, A., Bouché, N., et al. 2008, ApJ, 687, 59
Genzel, R., Tacconi, L. J., Gracia-Carpio, J., et al. 2010, MNRAS, 407, 2091
Genzel, R., Newman, S., Jones, T., et al. 2011, ApJ, 733, 101
Genzel, R., Förster Schreiber, N. M., Lang, P., et al. 2014, ApJ, 785, 75
Genzel, R., Tacconi, L. J., Lutz, D., et al. 2015, ApJ, 800, 20
Genzel, R., Schreiber, N. M. F., Übler, H., et al. 2017, Nature, 543, 397
Gnerucci, A., Marconi, A., Cresci, G., et al. 2011, A&A, 528, A88
Gonzalez-Perez, V., Lacey, C. G., Baugh, C. M., Frenk, C. S., & Wilkins, S. M. 2013, MNRAS, 429, 1609
Governato, F., Willman, B., Mayer, L., et al. 2007, MNRAS, 374, 1479
Granato, G. L., Lacey, C. G., Silva, L., et al. 2000, ApJ, 542, 710
Green, A. W., Glazebrook, K., McGregor, P. J., et al. 2014, MNRAS, 437, 1070

Grogin, N. A., Kocevski, D. D., Faber, S. M., et al. 2011, ApJS, 197, 35
Hainline, K. N., Shapley, A. E., Kornei, K. A., et al. 2009, ApJ, 701, 52
Hathi, N. P., Cohen, S. H., Ryan, R. E., et al. 2013, ApJ, 765, 88
Hayward, C. C., & Smith, D. J. B. 2015, MNRAS, 446, 1512
Hogg, D. W., Blanton, M. R., Eisenstein, D. J., et al. 2003, ApJ, 585, L5
Hogg, D. W., Blanton, M. R., Brinchmann, J., et al. 2004, ApJ, 601, L29
Hopkins, A. M., & Beacom, J. F. 2006, ApJ, 651, 142
Hopkins, P. F., Kereš, D., Oñorbe, J., et al. 2014, MNRAS, 445, 581
Ibar, E., Sobral, D., Best, P. N., et al. 2013, MNRAS, 434, 3218
Johnson, B. D., Schiminovich, D., Seibert, M., et al. 2007, ApJS, 173, 392
Juneau, S., Dickinson, M., Alexander, D. M., & Salim, S. 2011, ApJ, 736, 104
Kashino, D., Silverman, J. D., Rodighiero, G., et al. 2013, ApJ, 777, L8
Kassin, S. A., Weiner, B. J., Faber, S. M., et al. 2007, ApJ, 660, L35
—. 2012, ApJ, 758, 106
Kauffmann, G., White, S. D. M., Heckman, T. M., et al. 2004, MNRAS, 353, 713
Kauffmann, G., Heckman, T. M., Simon White, D. M., et al. 2003a, MNRAS, 341, 33
Kauffmann, G., Heckman, T. M., Tremonti, C., et al. 2003b, MNRAS, 346, 1055
Kelvin, L. S., Driver, S. P., Robotham, A. S. G., et al. 2012, MNRAS, 421, 1007
Kennicutt, R. C. 1998, ApJ, 498, 541
Kennicutt, Jr., R. C., Armus, L., Bendo, G., et al. 2003, PASP, 115, 928
Kereš, D., Katz, N., Fardal, M., Davé, R., & Weinberg, D. H. 2009, MNRAS, 395, 160
Kereš, D., Katz, N., Weinberg, D. H., & Dave, R. 2005, MNRAS, 363, 2
Kewley, L. J., Dopita, M. A., Leitherer, C., et al. 2013, ApJ, 774, 100
Kewley, L. J., Dopita, M. A., Sutherland, R. S., Heisler, C. A., & Trevena, J. 2001, ApJ, 556, 121
Koekemoer, A. M., Faber, S. M., Ferguson, H. C., et al. 2011, ApJS, 197, 36
Kong, X., Charlot, S., Brinchmann, J., & Fall, S. M. 2004, MNRAS, 349, 769
Kriek, M., & Conroy, C. 2013, ApJ, 775, L16
Kriek, M., van Dokkum, P. G., Franx, M., Illingworth, G. D., & Magee, D. K. 2009a, ApJ, 705, L71
Kriek, M., van Dokkum, P. G., Labbé, I., et al. 2009b, ApJ, 700, 221
Kriek, M., van Dokkum, P. G., Franx, M., et al. 2006, ApJ, 645, 44
—. 2007, ApJ, 669, 776
—. 2008, ApJ, 677, 219
Kriek, M., Shapley, A. E., Reddy, N. A., et al. 2015, ApJS, 218, 15
Kron, R. G. 1980, ApJS, 43, 305
Kulas, K. R., McLean, I. S., Shapley, A. E., et al. 2013, ApJ, 774, 130
Labbé, I., Bouwens, R., Illingworth, G. D., & Franx, M. 2006, ApJ, 649, L67
Laidler, V. G., Papovich, C., Grogin, N. A., et al. 2007, PASP, 119, 1325
Lang, P., Förster Schreiber, N. M., Genzel, R., et al. 2017, ApJ, 840, 92
Law, D. R., Steidel, C. C., Erb, D. K., et al. 2007a, ApJ, 669, 929
—. 2009, ApJ, 697, 2057

—. 2007b, ApJ, 656, 1
Law, D. R., Steidel, C. C., Shapley, A. E., et al. 2012a, ApJ, 759, 29
—. 2012b, ApJ, 745, 85
Leja, J., van Dokkum, P., & Franx, M. 2013, ApJ, 766, 33
Lim, P. L., Diaz, R. I., & Laidler, V. 2015, PySynphot User's Guide (Baltimore, MD: STScI), https://pysynphot.readthedocs.io/en/latest/
Liu, X., Shapley, A. E., Coil, A. L., Brinchmann, J., & Ma, C. 2008, ApJ, 678, 758
Longhetti, M., & Saracco, P. 2009, MNRAS, 394, 774
Ly, C., Malkan, M. A., Kashikawa, N., et al. 2012, ApJ, 747, L16
Madau, P., & Dickinson, M. 2014, ARA&A, 52, 415
Maiolino, R., Nagao, T., Grazian, A., et al. 2008, A&A, 488, 463
Mancini, C., Förster Schreiber, N. M., Renzini, A., et al. 2011, ApJ, 743, 86
Mannucci, F., Cresci, G., Maiolino, R., Marconi, A., & Gnerucci, A. 2010, MNRAS, 408, 2115
McCracken, H. J., Milvang-Jensen, B., Dunlop, J., et al. 2012, A&A, 544, A156
McLean, I. S., Steidel, C. C., Epps, H., et al. 2010, in Proceedings of SPIE, ed. I. S. McLean, S. K. Ramsay, & H. Takami, Vol. 7735, 77351E
McLean, I. S., Steidel, C. C., Epps, H. W., et al. 2012, in Proceedings of SPIE, ed. I. S. McLean, S. K. Ramsay, & H. Takami, Vol. 8446, 84460J
Mendez, A. J., Coil, A. L., Aird, J., et al. 2013, ApJ, 770, 40
Meurer, G. R., Carignan, C., Beaulieu, S. F., & Freeman, K. C. 1996, AJ, 111, 1551
Meurer, G. R., Heckman, T. M., & Calzetti, D. 1999, ApJ, 521, 64
Miller, S. H., Bundy, K., Sullivan, M., Ellis, R. S., & Treu, T. 2011, ApJ, 741, 115
Miller, S. H., Ellis, R. S., Sullivan, M., et al. 2012, ApJ, 753, 74
Miller, S. H., Sullivan, M., & Ellis, R. S. 2013, ApJ, 762, L11
Mo, H. J., Mao, S., & White, S. D. M. 1998, MNRAS, 295, 319
Momcheva, I. G., Lee, J. C., Ly, C., et al. 2013, AJ, 145, 47
Momcheva, I. G., Brammer, G. B., van Dokkum, P. G., et al. 2016, ApJS, 225, 27
Muzzin, A., Marchesini, D., Stefanon, M., et al. 2013a, ApJSS, 206, 8
—. 2013b, ApJ, 777, 18
Nelson, E. J., van Dokkum, P. G., Brammer, G., et al. 2012, ApJ, 747, L28
Nelson, E. J., van Dokkum, P. G., Momcheva, I., et al. 2013, ApJ, 763, L16
Nelson, E. J., van Dokkum, P. G., Förster Schreiber, N. M., et al. 2016, ApJ, 828, 27
Newman, A. B., Ellis, R. S., Treu, T., & Bundy, K. 2010, ApJ, 717, L103
Newman, S. F., Genzel, R., Förster-Schreiber, N. M., et al. 2012, ApJ, 761, 43
Newman, S. F., Genzel, R., Förster Schreiber, N. M., et al. 2013, ApJ, 767, 104
Newman, S. F., Buschkamp, P., Genzel, R., et al. 2014, ApJ, 781, 21
Noeske, K. G., Faber, S. M., Weiner, B. J., et al. 2007a, ApJ, 660, L47
Noeske, K. G., Weiner, B. J., Faber, S. M., et al. 2007b, ApJ, 660, L43
Oesch, P. A., Bouwens, R. J., Illingworth, G. D., et al. 2013, ApJ, 773, 75
Oser, L., Ostriker, J. P., Naab, T., Johansson, P. H., & Burkert, A. 2010, ApJ, 725, 2312
Osterbrock, D. E., & Ferland, G. J. 2006, Astrophysics of gaseous nebulae and active galactic

nuclei, 2nd edn. (Sausalito, CA: University Science Books)
Peng, C. Y., Ho, L. C., Impey, C. D., & Rix, H.-W. 2010, AJ, 139, 2097
Peth, M. A., Lotz, J. M., Freeman, P. E., et al. 2016, MNRAS, 458, 963
Pettini, M., Shapley, A. E., Steidel, C. C., et al. 2001, ApJ, 554, 981
Pizagno, J., Prada, F., Weinberg, D. H., et al. 2005, ApJ, 633, 844
Planck Collaboration, Ade, P. A. R., Aghanim, N., et al. 2014, A&A, 571, A15
Price, S. H., Kriek, M., Brammer, G. B., et al. 2014, ApJ, 788, 86
Price, S. H., Kriek, M., Shapley, A. E., et al. 2016, ApJ, 819, 80
Reddy, N. A., Erb, D. K., Pettini, M., Steidel, C. C., & Shapley, A. E. 2010, ApJ, 712, 1070
Reddy, N. A., Pettini, M., Steidel, C. C., et al. 2012, ApJ, 754, 25
Reddy, N. A., & Steidel, C. C. 2004, ApJ, 603, L13
—. 2009, ApJ, 692, 778
Reddy, N. A., Steidel, C. C., Fadda, D., et al. 2006, ApJ, 644, 792
Reddy, N. A., Kriek, M., Shapley, A. E., et al. 2015, ApJ, 806, 259
Roberts, M. S., & Haynes, M. P. 1994, ARA&A, 32, 115
Robitaille, T. P., Tollerud, E. J., Greenfield, P., et al. 2013, A&A, 558, A33
Rosario, D. J., Mozena, M., Wuyts, S., et al. 2013, ApJ, 763, 59
Sachs, R. K., & Wolfe, A. M. 1967, ApJ, 147, 73
Salpeter, E. E. 1955, ApJ, 121, 161
Savaglio, S., Glazebrook, K., Le Borgne, D., et al. 2005, ApJ, 635, 260
Schawinski, K., Urry, C. M., Simmons, B. D., et al. 2014, MNRAS, 440, 889
Schaye, J., Crain, R. A., Bower, R. G., et al. 2014, MNRAS, 446, 521
Sérsic, J. L. 1968, Atlas de Galaxias Australes (Cordoba, Argentina: Observatorio Astronomico)
Shapley, A. E. 2011, ARA&A, 49, 525
Shapley, A. E., Coil, A. L., Ma, C., & Bundy, K. 2005, ApJ, 635, 1006
Shapley, A. E., Erb, D. K., Pettini, M., Steidel, C. C., & Adelberger, K. L. 2004, ApJ, 612, 108
Sharples, R., Bender, R., Agudo Berbel, A., et al. 2013, The Messenger, 151, 21
Sharples, R. M., Bender, R., Lehnert, M. D., et al. 2004, in Proceedings of SPIE, ed. A. F. M. Moorwood & M. Iye, Vol. 5492, 1179
Shen, S., Mo, H. J., White, S. D. M., et al. 2003, MNRAS, 343, 978
Shivaei, I., Reddy, N. A., Shapley, A. E., et al. 2015, ApJ, 815, 98
Simard, L., & Pritchet, C. J. 1999, PASP, 111, 453
Simons, R. C., Kassin, S. A., Trump, J. R., et al. 2016, ApJ, 830, 14
Simons, R. C., Kassin, S. A., Weiner, B. J., et al. 2017, ApJ, 843, 46
Skelton, R. E., Whitaker, K. E., Momcheva, I. G., et al. 2014, ApJS, 214, 24
Snyder, G. F., Lotz, J., Moody, C., et al. 2015a, MNRAS, 451, 4290
Snyder, G. F., Torrey, P., Lotz, J. M., et al. 2015b, MNRAS, 454, 1886
Sobral, D., Best, P. N., Matsuda, Y., et al. 2012, MNRAS, 420, 1926
Springel, V., White, S. D. M., Jenkins, A., et al. 2005, Nature, 435, 629
Steidel, C. C., Rudie, G. C., Strom, A. L., et al. 2014, ApJ, 795, 165

Stott, J. P., Swinbank, A. M., Johnson, H. L., et al. 2016, MNRAS, 457, 1888
Straatman, C. M. S., Spitler, L. R., Quadri, R. F., et al. 2016, ApJ, 830, 51
Swinbank, A. M., Papadopoulos, P. P., Cox, P., et al. 2011, ApJ, 742, 11
Szomoru, D., Franx, M., Bouwens, R. J., et al. 2011, ApJ, 735, L22
Szomoru, D., Franx, M., van Dokkum, P. G., et al. 2013, ApJ, 763, 73
Tacconi, L. J., Genzel, R., Smail, I., et al. 2008, ApJ, 680, 246
Tacconi, L. J., Genzel, R., Neri, R., et al. 2010, Nature, 463, 781
Tacconi, L. J., Neri, R., Genzel, R., et al. 2013, ApJ, 768, 74
Taghizadeh-Popp, M., Fall, S. M., White, R. L., & Szalay, A. S. 2015, ApJ, 801, 14
Taylor, E. N., Franx, M., Brinchmann, J., van der Wel, A., & van Dokkum, P. G. 2010, ApJ, 722, 1
Teplitz, H. I., McLean, I. S., Becklin, E. E., et al. 2000, ApJ, 533, L65
Tomczak, A. R., Quadri, R. F., Tran, K.-V. H., et al. 2014, ApJ, 783, 85
Toomre, A. 1964, ApJ, 139, 1217
Torrey, P., Snyder, G. F., Vogelsberger, M., et al. 2015, MNRAS, 447, 2753
Tremonti, C. A., Heckman, T. M., Kauffmann, G., et al. 2004, ApJ, 613, 898
Tully, R. B., & Fisher, J. R. 1977, A&A, 54, 661
Übler, H., Förster Schreiber, N. M., Genzel, R., et al. 2017, ApJ, 842, 121
van de Sande, J., Kriek, M., Franx, M., et al. 2013, ApJ, 771, 85
van den Bosch, F. C. 2001, MNRAS, 327, 1334
van der Wel, A., Bell, E. F., Häussler, B., et al. 2012, ApJS, 203, 24
van der Wel, A., Franx, M., van Dokkum, P. G., et al. 2014a, ApJ, 788, 28
van der Wel, A., Chang, Y.-Y., Bell, E. F., et al. 2014b, ApJ, 792, L6
van Dokkum, P. G., Kriek, M., Rodgers, B., Franx, M., & Puxley, P. 2005, ApJ, 622, L13
van Dokkum, P. G., Brammer, G., Fumagalli, M., et al. 2011, ApJ, 743, L15
van Dokkum, P. G., Leja, J., Nelson, E. J., et al. 2013, ApJ, 771, L35
van Dokkum, P. G., Nelson, E. J., Franx, M., et al. 2015, ApJ, 813, 23
Vergani, D., Epinat, B., Contini, T., et al. 2012, A&A, 546, A118
Villar, V., Gallego, J., PérezâĂŘGonzález, P. G., et al. 2008, ApJ, 677, 169
Vogelsberger, M., Genel, S., Springel, V., et al. 2014, MNRAS, 444, 1518
Vogt, N. P., Forbes, D. A., Phillips, A. C., et al. 1996, ApJ, 465, L15
Watson, M. G., Schröder, A. C., Fyfe, D., et al. 2009, A&A, 493, 339
Weiner, B. J., Willmer, C. N. A., Faber, S. M., et al. 2006, ApJ, 653, 1049
Whitaker, K. E., Kriek, M., van Dokkum, P. G., et al. 2012a, ApJ, 745, 179
Whitaker, K. E., van Dokkum, P. G., Brammer, G., & Franx, M. 2012b, ApJ, 754, L29
Whitaker, K. E., Labbé, I., van Dokkum, P. G., et al. 2011, ApJ, 735, 86
Whitaker, K. E., Franx, M., Leja, J., et al. 2014, ApJ, 795, 104
White, M., & Hu, W. 1997, A&A, 321, 8
White, S. D. M., & Frenk, C. S. 1991, ApJ, 379, 52
White, S. D. M., & Rees, M. J. 1978, MNRAS, 183, 341
Wild, V., Charlot, S., Brinchmann, J., et al. 2011, MNRAS, 417, 1760
Wilkins, S. M., Bunker, A. J., Stanway, E., Lorenzoni, S., & Caruana, J. 2011, MNRAS, 417,

717

Williams, R. J., Quadri, R. F., Franx, M., van Dokkum, P., & Labbé, I. 2009, ApJ, 691, 1879

Williams, R. J., Quadri, R. F., Franx, M., et al. 2010, ApJ, 713, 738

Wisnioski, E., Glazebrook, K., Blake, C., et al. 2012, MNRAS, 422, 3339

Wisnioski, E., Förster Schreiber, N. M., Wuyts, S., et al. 2015, ApJ, 799, 209

Wright, S. A., Larkin, J. E., Law, D. R., et al. 2009, ApJ, 699, 421

Wright, S. A., Larkin, J. E., Barczys, M., et al. 2007, ApJ, 658, 78

Wuyts, S., Cox, T. J., Hayward, C. C., et al. 2010, ApJ, 722, 1666

Wuyts, S., Franx, M., Cox, T. J., et al. 2009, ApJ, 696, 348

Wuyts, S., Labbé, I., Schreiber, N. M. F., et al. 2008, ApJ, 682, 985

Wuyts, S., Labbe, I., Franx, M., et al. 2007, ApJ, 655, 51

Wuyts, S., Förster Schreiber, N. M., van der Wel, A., et al. 2011a, ApJ, 742, 96

Wuyts, S., Förster Schreiber, N. M., Lutz, D., et al. 2011b, ApJ, 738, 106

Wuyts, S., Förster Schreiber, N. M., Genzel, R., et al. 2012, ApJ, 753

Wuyts, S., Förster Schreiber, N. M., Nelson, E. J., et al. 2013, ApJ, 779, 135

Wuyts, S., Förster Schreiber, N. M., Wisnioski, E., et al. 2016, ApJ, 831, 149

Xue, Y. Q., Luo, B., Brandt, W. N., et al. 2011, ApJS, 195, 10

Yoshikawa, T., Akiyama, M., Kajisawa, M., et al. 2010, ApJ, 718, 112

Zheng, X. Z., Bell, E. F., Papovich, C., et al. 2007, ApJ, 661, L41

Appendix A

Average photometry of binned 3D-HST star-forming galaxies[1]

In addition to the stacked spectra (presented in Fig. 2.2), we also present the average photometry for each bin (see Fig. A.1). The photometry covers a much greater wavelength range, so the average photometry allows us to examine the average SED shape outside the limited range covered by the grism spectra. The photometry for each object is first normalized to match the grism normalization (see Section 2.2.3), and the central wavelength of each filter is de-redshifted using the object's grism redshift. The data are averaged within each bin, using the normalized fluxes and rest-frame wavelengths. If not all objects in the bin have coverage in a given filter, nearby filters are combined so each averaged photometric point contains at least the same number of measurements as number of objects in the bin, provided the photometry are not too widely separated in wavelength.

For comparison with the average photometry, we also show the average best-fit continuum model and the errors on the best-fit model. Plotting the continuum model and error allows us to examine the error in the amount of Balmer absorption. The average best-fit stellar population model and simulated best-fit models are calculated as described in Section 2.2.3. The $\pm 3\sigma$ continuum errors are estimated at every wavelength using the simulated continuum models.

The perturbations of the photometry of the individual objects do not lead to large variation in the stacked best-fit models, especially near the Balmer lines. The broad wavelength coverage of the photometry, specifically across the Balmer break, provides reasonably tight constraints on the average amount of Balmer absorption for the stacks.

---

[1] This chapter previously appeared as part of Price *et al.*, 2014, ApJ, 788, 86, and is reproduced with the permission of all coauthors and the copyright holder. Copyright 2014, The American Astronomical Society.

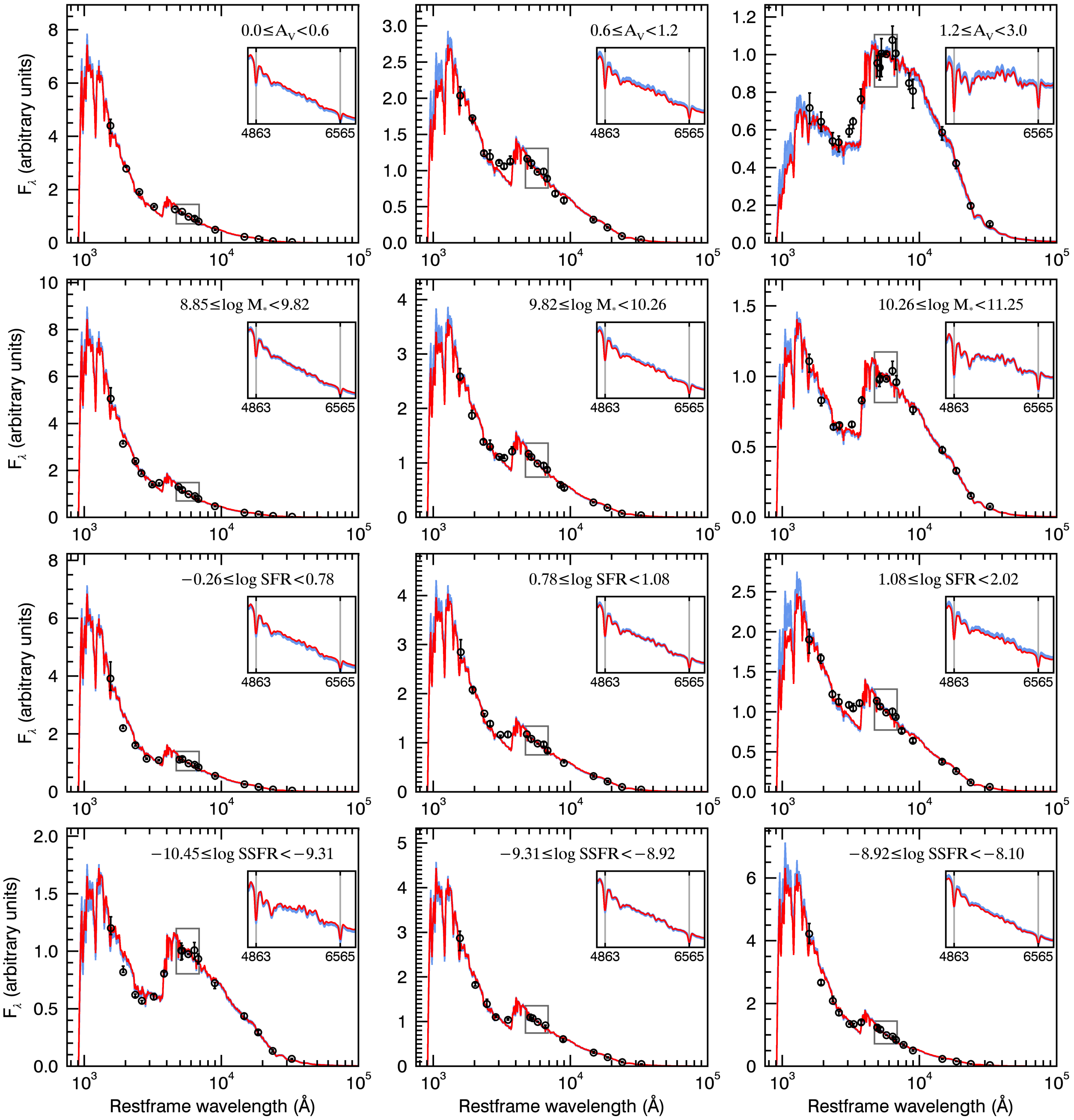

Figure A.1: Binned photometry and stacked best-fit stellar models for bins in stellar $A_{\rm V}$ (top), $\log M_*$ (second row), log SFR (third row) and log SSFR (bottom). The photometry is averaged in wavelength bins, and the error is taken to be the error on the mean. The binned photometry is shown by the black circles. The stacked best-fit FAST models are plotted in red. The 3σ errors in the stacked models are plotted in blue. The insets show the best-fit models (and 3σ errors) plotted linearly with wavelength near Hβ and Hα (denoted by left and right vertical grey lines, respectively).

Appendix B

Modeling of rotation in resolved disk galaxies[1]

B.1 Kinematic model definition

The multiplexing capabilities of MOSFIRE, which allow us to study many galaxies simultaneously, come at the price of not observing the galaxies along the kinematic major axis. Misalignment of the kinematic major and slit axes poses problems for the interpretation of kinematic measurements even for resolved disk galaxies. Issues to address include: How much kinematic information is lost because portions of the galaxy fall outside the slit? How much of the line broadening in a spatial row is caused by intrinsic velocity dispersion, and how much is caused by the inclusion of multiple line-of-sight velocities in that slice of the galaxy?

In this appendix, we describe how we model the internal kinematics of a disk galaxy, apply the appropriate inclination and position angle offset to the model, and then collapse the model along the line-of-sight and slit direction to calculate the observed kinematic signature of the object as a function of position along the slit.

To model an ideal disk galaxy with an arbitrary position angle offset with respect to the slit, we define coordinates as shown in Figure B.1. First, we consider a point on the galaxy at $(x_{\rm int}, y_{\rm int}, z_{\rm int})$, with distance in the plane of the disk of

$$r_{\rm int} = \sqrt{x_{\rm int}^2 + y_{\rm int}^2} \tag{B.1}$$

from the axis of rotation, and define the angle ψ as

$$\cos\psi = y_{\rm int}/r_{\rm int}, \tag{B.2}$$

which is the counterclockwise angle between the major axis $\hat{y}_{\rm int}$ and $(x_{\rm int}, y_{\rm int}, z_{\rm int})$ with respect to the rotation axis (see the left panel of Figure B.1). We incline our galaxy model

---

[1] This chapter previously appeared as part Price *et al.*, 2016, ApJ, 819, 80, and is reproduced with the permission of all coauthors and the copyright holder. Copyright 2016, The American Astronomical Society.

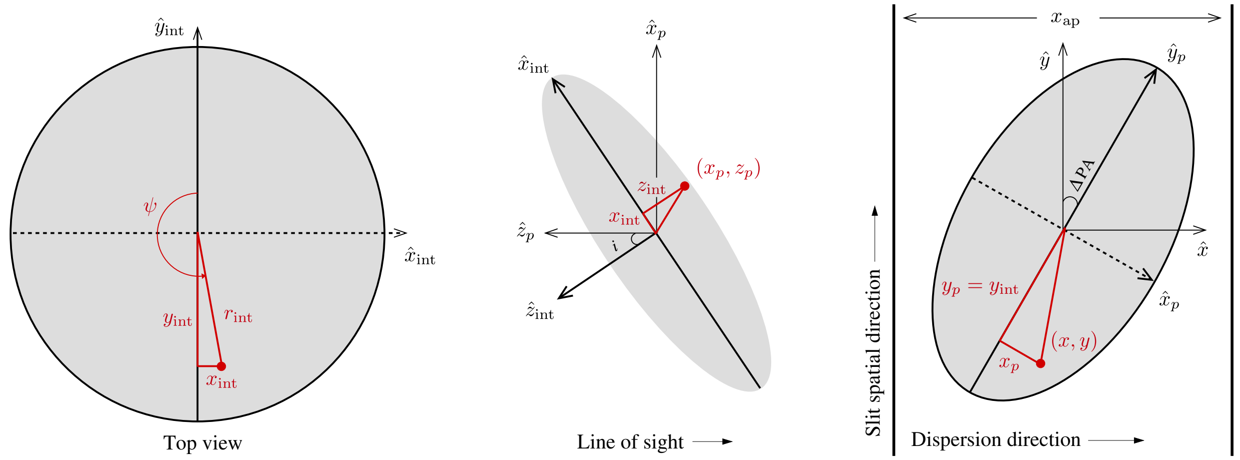

Figure B.1: Coordinate definition for an inclined disk galaxy misaligned with the slit axis. The left panel shows a top down view of the disk galaxy, depicting the $\hat{x}_{\rm int} - \hat{y}_{\rm int}$ plane, and the definition of $r_{\rm int}$ and the angle ψ. The center panel shows a side view of the inclined disk galaxy, with the line of sight extending to the right. Here we show the coordinate transformation due to inclination from the intrinsic $(x_{\rm int}, z_{\rm int})$ coordinates to the projected (x_p, z_p). The right panel shows the disk galaxy relative to the slit, including the position angle misalignment (ΔPA). The projected coordinates (x_p, y_p) are shown relative to the slit coordinates (x, y).

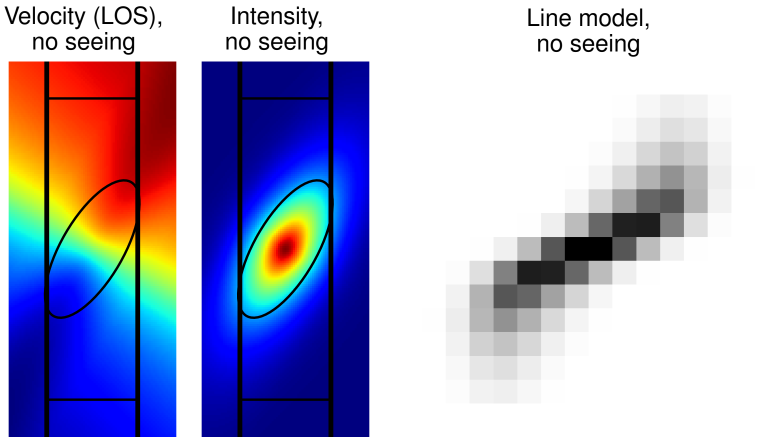

Figure B.2: Example of the line of sight (LOS) velocity field $V_{\rm obs}(x, y)$ collapsed along the LOS, z (left panel), assumed model intensity collapsed along z, $I(x, y) = \sum_z I(x, y, z)\Delta z$ (center panel), and final composite Hα emission line model (right panel) for a disk. The model shown has $\sigma_{V,0} = 0$, $R_E = 0\farcs6$, $b/a = 0.4$, $n = 1$, $\Delta\mathrm{PA} = 30^\circ$, $V_a = 200$ km/s, and $r_t = 0.4 r_s = 0.4(R_E/1.676)$. Here we ignore any seeing effects, assuming $\mathrm{FWHM}_{\rm seeing} = 0''$, and use a typical instrumental resolution width in calculating the Hα line model. The wide black lines show the slit width, $0\farcs7$, and the horizontal lines show the spatial aperture extent.

by rotating around the major axis $\hat{y}_{\text{int}}$. The inclination angle i is estimated as

$$\sin i = \sqrt{\frac{1-(b/a)^2}{1-(b/a)_0^2}}, \tag{B.3}$$

where a and b are semi-major and semi-minor axes lengths, respectively, from the Galfit parameterization. We assume an intrinsic disk axis ratio of $(b/a)_0 = 0.19$ (Miller et al. 2011). By inclining the model (see the middle panel of Figure B.1), the intrinsic coordinates are mapped to projected coordinates by

$$\begin{aligned} x_p &= x_{\text{int}} \cos i + z_{\text{int}} \sin i \\ y_p &= y_{\text{int}} \\ z_p &= -x_{\text{int}} \sin i + z_{\text{int}} \cos i. \end{aligned} \tag{B.4}$$

Finally, we apply the position angle offset, ΔPA, between the galaxy major axis and the slit. We rotate the projected model by ΔPA in the $\hat{x}_p - \hat{y}_p$ plane, mapping the projected coordinates into observed coordinates relative to the slit layout (see the right panel of Figure B.1) by

$$\begin{aligned} x &= x_p \cos \Delta\text{PA} + y_p \sin \Delta\text{PA} \\ y &= -x_p \sin \Delta\text{PA} + y_p \cos \Delta\text{PA} + y_0 \\ z &= z_p, \end{aligned} \tag{B.5}$$

where we also allow for an offset of the object center relative to the slit center in the $\hat{y}$ direction, through the parameter y_0. If we invert this set of coordinate transformations, we may calculate the intrinsic position $(x_{\text{int}}, y_{\text{int}}, z_{\text{int}})$ and intrinsic radius r_{int} within the galaxy for any given point (x, y, z) in the slit coordinate system (see Figure B.1, right panel).

To model the kinematics of a disk galaxy, we adopt the arctan model for rotation in exponential disks (Courteau 1997, Miller et al. 2011),

$$V\left(r, r_t, V_a\right) = \frac{2}{\pi} V_a \arctan\left(\frac{r}{r_t}\right), \tag{B.6}$$

where V_a is the asymptotic velocity and r_t is the turnover radius, which encodes a transition between the rising and flat parts of the rotation curve (Courteau 1997).

We must account for LOS velocity reductions due to projection effects. First, the inclination reduces the LOS velocity by a factor of $\sin i$. The LOS velocity is also reduced by $\cos\psi$, which accounts for the position of every point around the rotational axis of the galaxy. Together, the LOS velocity at each point (x, y, z) is

$$V_{\text{los}}(x, y, z) = V\left(r, r_t, V_a\right) \cdot \sin i \cdot \cos\psi, \tag{B.7}$$

where $r = r_{\text{int}}$ and $\cos\psi$ are evaluated given the slit coordinates (x, y, z). We assume the rotation is independent of z_{int}, so the model consists of nested cylindrical shells of varying radii, with each shell rotating at the appropriate velocity. We show an example LOS velocity field of a galaxy, integrated along the line-of-sight, in the left panel of Figure B.2.

However, our galaxies may not be ideal disks. Thus the galaxies may also have an intrinsic velocity dispersion component, as is the case with thickened disks. We assume the intrinsic dispersion component $\sigma_{V,0}$ is constant over the whole disk, or $\sigma(r) = \sigma_{V,0}$.

The composite kinematic profile of our model, as would be observed with slit spectroscopy, consists of the combination of all the kinematic information of the portions of the galaxy lying within each slit pixel. The relative weights of the individual kinematic components are determined by the associated intensities. Thus we must consider the light distribution of our galaxy model. We assume that the light follows a modified Sérsic intensity profile,

$$\begin{aligned} I(r, n, R_E, z_{\text{int}}) = & \\ & I_e \exp\left\{-b_n\left[\left(\frac{r}{R_E}\right)^{1/n} - 1\right]\right\} \exp\left[-\frac{z_{\text{int}}}{q_0 R_E}\right], \end{aligned} \tag{B.8}$$

where n and R_E are set to the GALFIT best-fit parameters, $b_n \approx 2n - 0.324$ (Ciotti & Bertin 1999), and approximating the vertical scale height as $z_0 = q_0 R_E$. We show a simple example intensity profile, integrated over the line-of-sight, in the center panel of Figure B.2.

The composite 2D line model is constructed by combining the line-of-sight velocity information and the assumed intensity profile. We begin by calculating the intensity $I(x, y, z)$ and observed velocity $V_{\text{los}}(x, y, z)$ at every point in our slit coordinates. To include the velocity dispersion, $\sigma_v(x, y, z)$, we assume that at every point (x, y, z) the intensity has a gaussian distribution with wavelength, with center $\lambda_{\text{los}}(x, y, z) = (1 + V_{\text{los}}(x, y, z)/c)\lambda_0$ and standard deviation $\sigma_\lambda = (\sigma_{V,0}/c)\lambda_0$. We thus expand our intensity cube into wavelength space as

$$I(x, y, z, \lambda) = \frac{I(x, y, z)}{\sigma_\lambda \sqrt{2\pi}} \exp\left[-\frac{(\lambda - \lambda_{\text{los}}(x, y, z))^2}{2\sigma_\lambda^2}\right], \tag{B.9}$$

where we normalize the intensity distribution to ensure $\int_\lambda I(x, y, z, \lambda) d\lambda = I(x, y, z)$.

We collapse the intensity over the z (line-of-sight) direction,

$$I(x, y, \lambda) = \int_{-\infty}^{+\infty} I(x, y, z, \lambda) dz, \tag{B.10}$$

to estimate the observable spectral cube, which contains the combined line-of-sight velocity and velocity dispersion at every point (x, y).

The observed intensity is convolved with the atmospheric seeing. We model the PSF as a 2D gaussian and take the blurred intensity cube to be $I(x, y, \lambda) \otimes \text{PSF}(x, y)$. The MOSFIRE spectra are taken through a slit, so there is only one dimension of spatial information. Thus we collapse the intensity model in the slit width axis, x, over the width of the slit, x_{ap} by taking

$$I(y, \lambda) = \int_{-x_{\text{ap}}/2}^{+x_{\text{ap}}/2} \left[I(x, y, \lambda) \otimes \text{PSF}(x, y)\right] dx. \tag{B.11}$$

Finally, we include the effects of instrumental resolution by convolving the model with a Gaussian with width $\sigma_{\lambda,\,\mathrm{inst}}$ (measured from the width of sky lines). An example Hα emission line model is shown in the right panel of Figure B.2.

In practice, we generate a model by performing these calculation over a finite grid of values in x, y, z, and λ. We set $x_{\mathrm{ap}} = 0\farcs7$ (MOSFIRE slit width), and y_{ap} equal to the spatial extent of the trimmed 2D spectrum to which we will compare the model. We set $z_{\mathrm{ap}} = y_{\mathrm{ap}}$, to probe the same spatial extent both along the line-of-sight and along the slit. We allow for sub-pixel sampling, and set the number of sub-pixels in x, y, z so that the sub-pixel width in each dimension is nearly equal, while preserving an integer number of whole pixels in the spectrum spatial direction, y. Additionally, we pad the grid by $0.5\,\mathrm{FWHM}_{\mathrm{seeing}}$ arcsec on both sides in the x and y directions, to accurately calculate the seeing-convolved intensity over the full $x_{\mathrm{ap}}, y_{\mathrm{ap}}$. We sample the model at the wavelengths of the associated 2D spectrum in the range around Hα. The array $I(y, \lambda)$ is oversampled in the y direction. Finally, we re-bin the data to match the observed spatial pixel size by adding the sub-pixels in y. The final model $f_{\mathrm{model}}(y, \lambda)$ now samples the intensity at the exact spatial positions y and wavelengths λ covered by the data.

The resulting model of the observed kinematic signature of a disk galaxy depends on fixed parameters ΔPA, n, R_E, and b/a, all derived from the Sérsic fits performed using GALFIT. The seeing FWHM and instrument resolution are additional fixed parameters. Because we do not probe the flat part of the rotation curves for our galaxy sample, we fix y_0 and λ_0. We mask missing pixels and skylines for the 2D spectrum, collapse over λ and fix y_0 to the peak of a Gaussian fit. We similarly collapse over y to fit λ_0. The free parameters are V_a, r_t, and $\sigma_{V,0}$. V_a and r_t describe the arctan disk rotation model, while $\sigma_{V,0}$ introduces additional broadening in the wavelength direction.

B.2 Procedure for measuring kinematics from 2D emission lines

In this appendix we describe how we measure rotation and dispersion velocities from Hα emission lines that exhibit resolved rotation. For each object, we start by subtracting out the continuum from the Hα 2D spectrum. First, we measure the continuum slope of the optimally extracted 1D spectrum using a noise-weighted linear fit in the wavelength range $6454.6\text{Å} \leq \lambda/(1+z_{\mathrm{MOS}}) \leq 6674.6\text{Å}$, where we mask the H$\alpha$ and [NII] lines from $6533.6\text{Å} \leq \lambda/(1+z_{\mathrm{MOS}}) \leq 6599.6\text{Å}$. We then assume that the slope of the continuum in each spatial slice of the 2D spectrum is equal to the 1D continuum slope value, and perform a weighted linear fit in each spatial slice where only the intercept is allowed to vary. We subtract the best-fit continuum from each spatial slice to leave only the Hα line emission. Next, we trim the continuum-subtracted emission line 2D spectrum to the wavelength range $6555.6\text{Å} \leq \lambda/(1+z_{\mathrm{MOS}}) \leq 6573.6\text{Å}$, to exclude the [NII] emission lines from our resolved line fitting. As we exclude objects with outflows or AGN with very broad emission lines, [NII] contamination within this trimmed range should be minimal. We also trim the spectrum in the spatial direction so that only the positive emission line is retained.

To ensure that the model comparisons include only high S/N portions of each spectrum, we construct a mask $m(x, y)$, where x is the wavelength dispersion direction of the spectrum and y is the spatial direction. First, we mask pixels with missing data. Second, we mask rows where $\mathrm{S/N}(y) < 2$, leaving only contiguous rows with high S/N unmasked. The row S/N is estimated to be the total row flux over the total row error, with the pixel errors added in quadrature. We mask pixels with missing data or columns affected by skyline contamination in this S/N measurement. The columns affected by skyline contamination are identified as those where the total column error, added in quadrature, is 2 and 3 times greater than the median error of all columns in the spectrum, for the K and H bands, respectively.[2] We do not mask pixels affected by skyline contamination when fitting the models to the data, as these pixels are down-weighted in the fitting procedure because of their large errors relative to the non-contaminated pixels.

To find the best-fit model to the data, we first match the model intensity to the data intensity profile. We perform a weighted least squares fit of the model $f_{\mathrm{model}}(x, y)$ to the data $f(x, y)$ (with errors $\sigma_f(x, y)$) at each y and measure the appropriate scaling $S(y)$ between the model and data spatial rows

$$S(y) = \frac{\sum_x m(x,y)\,[f(x,y) f_{\mathrm{model}}(x,y)/\sigma_f(x,y)^2]}{\sum_x m(x,y)\,[f_{\mathrm{model}}(x,y)^2/\sigma_f(x,y)^2]}, \tag{B.12}$$

where we mask missing data and columns contaminated by skyline emission with $m(x, y)$ (discussed in Section 3.3.1). We do not fix the scaling to the convolved and integrated (in the slit direction) Galfit profile, as the line emission may be distributed differently (see Nelson et al. 2012). Nonetheless, in modeling the kinematics, we adopt a Sérsic stellar light profile to determine the intensity-weighted velocities. In Section 3.5.6, we show that most objects have similar stellar light and Hα profiles, and also discuss the implications for the modeling results when the Hα profile differs from the stellar light profile.

The goodness-of-fit of the model is determined using a weighted χ^2 value. We choose the following weighting scheme to up-weight lower S/N rows, so the information in the fainter parts of the rotation curve is not lost:

$$w_y = [\mathrm{S/N}(y)]^{-1}. \tag{B.13}$$

The weighted goodness-of-fit criterion is then

$$\chi^2_{\mathrm{weighted}} = \sum_{x,y} w_y \left[m(x,y) \frac{f(x,y) - S(y) f_{\mathrm{model}}(x,y)}{\sigma_f(x,y)} \right]^2 \tag{B.14}$$

where we mask missing data and low S/N rows with $m(x, y)$, and the spectrum is dispersed in the x direction.

---

[2] The sky background in the K band is higher than in H, so we adopt a less conservative skyline identification criterion for the K band.

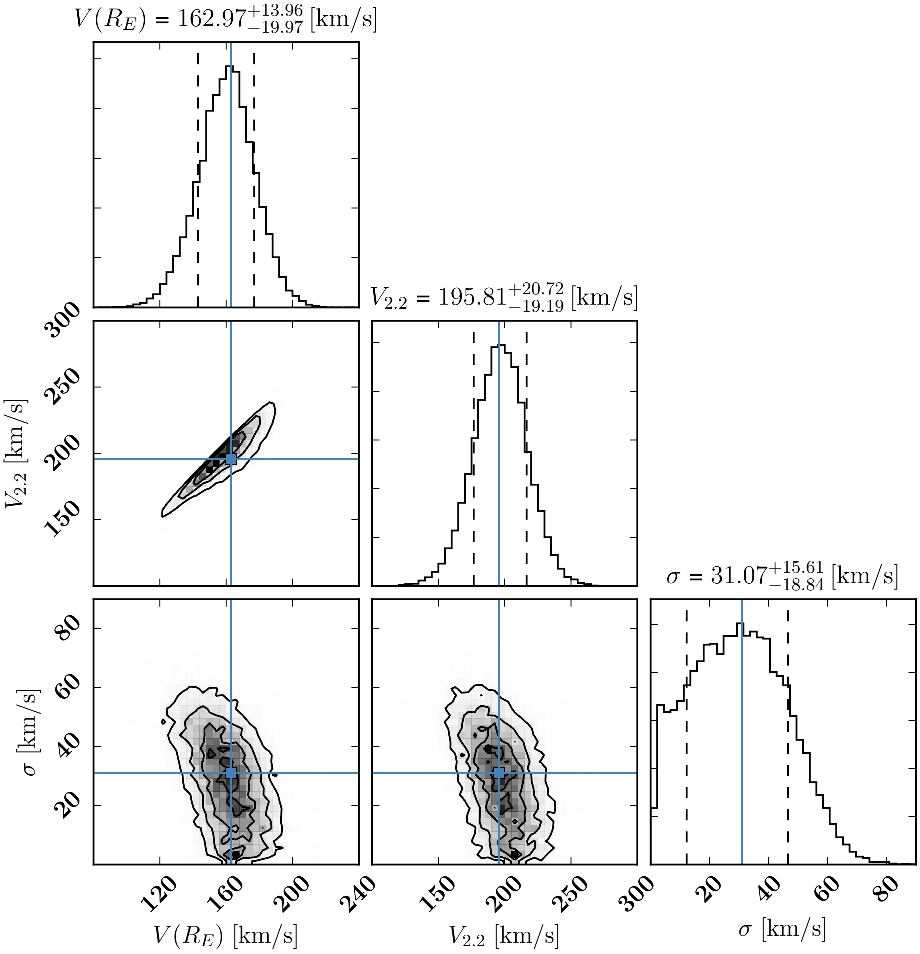

Figure B.3: Example posterior distribution for $V(R_E)$, $V_{2.2}$, and $\sigma_{V,0}$ for COSMOS-13701 (the second galaxy shown in Figures 3.2 and 3.16). The best-fit value of each parameter is taken to be the peak of the respective marginalized posterior distributions, and are shown as the blue lines in the histograms. The lower and upper 68% confidence intervals on each parameter are shown as the dashed black lines. The best-fit values are also shown as blue lines and blue squares in the various two-parameter posterior plots. Figure made using `corner.py` (Foreman-Mackey et al. 2014).

We use the `python` MCMC package, `emcee` (Foreman-Mackey et al. 2013) to find the best-fit models and confidence intervals. We define flat priors $\log p(X)$ for each parameter X (V_a, r_t, $\sigma_{V,0}$), with bounds calculated based on the spatial and wavelength coverage of the trimmed 2D spectrum, yielding composite prior $\log p(V_a, r_t, \sigma_{V,0}) = \Sigma_{\{X=V_a,r_t,\sigma_{V,0}\}} \log p(X)$. The log posterior probability is taken to be

$$\begin{aligned}\log P(V_a, r_t, \sigma_{V,0}|\lambda, f) = \\ \log \mathcal{L}(f|\lambda, V_a, r_t, \sigma_{V,0}) + \log p(V_a, r_t, \sigma_{V,0}) + \text{const},\end{aligned} \tag{B.15}$$

with log likelihood probability $\log \mathcal{L} = -0.5\chi^2_{\text{weighted}}$.

The rotation curve turnover is not well constrained in our data, so there is a degeneracy in the values of V_a and r_t. However, the values of $V(R_E)$ and $V_{2.2} = V(2.2r_s)$ are much better constrained. Thus we calculate $V(R_E)$ and $V_{2.2}$ for each pair of (V_a, r_t) values in the posterior sampling, to determine the posterior distributions on $V(R_E)$ and $V_{2.2}$. We take the best-fit values of $V(R_E)$, $V_{2.2}$, and $\sigma_{V,0}$ to be the peaks of the respective marginalized posterior distributions, and calculate the confidence intervals using the lower and upper 68-percentile bounds of the posterior distributions (e.g., see Figure B.3).

B.3 Position-velocity diagrams for galaxies with detected rotation

To demonstrate the agreement between the observed and modeled kinematics, we measure velocity as a function of position from both the observed and modeled 2D spectra for each of the 35 galaxies with detected rotation. For each unmasked, high S/N row (see Appendix B.2), we fit the flux $f(x, y)$ with a Gaussian and determine the central wavelength, $\lambda(y)$, constraining λ to fall within $\pm 1.25\,\text{FWHM}_{\lambda,\,\text{1D},\,\text{obs}}$ of the fixed central wavelength λ_0 (see Appendix B.1). We then calculate $V_{\text{obs}}(y)$ from $\lambda(y)$ and λ_0. We estimate the errors in $V_{\text{obs}}(y)$ by creating 500 realizations in which we perturb the flux $f(x, y)$ by the errors $\sigma_f(x, y)$, and repeat the fitting procedure on each realization. Finally, we correct the observed velocities for inclination, yielding $V_{\text{obs}}(y)/(\sin i)$. The velocity profiles are shown in Figure B.4. The observed and model velocity profiles are in good agreement, suggesting that our modeling approach works well.

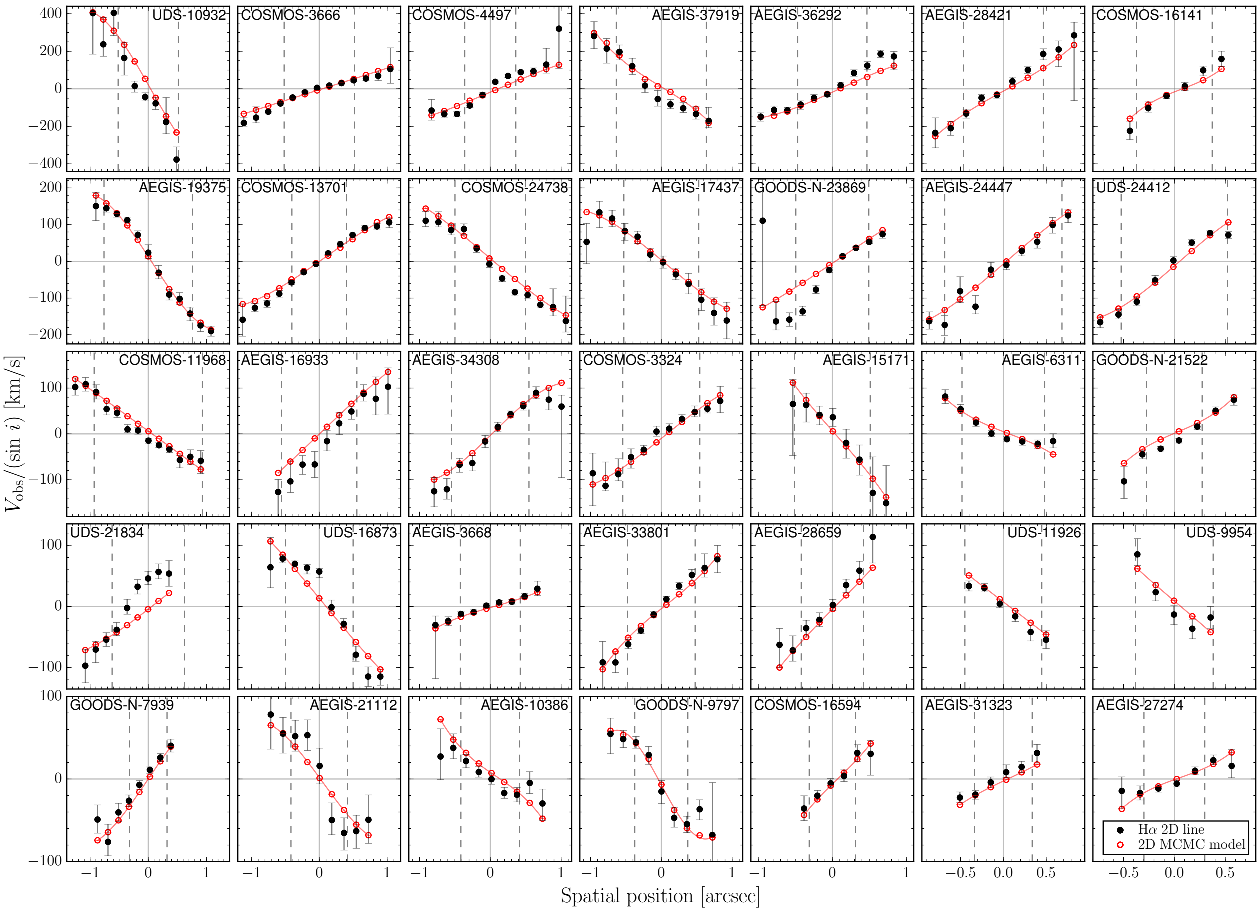

Figure B.4: Position-velocity diagrams for the 35 MOSDEF galaxies with detected rotation. The velocity profile corrected for inclination ($V_{\rm obs}(y)/(\sin i)$; y axis) is measured versus the spatial position (x axis) from the 2D Hα emission line spectrum (black circles) and from the best-fit 2D line model (open red circles) for each object. The error bars do not include uncertainties from the inclination correction. For reference, we fit a third order polynomial (red line) to the model velocity profile. The vertical grey dashed lines show the projected effective radius convolved to match the MOSFIRE seeing. The velocity profiles of the observed and model spectra are in good agreement.

Appendix C

Inclination and aperture correction for unresolved disk galaxies[1]

If a disk galaxy is too small, it will be spatially unresolved and its rotation will not be detected. Additionally, some of the kinematic information may be missing because of slit losses. Furthermore, as our 1D spectra are optimally extracted, the observed velocity profile will depend on the inclination angle and the angle between the slit and the major axis of the galaxy. In this appendix we estimate the correction between the intrinsic kinematics and the kinematics within the extracted aperture for galaxies without detected rotation, assuming that they are rotationally supported disk galaxies. We make models of disk galaxies that account for variable inclination angles and variable ΔPA and use these models to calculate the integrated RMS velocity within the slit. We follow the general method presented in Appendix B of van de Sande et al. (2013) to calculate the aperture correction for a given kinematic and brightness profile.

The kinematics of the disk galaxy model are defined in the same way as in Appendix B. The slit coordinate system relative to the intrinsic galaxy coordinates is defined following Equations B.4, B.5. We assume that the rotation can be described with the arctan model (Equation B.6). As we have no spatial information, we must assume a radial profile for the rotation curve, that is determined entirely through turnover radius, r_t. Based on the findings of Miller et al. (2011), we set $r_t = 0.4\, r_s = 0.4(R_E/1.676)$. Following Equation B.7, the relative line-of-sight radial profile of the model rotation curve is then $V_{\rm los}(x, y, z)/V(R_E)$, in which we do not assume an absolute velocity scale. Since our galaxies may not be ideal disks, we assume a simple constant dispersion velocity $\sigma_{V,0}$ and a fixed value of $(V/\sigma_{V,0})_{R_E} = V(R_E)/\sigma_{V,0}$.

Following Cappellari (2008), we assume the observed velocity dispersion is the square root of the second velocity moment, i.e. the RMS velocity, $V_{\rm RMS}^2 = \sigma^2 + V^2$. To obtain relative

---

[1] This chapter previously appeared as part Price *et al.*, 2016, ApJ, 819, 80, and is reproduced with the permission of all coauthors and the copyright holder.

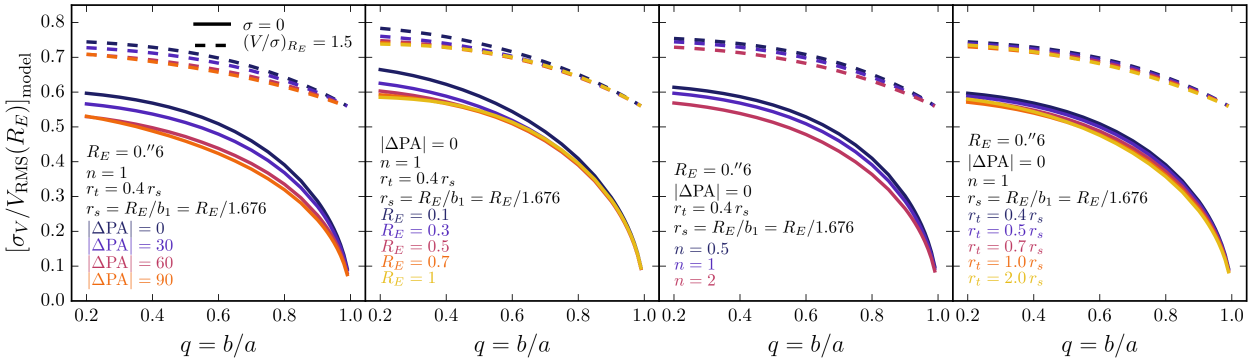

Figure C.1: Aperture corrections, $\sigma_{V,\,\mathrm{model}}/V_{\mathrm{RMS}}(R_E)_{\mathrm{model}}$, for disk galaxies without resolved rotation, as a function of (a) ΔPA, (b) R_E, (c) n, and (d) r_t. We show the aperture correction assuming no intrinsic velocity dispersion ($\sigma_{V,0}=0$, solid lines) and partial rotational support ($(V/\sigma_{V,0})_{R_E}=1.5$, dashed lines). The non-variable parameters in each panel are set to $\Delta\mathrm{PA}=0$, $R_E=0.''6$, $n=1$, and $r_t=0.4r_s=0.4(R_E/1.676)$. We assume a seeing FWHM of $0.''6$ for every model.

quantities, we divide both sides by $V(R_E)$:

$$\left(\frac{V_{\mathrm{RMS,\,los}}(x,y,z)}{V(R_E)}\right)^2=\left(\frac{1}{(V/\sigma_{V,0})_{R_E}}\right)^2+\left(\frac{V_{\mathrm{los}}(x,y,z)}{V(R_E)}\right)^2 \tag{C.1}$$

The total observed velocity dispersion of a galaxy is the combination of the intensity-weighted velocity dispersions at every point of the galaxy, so we must also assume a light profile to include in our models. As in Appendix B, we assume a modified Sérsic intensity profile $I(r,n,R_E,z_{\mathrm{int}},\sigma_z)$ (Equation B.8).

We calculate the intensity-weighted dispersion within the aperture from the RMS velocity relative to $V(R_E)$, following Equation B9 of van de Sande et al. (2013):

$$\left(\frac{\sigma_{V,\,\mathrm{model}}}{V(R_E)}\right)^2= \tag{C.2}$$
$$\frac{\sum\limits_{-X}^{X}\sum\limits_{-Y}^{Y}\left(\left[\sum\limits_{-Z}^{Z}\left(\frac{V_{\mathrm{RMS,los}}(x,y,z)}{V(R_E)}\right)^2 I(x,y,z)\Delta z\right]\otimes\mathrm{PSF}\right)g(y)\Delta x\Delta y}{\sum\limits_{-X}^{X}\sum\limits_{-Y}^{Y}\left(\left[\sum\limits_{-Z}^{Z}I(x,y,z)\Delta z\right]\otimes\mathrm{PSF}\right)g(y)\Delta x\Delta y}$$

Here we define $X=\frac{1}{2}x_{\mathrm{ap}}$, $Y=\frac{1}{2}y_{\mathrm{ap}}$, and $Z=\frac{1}{2}z_{\mathrm{ap}}$, and define $V_{\mathrm{RMS,los}}/V(R_E)$ from Equation C.1. We model the PSF as a 2D Gaussian with FWHM equal to that atmospheric seeing FWHM, and adopt the same spatial weighting function $g(y)$ as used in extracting the MOSDEF 1D spectra.

The dynamical masses of disk galaxies are calculated using the velocity at a specific radius, i.e. $V(R_E)$, instead of an integrated velocity dispersion. Thus, instead of calculating σ_e, the intrinsic intensity-weighted velocity dispersion within the effective radius R_E, we calculate the RMS velocity of the model at $r = R_E$, $V_{\mathrm{RMS}}(R_E)_{\mathrm{model}} = \sqrt{\sigma_{V,0}^2 + V(R_E)^2}$, relative to $V(R_E)$, which we write as:

$$\frac{V_{\mathrm{RMS}}(R_E)_{\mathrm{model}}}{V(R_E)} = \sqrt{1 + \frac{1}{(V/\sigma_{V,0})_{R_E}^2}}. \tag{C.3}$$

The observed velocity dispersion corrected for both aperture and inclination effects, and converted to a RMS velocity, is the combination of Equations C.2 and C.3:

$$V_{\mathrm{RMS}}(R_E)_{\mathrm{corr}} = \sigma_{\mathrm{obs}} \left(\frac{\sigma_{V,\,\mathrm{model}}}{V_{\mathrm{RMS}}(R_E)_{\mathrm{model}}} \right)^{-1}, \tag{C.4}$$

with

$$\frac{\sigma_{V,\,\mathrm{model}}}{V_{\mathrm{RMS}}(R_E)_{\mathrm{model}}} = \left(\frac{\sigma_{V,\,\mathrm{model}}}{V(R_E)} \right) \frac{(V/\sigma_{V,0})_{R_E}}{\sqrt{1 + (V/\sigma_{V,0})_{R_E}^2}}. \tag{C.5}$$

To calculate the correction $\sigma_{V,\,\mathrm{model}}/V_{\mathrm{RMS}}(R_E)_{\mathrm{model}}$ for individual galaxies, we use the best-fit GALFIT parameters for n, $R_E = a$ (the semi-major axis), and $q = b/a$. We set $x_{\mathrm{ap}} = 0\farcs7$, the slit width for all observations, and set $y_{\mathrm{ap}} = y_{\mathrm{extract}}$, the actual width used to extract the 1D spectra. We choose $z_{\mathrm{ap}} = y_{\mathrm{ap}}$, to probe the same spatial extent in the line-of-sight direction as we probe along the slit.

In practice, we initially pad coordinate grids in the x, y directions by $0.5\,\mathrm{FWHM}_{\mathrm{seeing}}$ arcsec, to accurately consider the convolution with the atmospheric seeing across the aperture edges. We include these pixels when calculating the collapse over z and the convolution with the seeing, then remove the padded pixels for the final sum within the aperture. We sample the model over a large number of pixels, and choose the pixel sizes so they are nearly equal in all dimensions, $\Delta y = \Delta z \approx \Delta x$, with the constraint that there must be an integer number of pixels within x_{ap} and y_{ap}.

The effects of varying the model parameters b/a, $\Delta\mathrm{PA}$, R_E, n, and r_t are demonstrated in Figure C.1. In all cases, we assume a typical seeing of $0\farcs6$. We adopt $x_{\mathrm{ap}} = 0\farcs7$, the slit width for all MOSDEF observations, and set $y_{\mathrm{ap}} = 4R_{E,\,\mathrm{proj+conv}}$, to approximate dependance of aperture size on the object size, misalignment, and seeing that is incorporated in the data extraction method.

The inclination angle has the largest influence on the correction value. At a fixed axis ratio, the inclusion of a finite $(V/\sigma_{V,0})_{R_E}$ value causes the largest difference in the aperture correction, as the intrinsic velocity dispersion increases the observed LOS velocity dispersion. The position angle offset causes larger variations for more edge-on disks ($b/a \approx (b/a)_0$) than for disks closer to face-on ($b/a \approx 1$), as the more face-on disks are much closer to being round, and the amount of the disk falling outside of the slit for any $\Delta\mathrm{PA}$ is similar. Variations with the Sérsic index n reflect how the different intensity profiles weight the velocity distribution. Changes of the assumed r_t affect the rotational velocity profile, with larger r_t moving the velocity turnover to larger radii. When combined with the Sérsic intensity weighting, this leads to smaller integrated velocity values. Finally, when the disk is aligned with the major axis, the aperture correction varies little with the effective radius R_E. The aperture correction varies more with R_E when combined with larger ΔPA offsets.